Forschungsbericht 2024-14

Aerodynamic Analyses of Retro Propulsion Assisted Descent and Landing of Launcher Configurations

Ansgar Marwege

Deutsches Zentrum für Luft- und Raumfahrt
Institut für Aerodynamik und Strömungstechnik
Abteilung Über- und Hyperschalltechnologien
Köln

DLR Deutsches Zentrum für Luft- und Raumfahrt

Aerodynamic Analyses of Retro Propulsion Assisted Descent and Landing of Launcher Configurations

Aerodynamische Analysen zur Rückführung und Landung von Raumtransportsystemen mit Hilfe von Retro-Propulsion

Von der Fakultät für Maschinenwesen der Rheinisch-Westfälischen Technischen Hochschule Aachen zur Erlangung des akademischen Grades eines Doktors der Ingenieurwissenschaften genehmigte Dissertation

vorgelegt von

Ansgar Georg Marwege

Berichter: Univ.-Prof. Dr.-Ing. Karl Alexander Heufer
Hon.-Prof. Dr.-Ing. Ali Gülhan

Tag der mündlichen Prüfung: 28.03.2024

Forschungsbericht 2024-14

Aerodynamic Analyses of Retro Propulsion Assisted Descent and Landing of Launcher Configurations

Ansgar Marwege

Deutsches Zentrum für Luft- und Raumfahrt
Institut für Aerodynamik und Strömungstechnik
Abteilung Über- und Hyperschalltechnologien
Köln

148 Seiten
139 Bilder
17 Tabellen
109 Literaturstellen

Deutsches Zentrum
DLR für Luft- und Raumfahrt

Herausgeber:

Deutsches Zentrum
für Luft- und Raumfahrt e. V.
Wissenschaftliche Information
Linder Höhe
D-51147 Köln

ISSN 1434-8454
ISRN DLR-FB-2024-14
Erscheinungsjahr 2024
DOI: 10.57676/ygyq-nt58

Retro-Propulsion, Windkanalversuche, vertikales Landen, wiederverwendbare Raumtransportsysteme, Aerodynamik

Ansgar MARWEGE
DLR, Institut für Aerodynamik und Strömungstechnik, Abteilung Über- und Hyperschalltechnologien, Köln

Aerodynamische Analysen zur Rückführung und Landung von Raumtransportsystemen mit Hilfe von Retro-Propulsion

RWTH Aachen University

Wiederverwendbare Raumtransportsysteme die mit Hilfe von „Retro-Propulsion“ beim Abstieg verzögert und vertikal gelandet werden, gelten als der nächste notwendige Schritt in der Evolution der Europäischen Trägersysteme um diese kosteneffizienter und kompetitiver zu machen. „Retro-Propulsion“ beschreibt dabei die Verzögerung des Fahrzeugs mit durch gegen die Flugrichtung gerichteten Triebwerken.
Im Projekt „RETALT“ wurden die Schlüsseltechnologien für diese mit Retro-Propulsion landenden Systeme untersucht. Diese Arbeit konzentriert sich auf die stationären und instationären aerodynamischen Phänomene, die während der drei Phasen des Abstiegs und der Landung auftreten. Die drei Phasen sind der Wiedereintrittszündung, die aerodynamische Phase und die Landezündung. Die Wiedereintrittszündung wurde im Hyperschallwindkanal Köln (H2K) getestet, die aerodynamische Phase in der Trisonischen Messstrecke Köln (TMK) und die Landezündung in der Vertikalen Messstrecke Köln (VMK). Die Abgasstrahlen in den Schubphasen wurden mit Druckluft simuliert.
Für die aerodynamische Phase wurde eine analytische Methode zur Auslegung der Steuerflächen entwickelt. Diese wurde mit Windkanalexperimenten validiert und eine gute Übereinstimmung gezeigt. Die Wiedereintrittszündung und die Landezündung wurden hinsichtlich ihrer stationären und instationären Strömungsphänomene untersucht. Für die Wiedereintrittszündung sind die dominierenden Ähnlichkeitsparameter der Schubkoeffizient und der Ruhedruck stromab des Bugstoßes. Die bestimmenden Ähnlichkeitsparameter für die Landezündung sind das Umgebungsdruckverhältnis (Ambient Pressure Ratio, APR) und das Impulsstromdichteverhältnis (Momentum Flux Ratio, MFR). Vor allem beim Landeanflug wurden stark dominante Frequenzen gefunden, die in Bereichen der kritischen Strouhalzahlen von Heckströmungen bei Aufstiegskonfigurationen liegen. Die normierten Druckschwankungen während des Landeanflugs sind eine Größenordnung größer als bei diesen Heckströmungen.

Retro-Propulsion, Wind Tunnel Tests, Vertical Landing, Reusable Launchers, Aerodynamics
(Published in English)

Ansgar MARWEGE
German Aerospace Center (DLR), Institute of Aerodynamics and Flow Technologies, Cologne

Aerodynamic Analyses of Retro Propulsion Assisted Descent and Landing of Launcher Configurations

RWTH Aachen University

Reusable launchers which are descending and landing vertically with the aid of firing the engines against the flight velocity, the so-called retro propulsion, are considered the next step in the evolution of European launchers to make them more cost efficient and competitive.
In the RETALT project key technologies for these retro propulsive landing configurations have been investigated. This thesis is focused on the steady and unsteady aerodynamic phenomena occurring during the three main flight phases of the descent and landing trajectory, namely, the reentry burn, the aerodynamic phase, and the landing burn.
The reentry burn was tested in the Hypersonic Wind Tunnel Cologne (H2K), the aerodynamic phase was tested in the Trisonic Wind Tunnel Cologne (TMK), and the landing burn was tested in the Vertical Free-Jet Facility Cologne (VMK). The exhaust plumes in the propelled phases were simulated with cold gas jets with pressurized air.
For the aerodynamic phase, an analytical model was developed for the design of the Aerodynamic Control Surfaces (ACS), which was validated against results of wind tunnel experiments and showed good agreement. The reentry burn and the landing burn were investigated regarding their steady and unsteady flow features. For the reentry burn the main scaling parameters are the thrust coefficient and the total pressure downstream of the bow shock. The main scaling parameters for the landing burn are the Ambient Pressure Ratio (APR) and the Momentum Flux Ratio (MFR). Strongly dominant frequencies were found especially during the landing approach, which are in the range of critical Strouhal numbers found for near-wake flows of ascent configurations. The normalized pressure fluctuations during the landing approach are one order of magnitude larger than for these near-wake flows.

Preface

At the time of writing my thesis, I realized that it was only possible for me to perform this work with the support of so many people.
It started with the first wind tunnel test series on CALLISTO, where Martin Achner, introduced me to force and moment measurements and the whole post-processing chain. He stayed with me until late in the evening to check every bit of the data. Thomas Gawehn taught me all the details beyond the measurements themselves, how to perform calibrations and how to assess uncertainties. When we started to work on RETALT, I really enjoyed working together with Josef Klevanski and Johannes Riehmer, who taught me the entire launcher design procedure. Daniel Kirchheck taught me how to design a project, set up schedules, assess costs, manage communication, and later, how to design wind tunnel models and set up measurements. Markus Miketta, designed the wind tunnel test models in detail and let the most challenging dreams come true. I also learned a lot from Prof. Dr. Ali Gülhan, who taught me how to put together a team, negotiate in a fair way, motivate people, and manage a project. I really appreciate the freedom I had in shaping the project and my work, and he always had an open door and was very approachable when I had questions or needed feedback on both the management and scientific sides. I also greatly appreciate the great teamwork and all the feedback I received from the colleagues working with me on the RETALT project at the DLR and at the partner companies. I especially want to mention Jan Vos, who was responsible for dissemination and communication in the project and reviewed all my papers before submission. He is a very good and quick reviewer. In preparing the retro propulsion experiments, Kevin Gutsche, was a Master's student supervised by me. Already back then he was a great researcher. He created a very good and fundamental understanding of the dominant effects for me to build on.
To not lose track of the PhD thesis itself, Dirk Allofs and I founded our PhD-Group. We scheduled milestones, discussed technical details, and motivated each other. Later on, Patrick Seltner and Daniel Kirchheck also joined this group. I am very grateful for these exchanges and the feedback. I also got a lot of feedback especially on frequency analysis and POD from Dennis Daub and Pascal Marquardt, and on fundamental aerodynamics from Dominik Neeb, Sebastian Willems and Thomas Thiele, which I am very grateful for.
In writing the thesis itself, I want to thank Prof. Dr. Ali Gülhan for supervising me, discussing the physics behind retro propulsion flow fields, the data evaluation, and the structure of the work. Equally, I want to thank Prof. Dr. Alexander Heufer for his support. He always read my work with great interest and provided very detailed comments. I really enjoyed the exchange on the thesis and learned a lot from it.
I also want to thank my family for their support. They were always interested in my progress and gave advice on how to solve challenges. A special thanks goes to Rebecca Marwege, my sister who is also writing a PhD thesis (even though in political theory), for the exchange on our progress and challenges, and proofreading of my work.
Finally, I don't want to forget my friends who supported me, especially mentally, by reminding me about the work life balance. I especially want to thank my flatmates, Thomas Systermans and Richard Orth, who supported me a lot during the thesis by always having an open ear for my stories and problems.
There are many other people I would like to thank for their support, including the colleagues at the Department of Supersonic and Hypersonic Technologies, the researchers, the wind tunnel engineers, the wind tunnel technicians, the controllers of our department, and the administration and the lawyers making all this possible. Listing them all here would simply not fit on one page.

Thank you all for all your support!

Ansgar Marwege

Abstract

Reusable launchers which are descending and landing vertically with the aid of firing the engines against the flight velocity, the so-called retro propulsion, are considered the next step in the evolution of European launchers to make them more cost efficient and competitive.
In the RETALT project key technologies for these retro propulsive landing configurations have been investigated. This thesis is focused on the steady and unsteady aerodynamic phenomena occurring during the three main flight phases of the descent and landing trajectory, namely, the reentry burn, the aerodynamic phase, and the landing burn. The reentry burn is a deceleration maneuver at high altitudes with several active engines, which serves to lower the dynamic pressure and heat loads in the aerodynamic phase. The aerodynamic phase is the unpropelled phase of the trajectory. The landing burn is the final retro propulsive maneuver which brings the velocity of the vehicle down to zero at touch down.
The reentry burn was tested in the Hypersonic Wind Tunnel Cologne (H2K), the aerodynamic phase was tested in the Trisonic Wind Tunnel Cologne (TMK), and the landing burn was tested in the Vertical Free-Jet Facility Cologne (VMK). The exhaust plumes in the propelled phases were simulated with cold gas jets with pressurized air. Proper Orthogonal Decomposition (POD) of high speed Schlieren recordings and spectral analyses of high frequency pressure measurements were performed and an average modal solution was proposed to describe the strongly unsteady flow field, especially in the propelled phases.
For the aerodynamic phase, an analytical model was developed for the design of the Aerodynamic Control Surfaces (ACS), which was validated against results of wind tunnel experiments and showed good agreement. The reentry burn and the landing burn were investigated regarding their steady and unsteady flow features. For the reentry burn the main scaling parameters are the thrust coefficient and the total pressure downstream of the bow shock. Configurations with different numbers of engines can be scaled with the total thrust coefficient. The main scaling parameters for the landing burn are the Ambient Pressure Ratio (APR) and the Momentum Flux Ratio (MFR). Strongly dominant frequencies were found especially during the landing approach, which are in the range of critical Strouhal numbers found for near-wake flows of ascent configurations. The normalized pressure fluctuations during the landing approach are one order of magnitude larger than for these near-wake flows.

Zusammenfassung

Wiederverwendbare Raumtransportsysteme die mit Hilfe von „Retro-Propulsion“ beim Abstieg verzögert und vertikal gelandet werden, gelten als der nächste notwendige Schritt in der Evolution der Europäischen Trägersysteme um diese kosteneffizienter und kompetitiver zu machen. „Retro-Propulsion“ beschreibt dabei die Verzögerung des Fahrzeugs mit durch gegen die Flugrichtung gerichteten Triebwerken.

Im Projekt „RETALT“ wurden die Schlüsseltechnologien für diese mit Retro-Propulsion landenden Systeme untersucht. Diese Arbeit konzentriert sich auf die stationären und instationären aerodynamischen Phänomene, die während der drei Phasen des Abstiegs und der Landung auftreten. Die drei Phasen sind der Wiedereintrittszündung, die aerodynamische Phase und die Landezündung. Die Wiedereintrittszündung ist ein Verzögerungsmanöver in großen Höhen mit mehreren Triebwerken, das zur Reduktion des Staudrucks und der Wärmelasten in der darauffolgenden aerodynamischen Phase dient. Die aerodynamische Phase ist eine Flugphase ohne aktiven Schub. Die Landezündung ist das finale Retro-Propulsion-Manöver, das die Geschwindigkeit des Fahrzeugs für die Landung auf null bringt.

Die Wiedereintrittszündung wurde im Hyperschallwindkanal Köln (H2K) getestet, die aerodynamische Phase in der Trisonischen Messstrecke Köln (TMK) und die Landezündung in der Vertikalen Messstrecke Köln (VMK). Die Abgasstrahlen in den Schubphasen wurden mit Druckluft simuliert. Zur Beschreibung der – insbesondere in den Schubphasen – stark instationären Strömungsfelder wurden orthogonale Zerlegungen (Proper Orthogonal Decomposition, POD) von Hochgeschwindigkeitsschlierenaufnahmen und Spektralanalysen von hochfrequenten Druckmessungen ausgewertet und eine gemittelte Lösung der Moden vorgeschlagen.

Für die aerodynamische Phase wurde eine analytische Methode zur Auslegung der Steuerflächen entwickelt. Diese wurde mit Windkanalexperimenten validiert und eine gute Übereinstimmung gezeigt. Die Wiedereintrittszündung und die Landezündung wurden hinsichtlich ihrer stationären und instationären Strömungsphänomene untersucht. Für die Wiedereintrittszündung sind die dominierenden Ähnlichkeitsparameter der Schubkoeffizient und der Ruhedruck stromab des Bugstoßes. Konfigurationen mit unterschiedlichen Anzahlen von Triebwerken können mit dem Gesamtschubkoeffizienten skaliert werden. Die bestimmenden Ähnlichkeitsparameter für die Landezündung sind das Umgebungsdruckverhältnis (Ambient Pressure Ratio, APR) und das Impulsstromdichteverhältnis (Momentum Flux Ratio, MFR). Vor allem beim Landeanflug wurden stark dominante Frequenzen gefunden, die in Bereichen der kritischen Strouhalzahlen von Heckströmungen bei Aufstiegskonfigurationen liegen. Die normierten Druckschwankungen während des Landeanflugs sind eine Größenordnung größer als bei diesen Heckströmungen.

Contents

List of Figures

List of Tables

Nomenclature

ACS	=	Aerodynamic Control Surfaces
APR	=	Ambient Pressure Ratio
CFD	=	Computational Fluid Dynamics
DNS	=	Direct Numerical Simulation
DRL	=	Down Range Landing
GLOW	=	Gross Lift-Off Weight
GTO	=	Geostationary Transfer Orbit
H2K	=	Hypersonic Wind Tunnel Cologne
LEO	=	Low Earth Orbit
TMK	=	Trisonic Wind Tunnel Cologne
VMK	=	Vertical Free-Jet Facility Cologne
LOX	=	liquid oxygen
LH2	=	liquid hydrogen
MECO	=	Main Engine Cut-Off
MFR	=	Momentum Flux Ratio
OFR	=	Oxidizer Fuel Ratio
POD	=	Proper Orthogonal Decomposition
PSD	=	Power Spectral Density
RTLS	=	Return to Launch Site
SRP	=	Supersonic Retro Propulsion
HRP	=	Hypersonic Retro Propulsion
SSTO	=	Single Stage to Orbit
TSTO	=	Two Stage to Orbit
A_e	=	nozzle exit area
A_B	=	reference base area
CoG	=	Center of Gravity
CA	=	axial force coefficient
CM	=	moment coefficient
$CM(CoG)$	=	moment coefficient in the center of gravity
CN	=	normal force coefficient
CY	=	side force coefficient
C_D	=	drag coefficient
C_p	=	pressure coefficient
C_T	=	thrust coefficient
C_p	=	pressure coefficient
D	=	diameter
F	=	force
F_T	=	thrust
M	=	Mach number
$\mathcal{M}$	=	moment
Re	=	Reynolds number
R_{mA}	=	momentum ratio
Sr_D	=	Strouhal number
T	=	temperature
f	=	frequency
p	=	static pressure
p'	=	pressure fluctuation
q	=	dynamic pressure
u	=	velocity
$\boldsymbol{x}$	=	image vector
x_S	=	downstream distance from bow shock

$\boldsymbol{u}$	=	left singular vector (spatial POD mode)
$\boldsymbol{v}$	=	right singular vector (time series of POD modes)
σ	=	singular value
$\boldsymbol{X}$	=	matrix of image vectors
$\boldsymbol{U}$	=	matrix of left singular vectors
$\boldsymbol{V}$	=	matrix of right singular vectors
$\boldsymbol{\Sigma}$	=	matrix of singular values
α	=	angle of attack
β_{max}	=	maximum deflection angle at which a solution with the oblique shock relations exists
γ	=	heat capacity ratio
δ	=	deflection angle
θ	=	surface inclination angle
μ	=	dynamic viscosity
ρ	=	density
ϕ	=	Angle between engine-plane and α-plane
K	=	Engine scaling parameter

Subscripts

∞	=	free stream condition
0	=	total condition
a	=	ambient condition
d	=	dead air region
e	=	wind tunnel model nozzle exit condition
j	=	jet flow
0,2	=	total condition downstream of the normal portion of the bow shock
CC	=	total condition in the wind tunnel model (CC: Combustion Chamber)
st	=	averaged mode
rms	=	root mean square
Fl	=	flight condition
exp	=	experimental condition

1. Introduction

1.1. Context and Motivation of this Work

The first successful landing of a Falcon 9 first stage by SpaceX in 2015 marked an important turning point in the global and the European launcher market. The prevailing opinion in Europe on reusability was shaped by the experience of NASA with the Space Transportation System (STS) with the Space Shuttle orbiter. In spite of the large amount of reusable parts of the STS with the reusable boosters and the Space Shuttle orbiter, high turnaround times and maintenance costs made it very expensive. This led to the general opinion in Europe that expendable launchers are more cost efficient than their reusable counterparts.

With the successful landing of the Falcon 9 first stage in 2015, this common opinion changed and a variety of national and international projects emerged to investigate vertical landing of launcher first stages with the aid of retro propulsion. Retro propulsion means here that one or several engines are fired against the velocity vector to decelerate the vehicle during descent and landing.

System studies were performed in projects like Ariane Next [1] and ENTRAIN [2], small scale demonstrators for GNC development were developed in EAGLE [3], FROG [4] and DTV [5], wind tunnel experiments and CFD tools were validated for such applications in RETPRO [6] and projects like CALLISTO [7] and Themis [8] focus on large scale demonstrators.

The approach taken by SpaceX of vertically landing the launcher first stage promises large cost savings as the descent and landing configuration is similar to the ascent configuration. Only few additional parts, such as aerodynamic control surfaces and landing legs, are needed for the landing approach, which keeps the complexity of the system low. Furthermore, the loads on the system and the structures are applied mainly in the axial direction, which is the same load direction as during the ascent. This keeps the need for additional structures low.

However, even though the concept of vertically descending and landing the first stage is promising and was implemented successfully in the USA, major challenges remain for its application in the European market. Furthermore, the research in the field is limited and often not openly accessible. Therefore, the RETALT (Retro Propulsion Assisted Landing Technologies) project was funded in the frame of the Horizon 2020 research and innovation framework program under grant agreement No 821890 by the European Union to investigate the key technologies for the successful implementation of vertically landing launchers with the aid of retro propulsion in Europe.

One of the tasks of the DLR in this project was the aerodynamic design of such vertically landing launchers and the investigation of the complex unsteady aerodynamics during descent and landing. The doctoral thesis at hand focuses on the extensive wind tunnel test series performed at the Supersonic and Hypersonic Technologies Department of the German Aerospace Center (DLR) in Cologne in this context and elaborates on the insights gained through the test data, and the design methodologies developed with it.

The Thesis is structured as follows. After the Introduction and a short summary of fundamentals, an overview of the state of the art in retro propulsion flow fields is given. Then the wind tunnel setups and the wind tunnel models are described, as well as the construction of an averaged modal

solution proposed in this thesis to analyze strongly unsteady flow fields. Hereafter, the results are presented. They are structured by the flight phases of the descent trajectory of a vertically landing launcher first stage. The reference trajectory of the heavy lift launcher reference configuration, RETALT1, which was investigated in the project, can be divided into three phases: the reentry burn, the aerodynamic phase and the landing burn.
First, the results of the aerodynamic phase tested in the Trisonic Wind Tunnel Cologne (TMK) are described. In this phase the engines are not active. The focus of this section is the development of an analytical method for the sizing of the aerodynamic control surfaces to achieve a trimmable configuration in this flight phase. Then, the results of the active retro propulsion phases are discussed. Here, first the reentry burn tested in the Hypersonic Wind Tunnel Cologne (H2K) is described. Then, the landing burn tested in the Vertical Free-Jet Facility (VMK) is elaborated on. The focus in the retro propulsive phases is on the general upstanding and description of the flow field, the prevailing similarity parameters and the dynamic flow features and their frequency content.
The thesis therefore gives an understanding of the underlying physics of the different flight phases of vertically landing launchers and provides methodologies, guidelines and critical load cases to be taken into consideration for their aerodynamic design.

1.2. Publications Incorporated in this Thesis

Parts of the content of this thesis were published in several journal and conference articles. These reference documents are listed in the following.

Journal Articles:

Publication	Journal	Section
Marwege, A., Gülhan, A., Klevanski, J., Hantz, C., Karl, S., Laureti, M., De Zaiacomo, G., Vos, J., Jevons, M., Thies, C., Krammer, A., Lichtenberger, M., Carvalho, J., and Paixão, S., "RETALT: review of technologies and overview of design changes," *CEAS Space Journal,* Vol. 14, No. 3, 2022, pp. 433-445, https://doi.org/10.1007/s12567-022-00458-9.	CEAS Space Journal	1, 3
Marwege, A., Hantz, C., Kirchheck, D., Klevanski, J., Gülhan, A., Charbonnier, D., and Vos, J., "Wind tunnel experiments of interstage segments used for aerodynamic control of retro-propulsion assisted landing vehicles," *CEAS Space Journal,* Vol. 14, No. 3, 2022, pp. 447-471, https://doi.org/10.1007/s12567-022-00425-4.	CEAS Space Journal	4.1.1, 4.2.1, 4.3.1, 5.1
Marwege, A., Kirchheck, D., Klevanski, J., and Gülhan, A., "Hypersonic retro propulsion for reusable launch vehicles tested in the H2K wind	CEAS Space Journal	4.1.2, 4.2.2, 4.3.2,

tunnel," *CEAS Space Journal,* Vol. 14, No. 3, 2022, pp. 473-499, https://doi.org/10.1007/s12567-022-00457-w.		5.2
Marwege, A. and Gülhan, A., "Unsteady Aerodynamics of the Retropropulsion Reentry Burn of Vertically Landing Launchers," *Journal of Spacecraft and Rockets,* Vol. 60, No. 6, 2023, pp. 1939-1953, https://doi.org/10.2514/1.A35647.	JSR	4.1.3, 4.2.3, 4.3.3, 5.3
Marwege, A. and Gülhan, A., "Aerodynamic Characteristics of the Retro Propulsion Landing Burn of Vertically Landing Launchers," *Experiments in Fluids,* (accepted).	Experiments in Fluids	4.3.2, 5.2

Conference Articles:

Publication	Conference	Section
Marwege, A., Gülhan, A., Klevanski, J., Riehmer, J., Karl, S., Kirchheck, D., Bonetti, D., Vos, J., Jevons, M., Krammer, A., and Carvalho, J., "Retro Propulsion Assisted Landing Technologies (RETALT): Current Status and Outlook of the EU funded project on Reusable Launch Vehicles," Washington D.C., USA, 2019, https://doi.org/10.5281/zenodo.5770046.	IAC2019	1, 3
Marwege, A., Klevanski, J., Hantz, C., Kirchheck, D., Guelhan, A., Karl, S., Laureti, M., Zaiacomo, G. D., Vos, J., Thies, C., Jevons, M., Krammer, A., Lichtenberger, M., Carvalho, J., and Paixão, S., "Key Technologies for Retro Propulsive Vertical Descent and Landing – RETALT – An Overview," *2nd International Conference on Flight Vehicles, Aerothermodynamics and Re-entry Missions and Engineering*, Heibronn, Germany, 2022, https://doi.org/10.5281/zenodo.6783915.	FAR2022	1, 3
Marwege, A., Hantz, C., Kirchheck, D., Klevanski, J., Vos, J., Laureti, M., Karl, S., and Gülhan, A., "Aerodynamic Phenomena of Retro Propulsion Descent and Landing Configurations," *2nd International Conference on Flight Vehicles, Aerothermodynamics and Re-entry Missions and Engineering*, Heibronn, Germany, 2022, https://doi.org/10.5281/zenodo.6783922.	FAR2022	4.2, 5.1, 5.2, 5.3

2. Fundamentals and State of the Art

2.1. Flow Properties and Definitions

Two main parameters define the free stream conditions in aerodynamics; the Mach number and the Reynolds number. The Mach number, M_∞, defines the velocity, u_∞, relative to the speed of sound, a_∞:

$$M_\infty = \frac{u_\infty}{a_\infty} \quad (1)$$

The Reynolds number defines the ratio of inertia to viscous forces [9] and is defined by:

$$Re_\infty = \frac{u_\infty \rho_\infty D_{ref}}{\mu_\infty} \quad (2)$$

with the density ρ_∞, the dynamic viscosity μ_∞ and the reference length D_{ref}. In this thesis the reference length for the nondimensionalization is the diameter of the first stage, which is 6 m in the case of RETALT1 (see section 3).

The Strouhal number describes the nondimensionalization of frequencies and is defined by:

$$Sr_D = \frac{f D_{ref}}{u_\infty} \quad (3)$$

with the frequency f, the reference length D_{ref} and the free stream velocity u_∞. The reference length was chosen to be the base diameter, as this makes the Strouhal numbers comparable to studies on near-wake flows of ascending space transportation systems where this definition was used [10].

The commonly used pressure coefficient is defined by:

$$C_p = \frac{p - p_\infty}{q_\infty} \quad (4)$$

where p is the pressure, p_∞ is the free stream pressure and q_∞ is the dynamic pressure.

Further similarity parameters which are specific for jet flows and hypersonic, supersonic and subsonic retro propulsion are defined in the sections 2.4, 2.5 and 2.6.

2.2. Shock-Wave/Boundary-Layer Interaction

If an incident shock impinges on a solid surface, and viscous effects are neglected, the shock is reflected from the surface as shown in Fig. 1. However, taking viscous effects into account, complex shock-wave/boundary-layer interactions can appear in such cases. At the point where the incident shock impinges on the surface and is reflected (point B in Fig. 1), in the inviscid case, the pressure is increased instantaneously, leading to a theoretical infinite adverse pressure gradient. If the adverse pressure gradient is large enough, the boundary layer at the surface separates, as depicted in Fig. 2. The separated boundary layer, in turn, disturbs the incoming freestream which is why a separation shock forms upstream of the separation region at the separation point. [9]

The shock-wave/boundary-layer interaction leads to strongly oscillating shock waves and high pressure fluctuations in the separation zone, as well as, high heat loads in the reattachment zone [11, 12].

As in the case of an incident shock, also a shock generated on a compression ramp configuration as shown in Fig. 3 for inviscid flows, can lead to boundary-layer separation and shock-wave/boundary-layer interactions, as shown in Fig. 4. If the shock is sufficiently strong the boundary layer separates and a separation bubble forms which leads to a separation shock upstream of the corner [13, 14]. The separation bubble grows with increasing ramp angle, and so does the separation length [13]. The size of the flow separation depends on the ramp angle, which determines the strength of the shock and the Reynolds number which determines how well the boundary layer resists to the adverse pressure gradient [13]. The separation shock strongly oscillates in an intermittent region and tends to be a lot weaker than the inviscid shock [13]. As for the impinging incident shock, shock-wave/boundary-layer interaction on corner flows lead to high unsteady pressure loads [13, 15], and heat loads [15]. The unsteadiness of the separation shock is similar for the two shock-wave/boundary-layer interaction cases [16].

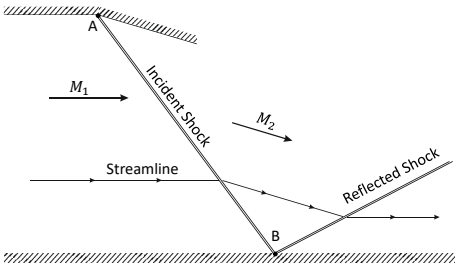

Fig. 1: Regular inviscid reflection of an incident shock on a surface (adapted from [9]).

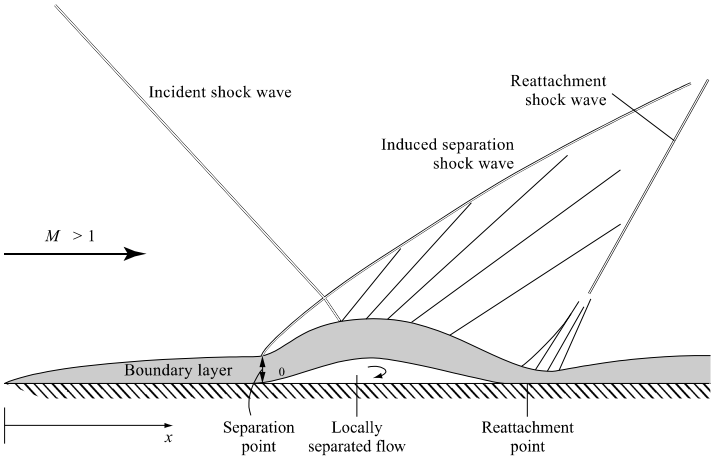

Fig. 2: Shock-wave/boundary-layer interaction of an incident shock impinging on a solid surface. [9]

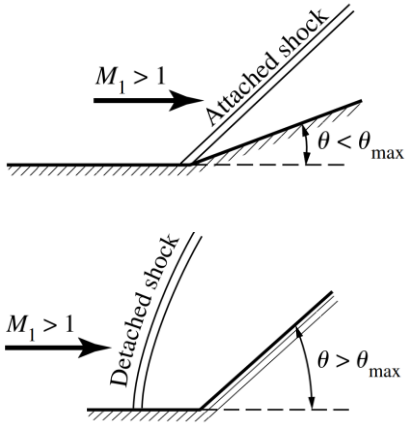

Fig. 3: Attached and detached shocks in corner flows [9]

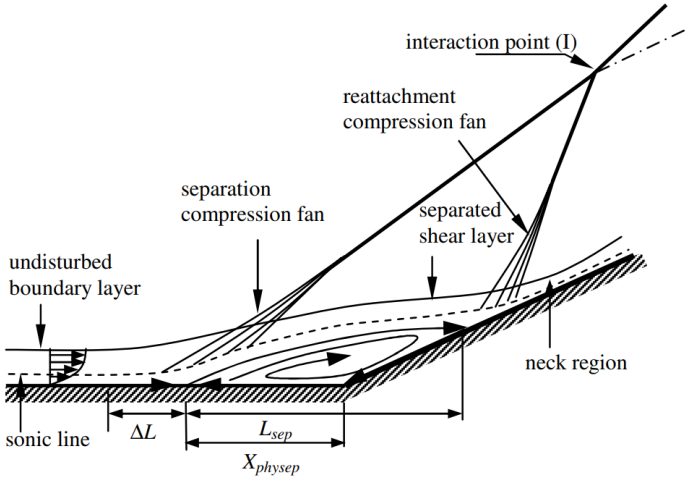

Fig. 4: Shock-wave/boundary-layer interaction on a compression ramp [15]

2.3. Hypersonic Flows

2.3.1. Blast Wave Analogy

The blast wave analogy transfers principles of an unsteady moving shock wave from an instantaneous energy release in a single point (of a blast at an origin) to a blunt body moving at hypersonic speeds [11]. The analogy is sketched in Fig. 5 for a blunt-nosed cylinder. For a blunt-nosed cylinder, Sakuri [17] obtained with the blast wave analogy the second approximation of the pressure distribution along the cylinder surface as follows:

$$\frac{p}{p_\infty} = 0.067 M_\infty^2 \frac{\sqrt{C_D}}{\frac{x_S}{D}} + 0.44 \qquad (5)$$

where $\frac{x_S}{D}$ is the distance downstream of the bow shock normalized with the diameter of the cylindrical body D, C_D is the drag coefficient, M_∞ is the free stream Mach number, p is the static pressure at the surface of the cylinder at the distance $\frac{x_S}{D}$ from the bow shock and p_∞ is the free stream pressure. The second approximation only differs from the first approximation in the constant 0.44 which is missing in the first approximation, see [11] and [18]. Lukasiewicz [19] suggests that p shall be set equal to p_∞ if the blast wave solution results in pressure values lower than $\frac{p}{p_\infty} = 1$. This can be seen in Fig. 6, where Lukasiewicz compared results of the blast wave analogy to results obtained with the method of characteristics by Van Hise [20].

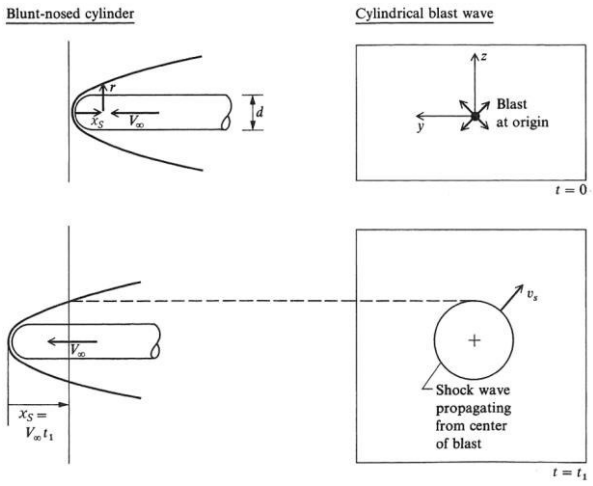

Fig. 5: Blast-wave analogy for a blunt-nosed cylinder [11]

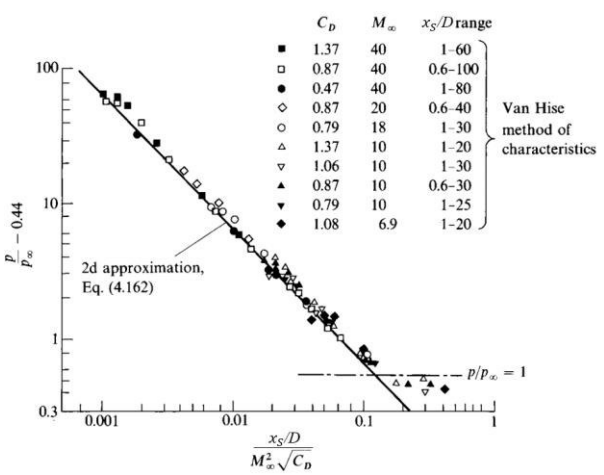

Fig. 6: Comparison of results with blast wave analogy to results of the method of characteristics (Ref. [19] taken from Ref. [11], Van Hise Ref. [20])

2.3.2. Modified Newtonian Law

The modified Newtonian Law is a modification of the Newtonian sine-squared law. This law was initially proposed by Isaac Newton in the propositions 34 and 35 of his *Principia*. For a flow impinging on a surface, it assumes that all momentum normal to the surface is lost, while all

momentum tangential to it is conserved. This ultimately leads to a pressure coefficient C_p on the surface, dependent on the surface angle θ: [11]

$$C_{p_{Newton}} = 2\sin^2\theta \quad (6)$$

While this distribution does not lead to good results in subsonic flows, it is a good first approximation in hypersonic flows [11]. Lees [21] proposed a modification of the Newtonian law with the pressure coefficient of the stagnation pressure downstream of a normal shock, $C_{p_{max}}$:

$$C_{p_{Newton}} = C_{p_{max}}\sin^2\theta \quad (7)$$

With the pressure downstream of the normal shock, $p_{0,2}$, $C_{p_{max}}$ is defined as:

$$C_{p_{max}} = \frac{p_{0,2} - p_\infty}{q_\infty} \quad (8)$$

This modified Newtonian law reaches very good results for the surface pressure distributions on blunt bodies for high free stream Mach numbers [11]. For example, in recent work Seltner et al. [22] showed a good agreement between the force and moment coefficients estimated with the modified Newtonian law, and measured force and moment coefficients during free flight experiments in the Hypersonic Wind Tunnel Cologne (H2K) at DLR in Cologne.

2.4. Supersonic Jets

Supersonic jets are commonly generated in converging diverging nozzles, so-called Laval nozzles. To reach supersonic Mach numbers at the nozzle exit, the sonic speed needs to be reached in its throat. For this, the critical pressure ratio needs to be exceeded, which is defined by the isentropic relations, for $M_{th} = 1$:

$$\frac{p_{th}}{p_0} = \left(1 + \frac{\gamma - 1}{2}M_{th}^2\right)^{-\frac{\gamma}{\gamma-1}} = \left(1 + \frac{\gamma - 1}{2}\right)^{-\frac{\gamma}{\gamma-1}} \quad (9)$$

where p_{th} is the static pressure in the throat, p_0 is the total pressure and M_{th} is the Mach number in the throat.

Then flow field at the nozzle exit mainly depends on the Ambient Pressure Ratio (APR), which is the ratio of the exit pressure p_e at the nozzle exit and the ambient pressure p_a surrounding it:

$$APR = \frac{p_e}{p_a} \quad (10)$$

Fig. 7 shows a scheme of the flow fields at different APRs. For $APR < 1$, the flow field is called overexpanded, for $APR > 1$ it is called underexpanded. For $APR = 1$, which is the design case of the nozzle, the flow field is called fully expanded.

For rocket engines, shock structures and flow separations in the nozzle are generally avoided as they can generate high asymmetric side forces [23]. Hence only the cases g to k in Fig. 7 are relevant for this thesis. To estimate the critical pressure at which flow separation in the nozzle occurs, the correlation proposed by Stark and Wagner [24] was used in this work:

$$\frac{p_{sep}}{p_a} = \frac{1}{M_{sep}} \quad (11)$$

where p_{sep} is the pressure at which flow separation occurs, and M_{sep} is the corresponding wall Mach number.

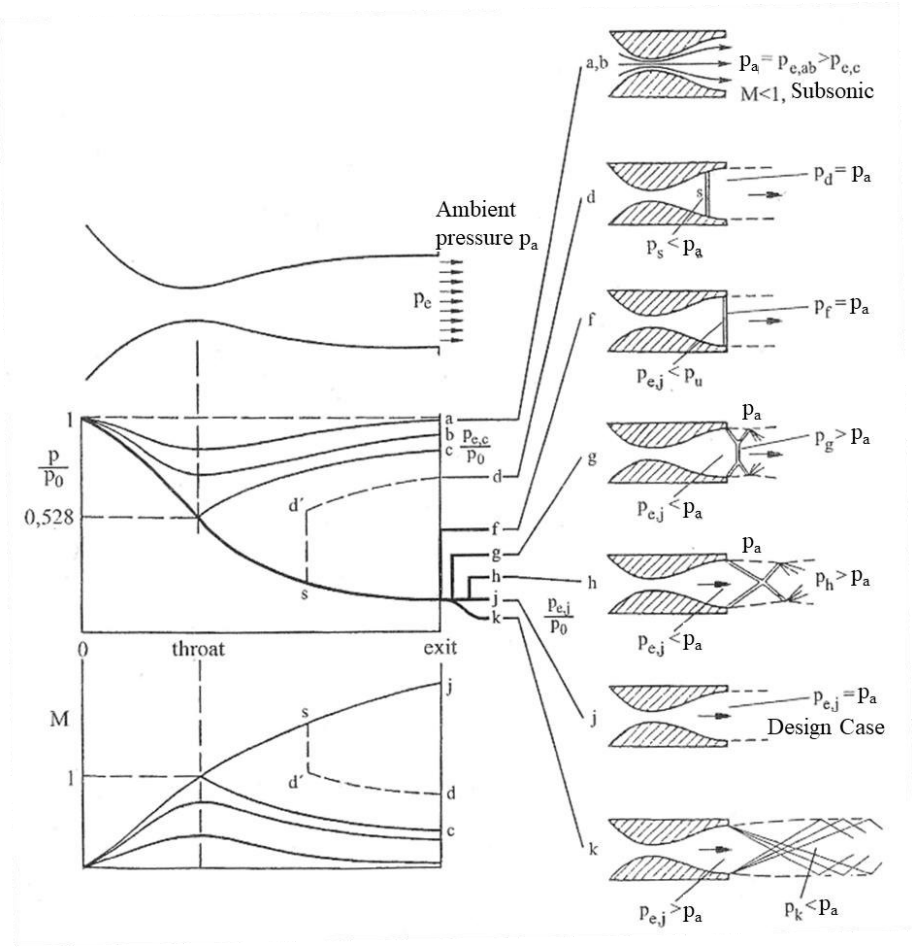

Fig. 7: Schematic of jet flows in a Laval nozzle in dependence of the pressure ratio [25]

2.4.1. Overexpanded Supersonic Jets

In the case of overexpanded supersonic jets, two main flow field cases can be considered, the regular reflection and the Mach reflection. These two cases are shown in Fig. 8. As the ambient pressure is larger than the exit pressure, the exit flow is compressed by an oblique shock, which emerges from the nozzle lip. In the case of the regular reflection, the shock is reflected at the symmetry axis. If the ambient pressure is too large in relation to the exit pressure, the deflection angle of the reflected lip shock would exceed the maximum possible deflection angle. Therefore, a regular reflection is not possible. This leads to the Mach reflection, where the core flow is decelerated, but not deflected, through a normal shock, commonly called Mach disc. The flow passing through the lip shock and its reflection on the Mach disc and the flow decelerated through the Mach disc are separated by a slip line, where the pressure and the flow angle are equal. [23]

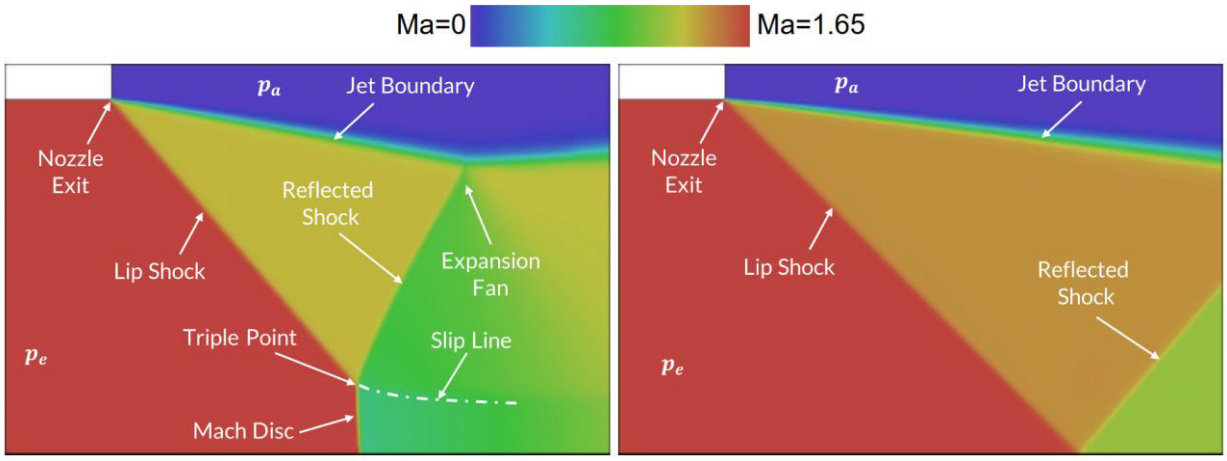

Fig. 8: Simulations of Mach reflection (left) and regular reflection (right). Images of the simulations taken from [23]

After passing through the reflected shock, the flow is expanded again, after which it is recompressed through a new incident shock, forming a shock cell (see Fig. 9). These shock structures can repeat several times with a decaying intensity in a so-called shock train [10].

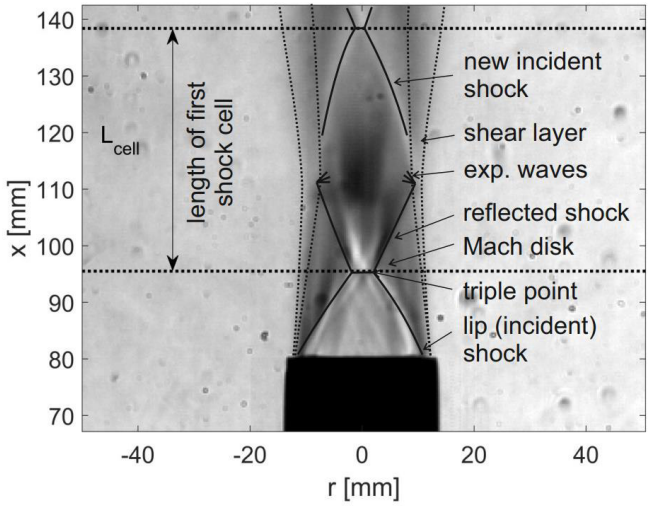

Fig. 9: First shock cell of a shock train [10]

2.4.2. Highly Underexpanded Supersonic Jets

A schematic of a highly underexpanded supersonic jet is shown in Fig. 10. If the ambient pressure is much smaller than the exit pressure ($APR \gg 1$), the exhaust flow is strongly expanded at the nozzle lip. Due to reflection of the characteristics of the expansion waves on the jet boundary and the recompression of the flow, an incident shock forms, also called intercepting or barrel shock [26]. Since the pressure difference is too large to be reduced by an oblique incident shock, the flow is decelerated through a slightly bent normal shock at the symmetry axis (similar to the Mach reflection in the overexpanded flow field, see section 2.4.1). The barrel shock is reflected at the Mach disc. The flow passing the barrel shock and its reflection at the Mach disc, and the flow

passing the Mach disc, are separated by a slip line. Even though Fig. 10 taken from [27], only refers to sonic jets with $M_e = 1$ at the nozzle exit plane, the flow features are also valid for exit Mach numbers larger than one.

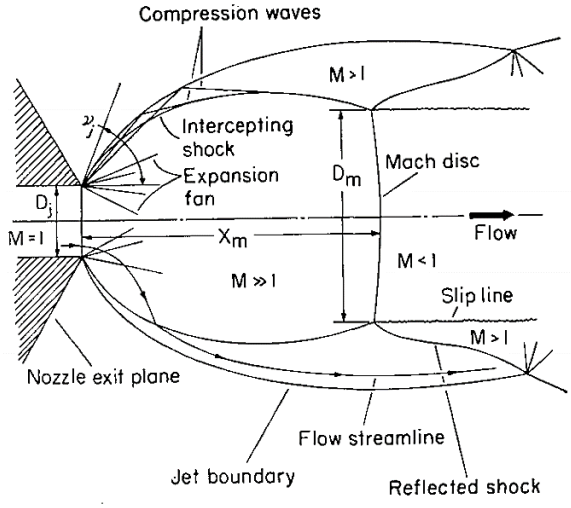

Fig. 10: Schematic of a highly underexpandend Jet [27]

2.5. Supersonic and Hypersonic Retro Propulsion

Supersonic Retro Propulsion (SRP) commonly refers to the direction of a supersonic jet against a supersonic free stream. These flow fields have been studied since the 1950s for Entry, Descent and Landing (EDL) applications [28]. The recent research in the USA foremostly concentrates on EDL missions for Mars [29-41]. Analytical approaches to model these flows have been developed by Korzun et al. [42] and Cordell and Braun [43] based on Finley [44] and Jarvinen and Adams [45]. The status of the Mars EDL research is summarized in [36]. Only some studies were published on launchers in the USA, e.g. [29]. In contrast, the research in Europe focuses on descent and vertical landing of launcher first stages [46-57]. The phenomena for these two applications are generally very similar, with the difference that the launcher first stages are more slender and the vehicles for Mars EDL commonly have a much larger cross surface area compared to the engine exit area. Furthermore, the mission profiles differ and the aerodynamic thrust coefficients for the vertical landing launchers are much larger. Also motivation exists in Europe and in India to adapt this technology to aerospike engines [58-60]. Comprehensive literature reviews of investigations in SRP can be found by Korzun et al. [28] and Mejia and Schmidt [61], where Mejia and Schmidt [61] link the research performed on SRP to research performed on Stagnation Point Injection (SPI), in which some findings made in SRP were discovered in parallel. A review of research in SPI can be found in [62]. In [51] (which is part of this thesis) and [63], the term Hypersonic Retro Propulsion (HRP) was used instead of SRP since the Mach numbers tested in the Hypersonic Wind Tunnel Cologne were above 5. The general flow field is, however, comparable to SRP flow fields.
SRP and HRP flow fields for a single active engine commonly appear in two flow modes, the so-called blunt mode (Fig. 11) and a long penetration mode (Fig. 12) [45, 64], which are described in the following.

In the case of the blunt mode the flow is composed of two components. The strongly underexpanded plume of the supersonic jet, and the bow shock of the free stream. These two flow fields meet at the contact surface. The highly underexpanded plume shows the flow features described in section 2.4.2. The flow is strongly expanded around the lip of the nozzle exit and is then recompressed and redirected towards the symmetry axis. In this case the barrel shock is very close to the jet boundary. For high thrust coefficients, the Mach disc in the retro propulsion flows can get strongly bent and exhibits a spherical shape. Also the reflection of the barrel shock on the Mach disc is visible. In the wake of the plume a recirculation zone forms. The incoming free stream is decelerated through the bow shock to subsonic speeds. It is then accelerated along the contact surface to supersonic speeds again.

As the pressure surrounding the nozzle exit is not the ambient pressure in these flow fields but the dead air pressure p_d present in the recirculation zone, the plume expansion in this case is dominated by the Exit Pressure Ratio (EPR) defined as [65]:

$$EPR = \frac{p_e}{p_d} \tag{12}$$

One of the challenges of the supersonic retro propulsion flow fields remains in the determination of the dead air pressure in the recirculation zone as it cannot be assessed analytically [65]. Therefore, Korzun and Cassel [30] proposed the use of the ratio of the exit pressure p_e to the total pressure downstream of the normal portion of the bow shock $p_{0,2}$ as a scaling parameter instead of the APR. Gutsche et al. [65] then proposed to also scale the surface pressures with $p_{0,2}$ instead of using the conventional pressure coefficient C_p for these flow fields. It was shown in CFD simulations that this leads to better similarity for varying Mach numbers, at least in the base area close to the plume [65].

The flow field features of the blunt mode (shock stand-off distance, Mach disc location, location of the triple point), were found to be dependent on the square root of the aerodynamic thrust coefficient [45, 65], where the thrust coefficient is defined as follows:

$$C_T = \frac{F_T}{q_\infty A_{ref}} \tag{13}$$

with the thrust F_T, the dynamic pressure q_∞ and a reference area based on the body diameter A_{ref}.

In the blunt mode the flow field is generally steady. Interchangeably for the aerodynamic thrust coefficient also the momentum ratio R_{mA} introduced in [66] can be used as similarity parameter [61]:

$$C_T = \frac{F_T}{q_\infty A_{ref}} = \frac{\rho_e u_e^2 A_e}{\frac{1}{2}\rho_\infty u_\infty^2 A_{ref}} = 2\,R_{mA} \tag{14}$$

where ρ_e and u_e are the density and the velocity at the nozzle exit with an area of A_e, and ρ_∞ and u_∞ are the density and velocity in the free stream. Equally, C_T can be rewritten in terms of the Momentum Flux Ratio (MFR) as defined in [67]:

$$MFR = \frac{\rho_e u_e^2}{\rho_\infty u_\infty^2} \tag{15}$$

which results in:

$$C_T = 2\,MFR\frac{A_e}{A_{ref}} \qquad (16)$$

This connects SRP flows with subsonic retro propulsion flows where the MFR is used as similarity parameter (see section 2.6). It shall be noted that in equation (14), the pressure loss in the thrust was neglected. The results discussed in section 5.2 are based on the thrust coefficient where the pressure loss was included.

The long penetration mode is shown in Fig. 12. Instead of the highly underexpanded plume structure, a jet train with several shock cells is formed, which ultimately terminates in a normal shock. In experiments, this clear shock train structure is not always observable and the flow is highly unsteady [45].

The condition for the switching of one to the other mode is still under discussion in the SRP community. Jarvinen and Adams [45] theorized that it is dependent on a certain exit pressure to ambient pressure ratio (p_e/p_∞), and it appears at thrust coefficients close to unity. Korzun and Cassel [30] argued that the switch appears at $C_T > 1$ and $p_e/p_{0,2} > 1$. Daso et al. [68] and Gutsche et al. [65] postulated that the switch could appear when the nozzle exit flow changes from being underexpanded to being overexpanded, and, therefore, would depend on the EPR. Furthermore, Gutsche et al. [65] theorized that the dead air pressure depends on the base geometry, which is why also the ratio of $p_e/p_{0,2}$ at which the modes switch depends on the geometry. The theory of the mode switch depending on weather the nozzle exit flow is under- or overexpanded is in contradiction to Venkatachari et al. [64] where the long penetration mode was found for underexpanded jets (see Fig. 12). Hence, it can be summarized, that the main parameters for the switch between the modes seem to be the ratio $p_e/p_{0,2}$, the EPR and the thrust coefficient. What is commonly agreed on in the SRP literature, is that the switch between blunt and long penetration mode appears at low thrust coefficients [30, 45, 65].

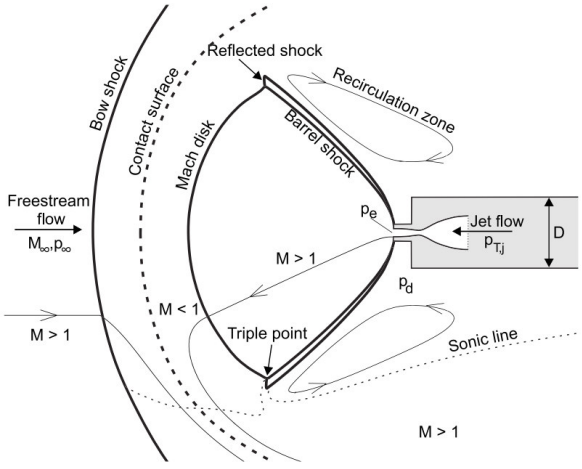

Fig. 11: Flow features of the blunt mode of a supersonic or hypersonic retro propulsion flow field for the single-engine case [65]

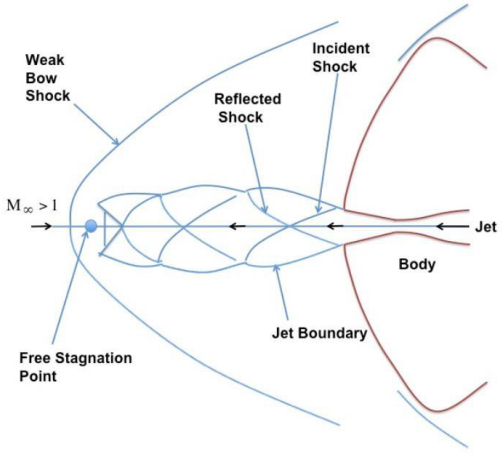

Fig. 12: Flow features of the long penetration mode of a supersonic or hypersonic retro propulsion flow field for the single-engine case [64]

Configurations with more than one engine were investigated in various studies with varying engine numbers and arrangements [37, 41, 43, 45, 47, 48, 69, 70]. Similar to the single-engine case, the blunt and the long penetration modes were observed. However, the flow field strongly depends on the arrangement of the engines and the coalescence of the exhaust plumes [47, 48, 70]. Exemplarily, Fig. 13 shows the plume structure for a case of three active engines for a generic descending launcher. It can be observed that the flow structure is very similar to the single-engine blunt mode. Fig. 14 shows the Mach contours of that same flow field, and a cut at 0.5 m below the nozzle exit plane. Close to the engines, oblique shocks are formed due to the interaction between the plumes [47]. The plume expands more widely in the direction perpendicular to the engine plane than in the engine plane itself [48].
Vos et al. [49] studied the flow field with three active engines in the alpha plane in more detail and varied the heat capacity ratio to assess its influence on the plume shape, showing that it is an important parameter for the extrapolation from wind tunnel experiments to flight conditions. The pressure coefficient on the base area of the vehicle is known to decrease with increasing thrust coefficient [30, 45, 65].

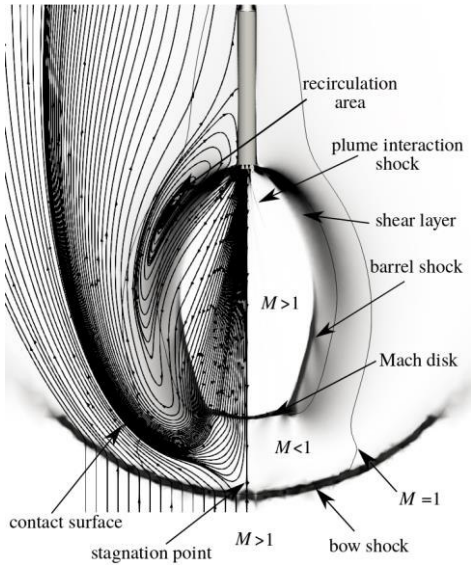

Fig. 13: Flow features of the blunt mode of a hypersonic retro propulsion flow field for three active engines, in the engine plane at Mach 9.45 [48, 65]

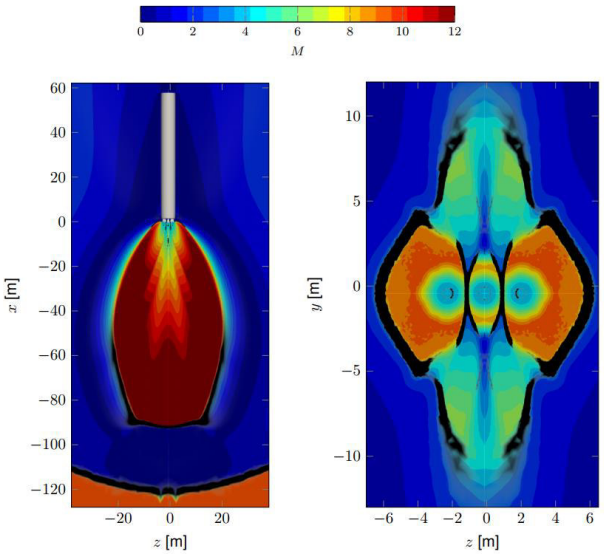

Fig. 14: Mach contours of flow field shown in Fig. 13, the shocks are in gray-scale. Engine plane (left) and cut 0.5 m below the nozzle exit (right) showing the plume coalescence [47, 48]

The flow field of the blunt mode of the SRP flow field is in general steady, where the strongest unsteady behavior is found in the triple point [41]. To characterize the dynamic flow features of the blunt mode of SRP flow fields, experimental data has been studied in detail by Bathel et al. [71] with means of spectral images and Proper Orthogonal Decomposition (POD). They found a fundamental frequency of 2 kHz. In [61] a POD of experimental data was performed which was combined with a spectral analysis of measured axial forces, and a fundamental frequency of 4.2 kHz was found to be associated with the flow motion. In [63] a spectral analysis of similar

experimental Schlieren videos was presented and was linked to high frequency pressure measurements. A dependence of the dominant frequency on the free stream Mach number was shown. Spectral analyses of resulting aerodynamic forces obtained with Computational Fluid Dynamics (CFD) have been presented by Montgomery et al. [72] and Chen el al. [73]. Chen el al. [73] went into further detail and linked the POD and spectral analyses and proposed a feedback model for the blunt and the long penetration mode. Chen et al. [73] found dominant frequencies at Strouhal numbers of 0.252 and 1.506.

Schauerhamer et al. [74] described a feedback mechanism for the unsteadiness of the blunt mode for a single nozzle case. Oscillations in the triple point generate pressure waves that propagate to the bow shock, generating small changes in the flow field of the incoming free stream. These effects then propagate down to the vehicle surface, where they are reflected and affect the pressure in the recirculation zone, which in turn, affects the EPR. The caused fluctuations in the EPR then close the feedback cycle by affecting the oscillation in the triple point. Codoni and Berry [40] analyzed the Power Spectral Density (PSD) of pressure measurements performed in wind tunnel experiments of the same configuration as described in [74]. They found distinctive frequency peaks, which are especially pronounced for an angle of attack of 0° and which weaken for higher angles of attack. They also analyzed configurations with three active engines, which were found to show less pronounced frequency peaks. In [63] surface pressures on the cylindrical part of a launcher configuration were analyzed for a single-engine case and dominant frequencies were shown to increase with increasing angle of attack in this region.

2.6. Subsonic Retro Propulsion

In the case of subsonic retro propulsion, the supersonic jet is directed against a subsonic free stream. Due to the absence of the bow shock, the exhaust plume extends farther into the free stream, exhibiting a multi cell jet train structure [31]. This mode is similar to the long penetration mode observed for SRP flow fields and is shown in Fig. 15 for a configuration with three active engines. In subsonic retro propulsion flows, the characteristic flow feature, the plume length, depends on the square root of the Momentum Flux Ratio (MFR), as Jarvinen and Hill [67] showed that it follows the following correlation:

$$\frac{x}{D_e} = 3.1\left(\frac{\rho_e u_e^2}{\rho_\infty u_\infty^2}\right)^{\frac{1}{2}}\left(\frac{T_{CC}}{T_e}\right)^{\frac{1}{2}} = 3.1\, MFR^{\frac{1}{2}}\left(\frac{T_{CC}}{T_e}\right)^{\frac{1}{2}} \quad (17)$$

where ρ_e, T_e and u_e are the density, the temperature and the velocity at the nozzle exit, T_{cc} is the total temperature in the combustion chamber and, ρ_∞ and u_∞ are the density and velocity in the free stream.

This is consistent as the MFR and the thrust coefficient can be used interchangeably if the pressure loss in the thrust is neglected (see section 2.5). Consequently, the MFR is a common similarity parameter for the large-scale flow features for both, supersonic and subsonic retro propulsion flow fields. As for the SRP flow fields, also in subsonic retro propulsion flow fields the pressure coefficient on the forward facing base area decreases with increasing aerodynamic thrust coefficients [45].

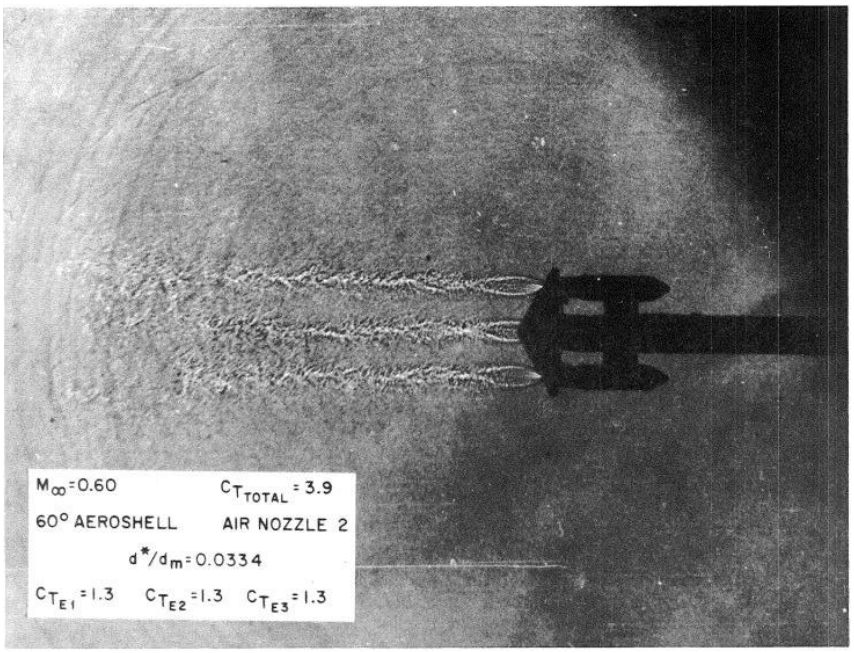

Fig. 15: Schlieren image of a subsonic retro propulsion flow field [52]

The dynamics of subsonic retro propulsion flows has been studied to a lesser extent in comparison to SRP flows. Detached Eddy Simulations (DES) were presented in [31, 37] and time series of aerodynamic force and moment coefficients have been reported. However, no modal analysis was performed.

3. Reference configuration RETALT1

3.1. Configuration Design and Mission Concept

To investigate the technologies studied in the RETALT project two reference configurations were defined [75]:

- RETALT1: A heavy lift launcher configuration able to bring a payload of up to 14 tons into the Geostationary Transfer Orbit (GTO)
- RETALT2: A smaller Single Stage To Orbit (SSTO) configuration able to bring a payload of 500 kg into Low Earth Orbits (LEO)

RETALT1 is a configuration more closely related to an application scenario which could be realized in Europe in the medium term, while RETALT2 is seen more as a technology test bed due to its nature of being an SSTO configuration with a quite small payload. Due to the higher importance of RETALT1 for the European launcher market in the medium-term, it was investigated in more detail in the project. In this thesis only results of the RETALT1 configuration are discussed.

To give a perspective of the size of RETALT1, in Fig. 16 it is compared to various launchers based on a comparison shown on the website of Blue Origin [76]. One can see that RETALT1 is in the size class of New Glenn.

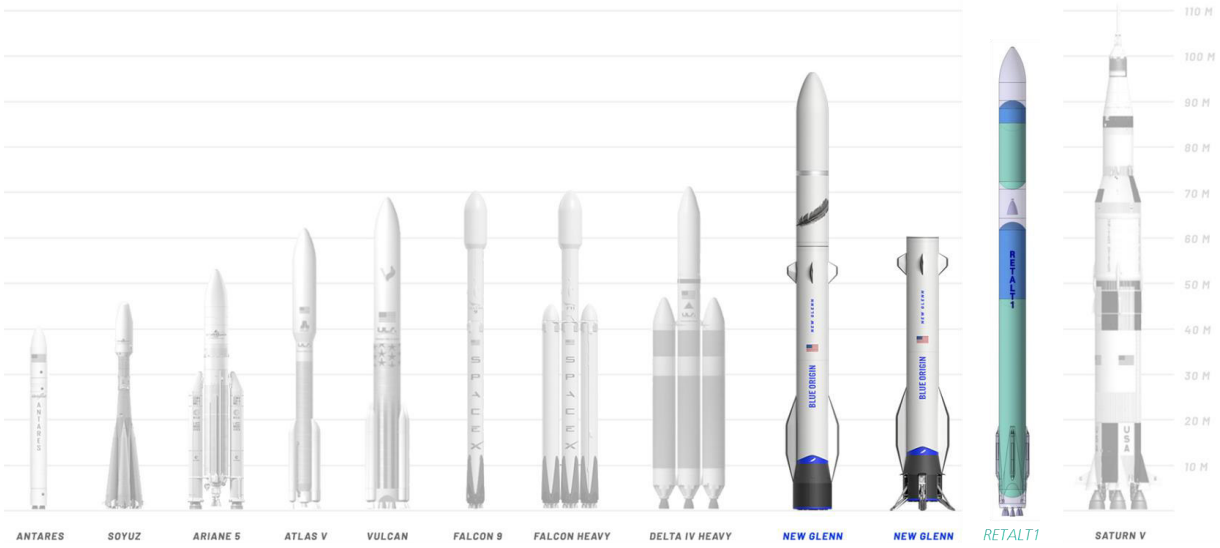

Fig. 16: Size comparison of RETALT1 with various launchers (Launcher comparison taken from [76])

As the project focused on European access to space, the configurations were based on existing European technologies. Hence, the RETALT1 configuration is using engines inspired heavily by the Vulcain 2. The configuration layout is shown in Fig. 17 and the main properties of the configuration are summarized in Tab. 1. Similar to the Falcon 9 by SpaceX, the RETALT1 configuration has 9 engines in the first stage and 1 engine in the second stage. The engines in the first stage are optimized for sea level conditions, while the second stage engine is optimized for vacuum conditions. As mentioned before, the configuration is based on engines similar to Vulcain 2 engines, with LOX/LH2 (Liquid Oxygen / Liquid Hydrogen) as propellant combination.

a) Configuration with Petals during descent

b) Configuration with grid fins during descent

c) Configuration with planar fins during descent

d) Configuration with folded planar fins during ascent

Fig. 17: RETALT1 configurations of aerodynamic control surfaces [75, 77]

Tab. 1: Characteristics of the RETALT1 configuration [75]

Stage Characteristics	1st Stage	2nd Stage	Fairing	Total
Number of Engines	9	1		10
Reusability	+	+/-	-	+/-
Height [m]	71.2	19.8	12.0	103.0
Diameter [m]	6.0	6.0		6.0
Mass full (GLOW) [t] (incl. Payload)	680.8	204.2	2.5	899.0
Stage Rate	75.7%	24.3%		
Structure Coefficient	8.7%	8.3%		
Mass structure [t]	59.3	16.7		75.9
Propellant mass (incl. descent propellant) [t]	621.5	187.5		809.0
Descent propellant [t]	50.0	0		50.0
Propellant reserve and residuals mass [t]	7.5	2.5		10.0
Engines	RETALT1-LHLOX-E15-FS	RETALT1-LHLOX-E70-FS		
Engine Cycle	Gas generator	Gas generator		
Oxidizer/Propellant	LOX/LH2	LOX/LH2		
Expansion Ratio	15.0	70.0		
Specific Impulse SL [s]	372.2	294.4		
Specific Impulse Vac [s]	401.6	431.9		
Thrust SL [kN]	9x1179 = 10614	1x930 = 930		
Thrust Vac [kN]	9x1273 = 11453	1x1364 = 1364		

The mission concept of RETALT1 is depicted in Fig. 18. As for the Falcon 9, a Return to Launch Site (RTLS) can be performed for missions with low orbits and payloads, and a Down Range Landing

(DRL) can be performed for more demanding missions. In the case of the Down Range Landing, after the Main Engine Cut Off (MECO) and the stage separation, the first stage is flipped over, such that its engines are pointing into the flight direction, and the Aerodynamic Control Surfaces (ACS) are deployed. Then, while reentering the atmosphere, a reentry burn is performed with three active engines in order to decelerate the vehicle, and reduce the heat loads and dynamic pressure during the following aerodynamic phase in which the engines are not active and the configuration is flying purely aerodynamically. In the final phase, a pinpoint landing is performed with the final landing burn. In the case of the Return To Launch Site scenario, a flip over maneuver and a boostback burn are performed after MECO to direct the stage back to the launch site. The other phases are the same as for the DRL scenario. In this thesis the reference trajectory was based on the DRL mission profile.

A novel concept was studied for this configuration where segments of the interstage (also called petals) were meant to be used as Aerodynamic Control Surfaces (ACS) (see Fig. 17a). This, however, proved to be challenging due to high structural loads and high hinge moments, leading to unfeasibly high structure and actuator masses [77]. This is why also planar fins were investigated as ACS (Fig. 17c, d) alongside grid fins (Fig. 17b) as reference for ACS operational to date (on the Falcon 9) [56, 77]. As proposed in the CALLISTO project (see e.g. [78]), the planar fins are folded along the main body during ascent (see Fig. 17d). In this thesis, the results obtained with the interstage segments and with the planar fins will be discussed, as these were the baseline configurations in the project, and were therefore investigated to much greater detail than the configuration with grid fins.

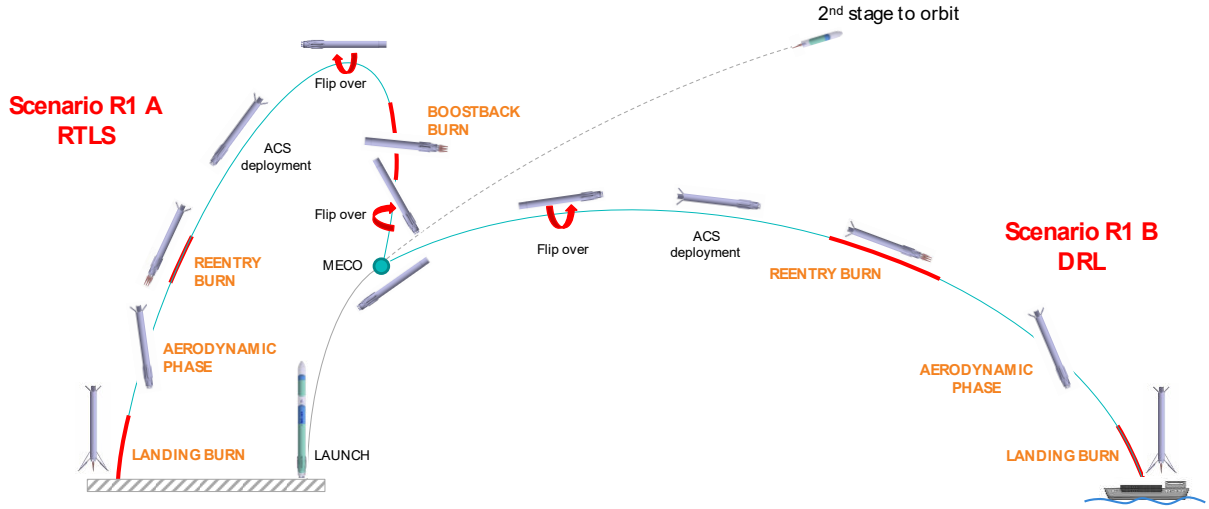

Fig. 18: RETALT1 return mission concept [79]

3.2. Engine Designs

The engines of the RETALT1 configuration are inspired by the Vulcain 2, which is the engine used for the center core of the Arian 5 ECA [80]. The rocket engine was reproduced in the commercial program Rocket Propulsion Analysis (RPA). It was adapted from an example given in the program which is based on [81]. For the first stage, it was adapted for sea level conditions to maximize the

thrust of the configuration at take-off and minimize gravity losses. Therefore, an expansion area ratio of $\epsilon = 15$ was selected. The second stage engine is ignited in higher altitude and does not need to deliver thrust at sea level conditions. Therefore, an expansion area ratio of $\epsilon = 70$ was selected, which is larger than the expansion ratio of the original Vulcain 2 engine, which is 58.2 [81]. Tab. 2 shows the engine specifications. The thermodynamic properties inside the engines are shown in Tab. 3. The estimated delivered performance can be seen in Tab. 4.

Tab. 2: RETALT1 engines specifications

		First stage engine	Second stage engine
Engine	**Chamber pressure**	117.3 bar	117.3 bar
	Mass flow rate	323 kg/s	322 kg/s
	Oxidizer/Fuel Ratio	6.7	6.7
	Cycle	Gas generator cycle	Gas generator cycle
	Area expansion ratio	15	70
Propellant	**Oxidizer**	O2 (Liquid)	O2 (Liquid)
	Fuel	H2 (Liquid)	H2 (Liquid)

Tab. 3: RETALT1 engines thermodynamic properties

	First stage engine		Second stage engine		
Parameter	**Nozzle inlet**	**Nozzle exit**	**Nozzle inlet**	**Nozzle exit**	**Unit**
Pressure	117.3	0.874	117.3	0.114	bar
Temperature	3624.7541	1740.1838	3624.7541	1172.3678	K
Isentropic exponent	1.1364	1.2229	1.1364	1.2593	
Density	5.6767	0.0905	5.6767	0.0175	kg/m³
Velocity	0	3820.9762	0	4227.2614	m/s
Mach number	0	3.516	0	4.6702	

Tab. 4: RETALT1 engines estimated delivered performance

	First stage engine		Second stage engine		
Parameter	**Sea level**	**Vacuum**	**Sea level**	**Vacuum**	**Unit**
Specific impulse (by weight)	372.1584	401.6361	294.3526	431.9149	s
Thrust	1179.364	1272.522	929.957	1364.294	kN

The geometry of the combustion chamber and nozzle is defined with the parameters as shown in Fig. 19. The parameters for the engine geometries are given in Tab. 5. The Vulcain 2 nozzle has a parabolic thrust optimized contour [23, 82, 83]. For the RETALT1 engines thrust optimized ideal contours were used. The resulting engine contours are shown in Fig. 20.

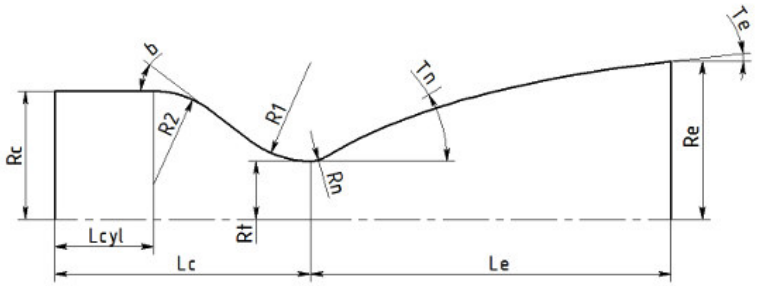

Fig. 19: Parameters for the definition of the engine geometry [84]

Tab. 5: Geometry parameters of the RETALT1 engines

Parameter	First stage engine	Second stage engine	Unit
Dc	469.91	469.91	mm
b	35.00	35.00	deg
R2	404.72	404.72	mm
R1	113.06	113.06	mm
L*	752.48	752.48	mm
Lc	356.38	356.38	mm
Lcyl	59.40	59.40	mm
Dt	282.64	282.64	mm
Rn	107.97	107.97	mm
Tn	24.87	32.11	deg (max)
Le	1545.81	3084.33	mm
Te	5.57	9.46	deg
De	1094.65	2364.72	mm
Ae/At	15.00	70.00	-

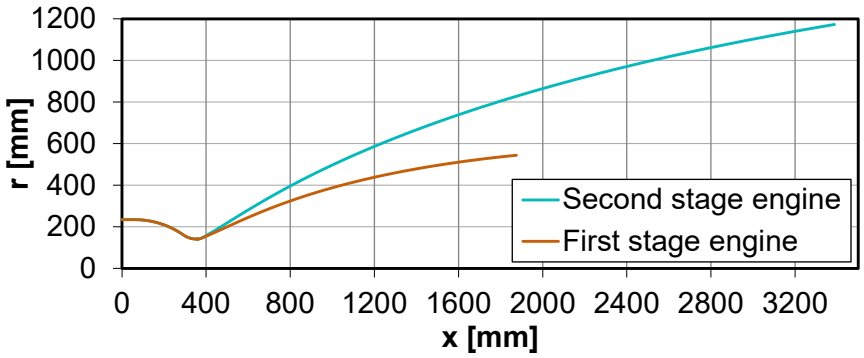

Fig. 20: Contours of the RETALT1 engines

4. Methodology

In this section, first, the wind tunnel facilities are described in which the test series were performed. Then, the wind tunnel models and the instrumentation of the experiments are summarized. Finally, the construction of the averaged modal solution is described, which is proposed to analyze highly unsteady flow fields.

4.1. Wind Tunnel Facilities

4.1.1. Trisonic Wind Tunnel Cologne

The aerodynamic phase was tested in the Trisonic Wind Tunnel Cologne (TMK). The wind tunnel is a blow down facility using pressurized air (up to 60 bar) which is expanded down to atmospheric conditions with a rectangular test section of 60 cm x 60 cm and an operational range of Mach numbers between 0.5 up to 4.5 without the use of the additional ejector and up to 5.7 with the use of the ejector. Fig. 21 shows the test section of the TMK. The operation range is shown in Fig. 22, and a scheme of the facility can be seen in Fig. 23.

The air is supplied from a high-pressure reservoir and passes through the storage heater, settling chamber, the Laval nozzle, the test chamber and the diffuser to ultimately flow out into the atmosphere. Due to a hydraulic adaptable nozzle, several Mach numbers can be tested in one run in the supersonic regime. In the subsonic regime the Mach numbers are set by the variation of the stagnation pressure (up to $p_0 = 25\ bar$) and the total temperature ($T_0 = 550\ K$). In the subsonic regime only one Mach number can be tested per run. A motion control device, on which the wind tunnel models are mounted, allows for continuous polars of the angle of attack.

In the subsonic and transonic regime ($M_\infty < 1.2$), the facility is commonly operated at a static pressure of $p_\infty \approx 1\ bar$. In the supersonic regime ($M_\infty > 1.2$) it is operated at a dynamic pressure of $q_\infty \approx 1\ bar$. The unit Reynolds number ranges from $Re = 1.2 \times 10^7\ m^{-1}$ ($M_\infty = 0.5$) to $Re = 3.7 \times 10^7\ m^{-1}$ ($M_\infty = 1.2$) in the subsonic and transonic regime. In the supersonic regime it can be varied between $Re = 2.6 \times 10^7\ m^{-1}$ and $Re = 7.6 \times 10^7\ m^{-1}$. This range can be enhanced by the use of the ejector. In the ejector, the pressure in the wind tunnel exhaust flow is lowered by an additional mass flow that is supplied through Laval nozzles, at supersonic speeds, tangential to the wind tunnel exhaust flow [85]. Hence, the pressure in the test section can be lowered without causing blockage of the wind tunnel. This results in lower Reynolds numbers that can be tested.

High speed Schlieren videos can be recorded in the supersonic regime through the quartz windows giving visual access to the test chamber. In the transonic and subsonic regime, a test section with perforated walls is installed downstream of the supersonic test section for boundary layer suction. For this reason, Schlieren imaging is not possible in these regimes.

A more detailed description of the wind tunnel facility TMK can be found in [86].

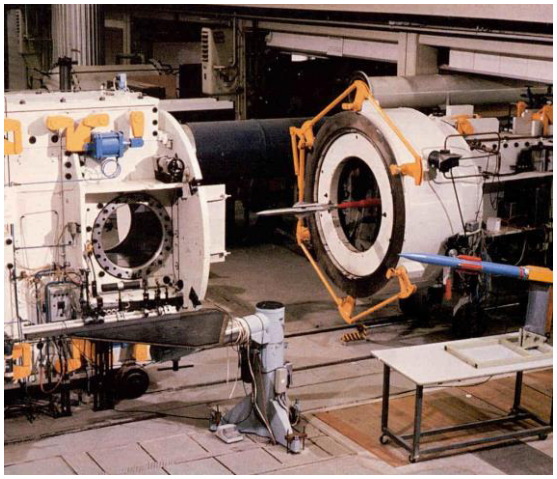

Fig. 21: Supersonic test section of the Trisonic Wind Tunnel TMK [86]

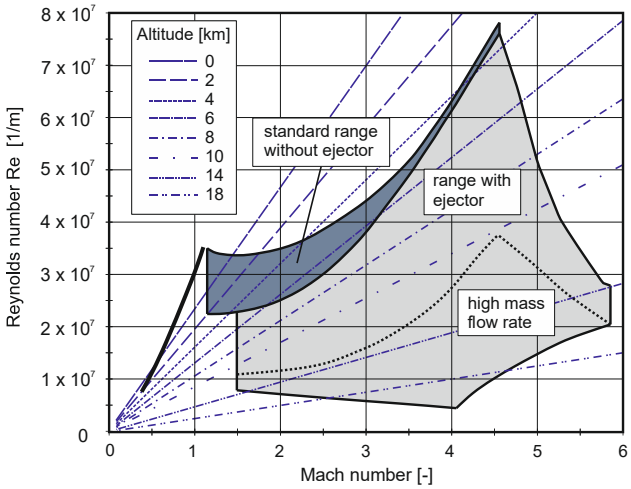

Fig. 22: Performance map of the Trisonic Wind Tunnel TMK [86]

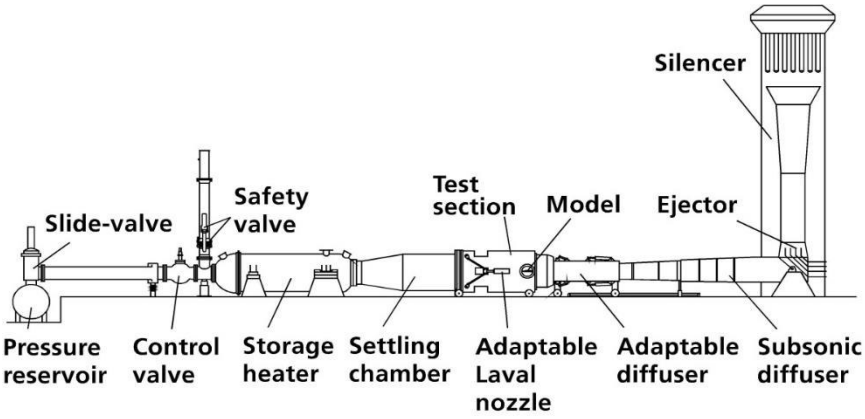

Fig. 23: Schematic of Trisonic Wind Tunnel TMK [86]

4.1.2. Hypersonic Wind Tunnel Cologne

The Reentry Burn of the RETALT1 configuration was studied in the Hypersonic Wind Tunnel Cologne. The exhaust plume was simulated with cold gas in this case. The Hypersonic Wind Tunnel Cologne is a blow down facility from 60 bar pressurized air down to vacuum. The wind tunnel nozzle with a diameter of 600 mm ends inside a free-jet test chamber. With the maximum total electrical power of 5 MW, stagnation temperatures of up to 1000 K can be reached. The typical test duration is around 30 s, depending on the test conditions. Mach numbers of 4.8, 5.3, 6.0, 7.0, 8.7 and 11.2 can be obtained by exchanging the wind tunnel nozzle. The operating range of unit Reynolds numbers is between 2.0×10^6 and 20.0×10^6 m^{-1}, depending on the total pressure and total temperature. Quartz glass windows provide visual access to the test chamber. The facility is described in more detail in [87].

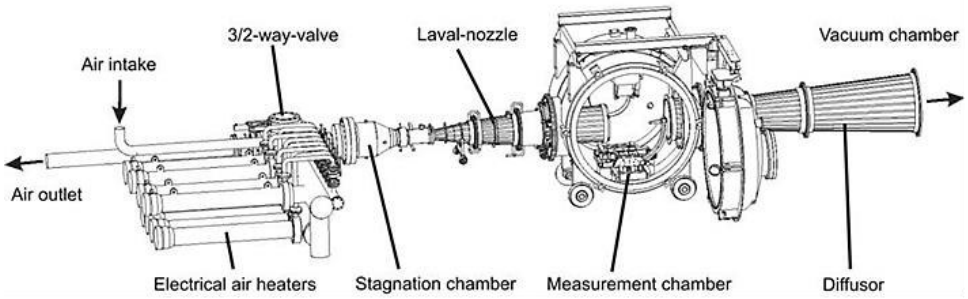

Fig. 24: Scheme of the Hypersonic Wind Tunnel Cologne (H2K) [87]

4.1.3. Vertical Free-Jet Facility Cologne

The landing burn of the RETALT1 configuration was tested in the Vertical Free-Jet Facility Cologne (VMK) at the Department of Supersonic and Hypersonic Technologies of the German Aerospace Center. The exhaust plume was simulated with a cold gas jet, as well as, with hot oxygen/hydrogen combustion in the combustion chamber inside the wind tunnel model. Due to the chemistry involved in the hot gas tests, in their evaluation a multitude of additional factors need to be considered, such as the local gas composition and post combustion in the exhaust plume. For this reason, this thesis focuses only on the results of the cold gas tests, as their thorough understanding is the basis for the analyses of the more complex hot gas tests in the future.

The VMK is a blow-down facility from pressurized air of up to 60 bar down to ambient pressure, with an open test section. This enables testing sea level conditions in the facility for Mach numbers up to 2.8. The maximum Mach number that can be tested in the facility is 3.2. The subsonic nozzle used in the experiments presented in this work has an exit diameter of 340 mm. A sketch of the wind tunnel is shown in Fig. 25a, the performance map is shown in Fig. 25b.

To perform hot gas testing with gaseous oxygen and hydrogen, an additional test stand infrastructure exists at the VMK, which operates at 130 bar and supplies the gases with up to 300 bar. This facility is also called the Hot Plume Testing Facility (HPTF) and is described in detail in [88].

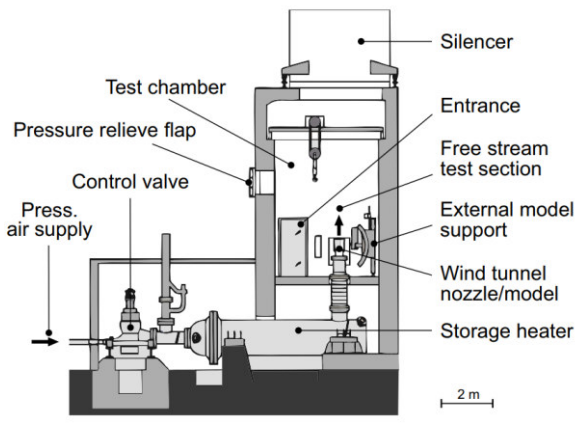

a) Schematic of the VMK facility layout around the test chamber [88]

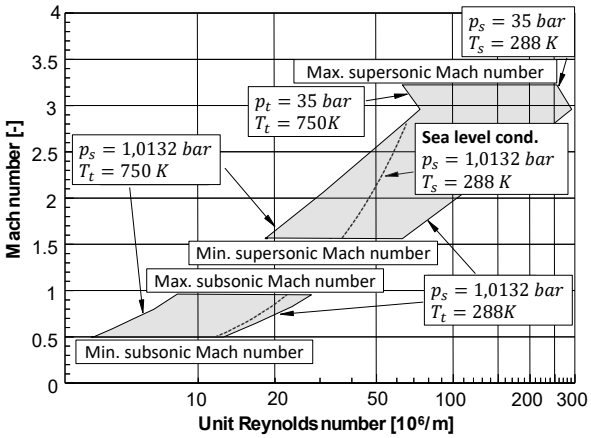

b) Operating range of the facility [88]

Fig. 25: Overview of Vertical Free-Jet Facility Cologne (VMK)

4.2. Wind Tunnel Models and Instrumentation

In the following, the models and the instrumentation used in the wind tunnel tests in the TMK, H2K and VMK are described.

4.2.1. Wind Tunnel Model for Trisonic Wind Tunnel Cologne

The aim of the test series in the TMK was to assess three main aspects: The stability and trimmability of the RETALT1 vehicle with the different types of control surfaces, the efficiency of the control surfaces to generate aerodynamic forces and moments, and the evaluation of pressure information on selected sensor positions.
The wind tunnel model configurations with the different types of ACS mounted in the wind tunnel are shown in Fig. 26. The scaling of the wind tunnel models is 1/130 from the original RETALT1 configuration which has a diameter of the first stage of 6 m and a length of 64.7 m excluding the interstage (see section 3).

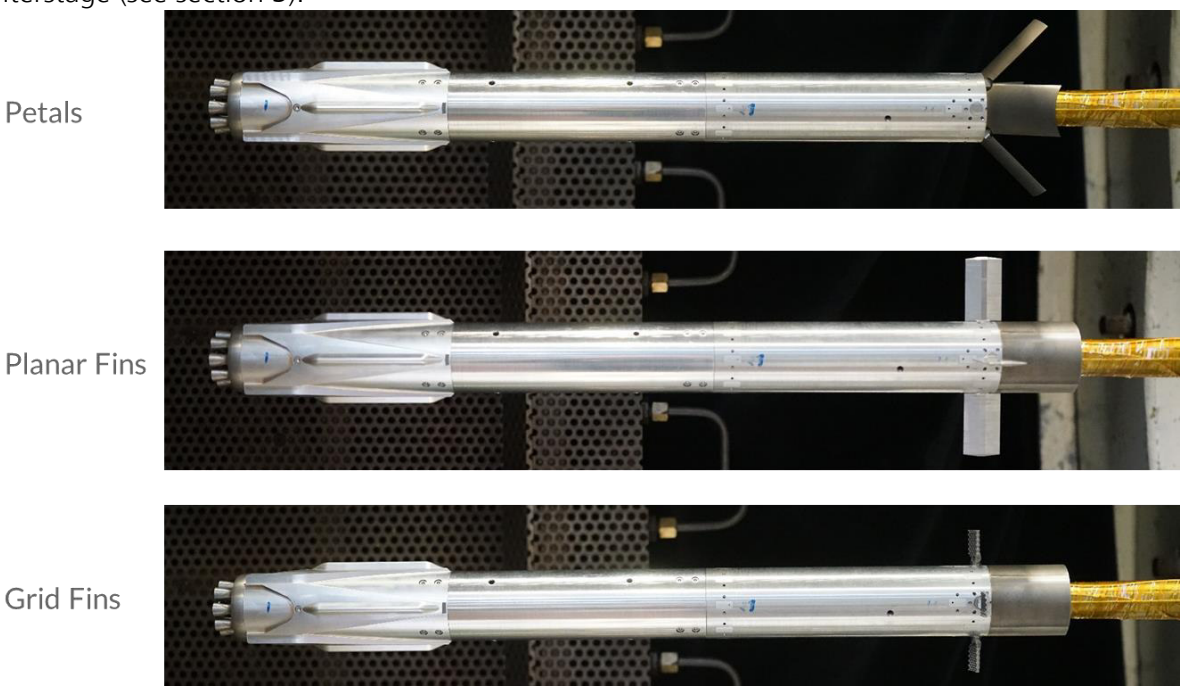

Fig. 26: RETALT1 wind tunnel model with petals, planar fins and grid fins mounted in the TMK

The reference frame used for the data acquisition is shown in Fig. 27a, where CA is the axial force coefficient, CN the normal force coefficient and CY the side force coefficient. CMx, CMy and CMz define the moment coefficients in the reference point around the respective axes. The reference point is defined to be the foremost point of the cylindrical body of the RETALT1 configuration in the x-axis excluding the interstage.
For the identification of the configurations the following definition was used:

- PF: Planar Fin
- GF: Grid Fin

- B: Petal ("Blume" is the German word for flower and is less confusing than a "P" for petal)

The deflection angles of the ACS are denoted separately behind the identifier for the ACS type. The aerodynamic control surfaces are numbered from 1 to 4 in the clockwise direction looking at the base plane of the configuration (see Fig. 29a).

Example:
B0,10,0,0 : Petals: Petal 1: 0°, Petal 2: 10°, Petal 3: 0°, Petal 4: 0° (resulting in a pitch moment)

For the planar fins the deflection angles are defined around the y and z-axis. The fin pointing in the direction of the axis has a positive deflection defined by the right-hand-rule around the axis. The opposite fin follows this definition (see Fig. 28).
For the Petals the deflection δ is defined from its folded state 0° which resembles a conventional interstage (see Fig. 29e). Some examples of different configurations are given in Fig. 29.

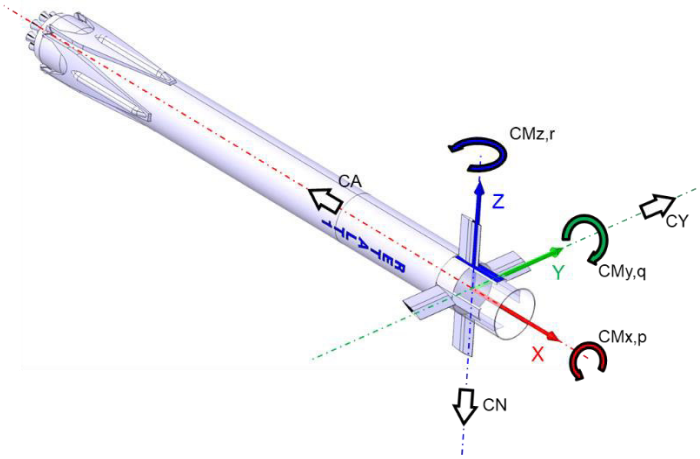

Fig. 27: Definition of the reference frame

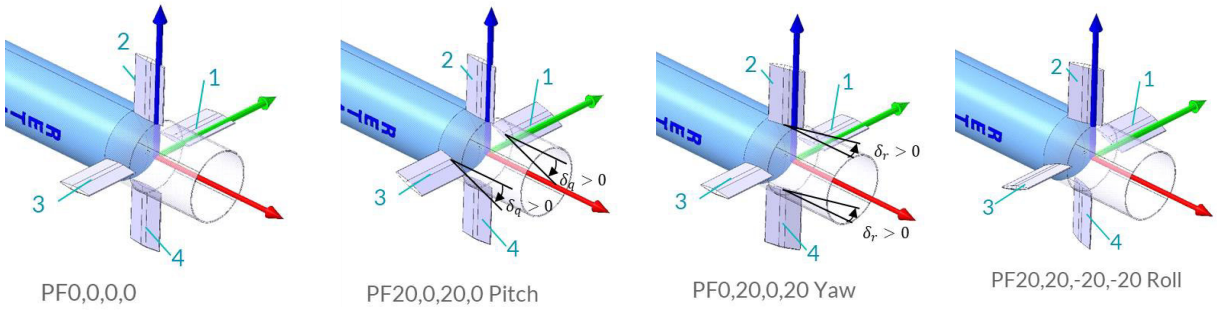

Fig. 28: Description of the configurations of Planar Fins

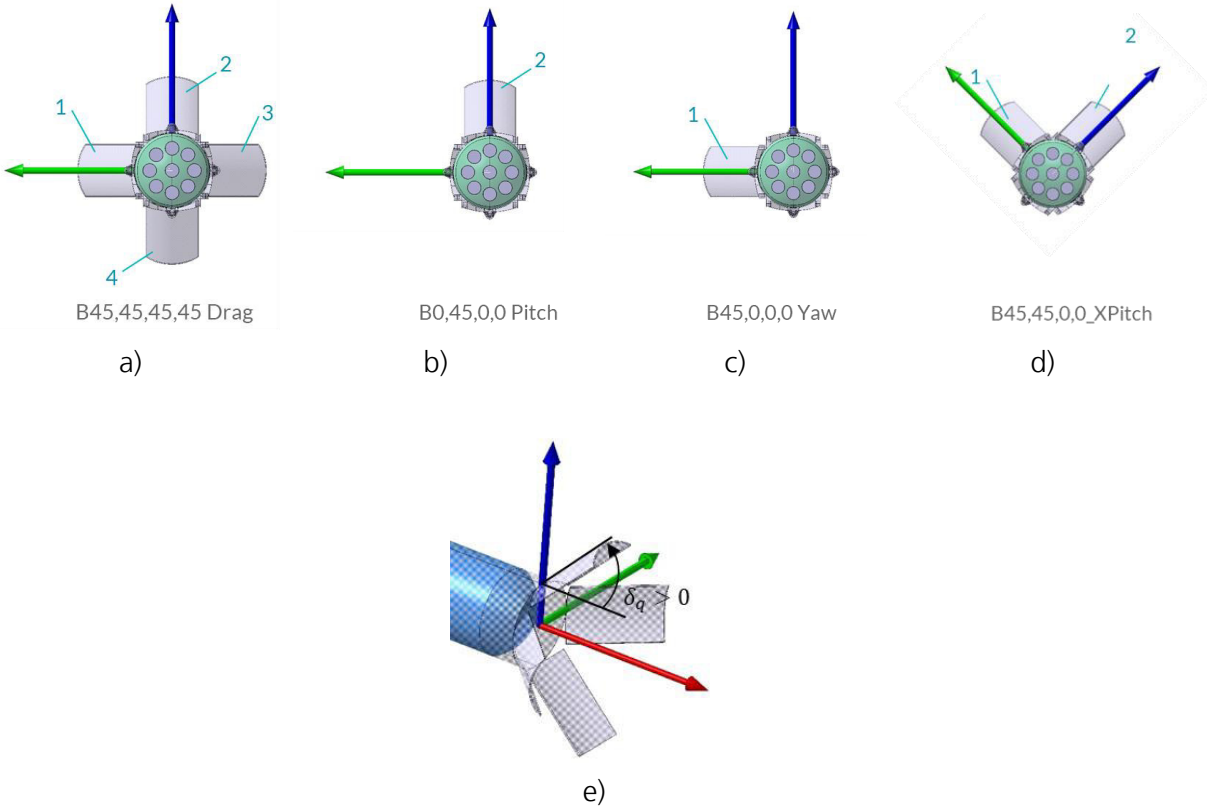

Fig. 29: Description of the configurations of Petals

For the measurement of the aerodynamic forces and moments, a DLR inhouse 6 components strain gauge balance was utilized. In Fig. 30 the model mounted on the balance is sketched out. Pressures were measured in three measurement planes as shown in Fig. 31. Plane 1 is close to the fins, plane 2 at roughly two thirds of the length of the model and plane 3 at the base plane. The sensor numbering follows the numbering of the aerodynamic control surfaces. Starting from the left (1) in clockwise direction with a view on the base plane, to the top (2), to the right (3), to the bottom (4). The sensors at the base plane have an additional number defining their radial position. While (1) is close to the x-axis, (2) is the position close to the outer diameter of the configuration. Kulite sensors were used for the pressure measurements due to their small form factor and their capabilities of measuring high frequencies. Due to spatial requirements LQ-062-3.5BARA sensors were used on the sensor locations on the cylindrical part of the configuration and XCQ-080-3.5BARA sensors were employed for the sensor location on the base plane. Additionally, two pressure tubes were implemented on the model support sting below the interstage segments (pSTAGE) (see Fig. 30) and in the balance (pBALANCE) for static pressure measurements.

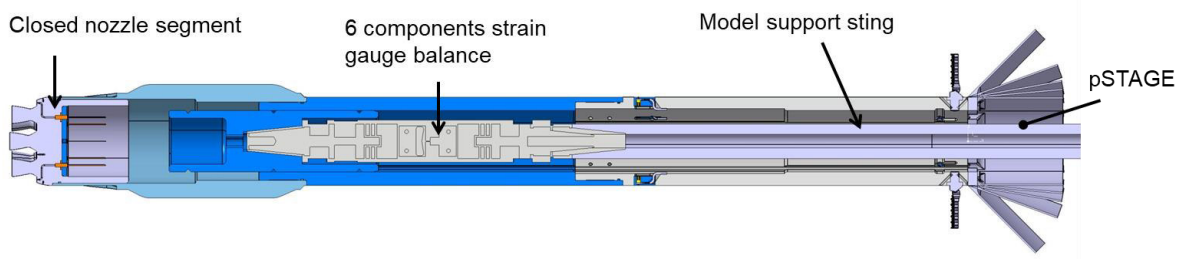

Fig. 30: RETALT1 Wind Tunnel Model with DLR 6 components strain gauge balance

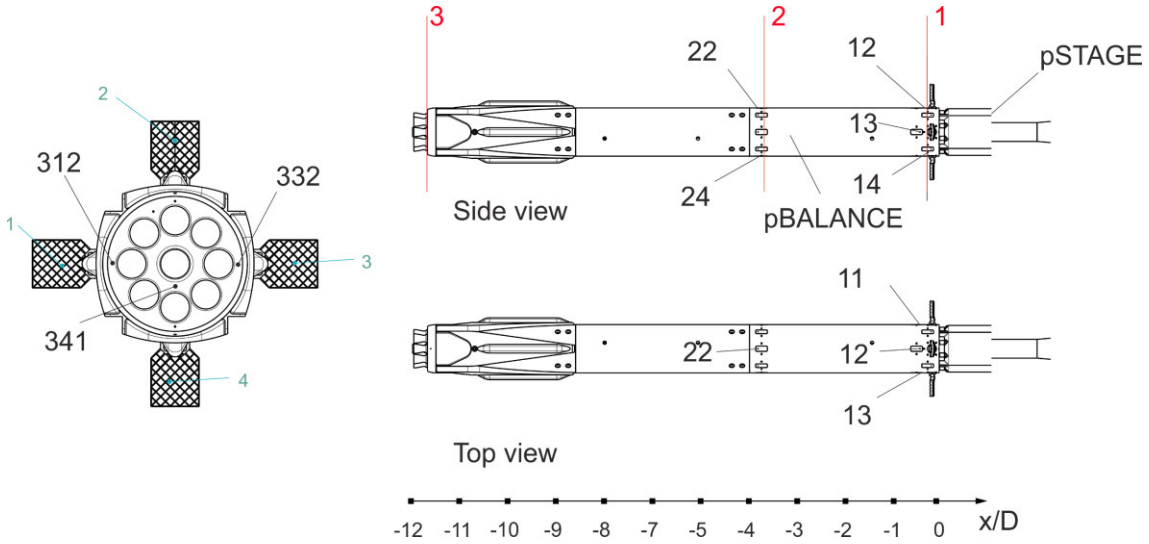

Fig. 31: Distribution of pressure measurements

4.2.2. Wind Tunnel Model for Hypersonic Wind Tunnel Cologne

In this section the wind tunnel model, designed for the H2K is described. First the general model design and the instrumentation is described. Then, the detailed design of the wind tunnel model nozzles, which are simulating the engines, is elaborated in detail, as it is crucial for the supersonic and hypersonic retro propulsion experiments.

4.2.2.1. Design of the Wind Tunnel Model

Some of the model parts of the H2K model are shared with the TMK model. A schematic of the RETALT1 model is shown in Fig. 32 and the wind tunnel model mounted in the H2K facility is shown in Fig. 33. The model is designed such that a short and a long version of it can be tested by adding or removing the cylindrical segment shown in Fig. 32. Various model supports and stings were designed to enhance the range of the axial positioning of the wind tunnel model in the test chamber.

While the long model version is used for force measurements, the short model version is intended for detailed analyses of the base flow using high frequency pressure measurements. In the test cases with the long model it needs to be positioned very close to the wind tunnel nozzle exit as otherwise the shock forming at the wind tunnel nozzle lip would impinge on the model. Therefore, the flow field is not entirely visible in the Schlieren images. Hence, in this work only results obtained

with the short model are discussed as the interpretation of those results is more strait forward as the flow field could be visualized in the Schlieren recordings. The model is scaled by 1/130 with respect to the RETALT1 flight configuration. The scaling resulted from a trade-off of fitting the tubular 4 components strain gauge balance and the pressure supply in the model while scaling the model as much as possible, as Gutsche et al. [65] showed that the thrust coefficients realizable in the wind tunnel is inversely proportional to the squared model diameter, which is why a small model size is preferable to increase the maximum thrust coefficient that can be tested. The reference length for the nondimensionalization is the diameter of 6 m in the flight configuration (hence 46.154 mm in the experiment). The reference area is the base area, A_B, of 28.27 m^2 for the flight configuration. For the simulation of the exhaust plume, air is blown out through a hollow model support sting and a model Laval nozzle (see Fig. 32). Various nozzle segments were manufactured for tests with different engine combinations, i.e. one active engine or three active engines, and different engine deflection angles. The locations of the high frequency pressure sensors are shown in Fig. 34. The pressure sensors are distributed in three measurement planes. One close to the interstage (plane 1), one close to the folded landing legs (plane 2), and one at the model base (plane 3). Furthermore, the sensors are numbered in clockwise direction, when looking at the base of the model. This is represented by the second index. The third index for the sensors on the base plane defines the radial positioning from a position close to the center with index 1 to the outermost sensor with index 3. The pressure in the wake was measured with a pressure tube (pSTAGE). The pressures in plane 1 and 2 were measured with LQ-062-0.7BARA Kulite pressure sensors, and the pressures in plane 3 were measured with XCQ-080-0.7BARA pressure sensors.
The model nozzles were designed with an expansion area ratio of 2.5, resulting in an exit Mach number of 2.443, with a throat diameter of 5.33 mm, an exit diameter of 8.42 mm and an exit angle of 5.57°. The contour was designed as parabolic approximation of a bell nozzle with a fixed expansion area ratio and a fixed nozzle exit angle. The exit angle was chosen to be 5.57° to match the nozzle exit angle of the RETALT1 first stage engine which has a thrust optimized contour with an area expansion ratio of 15 (see section 3.2). The choice of an expansion area ratio of 2.5 is discussed in detail in the next section.
High speed Schlieren videos were recorded with a FASTCAM SA-X2 high-speed camera at 20 kHz with an exposure time of 2.5 µs. A Z-type Schlieren setup with a focal length of 6 m and mirror diameter of 600 mm was used as described in [12, 89]. The knife edge was positioned vertically (perpendicular to the flow). The high frequency pressure measurements were performed at 50 kHz. Condensation was visualized with five laser beams with an optical power of 0.7 mW (class 2 laser) stretched out with a plano-concave cylindrical lens in the area were the plume was expected. The resulting laser lines in a plane parallel to the α-plane are shown in Fig. 35.

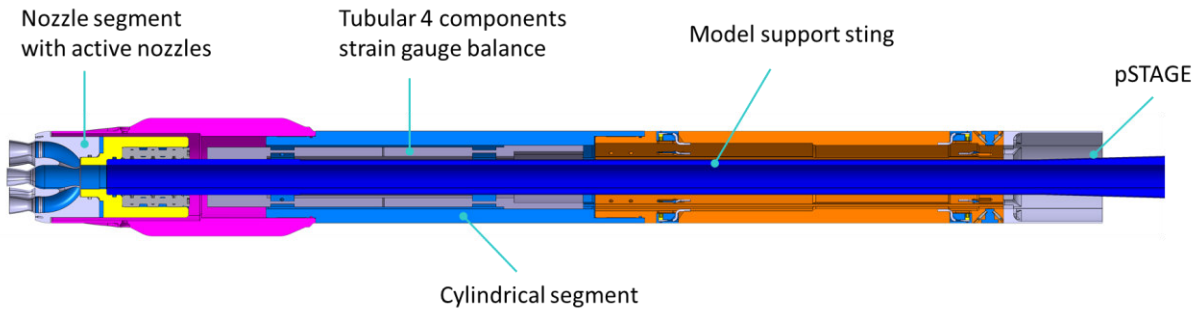

Fig. 32: RETALT1 wind tunnel model design

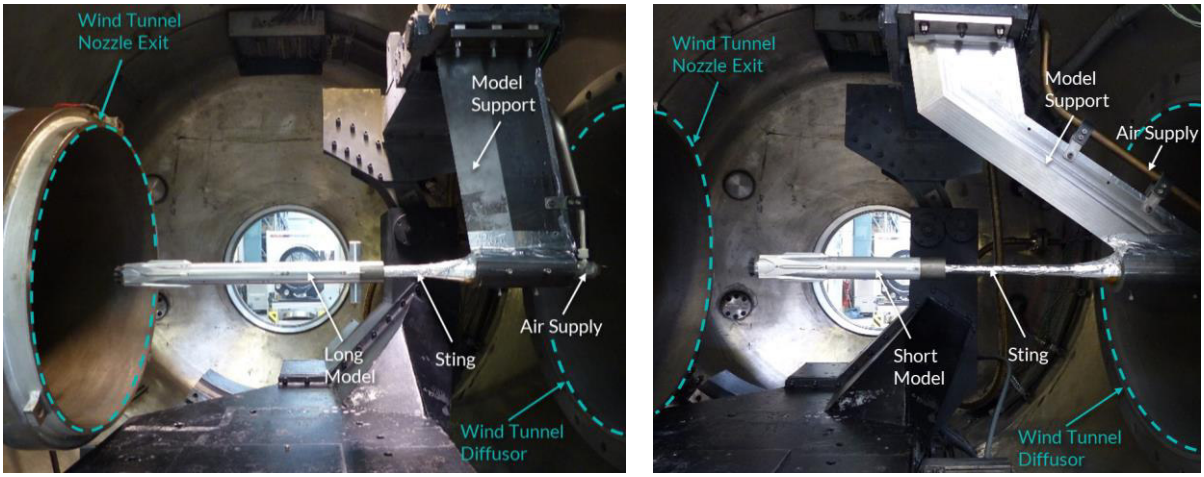

a) Long model version b) Short model version

Fig. 33: RETALT1 wind tunnel model mounted in H2K

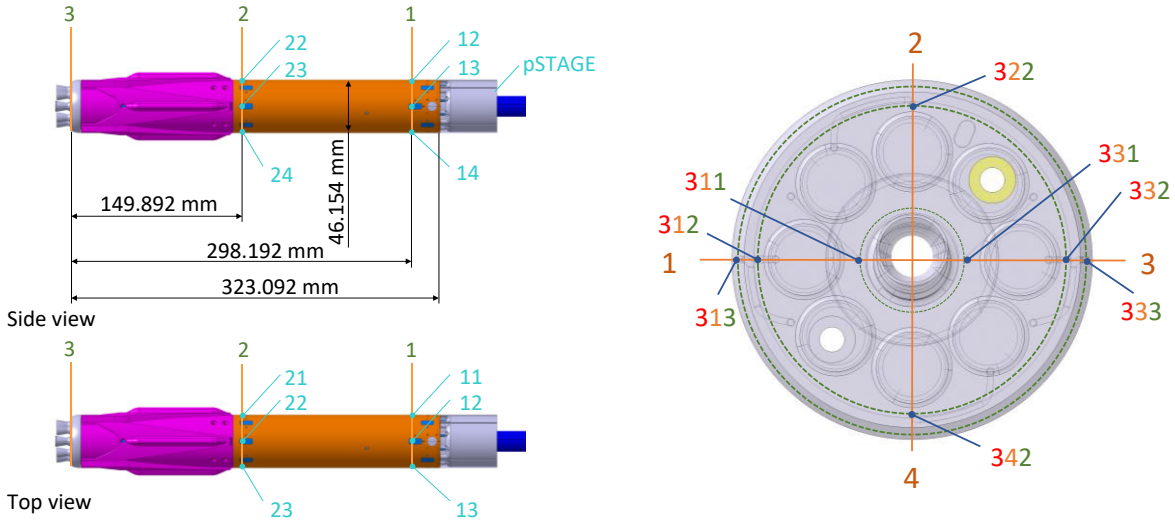

Fig. 34: RETALT1 distribution of pressure sensors

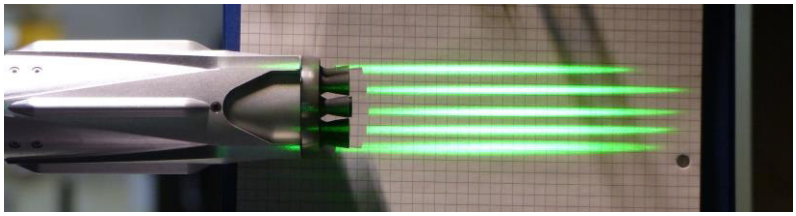

Fig. 35: Laser lines for the visualization of condensation in the plume

4.2.2.2. Design of the Wind Tunnel Model Nozzles

A detailed view of the inner flow contour inside the wind tunnel model for one and three active engines is shown in Fig. 36. The expansion ratio of the wind tunnel model nozzles was chosen to be 2.5, which is shortly motivated in the following.

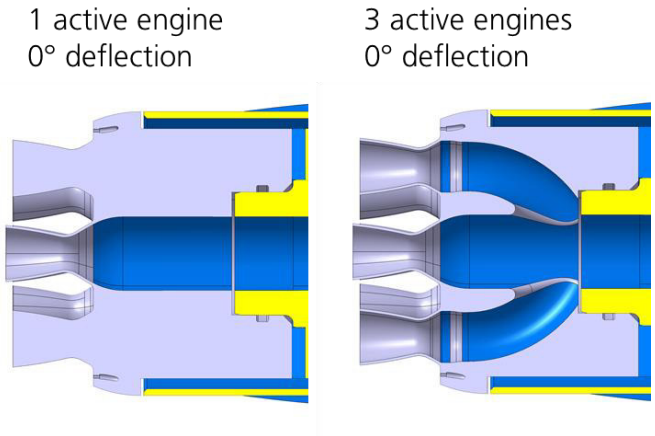

Fig. 36: Detail of the inner flow contour

The main similarity parameters to be matched for supersonic (and hypersonic) retro propulsion flows are the thrust coefficient and the ambient pressure ratio (APR) [45]. The ambient pressure is here the free stream static pressure p_∞, hence, the APR is p_e/p_∞. The thrust coefficient, C_T, is defined as:

$$C_T = \frac{F_T}{q_\infty A_B} \tag{18}$$

where F_T is the thrust, q_∞ is the dynamic pressure in the free stream and A_B is the reference area, which is the base area in the case of RETALT1. Neglecting the pressure loss of the engine, the thrust coefficient can be written as a function of the engine scaling parameter K [45]:

$$C_T = \frac{1}{M_\infty^2} \cdot \frac{p_e}{p_\infty} \cdot \frac{2A_e}{\gamma_\infty A_B}(1 + \gamma_e M_e^2) = \frac{1}{M_\infty^2} \cdot \frac{p_e}{p_\infty} \cdot \frac{1}{\mathrm{K}} \tag{19}$$

Here, C_T is the thrust coefficient, M_∞ and M_e are the freestream and nozzle exit Mach numbers, A_e is the nozzle exit area, and γ_e and γ_∞ are the heat capacity ratios at the nozzle exit and in the freestream.

Apart from the ratio of the nozzle exit area to the reference area (A_e/A_B) and the free stream heat capacity ratio (γ_∞), the engine scaling parameter only depends on the nozzle exit parameters [45]:

$$\mathrm{K} = \frac{\gamma_\infty}{2}\frac{A_B}{A_e}\frac{1}{1+\gamma_e M_e^2} \tag{20}$$

The thrust coefficient similarity and the APR similarity between the experiment (subscript exp) and the flight (subscript Fl) are proportional to the ratio of the engine scaling parameters which can be shown as follows:

$$\frac{C_{T,exp}}{C_{T,Fl}} = \frac{\frac{1}{M_{\infty,exp}^2}}{\frac{1}{M_{\infty,Fl}^2}} \cdot \frac{\left(\frac{p_e}{p_\infty}\right)_{exp}}{\left(\frac{p_e}{p_\infty}\right)_{Fl}} \cdot \frac{\frac{1}{\mathrm{K}_{exp}}}{\frac{1}{\mathrm{K}_{Fl}}} \tag{21}$$

$$\underbrace{\frac{C_{T,exp}}{C_{T,Fl}}}_{\substack{Thrust\ coefficient \\ similarity}} = \underbrace{\frac{M_{\infty,Fl}^2}{M_{\infty,exp}^2}}_{\substack{Mach\ number \\ similarity}} \cdot \underbrace{\frac{\left(\frac{p_e}{p_\infty}\right)_{exp}}{\left(\frac{p_e}{p_\infty}\right)_{Fl}}}_{\substack{Ambient\ pressure \\ ratio\ similarity}} \cdot \underbrace{\frac{\mathrm{K}_{Fl}}{\mathrm{K}_{exp}}}_{\substack{Engine\ scaling \\ parameter\ ratio}} \tag{22}$$

If the ratio of the engine scaling parameters equals one, and if the Mach number similarity is fulfilled, the thrust coefficient similarity and the APR similarity are matched at the same time.

Assuming that A_B, A_e, γ_∞ and γ_e are constants, the engine scaling parameter solely depends on M_e which depends on the nozzle expansion ratio of the model nozzle, ϵ. K versus the expansion ratio is plotted in Fig. 37; for reference also M_e is shown. The engine scaling parameter for the flight condition is 1.31. Hence matching this engine scaling parameter in the experiment would require an expansion ratio of 5.5 (see Fig. 37).

Defining the subscript $\frac{exp}{Fl}$ for the ratios of the various similarity parameters, eq. (22) can be rewritten as:

$$C_{T,exp/Fl} = M_{\infty,Fl/exp}^2 \cdot \left(\frac{p_e}{p_\infty}\right)_{exp/Fl} \cdot \frac{1}{\mathrm{K}_{exp/Fl}} \tag{23}$$

If $M_{\infty,Fl/exp}^2 = 1$ and $\left(\frac{p_e}{p_\infty}\right)_{exp/Fl} = 1$ it follows:

$$C_{T,exp/Fl} = \frac{1}{\mathrm{K}_{exp/Fl}} \tag{24}$$

If $M_{\infty,Fl/exp}^2 = 1$ and $C_{T,exp/Fl} = 1$ it follows:

$$\left(\frac{p_e}{p_\infty}\right)_{exp/Fl} = \mathrm{K}_{exp/Fl} \tag{25}$$

In Fig. 38 the equations (24) and (25) are plotted. This visualizes that at expansion ratios unequal to 5.5 if either the thrust coefficient similarity or the APR similarity is met, the other one is compromised. At an expansion ratio of 5.5 both similarities equal 1.

With the required exit pressure ratio similarity $\left(\frac{p_e}{p_\infty}\right)_{exp/Fl}$, and p_e and p_∞ known for the flight condition ($p_e = 0.874\ bar$, $p_\infty = 0.002125\ bar$ for Mach 5.3), the total pressure in the wind tunnel model p_{CC} can be derived with the isentropic relations. The baseline freestream total pressure for the experiments was chosen to be 4 bar. The total pressures in the wind tunnel model, necessary to reach the thrust coefficient similarity and the APR similarity for these test conditions are shown

in Fig. 39. At an expansion ratio of 5.5, both similarities are reached at a total pressure of 120 bar. This pressure is challenging for the design of the model as the wall thicknesses are limited due to the implementation of the balance and pressure sensors. In addition, it could not be guaranteed that these pressures could be provided by the high-pressure air supply of the wind tunnel facility. For this reason, p_{CC} was limited to 60 bar. As the thrust coefficient is the main similarity parameter, it was prioritized over the ambient pressure ratio and the nozzle expansion ratio was chosen to provide thrust coefficient similarity at 60 bar, which results in an expansion ratio of 2.5.
It is noted that the discussion in this chapter applies equally for the single- and for the three-engines case. For the case of three active engines the thrust multiplies by three, which translates to a multiplication of A_e by three in eq. (19). As this applies equally for flight and experiment, the similarity ratios are not affected.

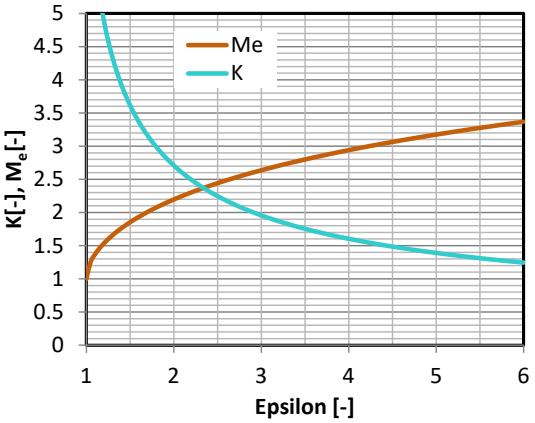

Fig. 37: Engine scaling parameter and nozzle exit Mach number in dependence of the expansion ratio

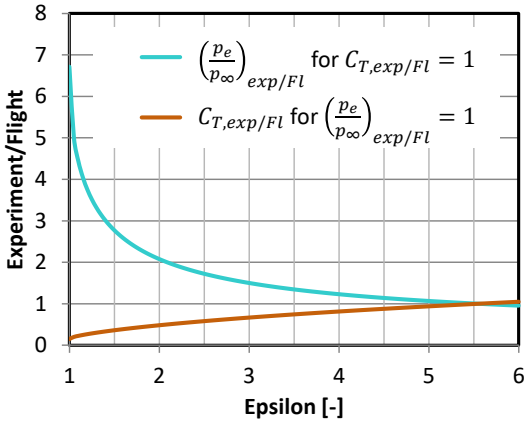

Fig. 38: Exit pressure ratio similarity and thrust coefficient similarity as function of the nozzle expansion ratio as in eq. (24) and (25) (for $M^2_{\infty,Fl/exp} = 1$)

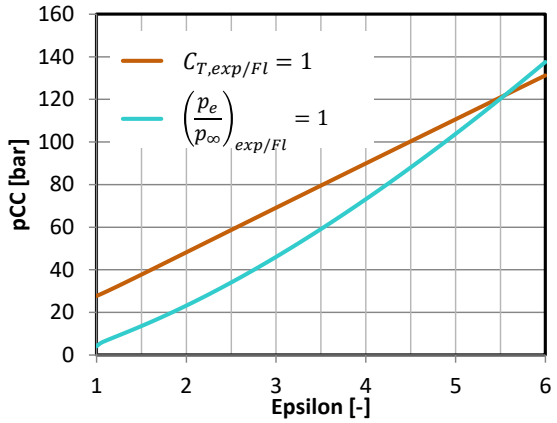

Fig. 39: Total pressure in the wind tunnel model for thrust coefficient and APR similarity as function of the nozzle expansion ratio

4.2.3. Wind Tunnel Model for Vertical Free-Jet Facility Cologne

In this section the wind tunnel model, designed for the VMK is described. First the general model design and the instrumentation is described. Then, the detailed design of the wind tunnel model nozzle, which is simulating the engine, is elaborated in detail, as it is crucial for the subsonic retro propulsion experiments.

4.2.3.1. Design of the Wind Tunnel Model

The test setup for the cold gas tests in the VMK with counterflow environment (retro propulsion) is shown in Fig. 40. The wind tunnel model concept is shown in Fig. 41. The model was prepared for hot gas testing with hydrogen and oxygen. For cold gas testing, high pressure air was supplied through the manifold assembly and blown out through the wind tunnel model nozzle. The wind tunnel model for the RETALT1 configuration has a scale of 7/600 with respect to the flight configuration. Hence, it has a base diameter of 70 mm. The reference area is the base area, A_B, of 28.27 m^2 for the flight configuration. The scaling follows a trade-off of best meeting the similarity parameters of the flight conditions, while keeping design restrictions. The model nozzle was designed as parabolic approximation of a bell nozzle with a fixed expansion area ratio and a fixed nozzle exit angle. It has an expansion area ratio of 5.5, resulting in an exit Mach number of 3.275 (for air), with a throat diameter of 5.45 mm, an exit diameter of 12.77 mm and an exit angle of 5.57°. As for the H2K wind tunnel model, the exit angle was chosen to be 5.57° to match the nozzle exit angle of the RETALT1 first stage engine which has a thrust optimized contour with an area expansion ratio of 15 (see section 3.2). The positioning of the model in the wind tunnel facility can be adjusted with the movable support drive. For the cold gas tests, the model was positioned at a distance of 183 mm from the wind tunnel nozzle.

The distribution of pressure sensor locations in the base area of the model is shown in Fig. 42. The first index shows the radial distance of the sensor, the second the angular position. The sensors on the right-hand side have positive signs, the ones on the left have negative signs. In the rings 0 and 1 steady pressure measurements were performed with pressure tubes. In rings 2 and 3 high frequency pressure measurements were performed with XCQ-080-3.5BARA and XCE-080-3.5BARA Kulite pressure sensors.

The tests were recorded with Schlieren imaging at 25 kHz. The high frequency pressure measurements were performed at 50 kHz. The knife edge was positioned horizontally (perpendicular to the flow).

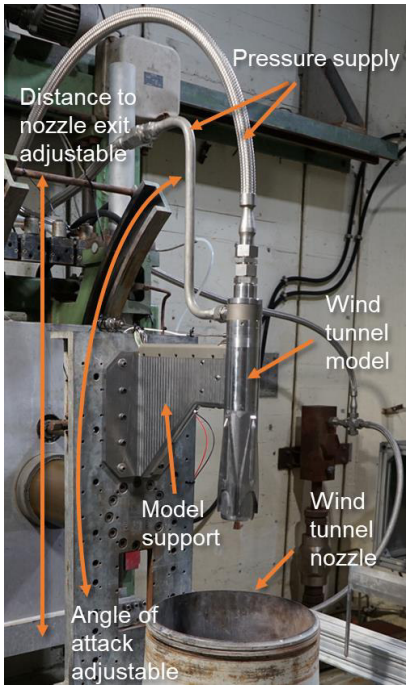

Fig. 40: Test Setup in VMK for cold gas tests [52]

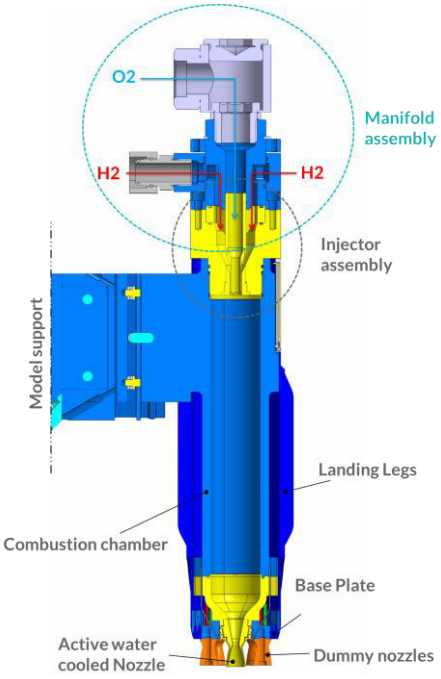

Fig. 41: Model concept for RETALT1

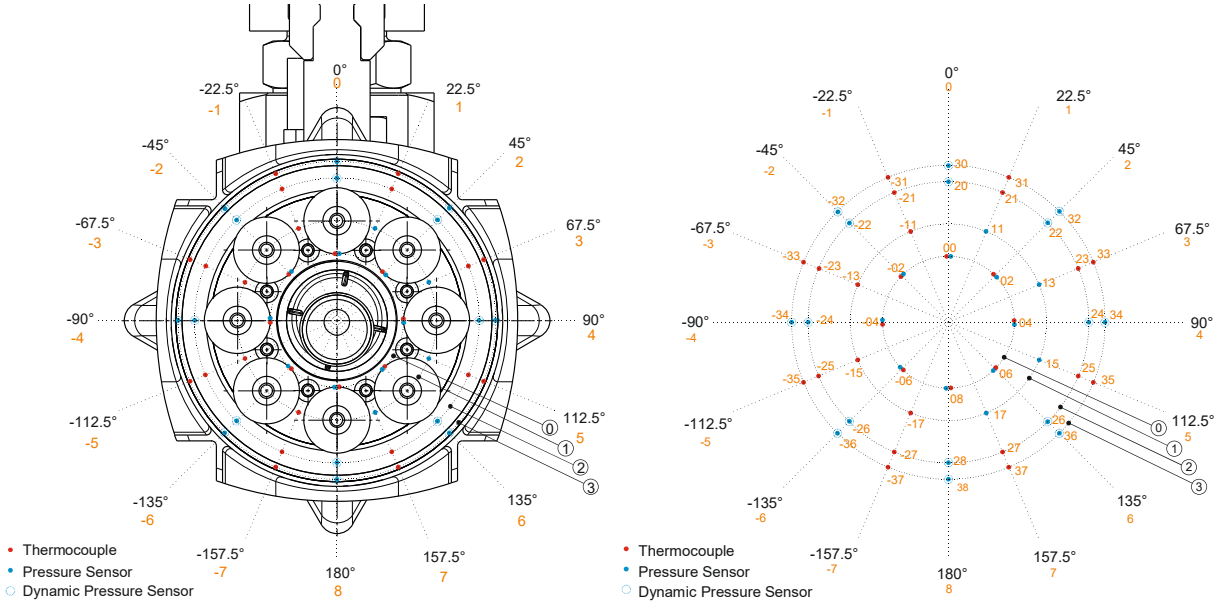

Fig. 42: Sensor distribution in the base area

4.2.3.2. Design of the Model Nozzles

As stated in section 2.6, the dominating similarity parameters for subsonic retro propulsion flows is the Momentum Flux Ratio. As further stated in section 2.6, the Momentum Flux Ratio and the thrust coefficient, where the pressure loss is neglected, can be used interchangeably. Furthermore, it was assumed that the Ambient Pressure Ratio (APR) is a second prevailing similarity parameter, which could be confirmed in the experiments later (see section 5.3.1).
As the thrust coefficient and the APR were also used for the design of the wind tunnel model nozzles of the H2K model, here the same procedure as described in 4.2.2.2 is applied.
Tab. 6 shows the two test conditions for which the wind tunnel model nozzles were sized. One condition at Mach 0.4 and one at Mach 0.8. As the VMK is a Free-Jet facility, the static pressure in the free stream, p_∞, can be assumed to be approximately 1 bar.
Fig. 43 shows the ratio of the APR and the thrust coefficient similarities for various expansion ratios. At an expansion ratio of 5.5 both similarities can be matched at the same time. It is noted that this plot is valid for both test conditions, as the equations (24) and (25) only depend on $\mathrm{K}_{exp/Fl}$ which is independent of the free stream conditions (except for γ_∞).
Fig. 44 and Fig. 45 show the pressures in the model necessary to reach the similarities. As the static pressure in flight is much lower for the higher altitude of the Mach 0.8 condition, the APR and thrust coefficients are much higher for this condition and, hence, a much higher pressure is needed in the wind tunnel model to achieve the similarity. The pressure for the Mach 0.4 condition is in the range of the maximum pressure of 80 bars which was defined for the combustion chamber. Therefore, an expansion ratio of 5.5 was chosen to reach similarity for the lower Mach numbers.

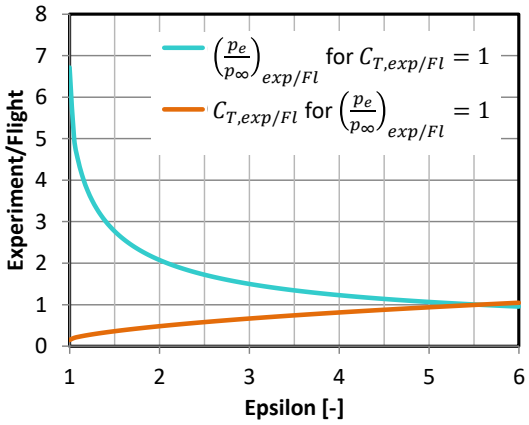

Fig. 43: Exit pressure ratio similarity and thrust coefficient similarity as function of the nozzle expansion ratio as in eq. (24) and (25) (for $M^2_{\infty,Fl/exp} = 1$)

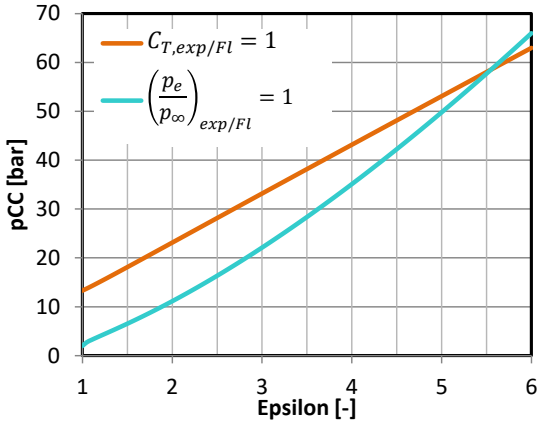

Fig. 44: Total pressure in the wind tunnel model for thrust coefficient and APR similarity as function of the model nozzle expansion ratio for the Mach 0.4 condition

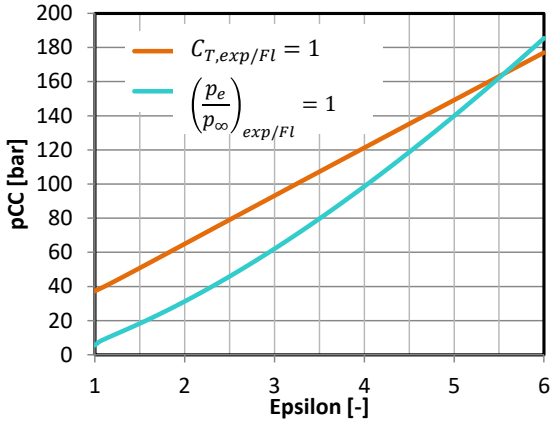

Fig. 45: Total pressure in the wind tunnel model for thrust coefficient and APR similarity as function of the model nozzle expansion ratio for the Mach 0.8 condition

Tab. 6: Flight (Fl) and experimental (exp) conditions for the design of the wind tunnel model nozzles

Mach	$p_{e,Fl}$ [bar]	$p_{\infty,Fl}$ [bar]	$p_{\infty,exp}$ [bar]
0.4	0.874	0.847	1.013
0.8	0.874	0.301	1.013

The nozzle contour was designed for the cold gas and the hot plume experiments. It was computed with the commercially available program RPA (Rocket Propulsion Analysis), in a way that the same nozzle exit angle as in the reference engine was achieved, which is 5.57°. An ideal contour was approximated with a parabola. The ideal nozzle contour strongly depends on the heat capacity ratio, which in turn depends on the gas or combustion products used in the experiments. In RPA a shifting chemical equilibrium model is used to compute the gas composition and properties along the nozzle [84].

Due to temperature changes in the flow, the heat capacity ratio can vary along the nozzle. For the hot plume experiments the Oxidizer Fuel Ratio (OFR) is the decisive factor for the heat capacity ratio. Therefore, the ideal nozzle contour was computed for air and for various OFRs of oxygen and hydrogen. They are shown in Fig. 46. Differences between the nozzle contours are observable, however, they can be considered to be small. The maximum absolute and percentage difference in the contours compared to the ideal contour for air is depicted in Fig. 47.

Especially for an OFR of 2.0 the differences of the contours are negligible. For other OFRs the deviation is below 0.05%. Hence, the contour for air was chosen for the experiments as the deviations in general are small and an OFR of 2.0 is a realistic value to be achieved in the experiments. Furthermore, this is advantageous, as in the cold gas experiments the same nozzle contour as in hot plume tests can be used.

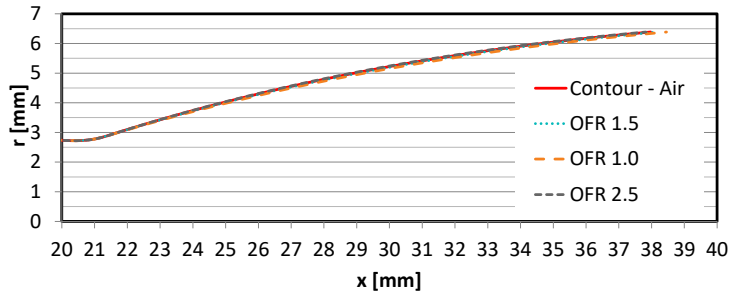

Fig. 46: Ideal Nozzle contours for air and several OFRs of oxygen and hydrogen

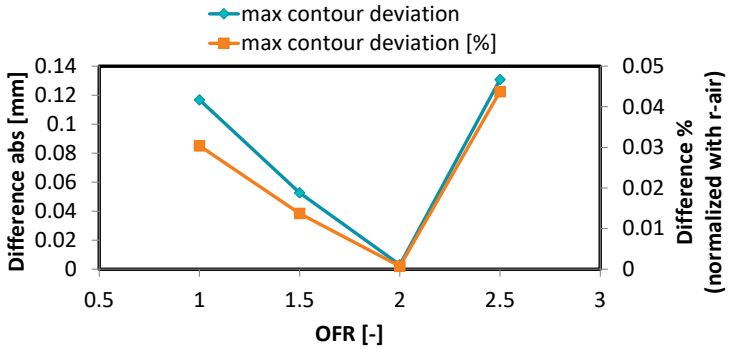

Fig. 47: Maximum deviation of nozzle contours for different OFRs of oxygen and hydrogen from the nozzle contour for air

4.3. Test Conditions

In Fig. 48 the Mach numbers tested in the wind tunnel facilities at DLR in Cologne are mapped on the reference trajectory of RETALT1. One can see that the wind tunnel facilities are well suited to rebuild the descent and landing trajectory of the vehicle as they cover all flight phases, and the retro propulsive landing phases can be simulated with cold gas jets in the H2K, and with cold and hot gas jets in the VMK. The test conditions are described in more detail in the following.

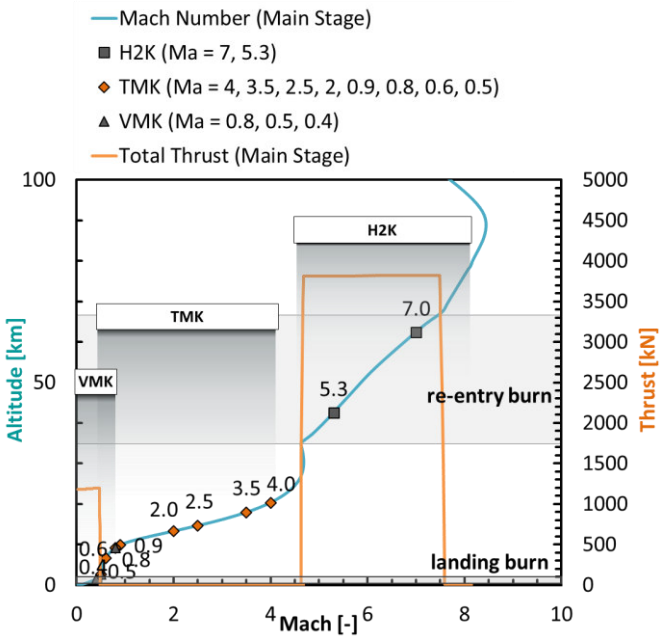

Fig. 48: Mapping of Mach numbers tested in the wind tunnel facilities at DLR in Cologne over the reference trajectory presented in [75]

4.3.1. Aerodynamic Phase in the TMK

The aerodynamic descent phase where the engines are off was rebuilt in the TMK. The tested Mach numbers were 4.0, 3.5, 2.5 and 2.0 in the supersonic regime and 0.9, 0.8, 0.6 and 0.5 in the subsonic regime. However, not all configurations were tested at all Mach numbers. Alpha polars of $\pm 10°$ were tested in all test runs, which was defined according to the mission design needs described in [79]. Fig. 54 shows a comparison of the Reynolds numbers of the flight configuration with the Reynolds numbers tested in TMK. The Reynolds numbers at flight conditions are about one order of magnitude larger than the Reynolds numbers simulated in the wind tunnel. Boundary layer tripping experiments were performed in the CALLISTO project in the TMK for configurations similar to RETALT1 [90, 91]. The results showed that the influence of the tripping on the measured forces and moments is minor, indicating that the Reynolds number has only a minor effect for these configurations. It shall be noted, however, that only planar fins were tested in these experiments.

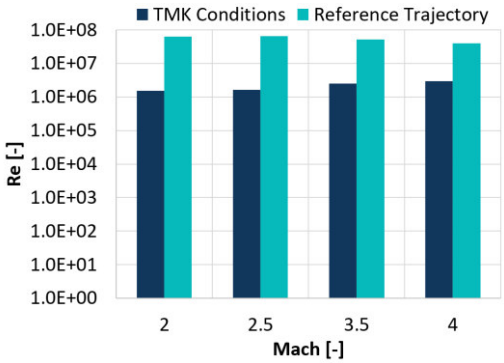

Fig. 49: Comparison of Reynolds numbers of the reference trajectory versus the wind tunnel conditions

4.3.2. Hypersonic Retro Propulsion Reentry Burn in H2K

The tests performed in the H2K simulated the hypersonic part of the retro propulsion maneuver during the re-entry burn. Tab. 7 summarizes the freestream conditions tested in the H2K. For comparison, also the Reynolds numbers of the reference trajectory for the respective Mach numbers are given. The characteristic length for the Reynolds number is the model diameter. The baseline test condition is at Mach 5.3 with a total pressure of 4 bar and a total temperature of 450 K. A Reynolds number variation was performed with the second condition at Mach 5.3 with a total pressure of 12 bar. In addition, tests were performed at Mach 7.0, with the Reynolds number matched to the baseline tests at Mach 5.3. At Mach 7.0 the Reynolds number is in the same order of magnitude as for the flight point in the reference trajectory.

Tab. 7: Freestream conditions tested in H2K

No.	M_∞ [−]	p_0 [bar]	T_0 [K]	Re_∞ [−]	Re_∞ [−] (reference trajectory)
1	5.3	4	450	2.36E+05	1.83E+06
2	5.3	12	450	7.07E+05	1.83E+06
3	7	12.73	610	2.36E+05	1.99E+05

As described in Section 4.2.2, a single-engine configuration and a three-engines configuration were tested. The total thrust for the three-engines case is defined as:

$$C_{T,Total} = 3 \cdot C_T \qquad (26)$$

The total thrust coefficient will be used in the remainder of this thesis.

To generate a better understanding of the three-engines case, it was tested in the two configurations visualized in Fig. 50. One with the engines active in the angle of attack plane (α-plane), and one perpendicular to it. The angle between the α-plane and the engine plane is denoted ϕ. Especially for an angle of attack of 0° the two cases represent the same configuration but it can be inspected via Schlieren imaging in two planes. The Schlieren view path is sketched in Fig. 50.

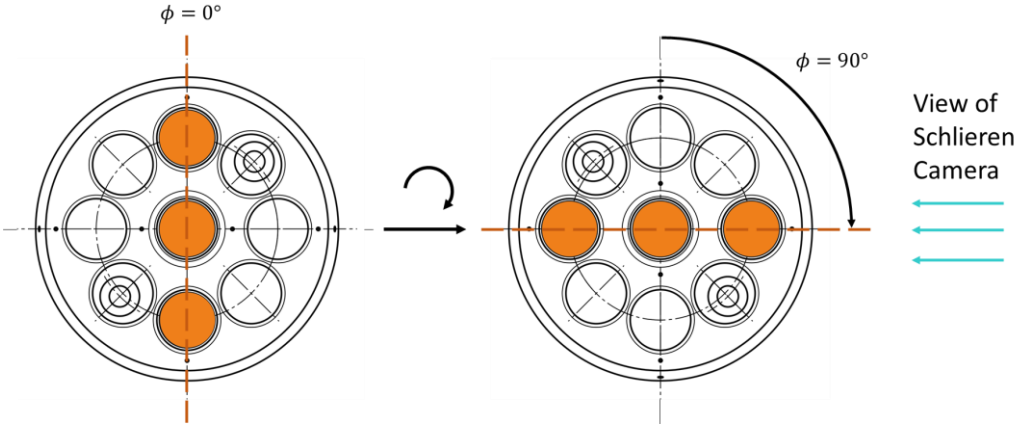

Fig. 50: Three-engine configurations with three active engines in the α-plane (left) and three active engines perpendicular to the α-plane

The thrust coefficients which could be tested were limited by two factors. As presented in [65] for large thrust coefficients, partial blockage of the wind tunnel freestream appears, which is first observed in the rear of the configuration. However, in the experiments presented here, it was observed that even before a noticeable disturbance of the pressures on the wind tunnel model appears, a rise in the wind tunnel nozzle exit pressure can be measured. Hence, the thrust coefficients were limited such that no influence of the retro plume on the wind tunnel nozzle exit pressure is observed. This leads to maximum total thrust coefficients of 3.8 for the single-engine case and 7.2 for the three-engine case. The total thrust coefficients for the flight points at Mach 5.3 and Mach 7.0 are 33.7 and 211.2, respectively. Hence the flight thrust coefficients cannot be matched in the experiments, which is why in this work the general trend of the data in dependence on the thrust coefficient is presented for an extrapolation to the flight configuration via CFD. An effort to assess extrapolation approaches from experiment to flight was published in [49] and [65]. For the baseline experiments, pressurized ambient temperature air ($T_{CC} \approx 300\ K$) was used for the generation of the exhaust jet. However, due to the high Mach numbers and, therefore, low pressures and temperatures, condensation was observed in the highly underexpanded retro plume in the experiments presented in [65]. To study the influence of the condensation on the flow field, the air was heated to a temperature of $T_{CC} \approx 600\ K$ in some tests. As the pressure sensors could not withstand these high temperatures, they were not installed in these tests. Tables with the detailed test conditions, and summaries of pressure measurements and normalized root mean square pressure fluctuations in the dynamic tests are given in the appendix A.1.

4.3.3. Subsonic Retro Propulsion Landing Burn in VMK

The free stream and jet conditions discussed in section 5.3 on the landing burn tested in the VMK are summarized in more detail in Tab. 8. In these tests, the free stream Mach number and the APR was varied. Tables that summarize the pressure measurements and the normalized root mean square pressure fluctuations are given in appendix A.2.

Tab. 8: Test conditions of subsonic retro propulsion tests in VMK

Run	M_∞ [-]	C_T [-]	$\frac{p_e}{p_\infty}$ (APR) [-]	MFR [-]	Re [-]	q_∞ [bar]	p_∞ [bar]	u_∞ [m/s]	ρ_∞ [kg/m³]	p_e [bar]	u_e [m/s]	ρ_e [kg/m³]	$p_{T,\infty}$ [bar]
4_4	0.6	0.0	0.000	0.00	1.17E+06	0.256	1.0065	191.43	1.399	0.000	0.00	-	1.287
4_5	0.7	0.0	0.000	0.00	1.40E+06	0.347	1.0098	220.14	1.432	0.000	0.00	-	1.402
4_6	0.8	0.0	0.000	0.00	1.68E+06	0.455	1.0124	247.35	1.487	0.000	0.00	-	1.545
5_1	0.9	0.0	0.000	0.00	1.94E+06	0.571	1.0157	273.85	1.523	0.000	0.00	-	1.71
10_3	0.6	0.52	0.307	9.12	1.18E+06	0.256	1.0108	189.89	1.417	0.310	617.91	1.221	1.290
10_4	0.7	0.38	0.307	6.68	1.43E+06	0.348	1.0114	218.80	1.456	0.310	617.45	1.221	1.405
10_5	0.8	0.29	0.306	5.14	1.69E+06	0.452	1.0110	246.15	1.493	0.309	616.84	1.221	1.540
10_6	0.9	0.23	0.305	4.07	1.97E+06	0.570	1.0115	272.34	1.537	0.309	616.33	1.221	1.706
28_4	0.7	0.51	0.390	8.50	1.42E+06	0.350	1.0155	219.89	1.449	0.397	614.96	1.574	1.411
28_5	0.8	0.39	0.389	6.52	1.68E+06	0.456	1.0165	247.31	1.491	0.396	613.96	1.577	1.550
28_6	0.9	0.31	0.389	5.17	1.96E+06	0.573	1.0164	273.29	1.535	0.395	612.78	1.579	1.715
8_5	0.8	0.50	0.486	8.15	1.68E+06	0.452	1.0110	246.31	1.491	0.491	622.02	1.906	1.540
8_6	0.9	0.40	0.485	6.44	1.98E+06	0.572	1.0115	272.45	1.540	0.491	621.16	1.909	1.708

4.4. Uncertainties

The uncertainties in the tests discussed in this work were determined with Gaussian error propagation of the measured quantities as defined in the norm DIN 1319-4 [92], assuming that the measurement quantities are not correlated. Let G be a model function that describes how a value y results from the measured quantities m_k. The uncertainty Δy of the value y is then expressed in terms of the partial derivatives of the model function G regarding the n measurement quantitates m_k, and the uncertainties in the measurement quantities themselves Δm_k [92]:

$$\Delta y(m) = \sqrt{\sum_{k=1}^{n} \left(\frac{\partial G}{\partial m_k}\right)^2 \Delta m_k^2} \tag{27}$$

This procedure is common for force, moment and pressure measurements performed in the TMK, H2K and VMK and was for example presented in [93, 94].

4.4.1. Uncertainty Estimation in Subsonic Tests

In the subsonic tests the Mach number is set by the ratio of the static to the total pressure in the free stream. Hence, the coefficients are expressed in terms of p_∞ and p_0.
The force coefficient can be expressed as:

$$C_F = \frac{4}{\pi} \cdot \frac{F}{\gamma_\infty \cdot p_\infty \cdot D_{ref}^2} \cdot \frac{\gamma_\infty - 1}{\left(\left(\frac{p_0}{p_\infty}\right)^{\frac{\gamma_\infty - 1}{\gamma_\infty}} - 1\right)} \tag{28}$$

with the force F, the heat capacity ratio γ_∞, the free stream Mach number M_∞, the total pressure in the free stream p_0 and the reference length D_{ref}. With C_F being the model function G, and with F, D_{ref}, p_0, p_∞ and γ_∞ being the measured quantities m_k, equation (27) then evaluates to:

$$\Delta C_F = \sqrt{\left(\frac{\partial C_F}{\partial D_{ref}}\Delta D_{ref}\right)^2 + \left(\frac{\partial C_F}{\partial p_0}\Delta p_0\right)^2 + \left(\frac{\partial C_F}{\partial p_\infty}\Delta p_\infty\right)^2 + \left(\frac{\partial C_F}{\partial \gamma_\infty}\Delta \gamma_\infty\right)^2 + \left(\frac{\partial C_F}{\partial F}\Delta F\right)^2} \tag{29}$$

In the same manner all uncertainties were evaluated.
The moment coefficient is written as:

$$C_M = \frac{\pi}{4} \cdot \frac{\mathcal{M} + F \cdot X_{SE} + F \cdot X_{ref-CoG}}{\gamma_\infty \cdot p_\infty \cdot {D_{ref}}^3} \cdot \frac{\gamma_\infty - 1}{\left(\left(\frac{p_0}{p_\infty}\right)^{\frac{\gamma_\infty - 1}{\gamma_\infty}} - 1\right)} \tag{30}$$

with the moment $\mathcal{M}$, the distance of the reference point of the balance to the reference point of the wind tunnel model X_{SE}, and the distance of the reference point to the center of gravity $X_{ref-CoG}$. Hence, ΔC_M is evaluated in dependence of $\mathcal{M}$,D_{ref}, p_0, p_∞, γ_∞, F, X_{SE} and $X_{ref-CoG}$.
The pressure coefficient is:

$$C_p = \frac{\gamma_\infty - 1}{\gamma_\infty \cdot p_\infty} \cdot \frac{p - p_\infty}{\left(\left(\frac{p_0}{p_\infty}\right)^{\frac{\gamma_\infty - 1}{\gamma_\infty}} - 1\right)} \tag{31}$$

Where ΔC_p is described in terms of p, p_0, p_∞ and γ_∞.

4.4.2. Uncertainty Estimation in Supersonic and Hypersonic Tests

In the supersonic and hypersonic tests, the Mach number is determined by the expansion ratio of the wind tunnel nozzle. Hence the coefficients are expressed in dependence of M_∞ and p_0. The force coefficient can be expressed as:

$$C_F = \frac{8}{\pi} \cdot \frac{F}{\gamma_\infty \cdot M_\infty^2 \cdot p_0 \cdot D_{ref}^2} \left(1 + \frac{\gamma_\infty - 1}{2} \cdot M_\infty^2\right)^{\frac{\gamma_\infty}{\gamma_\infty - 1}} \quad (32)$$

and its uncertainty ΔC_F is evaluated regarding F, D_{ref}, p_0, M_∞ and γ_∞.
The moment coefficient is written in terms of M_∞ and p_0:

$$C_M = \frac{8}{\pi} \cdot \frac{\mathcal{M} + F \cdot X_{SE} + F \cdot X_{ref-CoG}}{\gamma_\infty \cdot M_\infty^2 \cdot p_0 \cdot D_{ref}^3} \cdot \left(1 + \frac{\gamma_\infty - 1}{2} \cdot M_\infty^2\right)^{\frac{\gamma_\infty}{\gamma_\infty - 1}} \quad (33)$$

where its uncertainty ΔC_M is evaluated with respect to $\mathcal{M}$, D_{ref}, p_0, M_∞, γ_∞, F, X_{SE} and $X_{ref-CoG}$.
The pressure coefficient is:

$$C_p = \frac{p \cdot \left(1 + \frac{\gamma_\infty - 1}{2} \cdot M_\infty^2\right)^{\frac{\gamma_\infty}{\gamma_\infty - 1}} - p_0}{\frac{\gamma_\infty}{2} \cdot M_\infty^2 \cdot p_0} \quad (34)$$

where its uncertainty ΔC_p is expressed in dependence of p, p_0, M_∞ and γ_∞.
The thrust coefficient can be computed with [95]:

$$C_T = \frac{2 p_{CC} D_e^2 (\gamma_e M_e^2 + 1) \left(\frac{(\gamma_\infty - 1) M_\infty^2}{2} + 1\right)^{\frac{\gamma_\infty}{\gamma_\infty - 1}}}{p_0 \gamma_\infty M_\infty^2 D_{ref}^2 \left(\frac{(\gamma_e - 1) M_e^2}{2} + 1\right)^{\frac{\gamma_e}{\gamma_e - 1}}} \quad (35)$$

and its uncertainty ΔC_T, hence, depends on p_0, M_∞, γ_∞, D_{ref}, p_{CC}, M_e, γ_e and D_e.

4.4.3. Uncertainties in the Measurement Quantities

The uncertainties in the TMK test are given in Tab. 9. The uncertainties in the forces and moments were obtained from the calibration of the balance. As they are depending on the load condition, in Tab. 9, the range of lowest to highest uncertainty is given. The uncertainty in the distance X_{SE} is given by the measurement equipment with which the distance is measured. The error in $X_{ref-CoG}$ is a systematic error that arrises from modeling uncertainties in the mass distributions in the launcher. As it is not a measurement uncertainty it is neglected here and set to 0 mm. The total pressure in the free stream is measured with three different sensors depending on its magnitude (up to 3 bar, up to 10 bar or up to 30 bar). The uncertainties in the total pressure, in the static pressure and in the Mach number in the free stream are obtained from calibrations. Also the uncertainties in the pressure measurements on the model outer surface were obtained from the sensor calibrations. For D_{ref} the manufacturing tolerance was assumed, and the uncertainty in the heat capacity ratio is derived from data in [96].

Tab. 9: Uncertainties in measurement values in TMK tests

Sensor	Uncertainty	Source
Fx	[0.662, 2.138] N	Calibration
Fy	[0.032, 0.066] N	Calibration
Fz	[0.122, 2.274] N	Calibration
Mx	[1.224, 3.869] Ncm	Calibration
My	[2.616, 3.869] Ncm	Calibration
Mz	[6.925, 6.925] Ncm	Calibration
X_{SE}	0.1 mm	Specified by measurement equipment
$X_{ref-CoG}$	0 mm	Systematic value set to 0 mm
p_0 (3 bar)	0.0012 bar	Calibration
p_0 (10 bar)	0.004 bar	Calibration
p_0 (30 bar)	0.012 bar	Calibration
p_∞	0.001 bar	Calibration
High frequency pressure sensors (Kulites)	[0.0001, 0.0012] bar	Calibration for each sensor: p11: 0.00030 bar, p12: 0.00013 bar, p13: 0.0012 bar, p14: 0.00010 bar, p21: 0.00082 bar, p22: 0.00034 bar, p23: 0.00059 bar, p24: 0.00032 bar, p312: 0.00037 bar, p341: 0.00039 bar, p332: 0.00036 bar
Thermocouples	1.5 K	Common value
D_{ref}	0.05 mm	Manufacturing tolerance
M_∞	0.75	Calibration
γ_∞	0.005	Derived from data in [96]

The uncertainties in the measurement values for the H2K tests are shown in Tab. 10. The uncertainties for the wind tunnel specific values p_0 and M_∞ and the pressure in the model p_{CC} were derived from calibration data. For geometric values of the wind tunnel model, the manufacturing tolerance was used, except for the nozzle exit diameter, from which several measurements were taken and the maximum deviation was assumed for the uncertainty. This represents an upper value for the uncertainty as the measurement of the nozzle exit diameter proved to be challenging and the measured deviation includes uncertainties of those measurements themselves. The uncertainties in the model nozzle exit Mach number, M_e, was approximated from several CFD solutions of exit profiles. The temperature dependent error of the heat capacity ratios were approximated with data from [96] for the base line tests case of $p_0 = 4\ bar$ and $T_0 = 450\ K$ and for $p_e = 10\ bar$ and $T_e = 100\ K$. These are also approximations to the safe side as the pressure p_e was generally much lower, which would result in smaller errors.

Tab. 10: Uncertainties in measurement values in H2K tests

Sensor	Uncertainty	Source
p_0	0.0091 bar	Calibration
High frequency pressure sensors (Kulites)	0.0035 bar	Specification by manufacturer
Thermocouples	1.5 K	Common value
D_{ref}	0.05 mm	Manufacturing tolerance
M_∞	0.7	Calibration
γ_∞	0.005	Derived from [96] for the test conditions for $p_0 = 4\ bar$ and $T_0 = 450\ K$
M_e	0.01	Derived from Mach number exit profiles from CFD simulations
γ_e	0.03	Derived from [96] for $p_e = 10\ bar$ and $T_e = 100\ K$
D_e	0.1 mm	Derived from measured values. Represents an upper worst-case scenario.
p_{CC}	0.0083 bar	Calibration

Tab. 11 summarizes the uncertainties in the VMK tests. As the pressures in the VMK are higher, also their uncertainties are higher. The uncertainties were again extracted from calibrations. The uncertainty in the heat capacity ratio γ_∞ was again derived from data in [96].

Tab. 11: Uncertainties in measurement values in VMK tests

Sensor	Uncertainty	Source
p_0	0.01 bar	Calibration
p_∞	0.01 bar	Calibration
High frequency pressure sensors (Kulites)	0.0003 bar	Calibration
p_{CC}	0.236 bar	Calibration
γ_∞	0.003	Derived from data in [96]

4.5. Averaged Modal Solution

It was found that in subsonic retro propulsion flow fields, the average image over time does not reveal the relevant flow features (see for example Fig. 116 in section 5.3.1). Due to their strongly unsteady behavior they are averaged out. As a solution to this problem, it is proposed here to perform a Proper Orthogonal Decomposition (POD), then to exclude the zeroth mode, which corresponds mainly to the steady flow field, and just average over the remaining modes. This approach reveals the flow features of the flow field better without the need to plot all of the first modes. This averaged solution will be called the "averaged modal solution". The time history of this reconstructed mode can even capture the most important frequency information as shown in this section. The procedure is described in the following.

First a Proper Orthogonal Decomposition (POD) is performed as follows (similar to the description in [97]). The images of the Schlieren video are reshaped to one dimensional column vectors $\boldsymbol{x_0}, \boldsymbol{x_1}, \dots, \boldsymbol{x_{n-1}}$ with a length m, where n is the number of images and m is the number of pixels in the image. The image vectors are then stacked together to build a two-dimensional matrix $\boldsymbol{X} \in \mathbb{R}^{m \times n}$:

$$\boldsymbol{X} = \begin{bmatrix} | & | & & | \\ \boldsymbol{x_0} & \boldsymbol{x_1} & \dots & \boldsymbol{x_{n-1}} \\ | & | & & | \end{bmatrix} \tag{36}$$

A Singular Value Decomposition (SVD) of the matrix $\boldsymbol{X}$ is then performed:

$$\boldsymbol{X} = \boldsymbol{U}\boldsymbol{\Sigma}\boldsymbol{V}^T \tag{37}$$

To save storage, the economy SVD is performed. Therefore, $\boldsymbol{U} \in \mathbb{R}^{m \times n}$ are the left singular vectors $\boldsymbol{u_0}, \boldsymbol{u_1}, \dots, \boldsymbol{u_{n-1}}$, which correspond to the spatial modes, $\boldsymbol{\Sigma} \in \mathbb{R}^{n \times n}$ is the diagonal matrix with the singular values, $\sigma_0, \sigma_1, \dots, \sigma_{n-1}$, and $\boldsymbol{V} \in \mathbb{R}^{n \times n}$ are the right singular vectors representing the time history of the modes, $\boldsymbol{v_0}, \boldsymbol{v_1}, \dots, \boldsymbol{v_{n-1}}$:

$$\boldsymbol{U} = \begin{bmatrix} | & | & & | \\ \boldsymbol{u_0} & \boldsymbol{u_1} & \dots & \boldsymbol{u_{n-1}} \\ | & | & & | \end{bmatrix}, \ \boldsymbol{\Sigma} = \begin{bmatrix} \sigma_0 & 0 & 0 & \\ 0 & \sigma_1 & 0 & \\ 0 & 0 & \ddots & \\ & & & \sigma_{n-1} \end{bmatrix}, \boldsymbol{V}^T = \begin{bmatrix} - & \boldsymbol{v_0} & - \\ & \boldsymbol{v_1} & \\ - & \vdots & - \\ - & \boldsymbol{v_{n-1}} & - \end{bmatrix} \tag{38}$$

The idea in this section is to select a certain number of modes, starting with mode s and ending with r, and merge them in one quasi steady state mode. The matrices of the selected modes are $\widetilde{\boldsymbol{U}}$, $\widetilde{\boldsymbol{\Sigma}}$ and $\widetilde{\boldsymbol{V}}$:

$$\widetilde{\boldsymbol{U}} = \begin{bmatrix} | & | & & | \\ \boldsymbol{u_s} & \boldsymbol{u_{s+1}} & \dots & \boldsymbol{u_r} \\ | & | & & | \end{bmatrix}, \ \widetilde{\boldsymbol{\Sigma}} = \begin{bmatrix} \sigma_s & 0 & 0 & \\ 0 & \sigma_{s+1} & 0 & \\ 0 & 0 & \ddots & \\ & & & \sigma_r \end{bmatrix}, \widetilde{\boldsymbol{V}}^T = \begin{bmatrix} - & \boldsymbol{v_s} & - \\ - & \boldsymbol{v_{s+1}} & - \\ & \vdots & \\ - & \boldsymbol{v_r} & - \end{bmatrix} \tag{39}$$

To obtain the quasi-steady state solution the time histories of the POD modes are averaged over the time steps:

$$\widetilde{\boldsymbol{V}}^T = \begin{bmatrix} - & \boldsymbol{v_s} & - \\ - & \boldsymbol{v_{s+1}} & - \\ & \vdots & \\ - & \boldsymbol{v_r} & - \end{bmatrix} \xrightarrow{averaging} \bar{\widetilde{\boldsymbol{v}}}^T = \begin{bmatrix} \bar{v}_s \\ \bar{v}_{s+1} \\ \vdots \\ \bar{v}_r \end{bmatrix} \tag{40}$$

Then the averaged mode $\boldsymbol{u_{st}}$ is constructed by:

$$\boldsymbol{u}_{st} = \frac{\widetilde{\boldsymbol{U}}\widetilde{\boldsymbol{\Sigma}}\widetilde{\boldsymbol{v}}^{T}}{\left|\widetilde{\boldsymbol{U}}\widetilde{\boldsymbol{\Sigma}}\widetilde{\boldsymbol{v}}^{T}\right|} \quad (41)$$

The term $\widetilde{\boldsymbol{U}}\widetilde{\boldsymbol{\Sigma}}\widetilde{\boldsymbol{v}}^{T}$ is divided by its length such that $\boldsymbol{u}_{st}$ is a unitary vector. The time series $\boldsymbol{v}_{st}$ and the singular value σ_{st} of this new POD mode can be reconstructed as follows. The averaged modal solution shall reconstruct the original image snapshots $\boldsymbol{X}$:

$$\boldsymbol{X} = \boldsymbol{u}_{st}\sigma_{st}\boldsymbol{v}_{st}^{T} \quad (42)$$

Bringing $\boldsymbol{u}_{st}$ on the left side of the equation follows in:

$$\boldsymbol{u}_{st}^{+}\boldsymbol{X} = \sigma_{st}\boldsymbol{v}_{st}^{T} \quad (43)$$

where $\boldsymbol{u}_{st}^{+}$ is the pseudoinverse of $\boldsymbol{u}_{st}$. As $\boldsymbol{v}_{st}$ needs to be unitary it follows:

$$\boldsymbol{v}_{st} = \frac{\boldsymbol{u}_{st}^{+}\boldsymbol{X}}{|\boldsymbol{u}_{st}^{+}\boldsymbol{X}|} \quad (44)$$

and hence:

$$\sigma_{st} = |\boldsymbol{u}_{st}^{+}\boldsymbol{X}| \quad (45)$$

Side note: It should be mentioned that averaging the time series and constructing a spatial mode $\boldsymbol{u}_{st}$ from that is equivalent to averaging the reconstructed spatial flow field snapshots reconstructed from the selected modes. In other words, averaging the time series and then solving the matrix equation is equivalent to first solving the matrix equation and averaging afterwards:

$$\frac{\widetilde{\boldsymbol{U}}\widetilde{\boldsymbol{\Sigma}}\widetilde{\boldsymbol{v}}^{T}}{\left|\widetilde{\boldsymbol{U}}\widetilde{\boldsymbol{\Sigma}}\widetilde{\boldsymbol{v}}^{T}\right|} = \boldsymbol{u}_{st} = \frac{\overline{\widetilde{\boldsymbol{U}}\widetilde{\boldsymbol{\Sigma}}\widetilde{\boldsymbol{V}}^{T}}}{\left|\overline{\widetilde{\boldsymbol{U}}\widetilde{\boldsymbol{\Sigma}}\widetilde{\boldsymbol{V}}^{T}}\right|} \quad (46)$$

The averaged modal solution flow field for a subsonic retro propulsion flow field, resulting from the procedure described above is shown in Fig. 51 starting with mode 1 (s = 1).

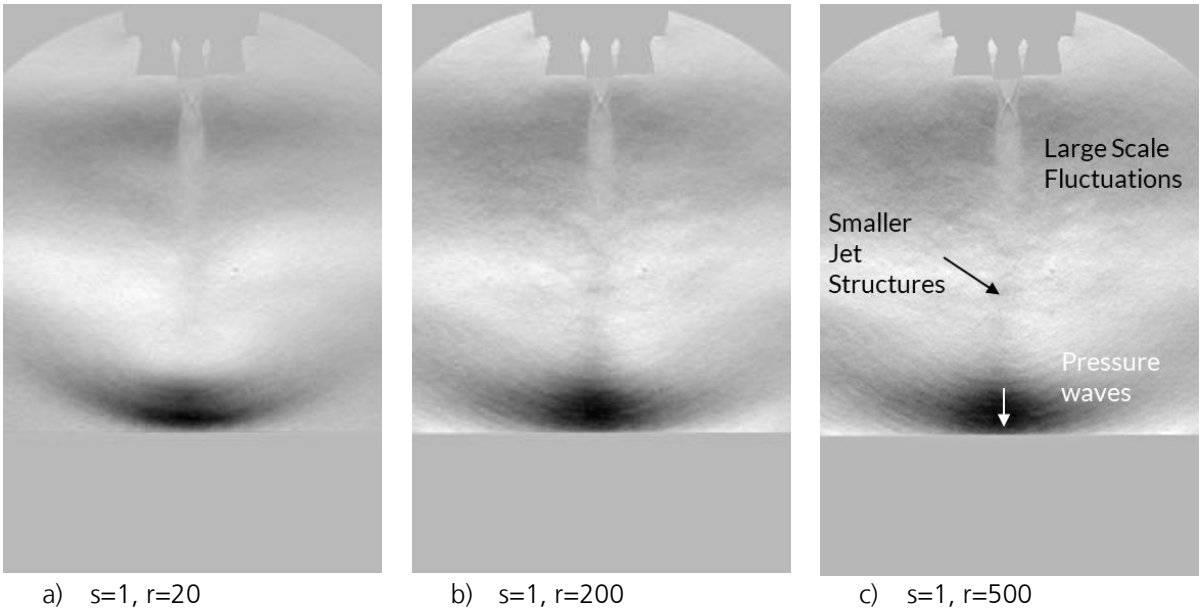

a) s=1, r=20 b) s=1, r=200 c) s=1, r=500

Fig. 51: Averaged modal solution of subsonic retro propulsion flow field for increasing number of modes $M_\infty = 0.8$, $APR = 0.389$, $MFR = 6.52$

One can see that, due to the exclusion of the zeroth mode, the structures of the unsteady flow features become visible (see Fig. 51c). The higher the number of included modes (larger r), the clearer the smaller structures are visible. Also the pressure waves in the flow field can be observed. As the antisymmetric modes cancel out, the flow field appears symmetric. The subsonic retro propulsion flow field will be discussed in more detail in section 5.3.

In Fig. 52 the average values of the time series of the original modes, $\bar{v}$, are depicted. For larger modes their values decay, which indicates that the smaller modes contribute more to the overall averaged modal solution, as also the singular values decay for larger modes. Fig. 53 shows the Power Spectral Density (PSD) of the time series of the averaged modal solution. For the computation of the PSD a short time Fourier transform was computed over 8000 time steps. It was performed with a Hann window with a length of 500, shifting the window by 16 time steps between single spectra. The spectra were then averaged over the time steps. The frequency was resolved with 2048 bins. The PSD is plotted for various included numbers of modes. Apparently, the PSD is quite independent of the number of included modes. It is compared here to the average of the PSDs of the first 12 original modes. The PSD of the averaged modal solution captures the low frequency peaks well, while the peaks of the higher frequencies are not resolved. The lower frequency peaks are slightly shifted to lower values.

This analysis shows that it is possible to reconstruct an averaged modal solution from the POD modes that can even capture the low frequency content in the flow field.

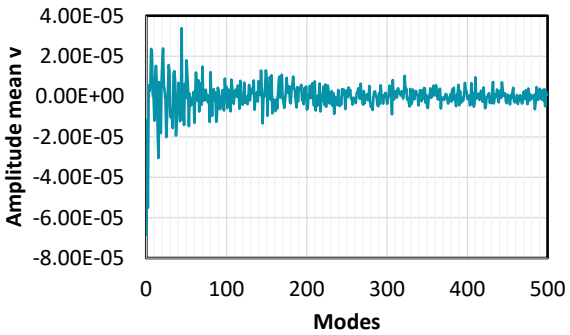

Fig. 52: Mean of time series of the modes for $M_\infty = 0.8$, $APR = 0.389$, $MFR = 6.52$

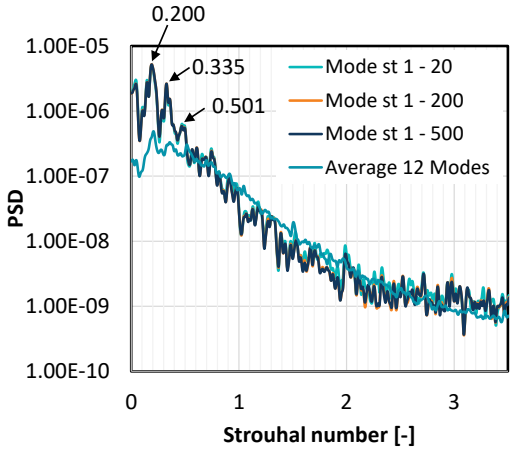

Fig. 53: PSD of the time series of the averaged modal solution for several numbers of included modes

5. Results

As described in the introduction, the results presented here are structured by the three flight phases during descent and landing, which are the reentry burn, the aerodynamic phase and the landing burn (see section 3). Firstly, the aerodynamic phase without an active engine is discussed. This is followed by the propelled flight phases, which are the reentry burn and the landing burn.

5.1. Aerodynamic Phase of the Descent Trajectory

In the aerodynamic phase the engines are not active. Here the vehicle decelerates purely aerodynamically. In this phase, the vehicle attitude and the trajectory are controlled with the aid of the Aerodynamic Control Surfaces (ACS). This is why the main focus in this phase was laid on the trimmability of the descending first stage with the ACS. For this goal, the free stream conditions at the ACS and the surface pressures on the configuration during this phase were assessed analytically and with the aid of experimental data.

5.1.1. Analytical Description of the Descending First Stage in Supersonic Flow

In the design phase of the aerodynamic control surfaces for the RETALT1 configuration an analytical approach was used for the estimation of the free stream conditions at the location of the fins in the supersonic regime, as this enabled a preliminary sizing of the ACS for the RETALT1 configuration without the use of CFD. Furthermore, the comparison with the theoretical results adds value to the interpretation of the measured data, and vice versa the analytical approach can be verified with the measured data. The analytical approach will be laid out in the following. It builds on classic methodologies for the modelling of hypersonic flows (see section 2.3) namely: the blast wave analogy, the modified Newtonian law, shock relations and isentropic relations.
Fig. 54 shows the RETALT1 first stage with petals as ACS, deflected by $\delta = 20°$, at a Mach number of 3.5. The free stream is coming from the left. A bow shock is forming in front of the engines i.e., the expansion nozzles without a plume. Downstream of the engines the flow is expanded around the base area. A shock system emerges from the folded landing legs and oblique shocks from the petals, which bend with further distance from the axis.

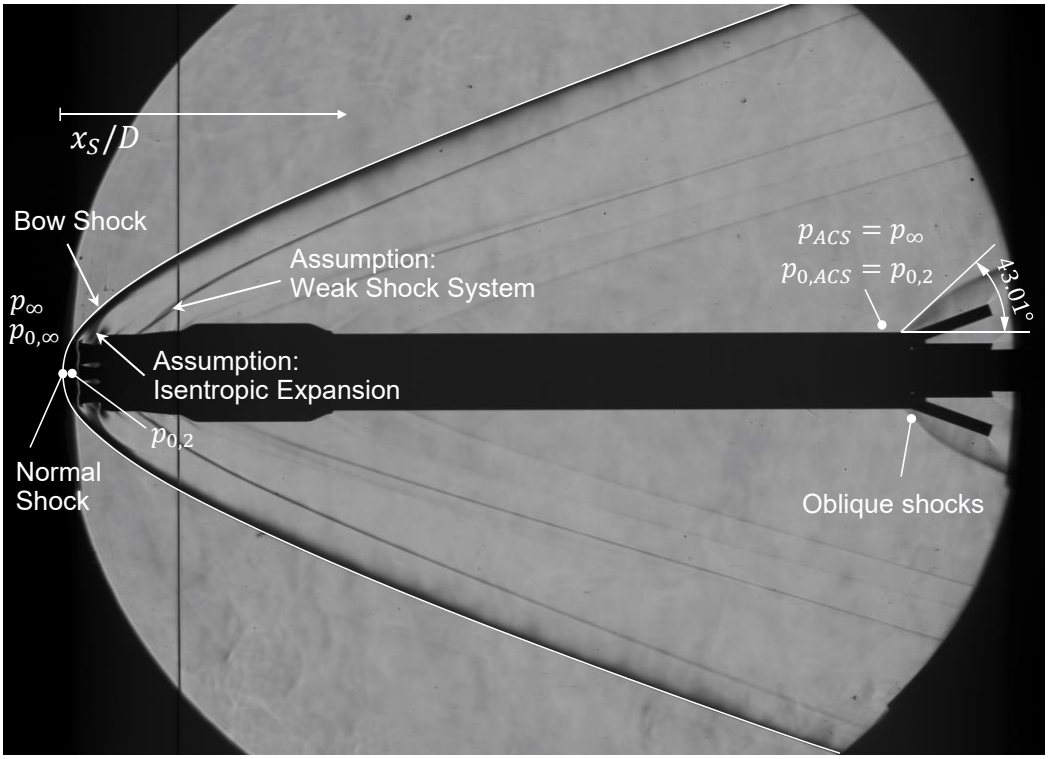

Fig. 54: Flow phenomena and assumptions for the analytical description.

The static pressure at the ACS location can be derived indirectly by the application of the blast wave analogy (see section 2.3.1). Referring to Fig. 54 it seems reasonable as a first approach to assume that the backwards oriented first stage of RETATL1 is similar to a blunt-nosed cylinder. As stated in section 2.3.1, for a blunt-nosed cylinder Sakuri [17] obtained with the blast wave analogy, the second approximation of the pressure distribution along the cylinder surface as follows:

$$\frac{p}{p_\infty} = 0.067 M_\infty^2 \frac{\sqrt{C_D}}{\frac{x_S}{D}} + 0.44 \qquad (47)$$

Where $\frac{x_S}{D}$ is the distance downstream of the bow shock normalized with the diameter of the cylindrical body D, C_D is the drag coefficient, M_∞ the free stream Mach number, p the static pressure at the surface of the cylinder at the distance $\frac{x_S}{D}$ from the bow shock and p_∞ the free stream pressure. Note that x_S defines the distance downstream of the bow shock (see Fig. 54) which is different from the overall x coordinate of the body fixed reference frame with its origin at the interstage as defined in Fig. 31. Lukasiewicz [19] suggests that p shall be set equal to p_∞ if the blast wave solution results in pressure values lower than $\frac{p}{p_\infty} = 1$ (see section 2.3.1).

Rearranging eq. (47) and isolating $\frac{x_S}{D}$ on the left-hand side of the equation yields:

$$\frac{x_S}{D} = \frac{0.067 M_\infty^2 \sqrt{C_D}}{\frac{p}{p_\infty} - 0.44} \qquad (48)$$

Setting $\frac{p}{p_\infty} = 1$ in eq. (48) results in the simple relation:

$$\frac{x_S}{D} > \frac{0.067 M_\infty^2 \sqrt{C_D}}{0.56} \rightarrow \frac{p}{p_\infty} \approx 1 \qquad (49)$$

Hence if x_S/D exceeds a certain value depending on the free stream Mach number M_∞ and the drag coefficient C_D, then p can be set equal to p_∞. In Fig. 55, eq. (49) is evaluated for several Mach numbers and drag coefficients. Referring back to Fig. 31 one can see that the pressure measurements close to the ACS are more than $x_S/\mathrm{D} = 11$ downstream of the base plane of the configuration. The pressure measurements in the plane 2 are roughly at $x_S/\mathrm{D} = 7$. Fig. 55 shows that for both sensor positions the value of $x_S/D(p/p_\infty = 1)$ lies below 4 for Mach numbers smaller than 4. Only for values of $C_D > 4$ it can get higher. However, as can be seen in the results discussed in [53], the drag coefficient of the cylindrical body lies in the range of 1.2 (in the concept phase this was known from preliminary computations). Hence, the pressure at the location of the ACS can be assumed to be equal to the static free stream pressure.

Further assumptions made are that the shock system coming from the folded landing legs is weak (see Fig. 54), and that the flow expansion downstream of the stagnation point behind the bow shock is isentropic. With these assumptions, it can be assumed that the total pressure downstream of the bow shock is conserved along the cylindrical body of the RETALT1 configuration.

With the normal shock relations, the total pressure behind the normal shock portion of the bow shock can be calculated. With the assumption that the static pressure at the ACS location equals the static free stream pressure upstream of the bow shock, and that the total pressure equals the total pressure downstream of a normal shock, the Mach number at the ACS location can be calculated directly with the isentropic relations. The Mach number at the location of the Aerodynamic Control Surfaces M_{ACS} can be expressed depending solely on the free stream Mach number M_∞ and the heat capacity ratio γ.

$$M_{ACS} = \sqrt{\left(\frac{\left(1 + \frac{\gamma - 1}{2} M_\infty^2\right)(\gamma + 1) M_\infty^2}{\left(1 + \frac{2\gamma}{\gamma + 1}(M_\infty^2 - 1)\right)^{\frac{1}{\gamma}} (2 + (\gamma - 1) M_\infty^2)} - 1 \right) \frac{2}{\gamma - 1}} \qquad (50)$$

Eq. (50) is plotted in Fig. 56. As visualized in Fig. 54, the shock angle at the petal was measured and the corresponding Mach number was computed from the 20° deflection of the petal for the free stream Mach numbers of 4.0, 3.5, 2.5 and 2.0. The experimental points fit the analytical model well and show that it is valid, as a first approach, to estimate the free stream conditions at the location of the ACS.

To estimate the static pressure on the windward side at the location of the ACS for $\alpha \neq 0°$, the angle of attack can be taken into account by adding the pressure coefficient resulting from the modified Newtonian law to the pressure coefficient resulting from the blast wave analogy. This approach was applied by Anderson [98] to describe the pressure distribution on the windward side of the Space Shuttle and shows a good fit with flight data.

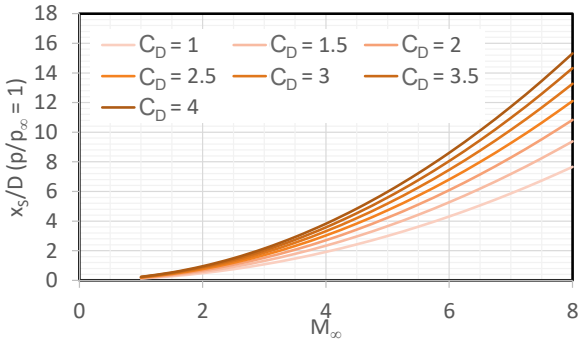

Fig. 55: Eq. (49) for several Mach numbers and drag coefficients

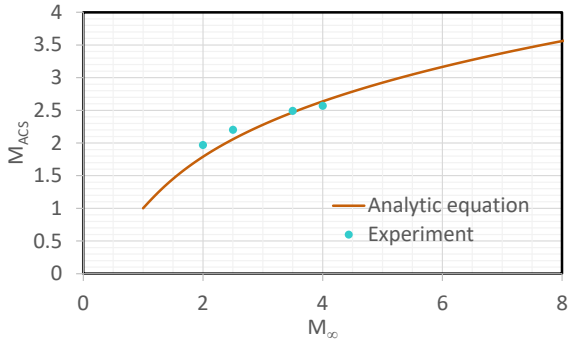

Fig. 56: Free Stream Mach number at the location of the aerodynamic control surfaces versus the free stream Mach number, eq. (50)

As discussed above, the pressure at the ACS location resulting from the blast wave analogy can be assumed to be equal to the free stream pressure. Hence, the C_p value following from the blast wave solution equals approximately zero. Therefore, the pressure on the windward side of RETALT1 at the ACS location is just defined by the C_p of the modified Newtonian law (see section 0), where the surface deflection angle θ is equal to the angle of attack α:

$$C_{p_{Newton}} = C_{p_{max}} \sin^2 \alpha \qquad (51)$$

$C_{p_{max}}$ is the pressure coefficient of the stagnation pressure downstream of the normal shock $p_{0,2}$ (see section 0):

$$C_{p_{max}} = \frac{p_{0,2} - p_\infty}{q_\infty} \qquad (52)$$

With the estimation of the varying pressure as function of the angle of attack, the variation of the Mach number at the ACS can be estimated with the same methodology as described above.

5.1.2. Discussion of Pressure Measurements

The measured pressures were translated into pressure coefficients, and Fig. 57 shows the results in plane 1, which is the plane with the pressure sensors close to the interstage of RETALT1 (see Fig. 31), for the configuration with all petals fully folded (B0,0,0,0). The data resampled to 500 Hz is shown by the brighter solid lines. It was filtered with 3 Hz with a low pass filter (darker solid lines). Due to low fluctuations of the pressures, the data resampled at 500 Hz and the filtered data only differ slightly. The uncertainties for the filtered data are shown by the dashed lines. The uncertainties in the angle of attack (which are ±0.25° [86]) are not shown. Additionally, the pressure coefficients of the sensor below the interstage (pSTAGE) and the sensor in the balance (pBALANCE) are plotted.

For an angle of attack of 0°, the pressure coefficients in plane 1 are very close to zero. This confirms the assumptions drawn from the blast wave analogy in section 5.1.1, that the pressures at the ACS locations are close to the free stream pressures.

The pressure coefficients are furthermore compared to the pressure coefficient obtained using the modified Newtonian law. It can be observed that the trend of the pressure coefficients is reflected well by the modified Newtonian law. The sensor 14 at the bottom side (windward side at positive

angles of attack) follows the modified Newtonian law for positive angles of attack. For Mach 2.5 (Fig. 57c) also the upper side pressure was measured with sensor 12. As expected, it follows the modified Newtonian law for negative angles of attack.
The shape of the pressure polars suggests plotting the modified Newtonian law with a negative sign:

$$C_{p_{Newton\,min}} = -C_{p_{max}} \sin^2 \alpha \qquad (53)$$

This line is denoted by "Cp Newton min" in the plots. It can be observed, that the pressure at the bottom of the model (sensor 14) follows the general trend of the negative modified Newtonian law down to angles of attack of $-7°$. For larger negative angles of attack, it tends to deviate.
The pressure coefficients at the sides of the model, sensors 11 and 13, are important when using planar fins or grid fins as ACS, as these define the local free stream condition experienced by the fins providing the pitch moment. If petals are applied, these sensors provide information on the flow conditions for the petals providing the yaw moment. It can be observed that these pressure coefficients closely follow the pressure coefficient at the leeward side of the model. They follow the trend of the negative modified Newtonian law up to an angle of attack of $\pm 7°$. At $\pm 8°$ a pressure plateau can be observed at Mach 4.0 and 3.5. Schlieren images of this configuration are shown in Fig. 58. The reason for the plateau is probably the stronger shock system at the landing legs at higher angles of attack. Hence, the assumption of a weak shock system and no loss of total pressure does not hold anymore. A flow separation at the leeward side seems not to be the reason, as this cannot be observed in the Schlieren images. Additionally, for angles of attack larger than $\pm 9°$ the pressure decreases further, which supports the reasoning that a flow separation is not causing the pressure decrease.
The pressure coefficients below the interstage and in the balance nearly coincide, which is reasonable, as the pressure in the wake region downstream of the interstage is present at both measurement locations. The absolute value of the pressure coefficients increases with decreasing Mach numbers.

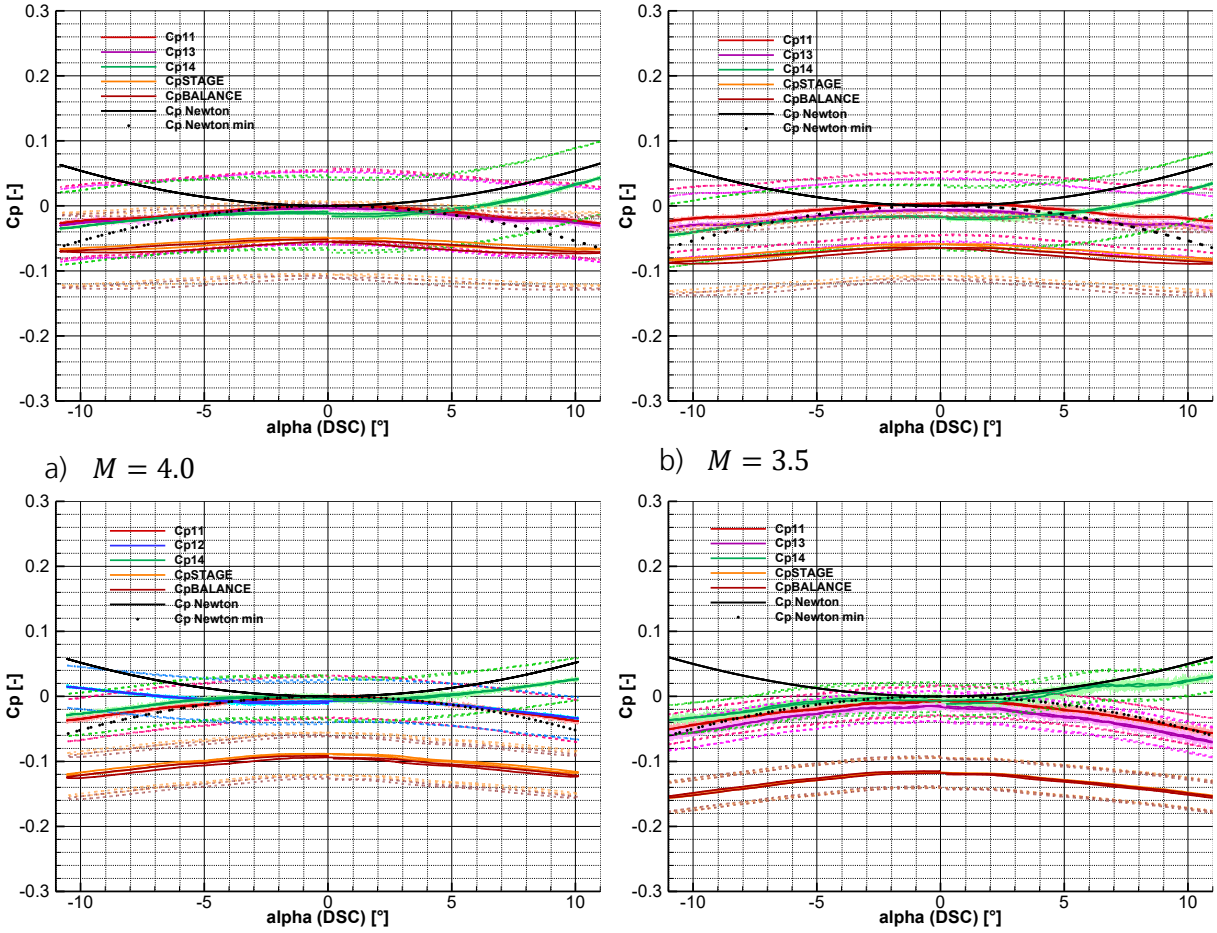

Fig. 57: Pressure coefficients in plane 1 near the interstage of RETALT1 for B0,0,0,0 in the supersonic regime (solid lines: low pass filter with 3 Hz, dashed lines: uncertainties, solid blight lines: measurement data at 500 Hz)

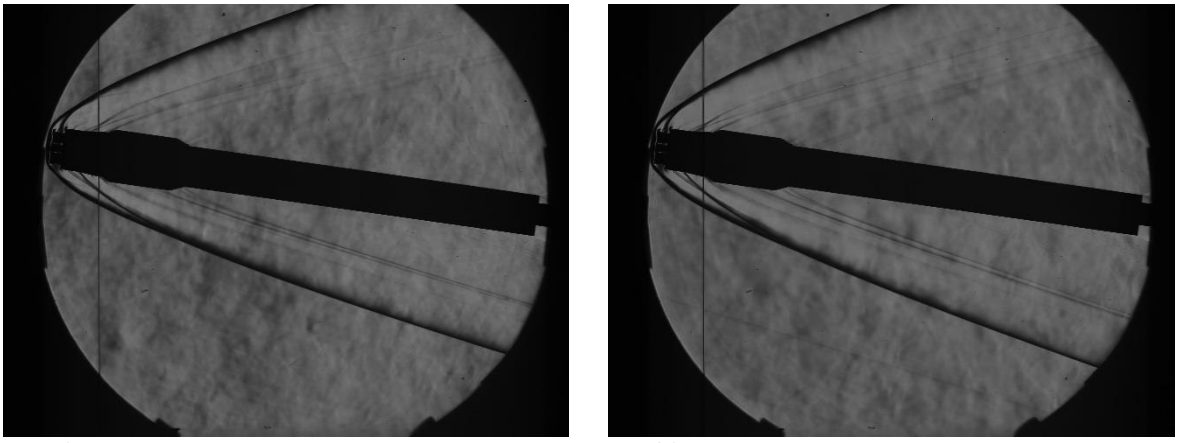

a) $\alpha = 8.12°$, $M = 4.0$ b) $\alpha = 8.23°$, $M = 3.5$

Fig. 58: Schlieren images of B0,0,0,0 at angles of attack of approx. 8°

Fig. 59 shows the pressure coefficients of the sensors in the second plane, again for the Mach numbers 4.0, 3.5, 2.5 and 2.0. While the measured pressure coefficient at the sensor at the bottom side (24) follows the modified Newtonian law well, the pressure coefficient of the sensor on the upper side (22) is shifted to negative values. The reason might be a slight side slip angle or a possible influence of the landing legs. However, the general trend of the modified Newtonian law can, also be observed in this plane. For lower Mach numbers (Mach 2.0 and 2.5) a pressure coefficient plateau around the angle of attack of 0° can be observed. It seems that for the lower Mach numbers the shielding effect of the landing legs is stronger, such that higher angles of attack need to be reached before the pressure coefficient increases.

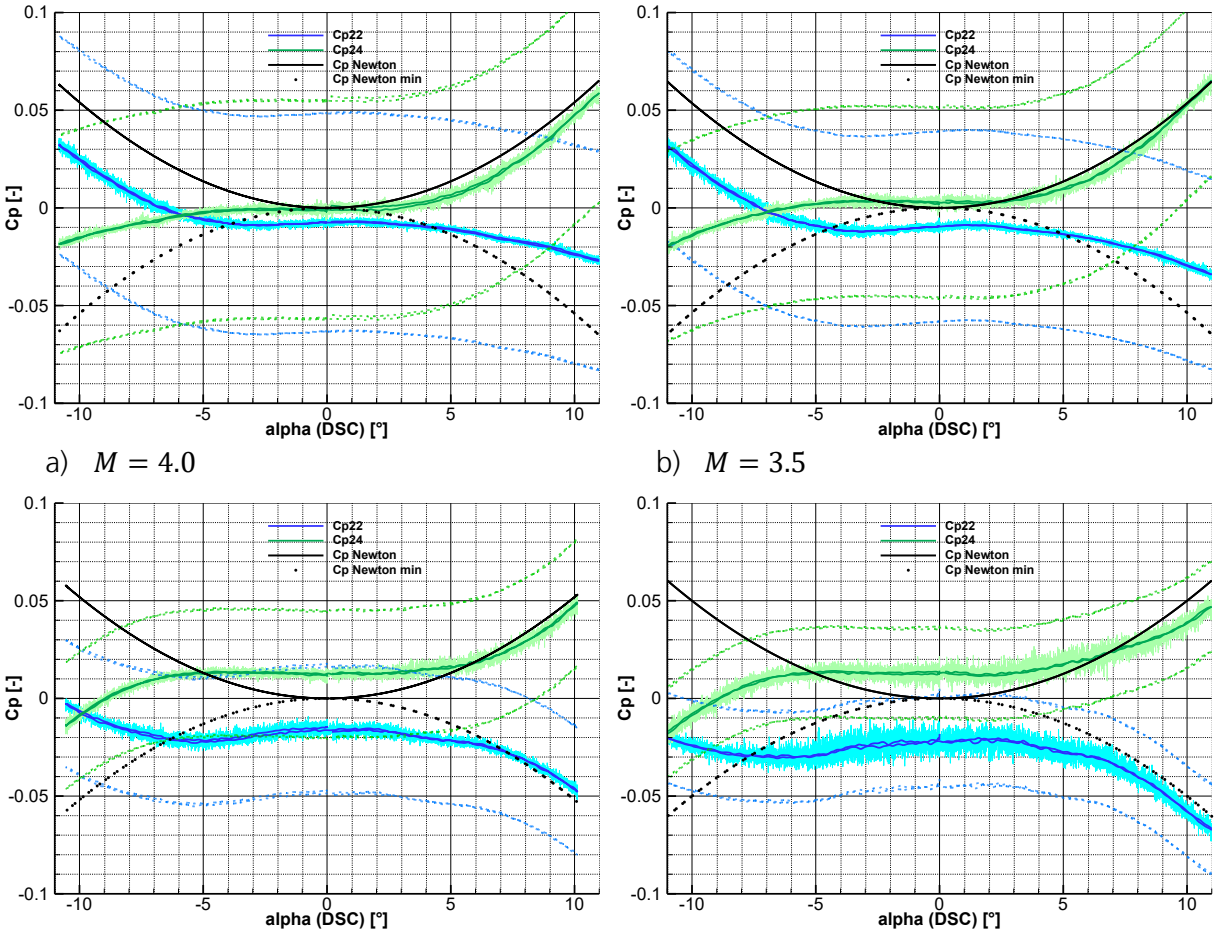

Fig. 59: Pressure coefficients in plane 2 of the RETALT1 configuration for B0,0,0,0 in the supersonic regime (solid lines: low pass filter with 3 Hz, dashed lines: uncertainties, solid bright lines: measurement data at 500 Hz)

Fig. 60 shows the pressure coefficients in plane 3, which is the base plane of the RETALT1 configuration. For the positioning of the sensors refer to Fig. 31. While the sensors 312 and 332 are in the plane perpendicular to the alpha plane, 341 lies in the alpha plane. Furthermore, the

sensor 341 lies in between the central nozzle and the circle of outer nozzles, while the sensors 312 and 332 lie outside of the outer engine circle.
As the sensors are positioned on the base plane, which is offset downstream of the plane of the nozzle exits, the pressures are smaller than the total pressure downstream of the bow shock (the Pitot pressure). Due to their position on the plane perpendicular to the alpha plane, the pressure polars of sensors 312 and 332 are symmetric for negative and positive angles of attack. Due to its position in the alpha plane, the pressure of sensor 341 is slightly dependent on the angle of attack. As it is positioned more central on the base plane the pressure is higher than for sensors 312 and 332.
Additionally, it can be observed, that the pressure fluctuations at the base plane are high compared to the fluctuation in the other planes, especially at an angle of attack of 0°.

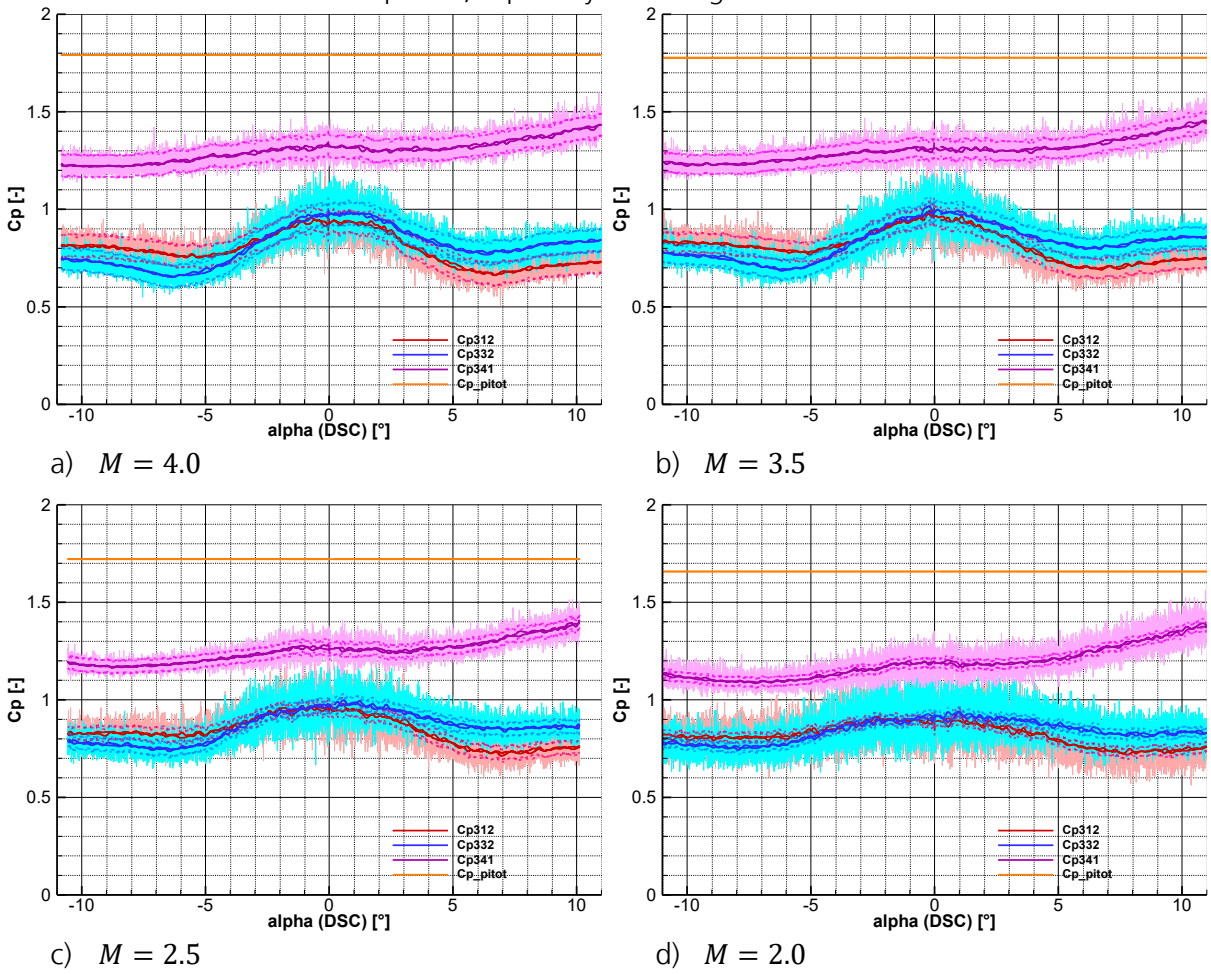

a) $M = 4.0$ b) $M = 3.5$

c) $M = 2.5$ d) $M = 2.0$

Fig. 60: Pressure coefficients in plane 3 (on the base area) of RETALT1 for B0,0,0,0 in the supersonic regime (solid lines: low pass filter with 3 Hz, dashed lines: uncertainties, solid bright lines: measurement data at 500 Hz)

Fig. 61 shows the pressure coefficients in plane 1 for the configurations with all petals deflected by 20° (B20,20,20,20) and 45° (B45,45,45,45) in comparison with the configuration of 0° deflection (B0,0,0,0) that was already shown in Fig. 57. First the configuration of 0° and 20° deflection will

be compared in the following. Then they are compared to the configuration with a deflection of 45°.

The pressure in the wake of the configuration is measures by pSTAGE and pBALANCE. For 0° deflection of the petals and 0° angles of attack, the Cp values for the pressure were calculated analytically with the procedure propose by Jarvinen et al. [99] based on [100] and [101] as shown in Fig. 62. The expansion conditions at the wake are calculated as a Prandtl-Meyer expansion and the pressure in the wake follows from the condition, that the total pressure along the dividing streamline of the wake and the uniform stream around it, must equal the static pressure downstream of the reattachment shock. Jarvinen et al. replaced the ratio of velocities along the dividing stream line of the wake, presented for laminar flow fields by Chapman et al. [100], by the turbulent values presented by Korst [101]. The Mach number at the ACS was calculated with equation (50). In Fig. 62 the resulting laminar and the turbulent solutions are plotted and are compared against the measured values of CpSTAGE for B0,0,0,0. The pressure in wake rises with increasing free stream Mach numbers, due to changing Mach numbers at the ACS and the resulting changes in the expansion conditions. The analytical approach matches the experimental results especially well in the higher supersonic regimes, probably as in this regime the simplifications for the calculations of the Mach number at the ACS are better applicable. It can be seen that the laminar solution matches the test results better than the turbulent one.

In Fig. 61 it can be observed that the base pressures (pSTAGE and pBALANCE) decrease with an increase of the deflection of the petals from 0° to 20 °. This could possibly be attributed to the fact that the shocks which form in this case upstream of the petals, reduce the total pressure in the flow around them. This reduces the total pressure in the wake region which is necessary to overcome the pressure at the reattachment point. This, in turn, results in more negative pressure coefficient of pSTAGE and pBALANCE. However, a multitude of factors influence the pressures in this region, e.g. the expansion of the flow around the edges of the petals, the fact that the petals are rounded, the extend of the wake and the velocities in the wake region. Furthermore, parts of the flow are passing through between the petals and the cylinder, which increases the mass flow entering the wake region, which could further decrease the pressures in the wake.

In the region near the petals the pressure coefficients are not influenced much by their deflection up to a deflection of 20°. However, this behavior changes for a deflection of all petals by 45° (see Fig. 61). The pressures reach a plateau at an angle of attack of 0°. This plateau is larger for smaller Mach numbers and occurs up to higher angles of attack.

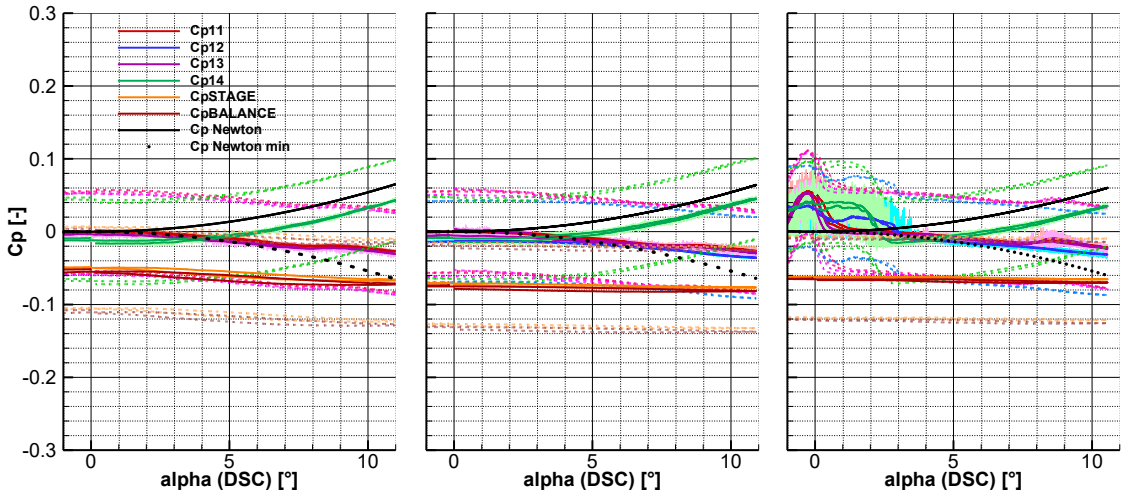

B0,0,0,0 B20,20,20,20 B45,45,45,45

a) $M = 4.0$

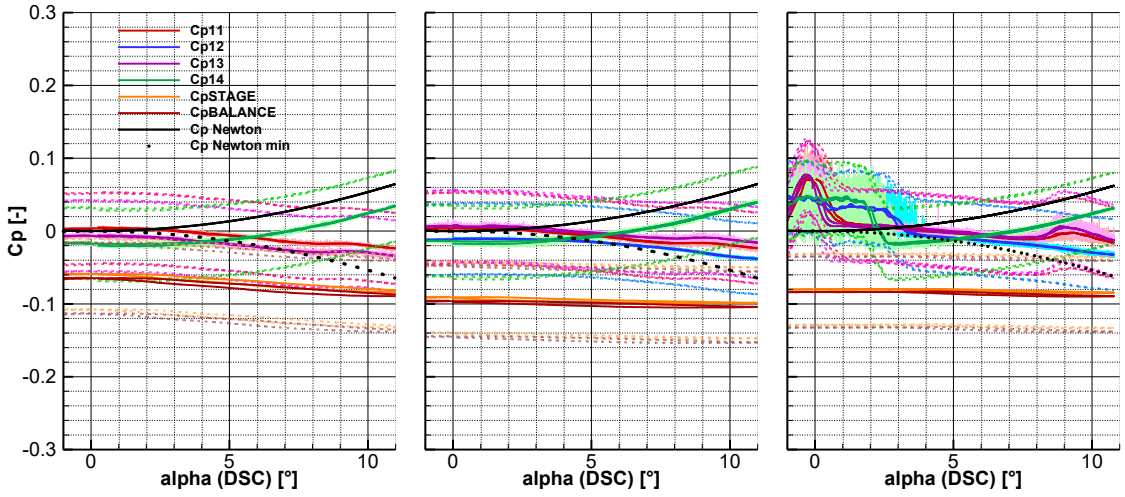

B0,0,0,0 B20,20,20,20 B45,45,45,45

b) $M = 3.5$

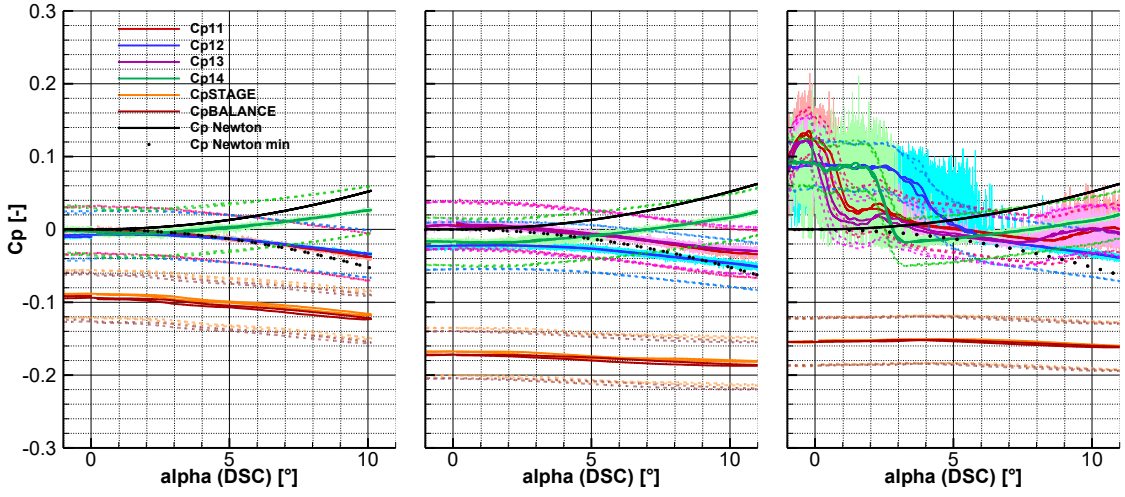

B0,0,0,0 B20,20,20,20 B45,45,45,45

c) $M = 2.5$

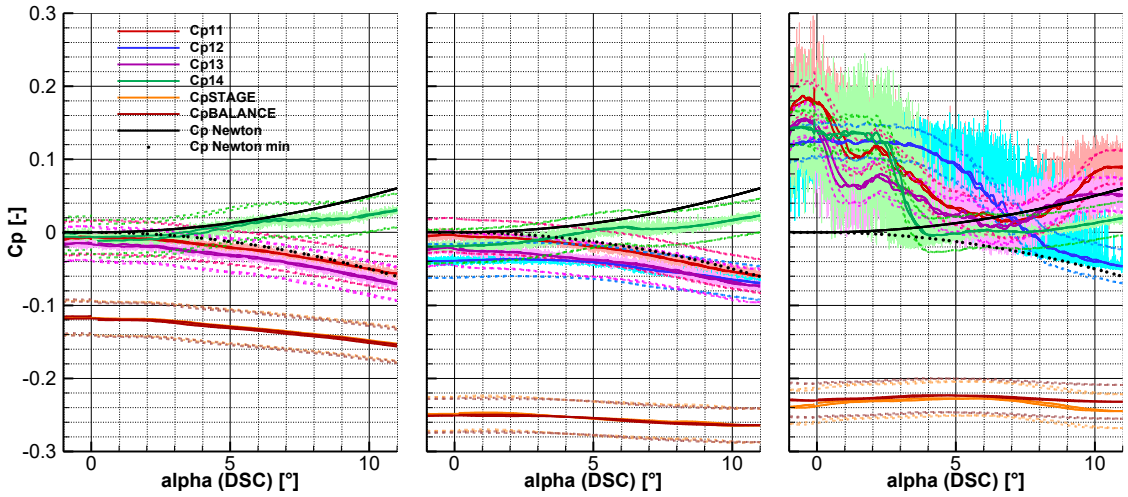

d) $M = 2.0$

Fig. 61: Pressure coefficients in plane 1 near the interstage of RETALT1 for B0,0,0,0; B20,20,20,20; and B45,45,45,45 in the supersonic regime (solid lines: low pass filter with 3 Hz, dashed lines: uncertainties, solid bright lines: measurement data at 500 Hz (B0,0,0,0) and 1000 Hz (B20,20,20,20; B45,45,45,45))

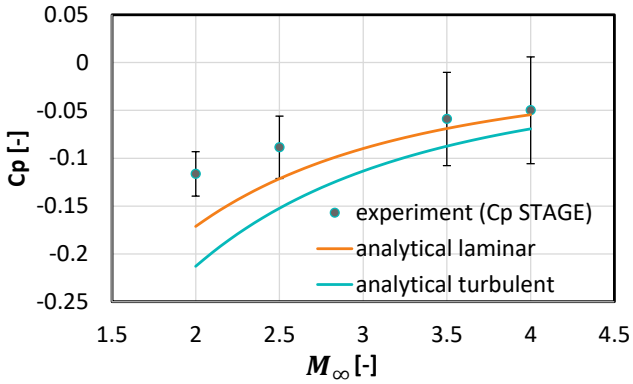

Fig. 62: CpSTAGE for B0,0,0,0 and 0° angle of attack in comparison to analytical estimation based on [99], [100] and [101]

In Fig. 63 the Mach numbers at the location of the ACS are plotted as calculated with the methodology described in section 5.1.1. Furthermore, Fig. 63 shows the angle β_{max}, which is the maximum deflection angle at which a solution with the oblique shock relations exists for the Mach number at the ACS location. Here the static pressures from the modified Newtonian law and the negative counterpart were used to estimate the dependency of the Mach number and β_{max} on the angle of attack. For all Mach numbers, β_{max} is smaller than 45°. However, except for the case of Mach 2.0, β_{max} is larger than 20°.

In Fig. 64 the flow fields for $\delta = 20°$ and $\delta = 45°$ are shown at Mach 4.0. For $\delta = 20°$, an oblique shock is forming upstream of the petal transforming to a bow shock which passes the outer part of the petal, for $\delta = 45°$, a large unsteady region upstream of the petal and a separation shock can be observed. As for $\delta = 45°$, the deflection angle exceeds β_{max}, in an inviscid flow a detached bow

shock would form upstream of the petal (see Fig. 3). However, the strong shock creates a large adverse pressure gradient which leads to a separation of the boundary layer, resulting in a shock-wave/boundary-layer interaction (see section 2.2). The flow separation creates a separation bubble which leads to the formation of a separation shock far upstream of the petal. As the separation shock tends to be a lot weaker than the inviscid shock (see section 2.2), this could explain why the pressure in the wake (pSTAGE) is slightly higher for $\delta = 45°$ than for $\delta = 20°$ (see Fig. 61). In Fig. 64, also the sensor plane 1 is depicted. The detached separation shock moves over the sensor position, which is why large pressure fluctuations are measured. Such large pressure fluctuations caused by shock-wave/boundary-layer interactions can lead to high structural loads [12, 15], here the ACS, and should, therefore, be avoided.

Fig. 65 shows the complete model for Mach 2.0 and 4.0 for angles of attack of 0° and 10° (note that in Fig. 65 for Mach 4.0, reflections of the bow shock on the Schlieren windows are visible, which are not obstructions of the flow field). It can be observed that the separation region gets smaller with increasing angle of attack. On the leeward side, this is partly due to the reduced effective angle of attack of the petal. Furthermore, on the windward and on the leeward side, due to the angle of attack, the petals are not located downstream of the landing legs anymore. This probably leads to thinner boundary layers and therefore to reduced shock-wave/boundary-layer interactions. Fig. 66 shows the same Schlieren images for the deflection of $\delta = 20°$. A close inspection reveals, that also for these cases, the oblique shock upstream of the petal is slightly offset in the upstream direction, indicating, that also at the lower deflection angles already weak shock-wave/boundary-layer interactions exist. It should be mentioned that the shock-wave/boundary-layer interactions depend on the Reynolds number, which is why in the future, a Reynolds number variation should be performed to assess this dependency. Furthermore, experiments with more deflection angles between 20° and 45° should be tested to better understand the dependency of the appearance of shock-wave/boundary-layer interactions with higher deflection angles.

Concluding this analysis, four main key facts can be pointed out:

1) The pressure on the windward side near the ACS follows approximately the modified Newtonian law.
2) The pressure on the leeward side near the ACS follows approximately a negative modified Newtonian law up to a certain angle of attack (in this case approximately $\pm 7°$).
3) The pressure on the sides near the ACS follows the pressure of the leeward side, meaning approximately the negative modified Newtonian law.
4) Deflecting the petals by large angles can lead to largely unsteady flow due to shock-wave/boundary-layer interactions which can be critical for the structural loads on the ACS.

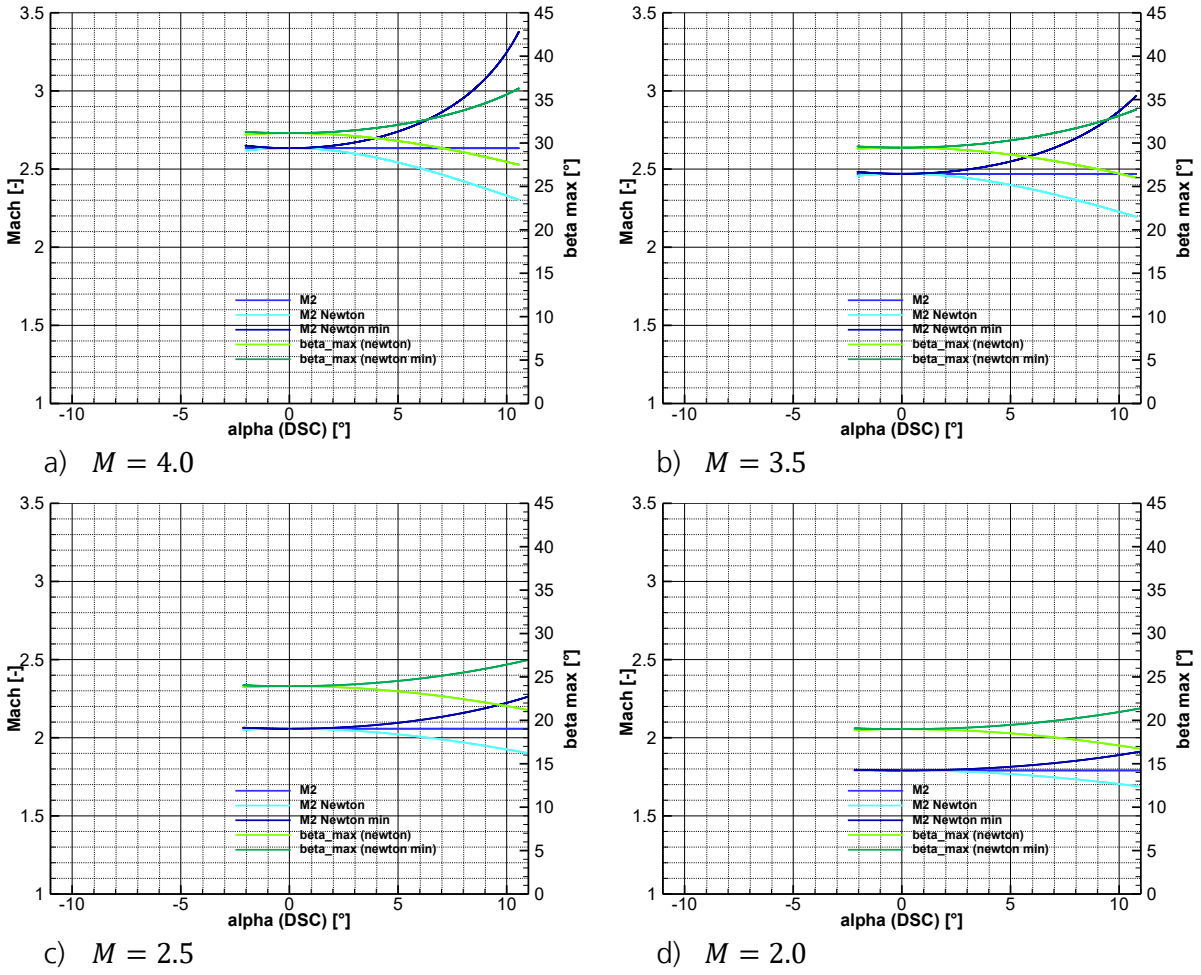

Fig. 63: Mach numbers and maximum deflection angles at the location of the ACS as calculated with the methodology described in section 5.1.1

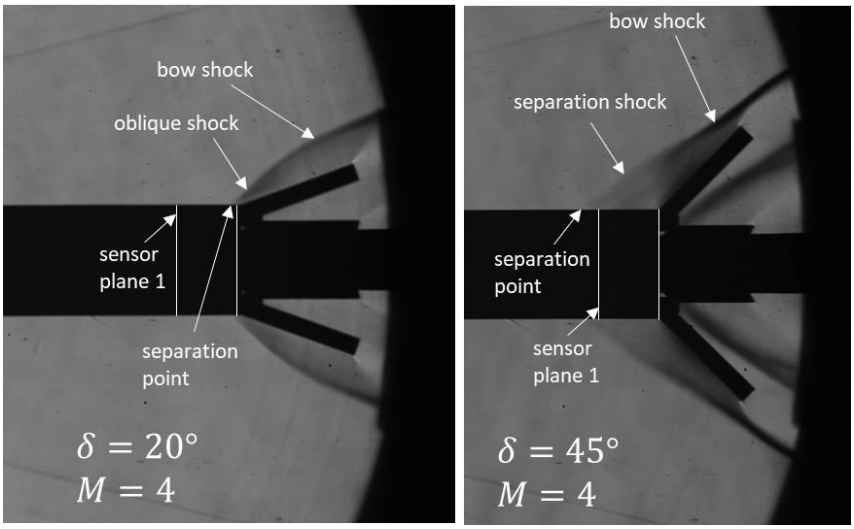

Fig. 64: Detail of flow phenomena for petal deflection of $\delta = 20°$ and $\delta = 45°$ at Mach 4.0

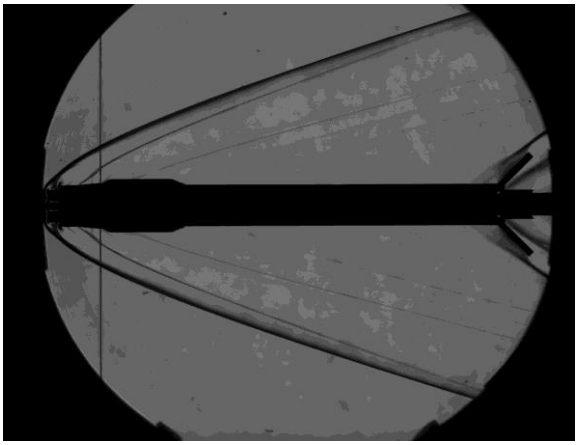

a) $M = 4.0, \alpha = -0.18$

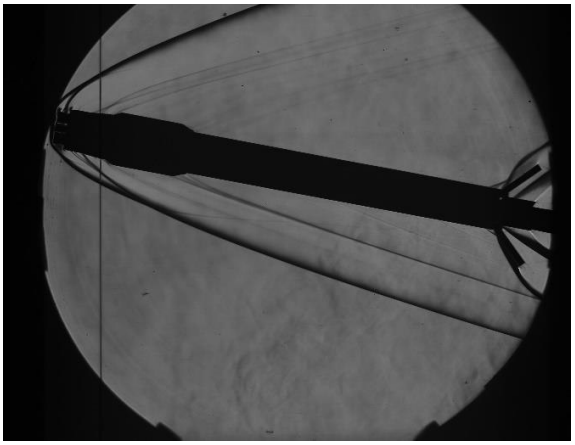

b) $M = 4.0, \alpha = 10.57$

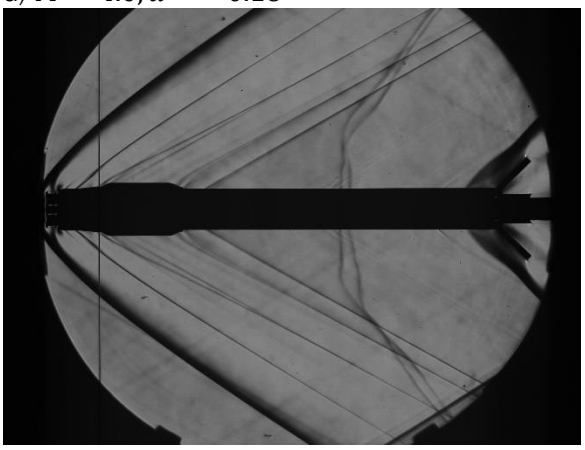

c) $M = 2.0, \alpha = -0.01$

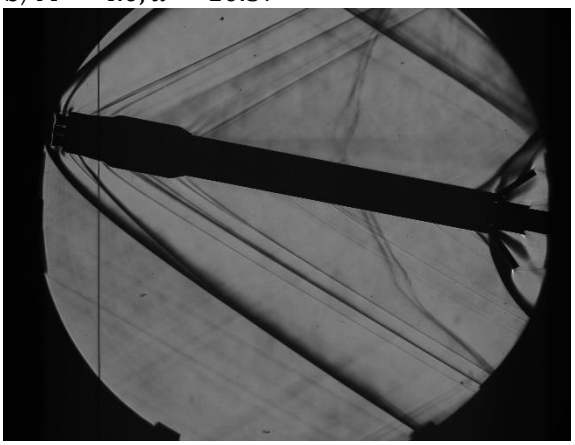

d) $M = 2.0, \alpha = 10.85$

Fig. 65: Schlieren images of B45,45,45,45 for several Mach numbers and angles of attack

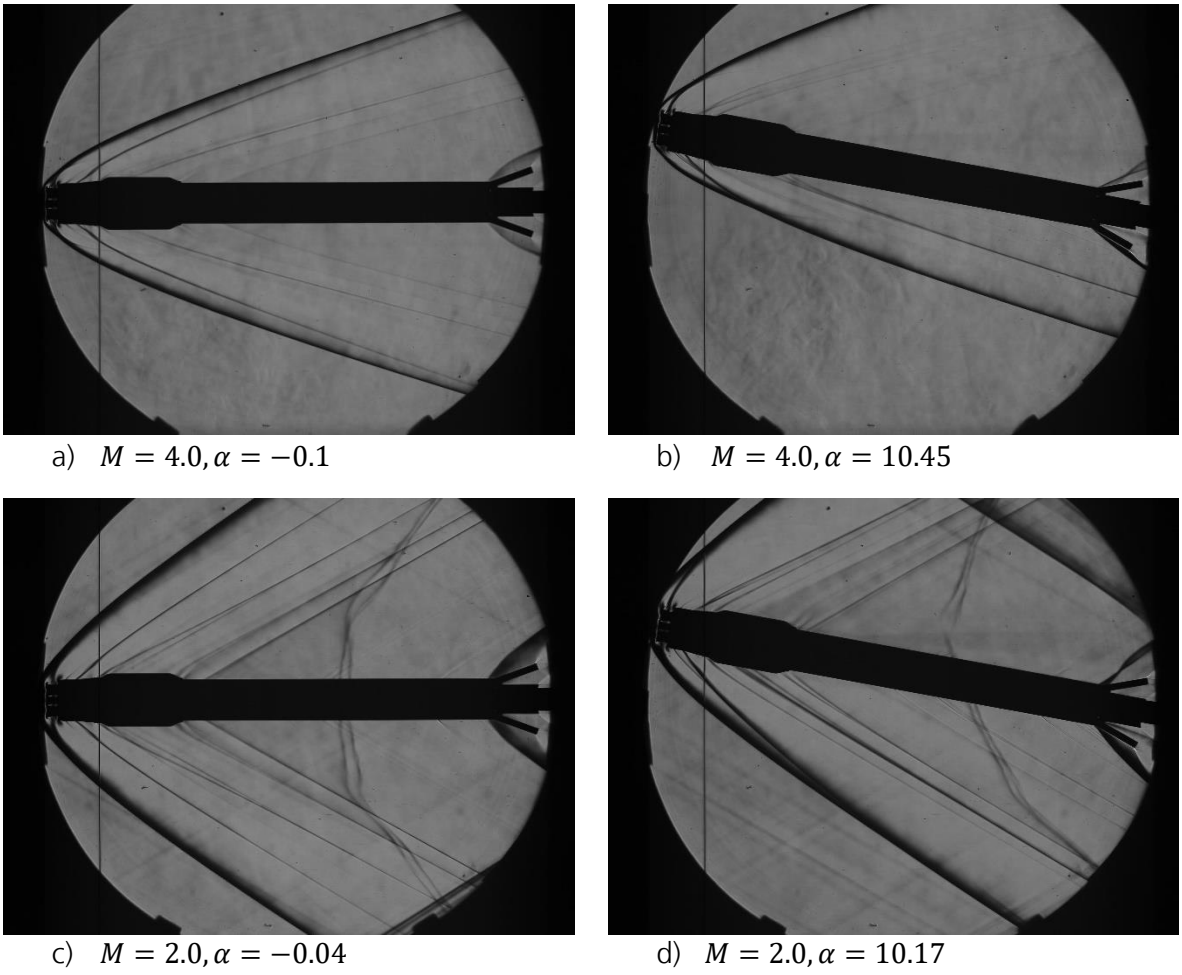

a) $M = 4.0, \alpha = -0.1$ b) $M = 4.0, \alpha = 10.45$

c) $M = 2.0, \alpha = -0.04$ d) $M = 2.0, \alpha = 10.17$

Fig. 66: Schlieren images of B20,20,20,20 for several Mach numbers and angles of attack

5.1.3. Verification of the Analytical Method Based on Planar Fins

With the aid of the analytical models described in the sections 5.1.1and 5.1.2, the planar fins for the RETALT1 configuration were sized and designed. This was described in ref. [77].
This approach was then verified by a comparison of the force and moment coefficients resulting from the analytical model with the wind tunnel data. For that, the measured data of the plain configuration of RETALT1 without any control surfaces (B0,0,0,0) is superimposed with the planar fins. The results are then compared to the measured data of the planar fin configuration (PF0,0,0,0). Fig. 67 shows the profile of the planar fins.

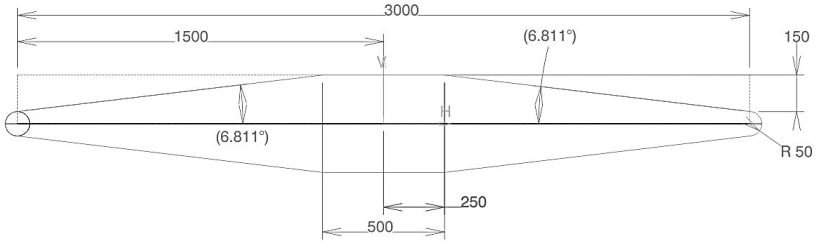

Fig. 67: Profile of planar fins of RETALT1 [77]

In Fig. 68 the normal force coefficient is shown. The blue line represents the plain configuration. The black line shows the measured planar fin data. The symbols show three analytical approaches. As described in section 5.1.1, the free stream conditions at the ACS were obtained assuming the total pressure downstream of a normal shock and the static pressure of the free stream.
The squares show the planar fins calculated with oblique shock relations. However, due to the blunt leading edge of the fins (see Fig. 67), the stream lines close to the surface pass a normal shock upstream of the leading edge before running along the surface. Therefore, the black triangles show the corrected approach of estimating the pressures on the surface of the fins by assuming the total pressure downstream of a normal shock, but the static pressure passing through an oblique shock. It can be observed that this data fits the measured data better. For the white triangles the static pressure at the ACS was corrected with the negative modified Newtonian law described above. With this correction, the superimposed CN fits the measurements very well for angles of attack up to $\pm 8°$. For higher angles of attack the method seems to underestimate the CN. This is reasonable as for angles of attack higher than $\pm 7°$ the negative modified Newtonian law does not hold anymore (see Fig. 57b in section 5.1.2). In Fig. 69 the pitch moment coefficient around the center of gravity (CM(CoG)) resulting with the superimposed CN is shown. As for the CN up to angles of attack of $\pm 7°$ the CM(CoG) is well approximated with the analytical method for the fins, for higher angles of attack it tends to deviate.
Fig. 70 shows the CM(CoG) for various fin deflections. For a deflection of the fins, the assumptions taken in the analytical approach are less valid, as the fins see more complex free stream conditions. The analytical method generally overestimates the efficiency of the fins, even though the general trend of the CM(CoG) is captured well.

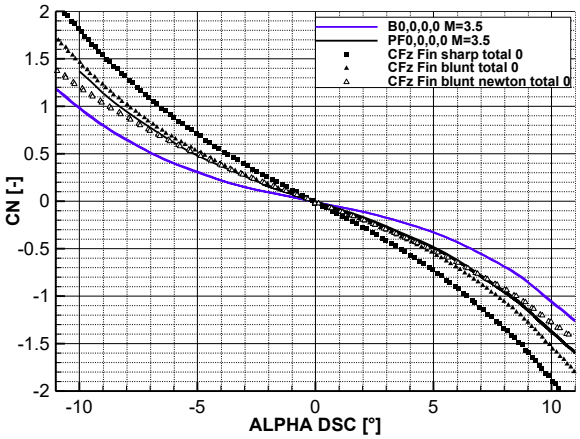

Fig. 68: Comparison CN for superimposed planar fins with measured planar fin configuration with $\delta = 0°$ for Mach 3.5

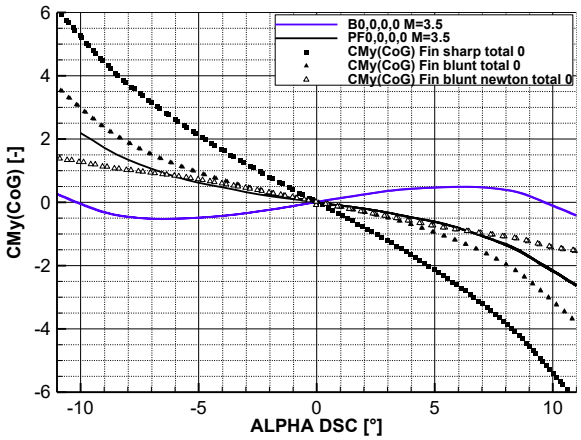

a) Fig. 69: Comparison CM(CoG) for superimposed planar fins with measured planar fin configuration with $\delta = 0°$ for Mach 3.5

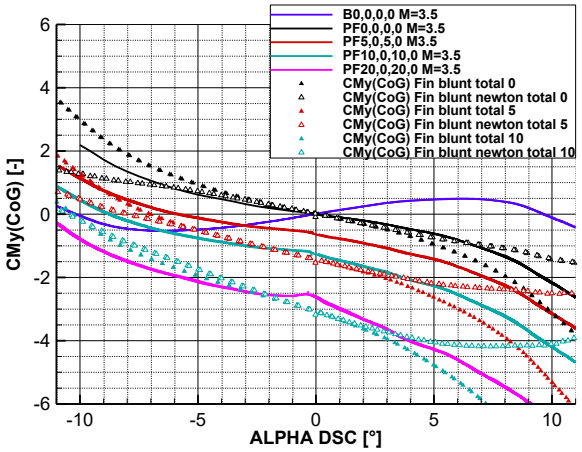

b) Fig. 70: Comparison CM(CoG) for superimposed planar fins with measured planar fin configuration for several deflection angles for Mach 3.5

5.1.4. Conclusions regarding the Aerodynamic Phase

The main focus of this section was the determination of the free stream conditions at the Aerodynamic Control Surfaces (ACS) for a reusable launcher configuration. It was shown that they can be estimated with classic methodologies for hypersonic flow. The analytical method could be verified with a comparison of the method with wind tunnel test data. An analysis of pressure measurements close to the ACS showed that the deflection angle of the ACS should not exceed the maximum deflection at which a solution with the oblique shock relations exists, as larger deflection angles can lead to largely unsteady flow fields that generate high structural loads on the ACS, and has a potential negative impact on the flying qualities of the spacecraft. If high deflection angles are required for future configurations, this phenomenon should be analyzed further by performing an analysis of the power spectral density of the pressure measurements to extract dominant frequencies of the occurring pressure fluctuations.

5.2. Reentry Burn – Hypersonic Retro Propulsion Deceleration Maneuver

The reentry burn occurs at high altitudes during the reentry of the descending first stage. Its aim is to decelerate the vehicle to limit heat loads and dynamic pressures during the following aerodynamic phase (see section 3). It is commonly performed with three engines. In this section it is analyzed for one and for three active engines.

5.2.1. Discussion of Flow Field Features

First the single-engine case is analyzed. Fig. 71 shows a Schlieren image for a thrust coefficient of 3.69 at a Mach number of 5.3, where the most important flow features are highlighted.

The flow field is balanced between the freestream coming from the left and the jet stream from the right. The two streams are separated by the contact surface. The freestream is decelerated by a bow shock and a subsequent subsonic deceleration. The jet stream is expanded in a highly underexpanded plume and is then decelerated over a Mach disc and a subsequent subsonic deceleration. At the free stagnation point the total pressure of the freestream and the jet stream are equal. For a more detailed description of the flow features of supersonic and hypersonic flow fields see section 2.5.

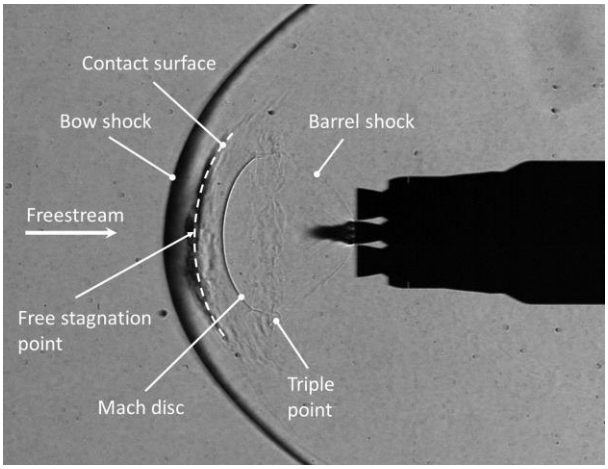

Fig. 71: Schlieren image with highlighted flow features for $M_\infty = 5.29$ and $C_T = 3.69 \pm 0.21$

In the experiments an interesting dynamic phenomenon was observed: frequently vortex rings emerged from the Mach disc, moved away from it and interacted with the subsonic area in the contact surface. This is shown in Fig. 72. The majority of the vortex rings are small and do not generate large flow field disturbances, especially if the vortex is formed on the symmetry line of the model nozzle. This can be observed in the time series depicted in Fig. 73. However, as can be observed in Fig. 74, if the vortex rings do not appear symmetrically, the vortex is subjected to different flow fields around its perimeter. This can result in an unsymmetrical energy absorption of the vortex, which leads to a growing single vortex, rolling off to one side of the Mach disc and consequently leading to large flow field disturbances.

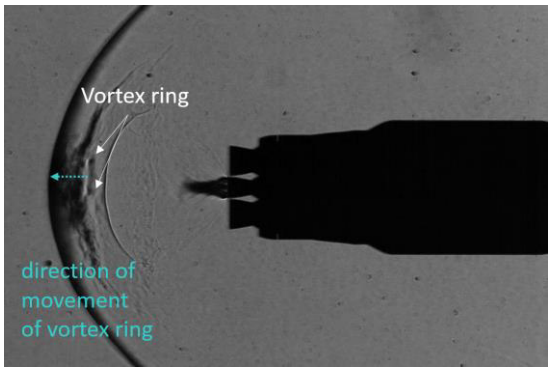

Fig. 72: Vortex ring formation moving away from the Mach disc (Schlieren image at $M_\infty = 5.29, C_T = 3.69 \pm 0.21, T_{CC} = 300K, p_0 = 4\ bar, T_0 = 450\ K$)

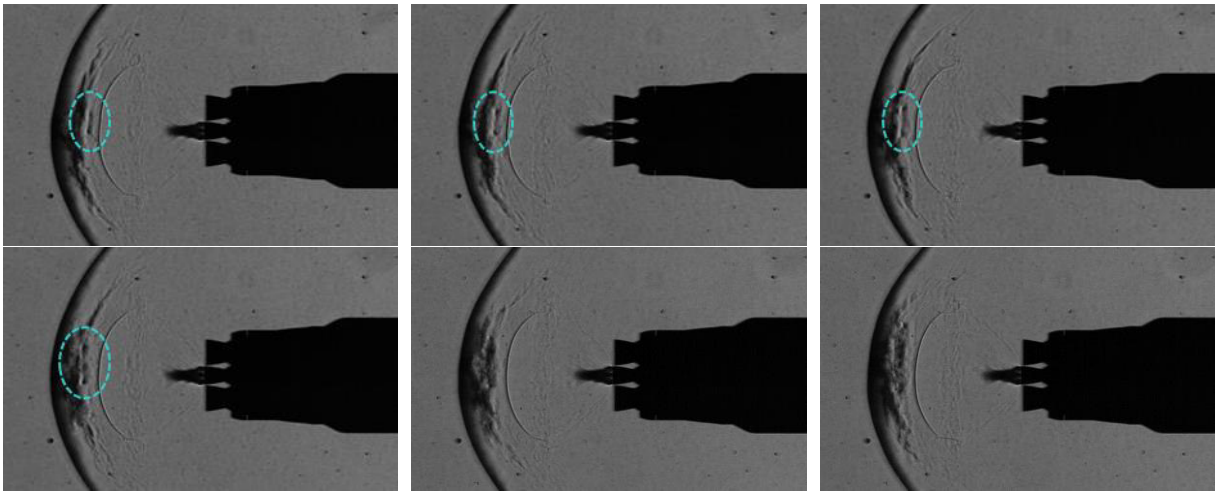

Fig. 73: Symmetric dynamic vortex rings at $M_\infty = 5.29, C_T = 3.69 \pm 0.21, T_{CC} = 300\ K, p_0 = 4\ bar, T_0 = 450\ K$ with a time step of $50\ \mu s$ (frame rate of 20 kHz) (vortex rings highlighted with dashed circle)

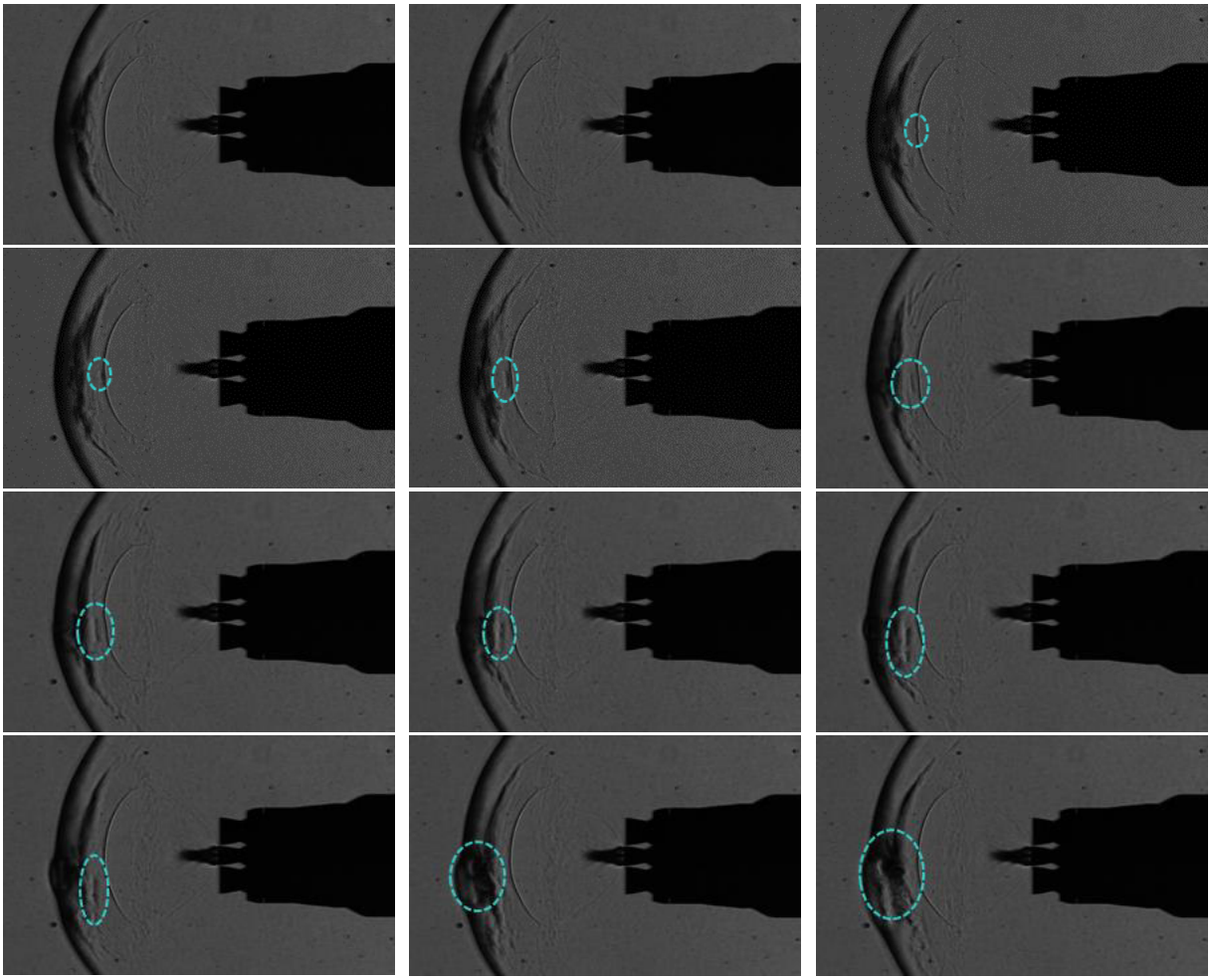

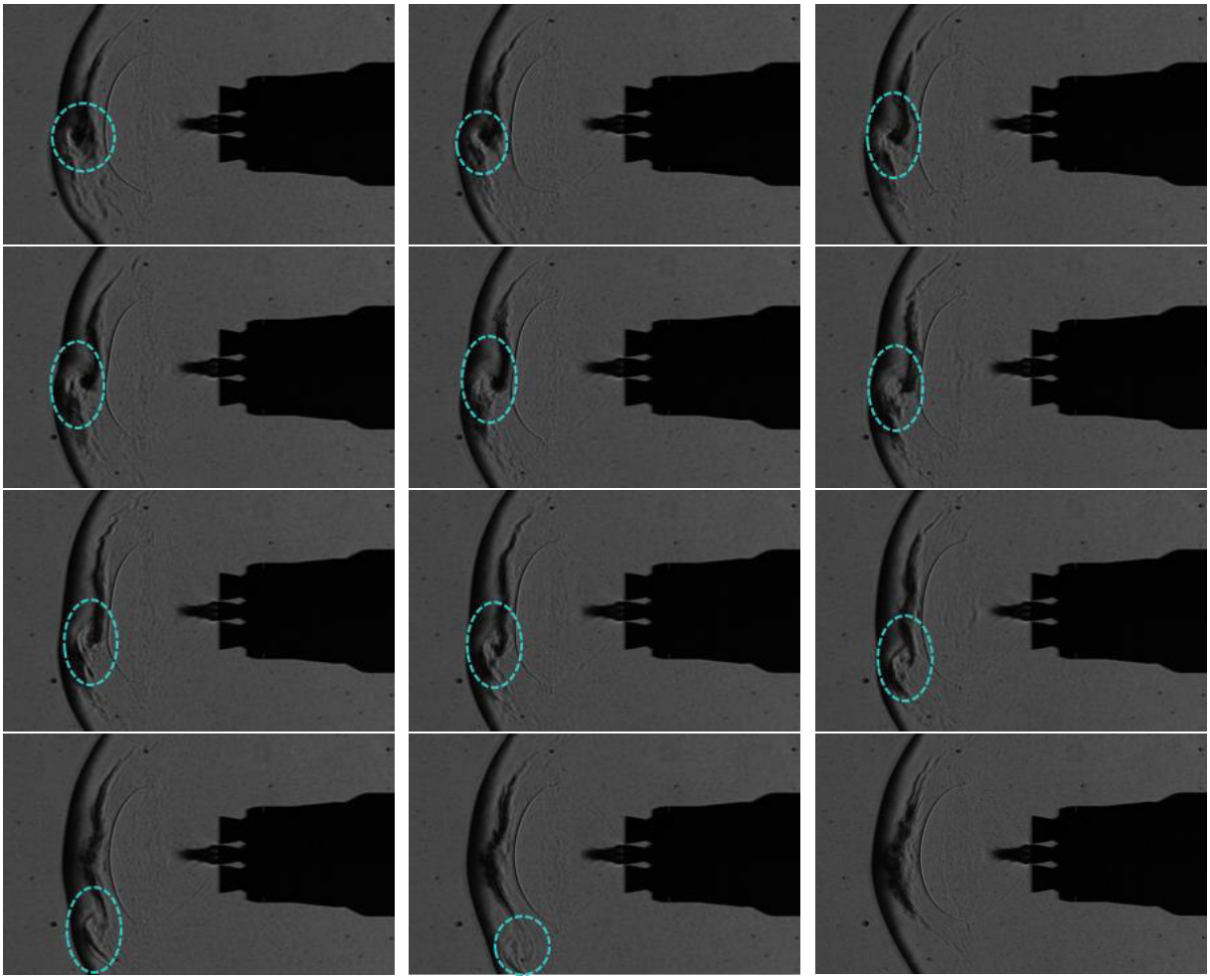

Fig. 74: Asymmetric dynamic vortex rings at $M_\infty = 5.29, C_T = 3.69 \pm 0.21, T_{CC} = 300K, p_0 = 4\ bar, T_0 = 450K$ with a time step of $50\ \mu s$ (frame rate of 20 kHz) (vortex rings and resulting larger vortices highlighted with dashed circle)

An attempt to explain this effect is made in the following with the aid of Fig. 75 and Fig. 76.
In Fig. 75 the flow properties on the centerline are calculated analytically for specific points. At the stagnation point between the free stream and the jet plume, the total pressure of the free stream and of the jet are equal [30, 65]. As the total pressure drop over the bow shock is known, the total pressure in the stagnation point is known. Hence, with the known total pressure in the stagnation point and with the measured total pressure in the wind tunnel model, the Mach number upstream of the Mach disc can be computed iteratively. In Fig. 75 from the free stream side, point 1 is upstream of the bow shock and 2 downstream of it, and 0,2 is the stagnation point from the free stream side. From the jet side, 1j is upstream of the Mach disc and 2j downstream of it, and 0,2j is the stagnation point from the jet side.
The turquoise line in Fig. 75 represents the regular flow field in the blunt mode. The static pressure in the free stream is increased over the bow shock and the static pressure in the jet is increased over the Mach disc. In the stagnation region the flow is decelerated to zero velocity and the total pressures from the free stream side and from the jet side match.

Fig. 76 shows a scheme of the vortex rings building up. In this case disturbances in the stagnation region propagate upstream (with respect to the jet flow) to the Mach disc. Here they locally increase the pressure. Hence, the Mach disc locally moves upstream (with respect to the jet flow) towards lower Mach numbers in the plume, such that it matches the new pressure ratio of p_{2j}/p_{1j}. To visualized this effect in Fig. 75, the Mach number upstream of the Mach disc M_{1j} was decreased from 7.74 to 7 (orange line). The decrease in the Mach number upstream of the Mach disc leads to a slight increase in the velocities downstream of it. Hence, between the undisturbed and the disturbed region, the pressures and velocities don't match, leading to a shear layer between them. The higher velocities and higher pressures in the disturbed area lead to the vortices rolling-up and turning outwards, similar to vortex rings rolling-up from sharp edges of nozzles in impulsively started flows as described e.g. in [102]. Fig. 77 shows a Schlieren image, where the recessed Mach disc can be seen. Also the onsets of a vortex ring is visible.
The higher pressures in the disturbed case, theoretically lead to higher total pressures in the stagnation region from the jet side, as the shock of the Mach disc in the disturbed case, for lower Mach numbers, is weaker and hence the total pressure loss is lower. This leads to a discontinuity in the total pressure in the stagnation point (see Fig. 75). If this condition would appear instantly, and if the inviscid flow field is considered, the discontinuity would give rise to a Riemann problem. The pressure discontinuity would result in a shock wave moving upstream in the direction of the free stream (towards the bow shock) and an expansion wave would move upstream in the direction of the jet (towards the Mach disc). Due to viscous effects and as energy is taken up by the vortices, the effect can, however, not be observed in the experiments.
To verify that the appearance of vortex rings is not specific for the particular wind tunnel model of RETALT1, the data of the preparatory experiments presented in [65] was examined for this effect, where it could also be observed. In [65] the nozzle shape was designed as an ideal contour with the method of characteristics. The emerging of vortex rings followed by a larger single vortex was also observed in the data of [65] (see Fig. 78). Even though not mentioned explicitly in their paper, such vortex rings were also predicted by a DNS (Direct Numerical Simulation) performed by Montgomery et al. [72], which can be observed in a video provided as complementary data to the paper [103]. As the simulation was performed as an axisymmetric computation, the vortex naturally appears in the symmetrical configuration and hence, as stated above, leads to only little disturbing effects on the flow field. Unsteady three dimensional CFD computations of these effects in the future, would be helpful to further understand their underlying physics.

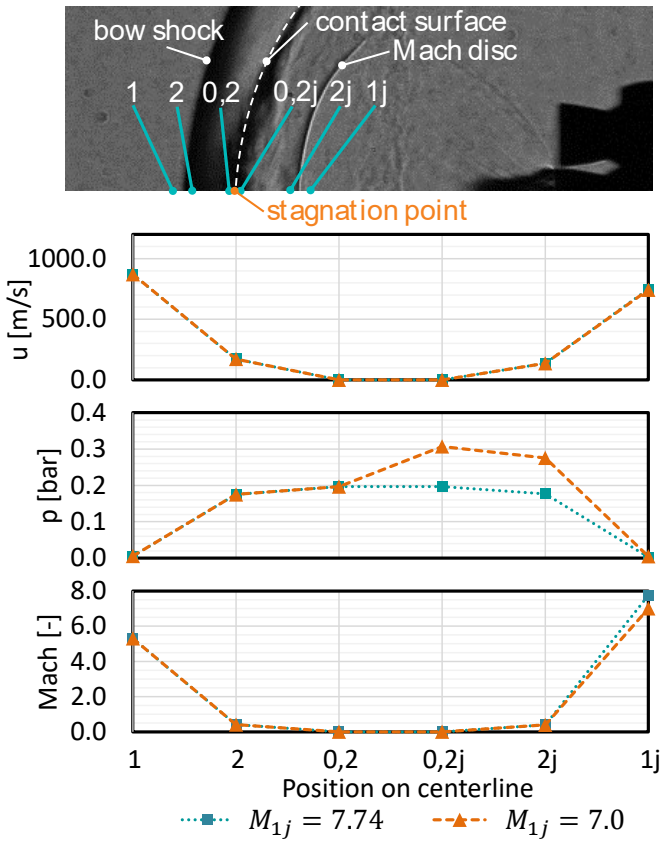

Fig. 75: Analytically calculated flow properties at selected points on the centerline for the single-engine case for the undisturbed flow field and for an assumed disturbance of M_{1j} ($C_T = 3.78$, $M_\infty = 5.3$, $p_0 = 4\ bar$, $T_0 = 445\ K$, $p_{CC} = 20\ bar$, $T_{CC} = 303\ K$)

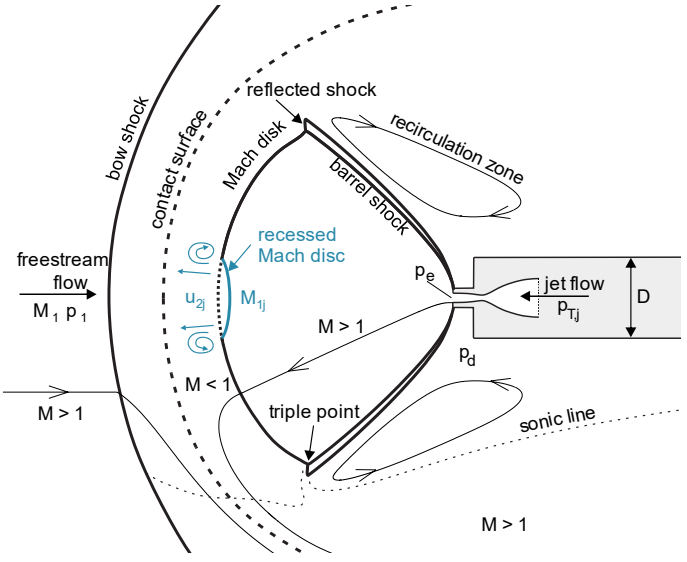

Fig. 76: Scheme of the build-up of vortex rings in the blunt mode of supersonic retro propulsion flow fields. (based on the flow field scheme of [65])

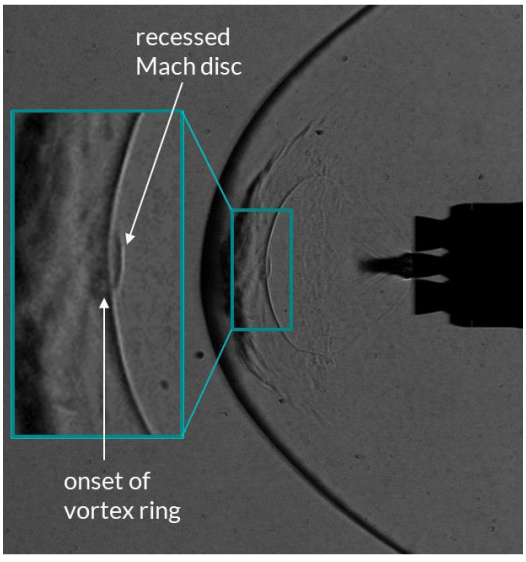

Fig. 77: Recessed Mach disc and vortex build-up in Schlieren image ($M_\infty = 5.29, C_T = 3.69 \pm 0.21, T_{CC} = 300K, p_0 = 4\ bar, T_0 = 450\ K$)

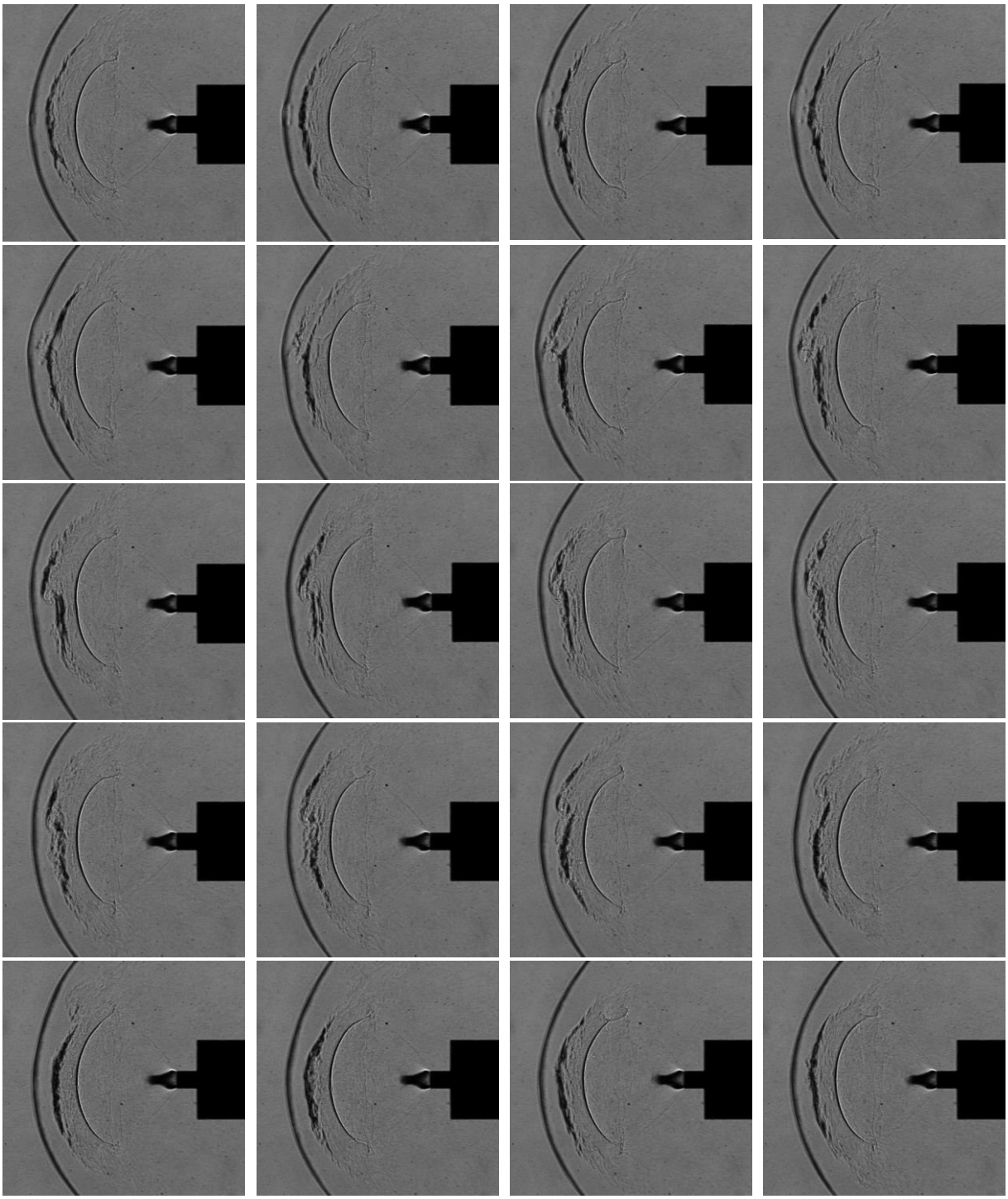

Fig. 78: Vortex emerging from the Mach disc observed in the preparatory experiments for $C_T = 4.16 \pm 0.23, M_\infty = 5.287, \epsilon = 2.5$; from left to right and from top to bottom with a time step of $80\ \mu s$ (frame rate of 12.5 kHz)

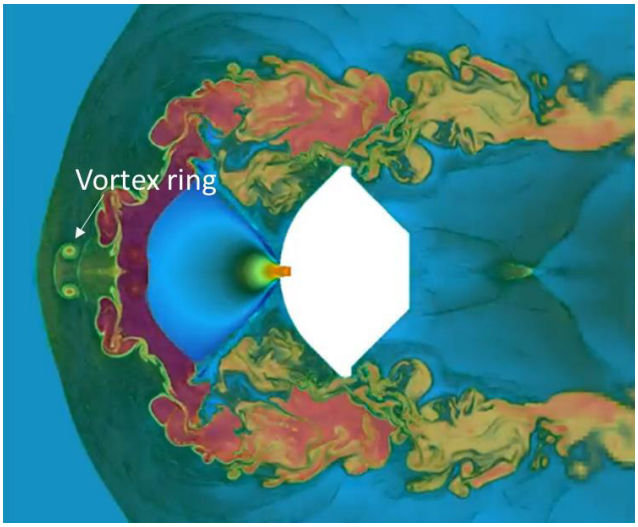

Fig. 79: Vortex ring observable in a snapshot of the video provided in [103] complementing [72] ($M_\infty = 2.0$)

In Fig. 80 the flow field is shown for a test run for the three-engines case where the engines are active in the α-plane. In general, the flow field is dominated by the coalescence of the three nozzle plumes and the balancing of the exhaust jets with the freestream. It can be observed that similar to the single-engine case, there are two modes: a blunt mode shown in Fig. 80a and Fig. 80b and a long penetration mode shown in Fig. 80c. The blunt mode does not occur in a symmetrical configuration, but tends to stabilize in an asymmetrical configuration where the bow shock stand-off distance is either larger above the symmetry plane of the nozzle exits (Fig. 80a) or below it (Fig. 80b). The long penetration mode (Fig. 80c) shows a stronger symmetry, however, also this configuration showed strong unsteady behavior. In general, the flow field is very unstable and constantly changes between the blunt modes and the long penetration mode with other flow field structures appearing between them; as can be seen in Fig. 80e and Fig. 80f where a symmetrical blunt mode and a snapshot of the transition of the long penetration mode to the blunt mode are shown. Hence, the modes do not appear to be stable points but rather labile. As for the single-engine case, the condition needs to be satisfied that the total pressure of the free stream and the jet stream are equal on the contact surface. Hence, the reason for the longer persistence of the penetration modes and the asymmetric blunt modes in the flow field is presumably due to their better match of this condition. In Fig. 80d, the Schlieren image of the experiment was compared to RANS (Reynolds Averaged Navier Stokes) computations which was presented in [50]. The CFD results converged at the long penetration mode and matched the overall flow structure well.

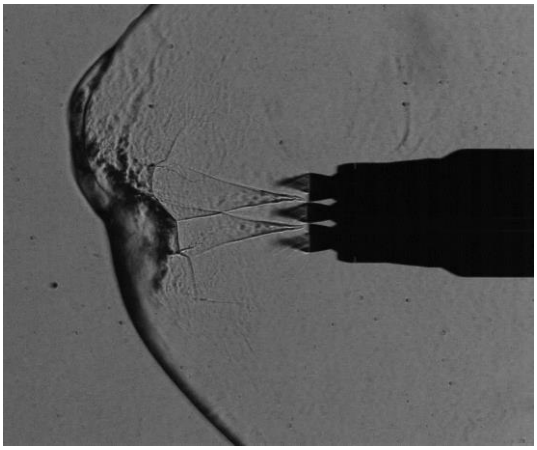

a) Blunt mode with larger stand-off distance above the symmetry plane

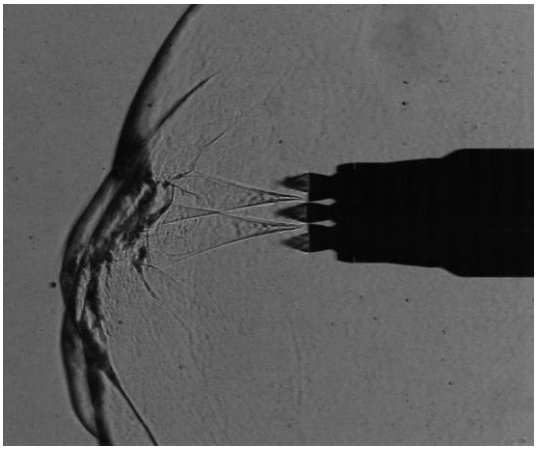

b) Blunt mode with larger stand-off distance below the symmetry plane

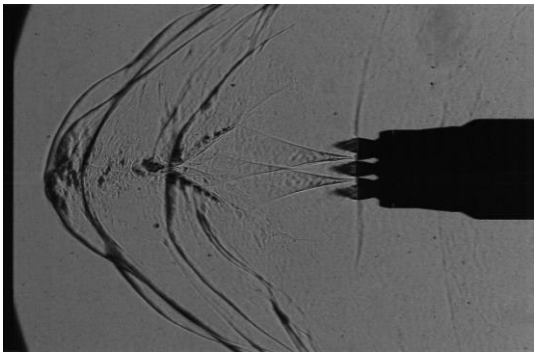

c) Long penetration mode

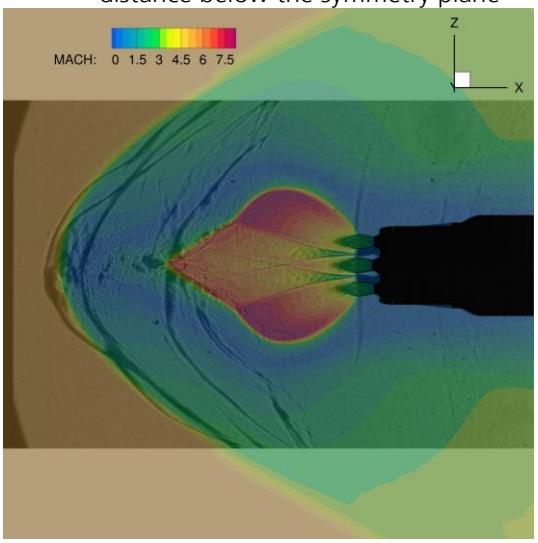

d) Comparison of a Schlieren image with CFD computations presented in [50]

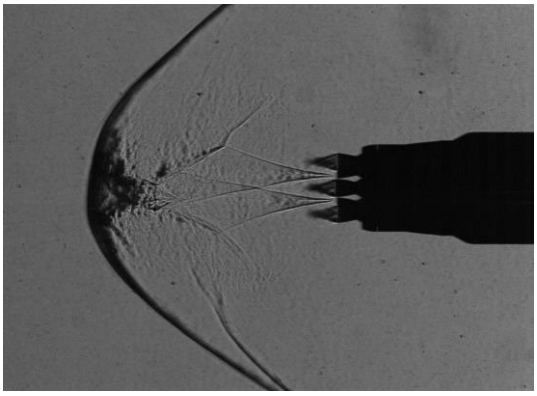

e) Symmetrical blunt mode

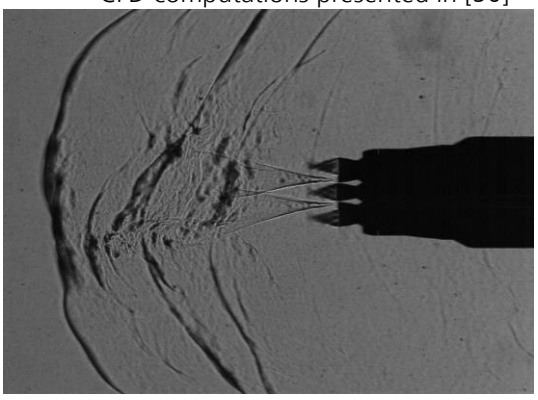

f) Snapshot of transition between long penetration mode and blunt mode

Fig. 80: Three-engines configuration in the α-plane for $M_\infty = 5.29, C_T = 2.29 \pm 0.13, T_{CC} = 300K, p_0 = 4\ bar, T_0 = 450\ K$

When considering the plane perpendicular to the α-plane for the three-engines case, one can observe a good similarity with the single-engine case (compare Fig. 81 with Fig. 71). Fig. 81a and Fig. 81b show the blunt and the long penetration mode for the same thrust coefficient as in Fig. 80 (where the engines are active in the α-plane). Fig. 81c and Fig. 81d show the two modes for smaller thrust coefficients.

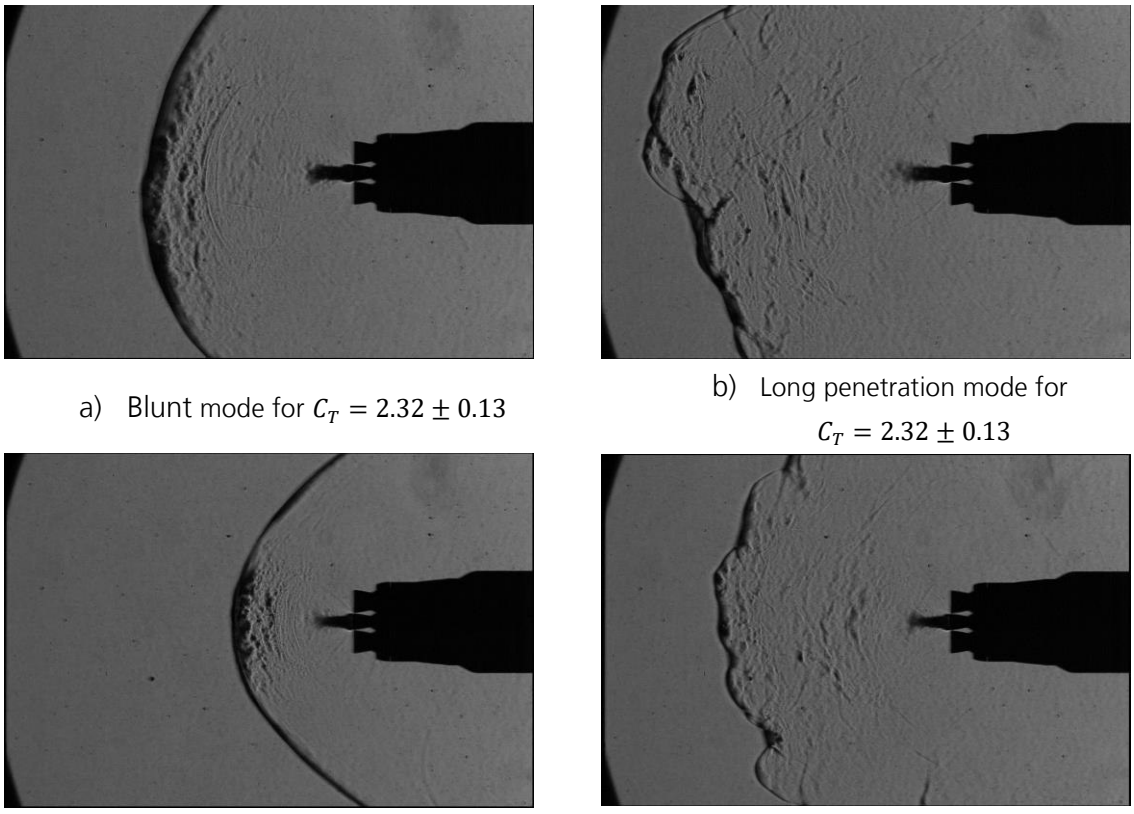

a) Blunt mode for $C_T = 2.32 \pm 0.13$

b) Long penetration mode for $C_T = 2.32 \pm 0.13$

c) Blunt mode for $C_T = 1.40 \pm 0.08$

d) Long penetration mode for $C_T = 1.40 \pm 0.08$

Fig. 81: Three-engine configuration observed perpendicular to the α-plane for $M_\infty = 5.29$, $T_{CC} = 300K, p_0 = 4\ bar, T_0 = 450\ K$

To quantify these observations, the axial and radial distance of the triple point and the axial distance of the Mach disc location and bow shock location were measured from the nozzle exit and were tracked throughout two tests where the thrust coefficient was successively increased for the single-engine and the three-engines cases. The bow shock location for the three-engines case was extracted from the configuration of active engines perpendicular to the α-plane. For this configuration the flow structure appears symmetrically for the blunt modes, and hence, the bow shock location is more clearly defined (see Fig. 81a and c). For the long penetration mode, the distance at the symmetry axis was used. The flow features plotted versus the square root of the thrust coefficient are depicted in Fig. 82, where the single-engine case is represented by the orange lines and the pink line, and the three-engines case is represented by the blue line.

For the single-engine case, the plotted results show the blunt mode, which was found for $C_T \gtrsim 0.25$. In [45] it was found that the transition of the long penetration mode to the blunt mode appears near $C_T = 1.0$ and that it depended on the ratio of the nozzle exit pressure (p_e) and the freestream pressure (p_∞). Korzun and Cassel [30] linked the transition to the ratio of the nozzle exit pressure to the total pressure in the stagnation point. Daso et al. [68] postulated that the transition occurs due to a change of the exhaust jet transitioning from being overexpanded to fully expanded, to underexpanded. Gutsche et al. [65] stated that there might not be a universal C_T value for the determination of the transition. However, what can be stated generally, is that the transition commonly occurs at low thrust coefficients [30, 45, 65]. This correlation seems to be valid throughout the literature, even though it cannot be fixed to one specific value. In [45] the transition was observed at lower thrust coefficients for higher freestream Mach numbers. As the Mach numbers tested in this test series were relatively high, this might explain the comparably small thrust coefficient at which the transition occurred (for comparison, Jarvinen and Adams [45] observed a transition at $C_T = 1$ for $M_\infty = 2.0$ and at $C_T = 2$ at $M_\infty = 1.5$). This underpins the statement made above in this section, that the long penetration mode is not decisive for the single-engine case, as the thrust coefficients of interest for the reentry burn of a returning first stage are much larger than unity. In the case of RETALT1 they are 11.1 and 76.8 for Mach 5.3 and Mach 7.0, respectively.
It was observed and stated by Jarvinen and Adams [45] that the flow features of the supersonic retro propulsion flow in the blunt mode vary with the square root of the thrust coefficient. For the detailed reasoning for this statement Jarvinen and Adams referred to [99]. The analytical procedure applied by Jarvinen and Adams is closely linked to the analysis performed earlier by Finley [44]. Finley based his analysis on a correlation by Love et al. [104] which states a linear dependency of the flow features of a jet exhausting into still air with the square root of the exit pressure ratio at the nozzle exit with the ambient air. In the case of the blunt mode retro propulsion flow field, this ratio is p_e/p_d (the EPR) were p_d is the dead air pressure in the recirculation zone (see section 2.5). Jarvinen and Adams, however, use the correlation by Charwat [105] to model the jet boundary, which suggests a dependency of the radial extent of the jet on the pressure ratio of $(p_e/p_d)^{\frac{1-\gamma}{4\gamma}}$. In Fig. 82 a linear fit of the different measured distances with the square root of the thrust coefficients was added (dashed lines) as well as a fit with $C_T^{\frac{1-\gamma}{4\gamma}}$ (dotted lines). It can be observed that for the single-engine case all flow features follow the linear trend of the thrust coefficient well. A scaling of the features with $C_T^{\frac{1-\gamma}{4\gamma}}$ seems to fit better for $\sqrt{C_T} < 0.7$. However, the general trend is better captured by the linear correlation. For the thrust coefficients studied here, the differences between both correlations are small.
For the three-engines case the bow shock distance is plotted in blue in Fig. 82. Two dashed lines indicate the linear fit for the blunt mode and the long penetration mode for this configuration. The linear trend with the square root of the thrust coefficient can be observed for both modes. In contrast to the single-engine case, the bow shock distance is constantly switching between the blunt mode and the long penetration mode along the complete range of thrust coefficients tested. The trend of the blunt mode follows the bow shock distance of the blunt mode of the single-engine

case closely, while the slope for the increase of the bow shock distance for the long penetration mode is steeper.

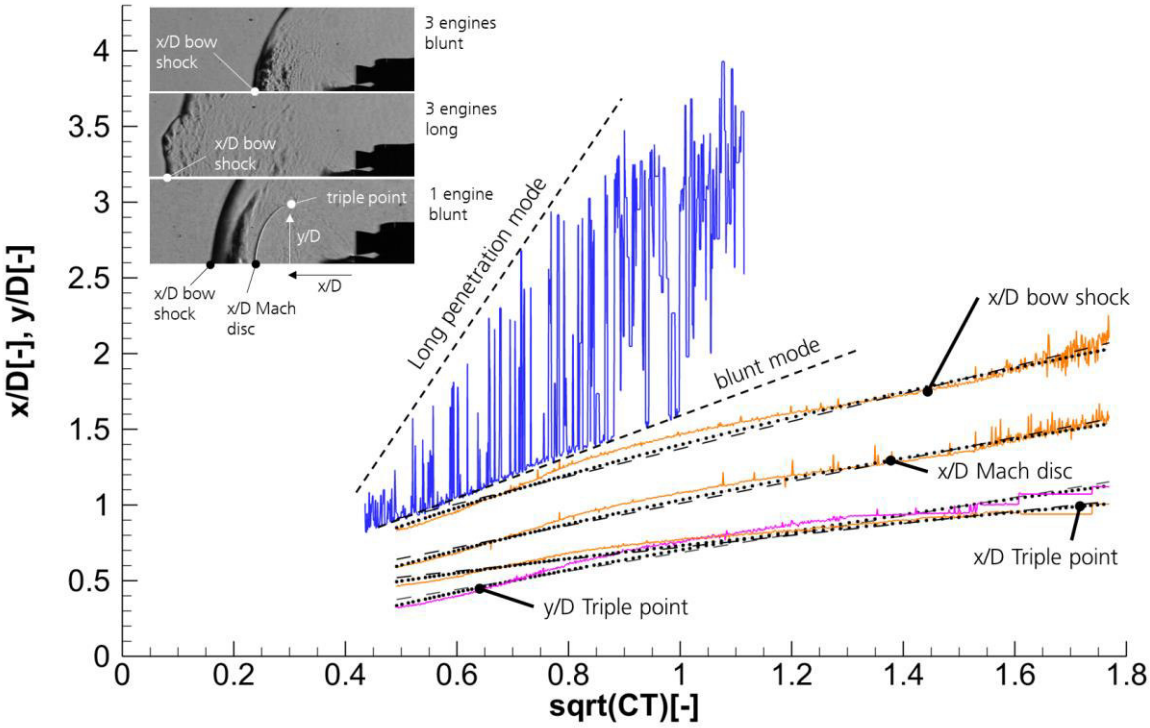

Fig. 82: Measured distances of single-engine and three-engines cases for varying thrust coefficients (orange/pink: single-engine case, blue: three-engines case, dashed: linear fit, dotted: $C_T^{\frac{1-\gamma}{4\gamma}}$ fit); $(M_\infty = 5.29, T_{CC} = 300K, p_0 = 4\ bar, T_0 = 450K)$

5.2.2. Comparison of Cold and Heated Jets

Computations in [65] showed that condensation occurs in larger regions in the highly underexpanded plume of the retro propulsion jet. In experiments this was locally visualized using a laser beam, crossing the jet flow region. Furthermore, Bykerk et al. [106] recently implemented a condensation model in the DLR flow solver TAU and assessed the influence of the condensation on the flow field and the surface pressures on a single-engine retro propulsion configuration in blunt mode. It was found that the condensation slightly alters the flow field. As expected, the condensation leads to higher temperatures in the plume and therefore to lower Mach numbers. The overall flow filed was, however, not found to be greatly affected. The surface pressures were up to 5% lower, if condensation was considered. Therefore, to assess the influence of the condensation on the flow field, in this section, the baseline test cases with cold air are compared to test cases in which the supply air was heated, in order to mitigate condensation.

First, it was investigated whether the condensation could be visualized in a larger region of the plume to prove that it is not a local phenomenon. Therefore, as described in section 4.2.2.1, five laser beams were stretched out in the plume area. This revealed that the condensation is not local but appears in larger parts of the plume area. This is shown in Fig. 83 for the single-engine case

(Fig. 83a) and the three-engines case (Fig. 83b) for the baseline flow condition no. 1 ($M_\infty = 5.3$, $p_0 = 4\ \text{bar}, T_0 = 450\ \text{K}$) and a total temperature of the jet of $T_{CC} \approx 300\ \text{K}$. Due to the condensation, the laser lines in the α-plane are clearly visible, they are highlighted with the dashed circle in Fig. 83. The effect is the largest for the larger thrust coefficients shown here, but it was also observed for lower values of the thrust coefficient. To mitigate the condensation, the stagnation temperature in the model was raised to 600 K. For these temperatures, no condensation was observed. This is shown for a single-engine case with a thrust coefficient of 6 in Fig. 83c.

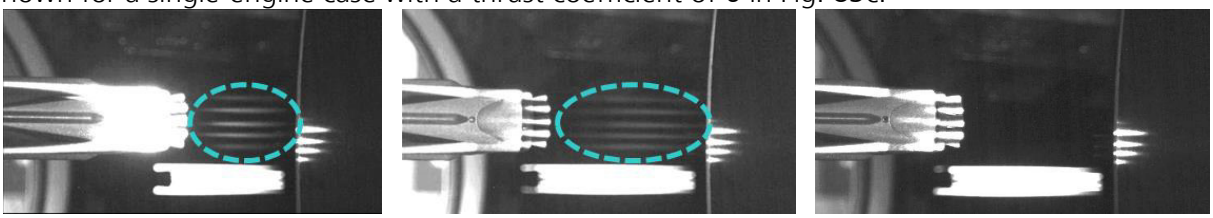

a) Single-engine case for $C_T \approx 7$, $T_{CC} = 300\ \text{K}$

b) Three-engines case for $C_T \approx 16$, $T_{CC} = 300\ \text{K}$; engine plane perpendicular to α-plane

c) Single-engine case for $C_T \approx 6$, $T_{CC} = 600\ \text{K}$; no condensation observable

Fig. 83: Visualization of condensation in the retro plume, highlighted with dashed circle ($M_\infty = 5.29,\ p_0 = 4\ bar, T_0 = 450\ K$)

In Fig. 84 the Schlieren images of the single-engine case are compared for the cold gas case (303 K) and the heated air case (589 K). The knife edge was positioned vertically, perpendicular to the flow, in those experiments. Due to the heating of the supply air, the density in the heated case is lower, and therefore the Schlieren images have a slightly different appearance. However, it is apparent that the flow features are very similar. Due to a slight difference in the thrust coefficients, the locations of the Mach disc, the contact surface and the bow shock are slightly offset.

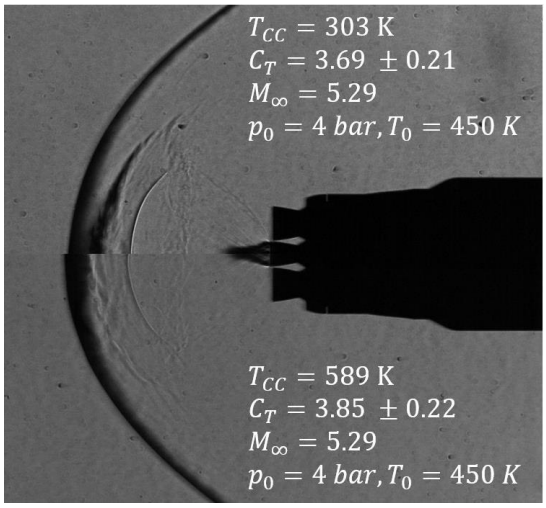

Fig. 84: Comparison of cold air (upper part) vs. heated air (lower part) in retro plume – single-engine case

As in section 5.2.1, the flow properties were calculated analytically for specific points on the centerline for the cold and the heated air case, which can be seen in Fig. 85. For comparison the free stream conditions and the jet conditions were kept constant and only the total temperature in the jet was varied.

Assuming a constant heat capacity ratio, the ratios of the density and the temperatures over the shocks and due to isentropic acceleration or decelerations only depend on the Mach number. The Mach number on the centerline is equal in both cases, hence also the ratios between the points, 1, 2 and 0,2 on the free stream side, and 1j, 2j and 0,2j on the jet side equal. However, due to the higher temperatures in the heated air case, the same ratios lead to higher gradients in the temperature along the centerline for the same Mach numbers. In turn, lower densities lead to lower density gradients. This is why in Fig. 84 the Mach disc is less clearly visible in the heated air case. Furthermore, it can be noted, that the gradient in the contact point (between 0,2 and 0,2j) is positive in the cold case, leading to a dark appearance of the contact surface, while it is negative in the heated air case, which leads to a white appearance. Hence, the flow field appearance changes, due to the heating. However, the Mach number, the pressures and the momentum flux on the centerline are not affected by the temperature increase as can be seen in Fig. 85. As these quantities are the main drivers for the similarity of the flow field, the main flow field features (bow shock stand-off distance, Mach disc location, location of the triple point) are not changed by increasing the temperature of the air.
In Fig. 86 the comparison between the cold and the heated case is shown for the three-engines case for the long penetration mode. Also for this case the heating seems to have a minor influence on the flow field structure. For the heated case the blunt mode can be observed for the three-engines case too (see Fig. 87).

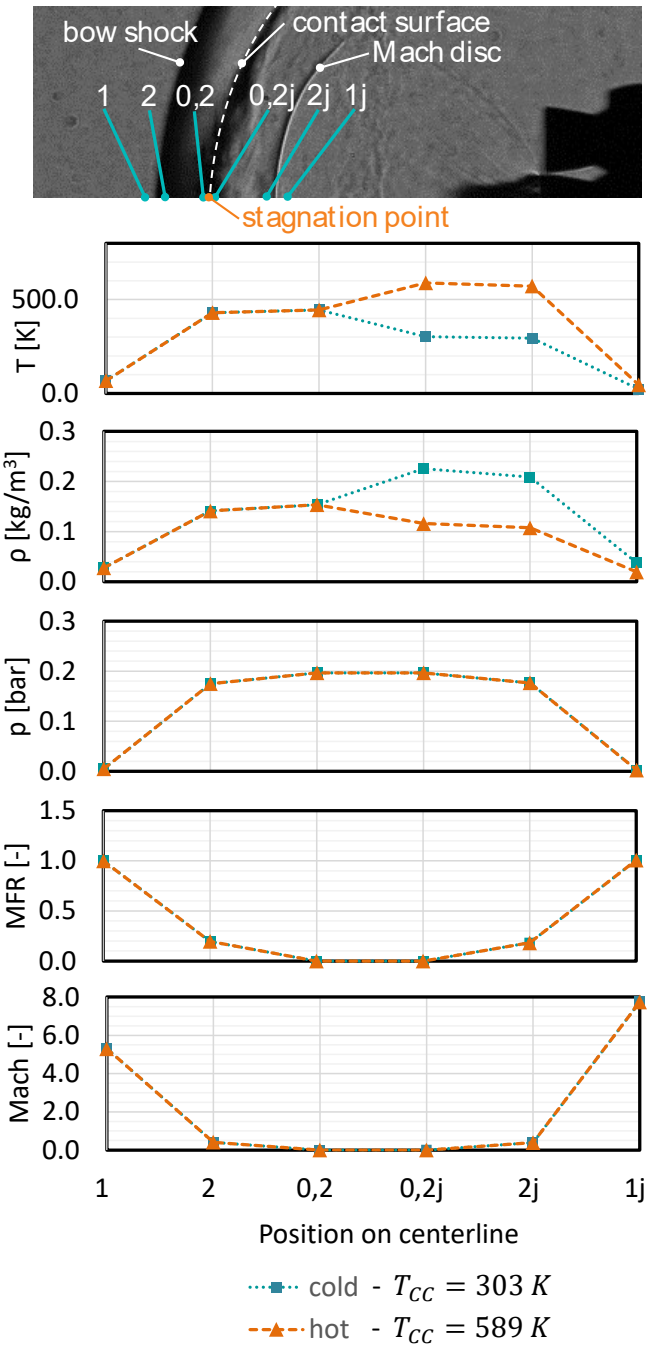

Fig. 85: Analytically calculated flow properties at selected points on the centerline for the single-engine case for cold and heated air ($C_T = 3.78$, $M_\infty = 5.3$, $p_0 = 4\ bar$, $T_0 = 445\ K$, $p_{CC} = 20\ bar$)

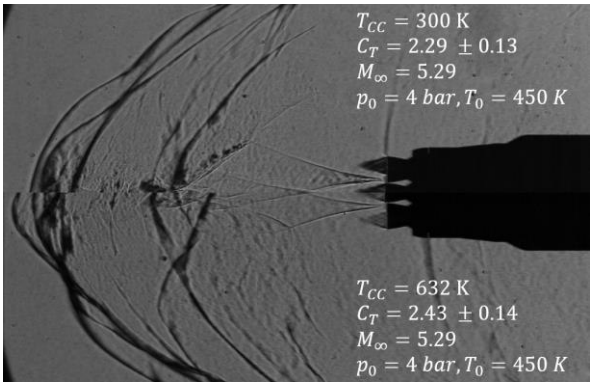

Fig. 86: Comparison of cold air (upper part) vs. heated air (lower part) in retro plume – three-engines case

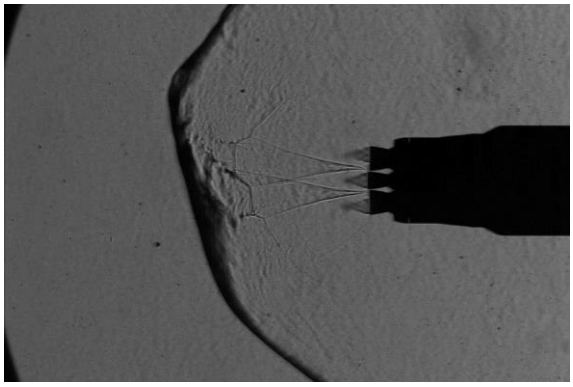

Fig. 87: Blunt mode for the three-engines case with heated air ($T_{CC} = 632$ K, $C_T = 2.43 \pm 0.14, M_\infty = 5.29, p_0 = 4\ bar,\ T_0 = 450\ K$)

As for the cold gas case, the build-up of vortex rings was observed in the single-engine heated air case. It seems that these vortices are larger than the ones that occurred for the cold case. An example is shown in Fig. 88.

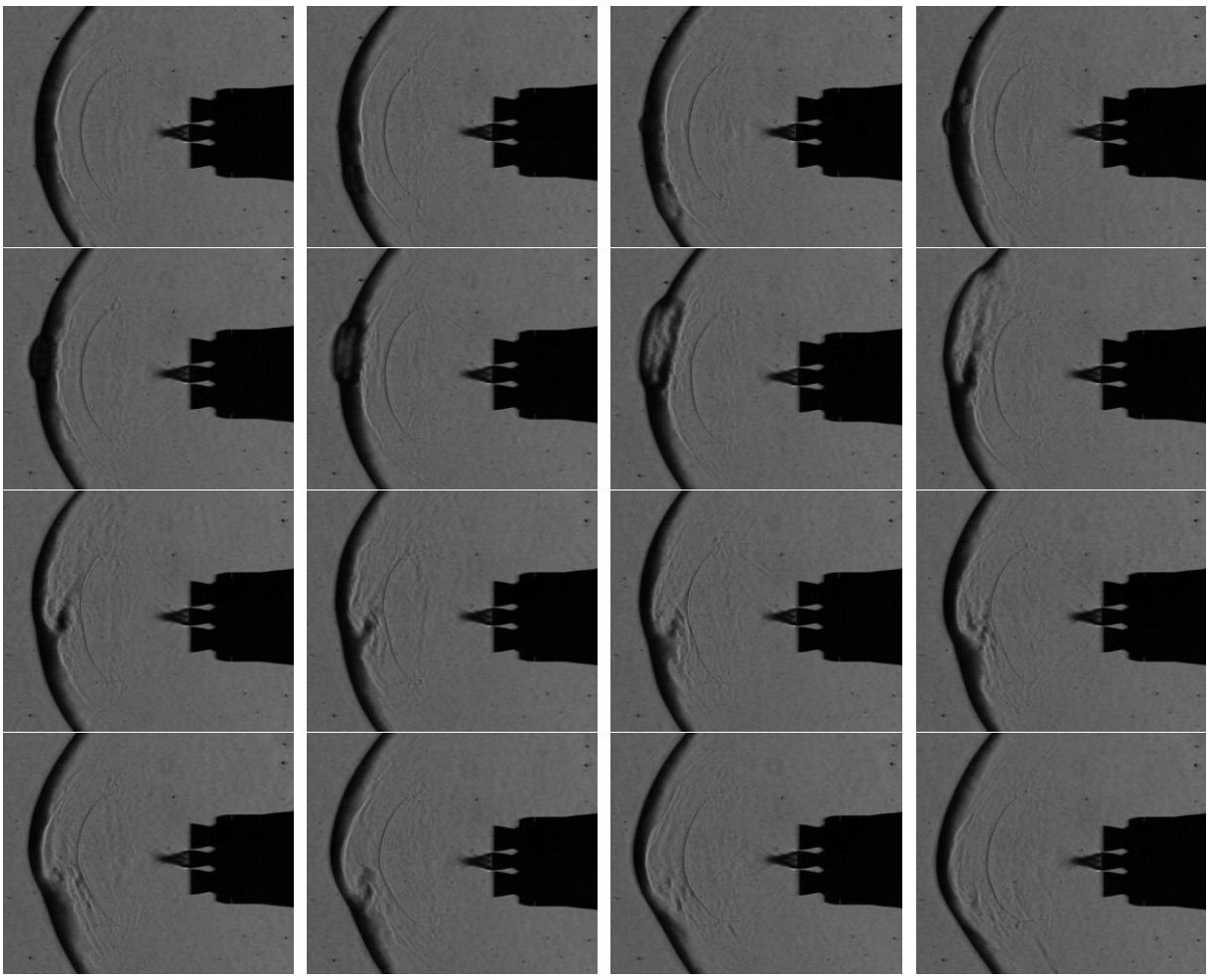

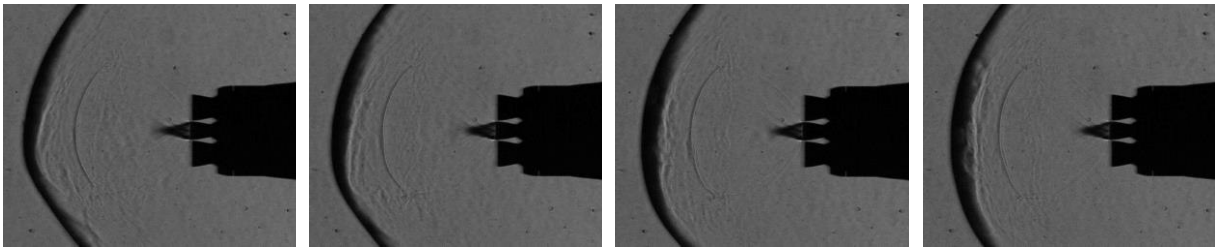

Fig. 88: Vortex ring formation in heated single-engine case ($T_{CC} = 589\,K,\ C_T = 3.85\ \pm 0.22$, $M_\infty = 5.29$ $p_0 = 4\,bar$, $T_0 = 450\,K$), with a timestep of $50\mu s$ (frame rate of 20 kHz)

5.2.3. Discussion of Pressure Measurements

In this section the pressure measurements performed in the wind tunnel tests are discussed. The pressure sensors were sampled at 50 kHz. For the static evaluation performed in the following they were resampled to 1000 Hz and then filtered using a low-pass filter with a cut-off frequency of 4 Hz.

5.2.3.1. Single-Engine Case

In Fig. 89 the pressure coefficients are shown for the single-engine case and the baseline flow condition ($M_\infty = 5.29, p_0 = 4\ \mathrm{bar},\ T_0 = 450\ \mathrm{K}$). The coefficients are plotted over the square root of the thrust coefficient. To allow for a clearer plot, the error bars are only shown in the top for the larger pressure coefficients and at the bottom for the lower pressure coefficients. It can be observed, as expected from literature [45, 65], that the pressure coefficients do not follow a linear trend with the square root of the thrust coefficient. Hence, in the following, the pressure coefficients are plotted over the thrust coefficient. The pressure coefficients for the same conditions as in Fig. 89, but plotted against the thrust coefficient, are shown in Fig. 90.
As expected, the pressure coefficients generally tend towards zero for larger thrust coefficients [44, 45]. The pressures in plane 1, which are the sensors that are positioned the farthest downstream along the cylindrical body, are close to ambient pressure. In sections 5.1.1 and 5.1.2 it was shown, that pressure coefficients in this location of the configuration are expected to be close to zero in the aerodynamic phase where the engines are not active. Here it seems that this assumption also holds for the retro propulsion phase. The pressure sensors in plane 2 (sensors 21, 22, 23 and 24) are located directly behind the folded landing legs. These pressure coefficients slightly rise with increasing thrust coefficient. The pressure coefficients at the base area of the configuration in plane 3 also generally tend towards very small values with increasing thrust coefficients. The pressure sensors located closer to the center of the base (sensors 311 and 331), see higher pressure coefficients if the engine is not active, as they are close to the stagnation region. However, the pressure coefficients for these sensors decrease more rapidly with increasing thrust coefficient, as the shielding effect of the exhaust plume is the strongest for these sensors and, as they are placed in its recirculation region. The pressure coefficient in the wake of the configuration (denoted CpSTAGE in the figure) is relatively independent of the thrust coefficient. In the following, the conditions described in Fig. 90 are used as baseline for the discussion of parameter variations.

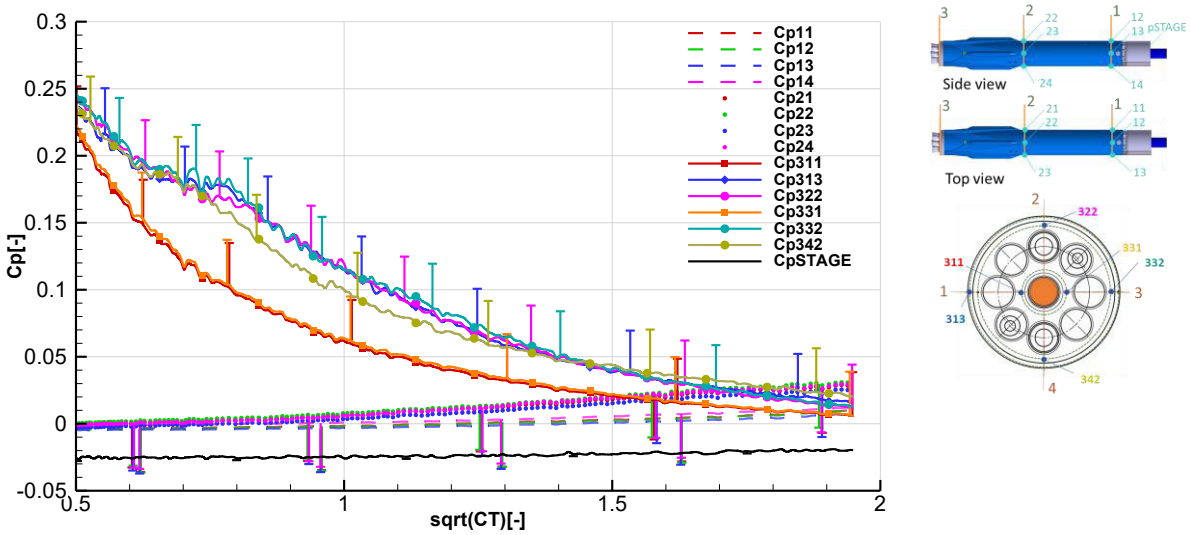

Fig. 89: Pressure coefficients C_p over square root of the thrust coefficient for the single-engine case ($M_\infty = 5.29$, $p_0 = 4\ bar$, $T_0 = 450\ K$)

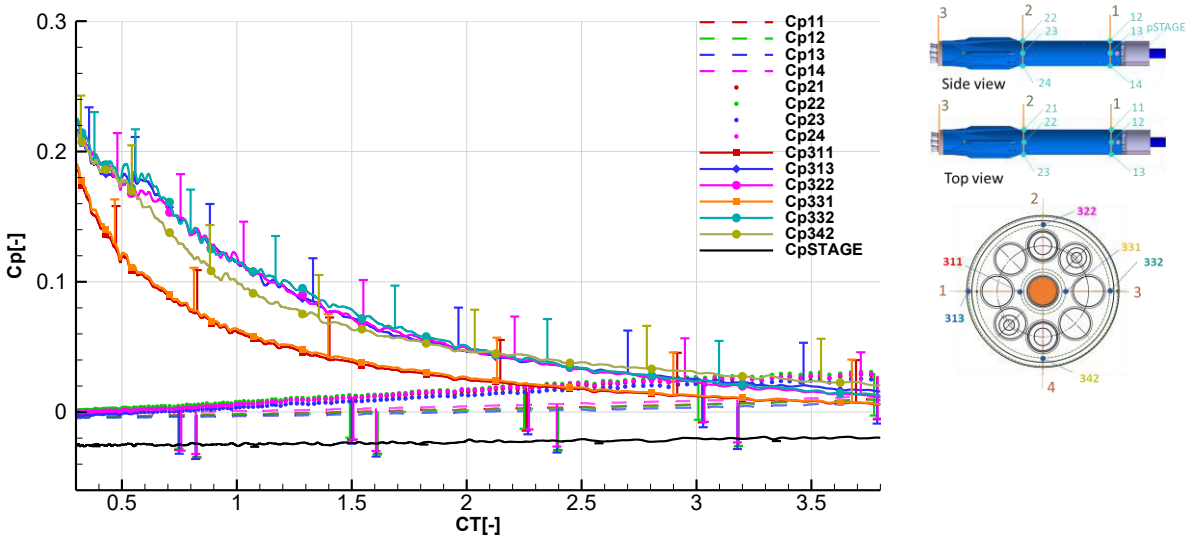

Fig. 90: Pressure coefficients C_p over thrust coefficient for the single-engine case ($M_\infty = 5.29$, $p_0 = 4\ bar$, $T_0 = 450\ K$)

Fig. 91a shows the influence of a variation of the freestream Mach number on the pressure coefficients. The Mach number was increased to 7 but the Reynolds number was kept at the baseline value of 2.36E+05. The thin lines represent the baseline configuration while the variation is shown by the thick lines. It can be observed that the values have the same trends. Especially in plane 1 and 2 the pressure coefficients are nearly equal. The pressure in the base is offset from the baseline case for higher thrust coefficients. Gutsche et al. [65] proposed to use the total pressure behind the bow-shock, $p_{0,2}$, for the scaling of the pressures. It was reasoned that this would lead to better similarity close to the engine, which would relate well with the work by Korzun and Cassel [30], suggesting the ratio of exit pressure to total pressure as scaling parameter for the expansion conditions. They reason, that the surrounding pressure at the nozzle exit is not the ambient pressure

in the free stream, but the dead air pressure in the recirculation region [30, 65]. Furthermore, Gutsche et al. [65] showed that the Exit Pressure Ratio (EPR) of the nozzle exit pressure to the dead air pressure is independent of the free stream Mach number, while the Ambient Pressure Ratio (APR) of the exit pressure to the free stream static pressure is strongly depending on the Mach number. This is why, the APR is not the optimal scaling parameter for the pressures close to the nozzle exit. The post-shock stagnation pressure $p_{0,2}$, however, connects the two flow fields as it equals the total pressure downstream of the Mach disk, $p_{0,2j}$ (see section 5.2.1). This makes it a good reference pressure for both flow fields. Furthermore, for high Mach numbers, the post-shock stagnation pressure can be considered independent of the free stream Mach number, and, in contrast to the dead air pressure, it can be computed analytically [65]. Fig. 91b shows the pressures normalized with $p_{0,2}$. Indeed, it can be observed that for the pressures in the base area close to the plume (plane 3), a better similarity for different Mach numbers is achieved with the normalization with $p_{0,2}$. This also holds for the pressure in the wake area pSTAGE. For the pressures along the cylindrical body of the configuration (plane 1 and plane 2), the conventional pressure coefficients reaches a better similarity. In contrast to the normalization with $p_{0,2}$, the definition of the conventional pressure coefficient has the additional benefit that it can be well related to the force coefficient generated by the pressure. For example, if the pressure in one point on the base is applied to the complete reference area and if the back pressure in the wake of the vehicle is assumed to be the static pressure of the free stream, p_∞, the pressure coefficient corresponds to the axial force coefficient:

$$C_A = \frac{F_A}{q_\infty A_{ref}} \approx \frac{(p - p_\infty)A_B}{q_\infty A_B} = \frac{p - p_\infty}{q_\infty} = C_p \qquad (54)$$

where F_A is the axial force.

Hence, the conventional pressure coefficient gives a better intuition for the contribution of the pressures to the force coefficients. In the design of vehicles applying retro propulsion, both similarities could be combined. For the interpolation of pressure between Mach numbers or for the extrapolation to higher Mach numbers, the similarity with $p_{0,2}$ could be applied. Then the pressures could be expressed in the form of C_p for better interpretability.

In Fig. 92 the pressure coefficients of a variation in Reynolds number are shown. It can be observed that the measured pressure coefficients are independent of the two Reynolds numbers tested. The Reynolds number, hence, seems not to be the main driver for the retro propulsion flows. However, it should be remarked that for the higher Reynolds number, the fluctuations in the pressure coefficients are lower. Due to the higher measured overall pressures, the uncertainties in the pressure coefficients decrease.

The influence of a variation of the angle of attack is shown in Fig. 93. As expected, the pressure coefficient on the base on the windward side (sensor 342, see Fig. 34) is increased as it is moved further in the wind and the shielding of the plume is less efficient. The pressure coefficient on the leeward side (sensor 322), in turn, is decreased. The pressure coefficients close to the engine (sensors 331 and 311) are not affected by the angle of attack, and the pressure coefficients of sensors 313 and 332, which are on the outer rings of the sensor positions but perpendicular to the

alpha plane, are only affected by the angle of attack when the thrust coefficient is very low ($C_T < 0.6$). For larger thrust coefficients they equal the pressure coefficients at 0° angle of attack. In plane 2, where the pressure sensors are positioned behind the landing legs, the pressure coefficient on the windward side increases (sensor 22), the pressure coefficients perpendicular to the α-plane (sensors 21 and 23) decrease, but the pressure coefficient on the leeward side remains close to zero as for the case with 0° angle of attack. In plane 1 far downstream, the pressure coefficients on the windward side are increased by the angle of attack, the ones on the leeward side are decreased, and the pressure coefficients on the plane perpendicular to the α-plane (11 and 13) follow the trend of the pressure coefficients on the leeward side. This can be explained by the fact that these sensors are less influenced by the plume and hence follow a pressure trend similar to the trend in the aerodynamic phase with no active engines (see section 5.1). However, it can be observed that for the sensors on the windward side, the pressure decreases notably with increasing thrust coefficient, showing an effect of the plume shielding, while the pressures on leeward side and the perpendicular pressures are relatively independent of the thrust coefficient.

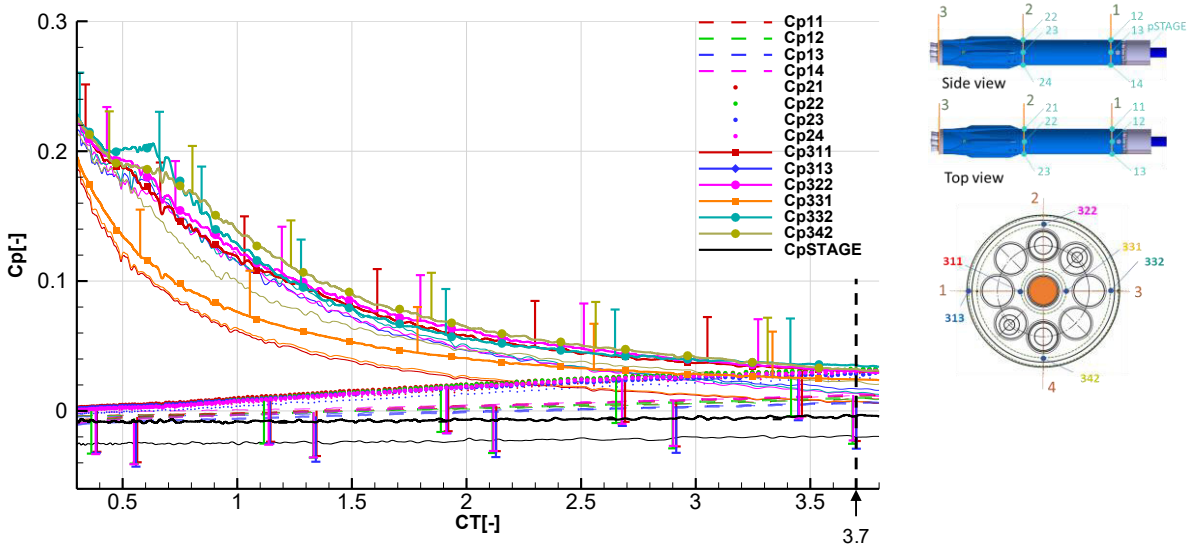

a) Pressure coefficients

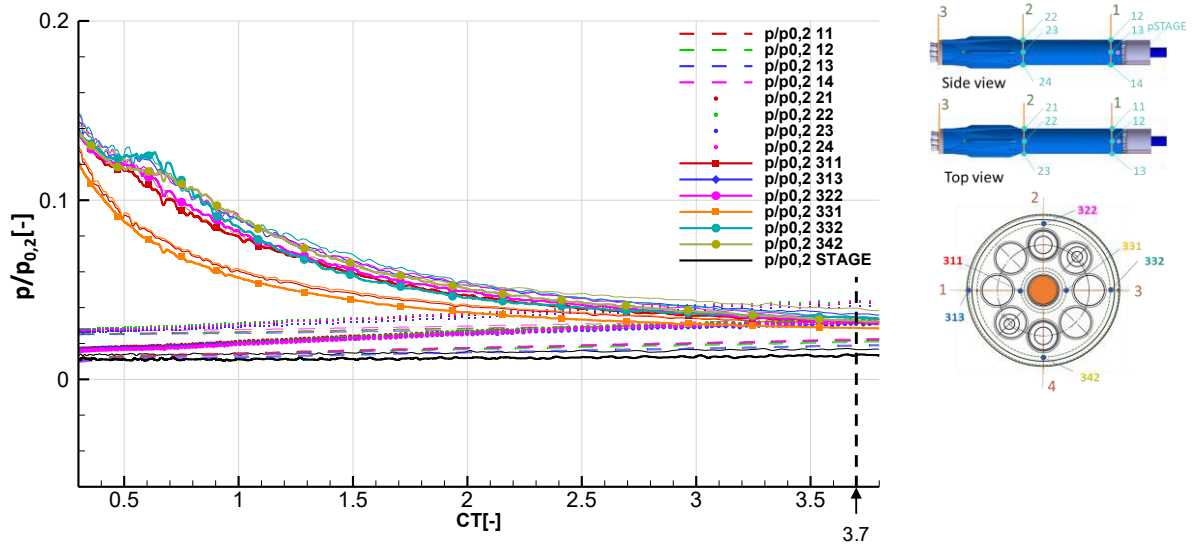

b) Normalization with total pressure in the stagnation point

Fig. 91: Mach number variation for the single-engine case for $M_\infty = 5.29$ (thin lines) and $M_\infty = 7.04$ (thick lines) ($M_\infty = 5.29$, $p_0 = 4\ bar$, $T_0 = 450\ K$ and $M_\infty = 7.04$, $p_0 = 12.73\ bar$, $T_0 = 610\ K$)

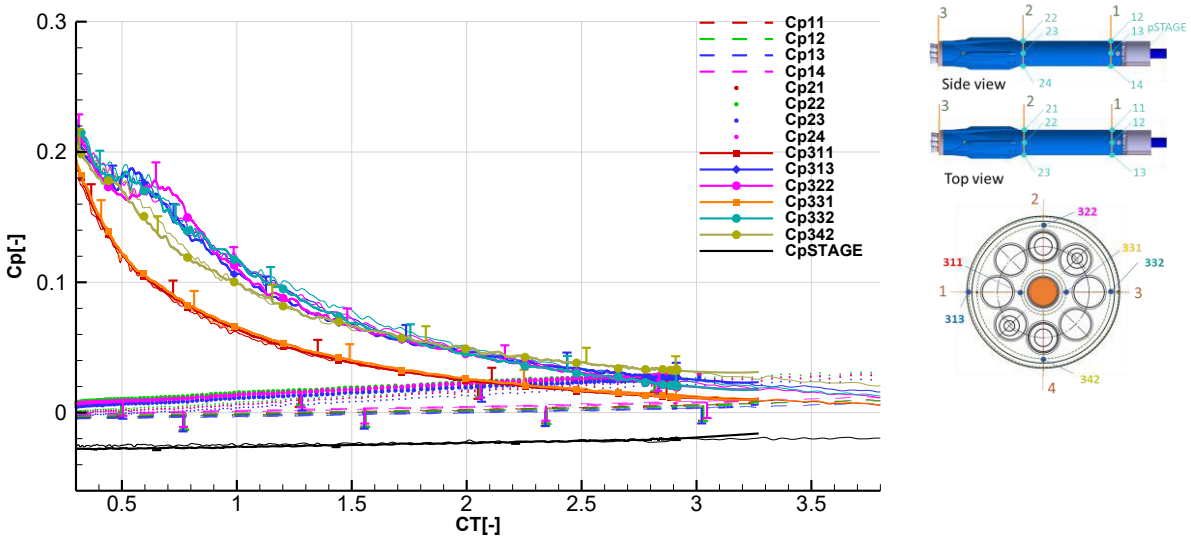

Fig. 92: Reynolds number variation for the single-engine case with $Re_\infty = 2.36E + 05$ (thin lines) and $Re_\infty = 7.07E + 05$ (thick lines)
($M_\infty = 5.29$, $p_0 = 4\ bar$, $T_0 = 450\ K$ and $M_\infty = 5.32$, $p_0 = 12\ bar$, $T_0 = 450\ K$)

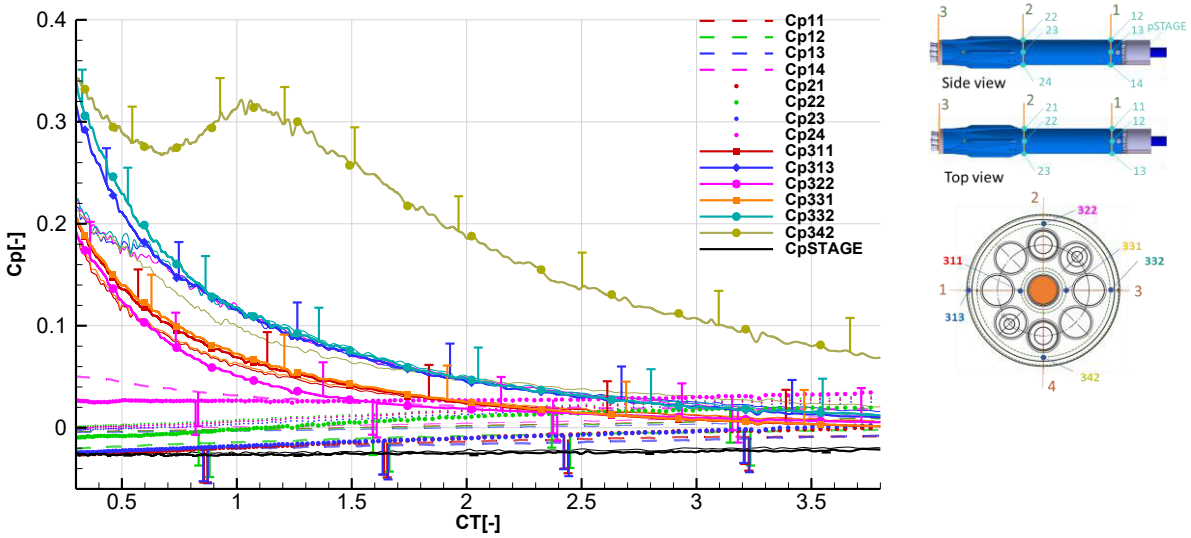

Fig. 93: Angle of attack variation for the single-engine case, for $\alpha = 0°$ (thin lines) and $\alpha = 10°$ (thick lines) ($M_\infty = 5.29$, $p_0 = 4$ bar, $T_0 = 450$ K)

5.2.3.2. Three-Engines Case

In the following, the results of the pressure measurements for the three-engines configuration are discussed. Fig. 94 shows a comparison of the pressure coefficients of the single-engine and three-engines configurations for the baseline freestream condition. They are compared for the total thrust coefficient, which corresponds to three times the single-engine thrust coefficient for the three-engines case. The pressure coefficients in plane 1 and 2 for the three-engines case are very similar to the single-engine case, showing that the total thrust coefficient is an adequate scaling parameter to assess the influence of retro propulsion flows even between different engine configurations,

especially for the pressures farther downstream of the plume. For the three-engines case the engines are active in the α-plane. In plane 3, the pressure coefficients close to the center engine are the lowest (sensors 311 and 331), followed by the pressure coefficients on the outer ring but in the plane of the active engines (322 and 342), and finally the pressure coefficients with the largest distance to the plume (sensors 313 and 332). While the sensors close to the plumes experience similar pressure coefficients as in the single-engine case, the ones with the largest distance to the plumes (sensors 313 and 332) experience higher pressure coefficients as in the single-engine case. The reason for this effect is, that the total thrust coefficient describes the overall plume extension well. However, as the engines are distributed in a row, for the pressures on the base area, the influence of the single plumes of each engine play an important role. The sensors furthest away from the engines are less shielded by the plume of the three engines, than they are by the equivalent plume of one engine. However, if the single-engine thrust coefficient is taken for the scaling, it is apparent that also for these locations the pressure coefficients are significantly smaller than in the single-engine case. Hence, if the single-engine thrust coefficient is taking for the scaling, the effect of the additional plumes, leads to smaller pressure coefficients on the base in comparison to just one active engine.

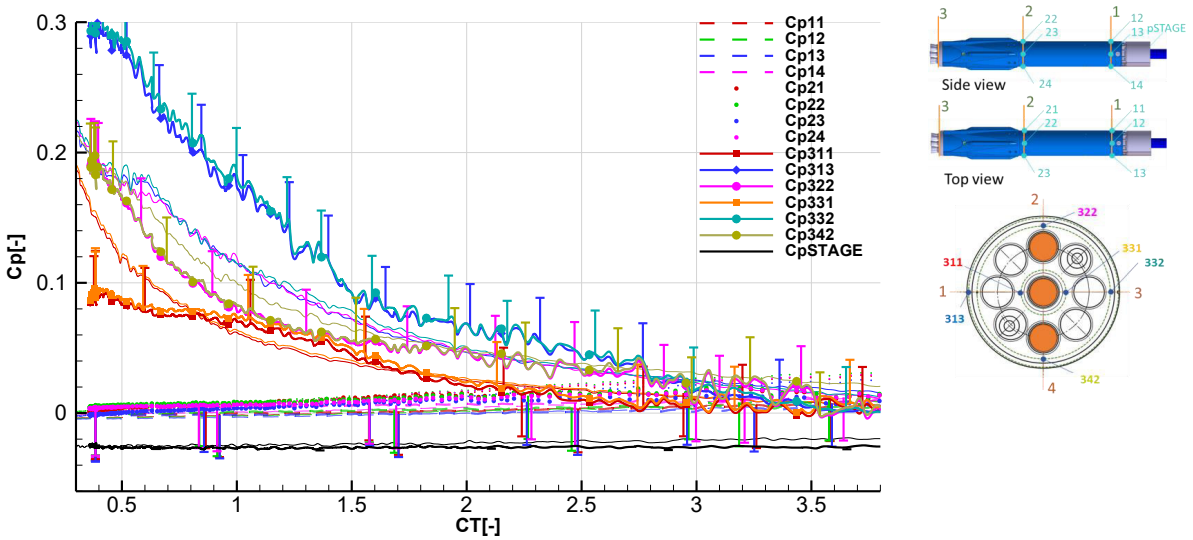

Fig. 94: Comparison of the single-engine case (thin lines) and three-engines case (thick lines) active in the α-plane ($M_\infty = 5.29$, $p_0 = 4$ bar, $T_0 = 450$ K)

As for the single-engine case, a Mach number variation was performed in Fig. 95. Fig. 95a shows the pressure coefficients, Fig. 95b shows the scaling with $p_{0,2}$. The same trend as for the single-engine case can be observed, which means that in the base area and in the wake area a better similarity is achieved with $p_{0,2}$, while the conventional pressure coefficient reaches better similarities at the cylindrical body of the launcher.

Additionally, a Reynolds number variation (Fig. 96), and a variation of the angle of attack (Fig. 97, Fig. 98) was performed. Note that the scale for the thrust coefficient was extended to larger thrust coefficients as larger total thrust coefficients were measured for the three-engines cases. The Mach number variation shows that mainly the pressure coefficients close to the central engine (sensors

311 and 331) are offset from the baseline case. For all other pressure locations, the Mach number variation has little influence. For higher thrust coefficients, however, the offset becomes small. The Reynolds number variation (Fig. 96) shows that as for the single-engine case, the Reynolds number is not a driving similarity parameter. The influence on the static pressures seems to be negligible. The angle of attack variation (Fig. 97) shows that due to the larger plume building up for the three-engines case, the influence of the angle of attack on the surface pressures is smaller than for the single-engine case. In general, the pressures on the windward side are higher (sensors 331, 21, 11) while the pressures on the leeward side are lower (sensors 322, 24, 14). For higher thrust coefficients, however, the pressure coefficients at all pressure locations vanish. Higher pressures only persist at sensors directly in the wind and far enough downstream of the plume (sensors 24, 14). It should be noted, that these pressures seem to be independent of the thrust coefficient, meaning that also at high thrust coefficients the influence of the angle of attack on the normal force coefficient and on the moment coefficient is not negligible for this configuration.
In Fig. 98 the configuration was rotated by 90° such that the active engines were positioned in the plane perpendicular to the α-plane (note that also the sensor locations are rotated by 90°). It is compared to the case shown in Fig. 97. Generally, the measured pressures still follow the same trend as the baseline configuration. However, it is noticeable that the pressure coefficient at 332, which is in this case the most windward position, is considerably higher and only vanishes for thrust coefficients larger than 4. This is comparable to the single-engine case (see Fig. 93). Hence, if the engines are active in the α-plane, they provide a stronger shielding effect for the pressures on the base plane than if they are active in the plane perpendicular to the α-plane. However, the pressures in plane 1 and 2 are smaller for this configuration. Finally, a variation of the location of the exit plane of the central engine was performed (Fig. 100). In the reference configuration the nozzle exit plane of the central engine is offset by 150 mm (in flight scale) with respect to the nozzle exit planes of the outer engines, for this variation it was moved back into the same plane (see Fig. 99). This change in configuration only seems to have an influence on the pressures very close to the center engine (sensors 311 and 331). They are higher for lower thrust coefficients. However, for thrust coefficients larger than 1.5 the pressures are nearly equal.
To conclude this section, the following observations and statements can be made:

1) For high thrust coefficients the pressure coefficients along the configuration with retro propulsion generally tend to very small values.
2) The total thrust coefficient is suitable as a similarity parameter for the comparison of configurations with different engine configurations.
3) The thrust coefficient is the dominating similarity parameter. The Mach number is of subordinate importance, and the Reynolds number effect, as far as static pressure evaluations are considered, can probably be neglected.
4) The pressures in the forward-facing base and in the wake scale well with the total pressure behind the normal portion of the bow shock $p_{0,2}$, the pressures on the cylindrical body scale well with the conventional pressure coefficient.

5) Due to the shielding effect of the plume, the angle of attack is of less importance, however, at locations far enough downstream of the plume its influence seems to not be fully negligible.
6) The relative position of the exit plane of the center engine in relation to the outer engines has only minor effects on the pressures on the base of the vehicle.

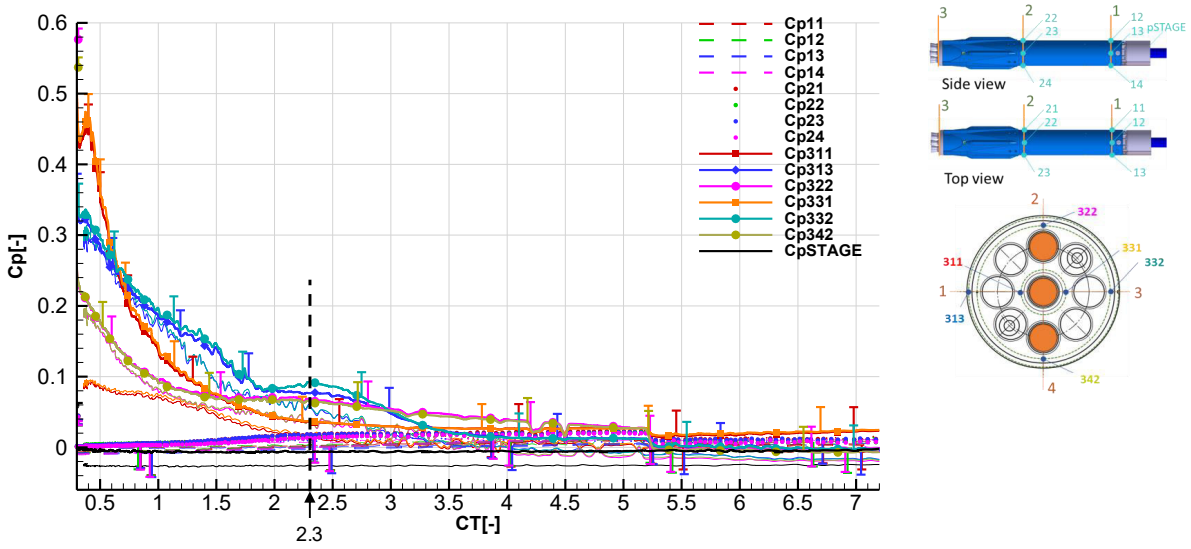

a) Pressure coefficients

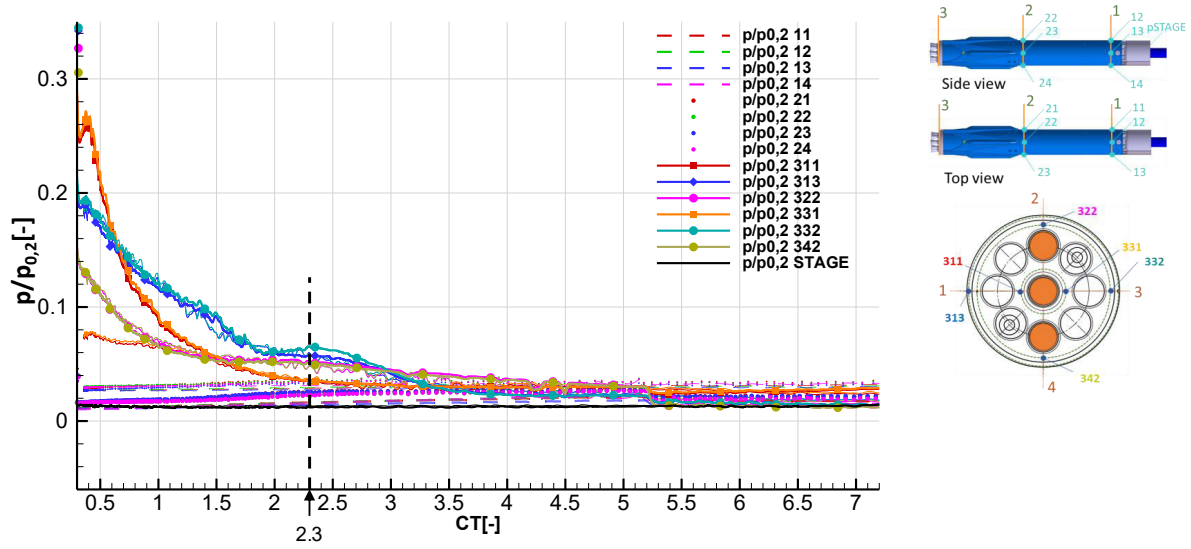

b) Normalization with total pressure in the stagnation point

Fig. 95: Mach number variation for the three-engines case for $M_\infty = 5.29$ (thin lines) and $M_\infty = 7.04$ (tick lines) ($M_\infty = 5.29$, $p_0 = 4$ bar, $T_0 = 450$ K and $M_\infty = 7.04$, $p_0 = 12.73$ bar, $T_0 = 610$ K, engine plane: α-plane)

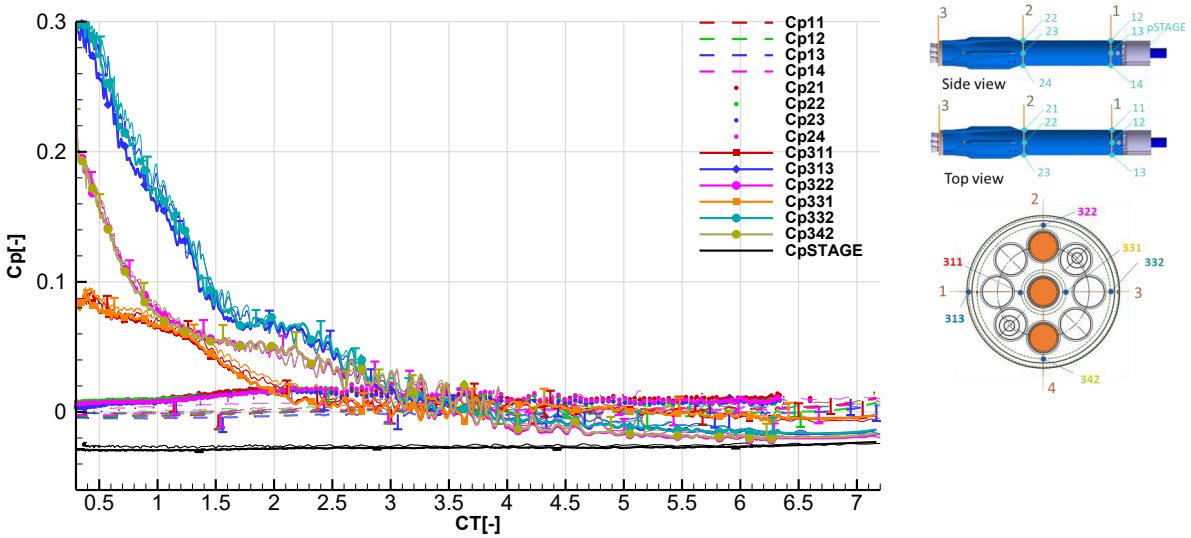

Fig. 96: Reynolds number variation for the three-engines case $Re_\infty = 2.36E + 05$ (thin lines) and $Re_\infty = 7.07E + 05$ (thick lines)
($M_\infty = 5.29$, $p_0 = 4\ bar$, $T_0 = 450\ K$ and $M_\infty = 5.32$, $p_0 = 12\ bar$, $T_0 = 450\ K$, engine plane: α-plane)

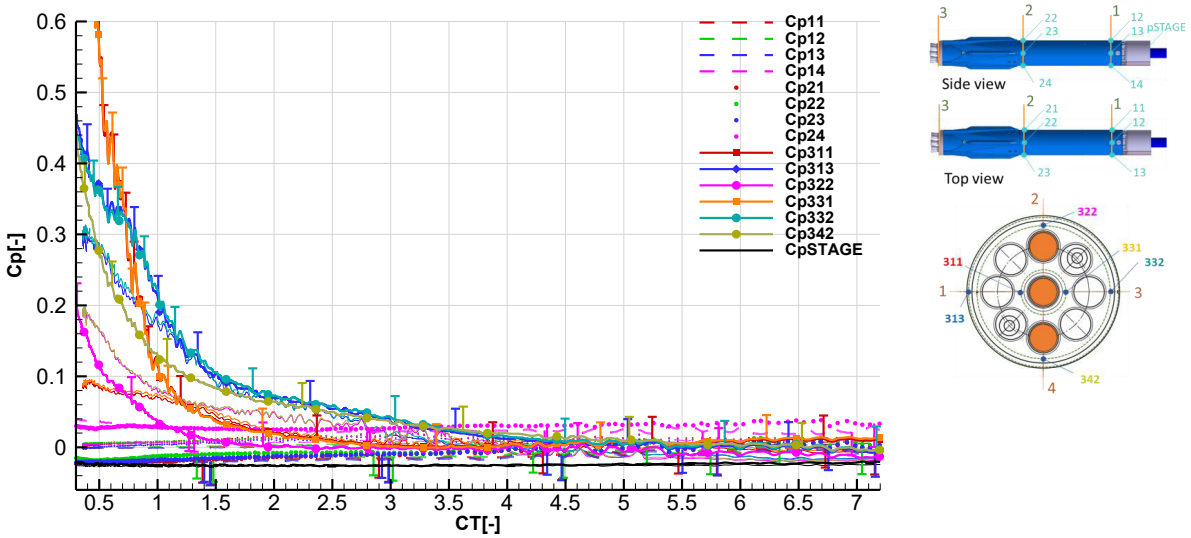

Fig. 97: Angle of attack variation for pressure coefficients C_p vs. thrust coefficient for the single-engine case, for $\alpha = 0°$ (thin lines) and $\alpha = 10°$ (thick lines)
($M_\infty = 5.29$, $p_0 = 4\ bar$, $T_0 = 450\ K$, engine plane: α-plane)

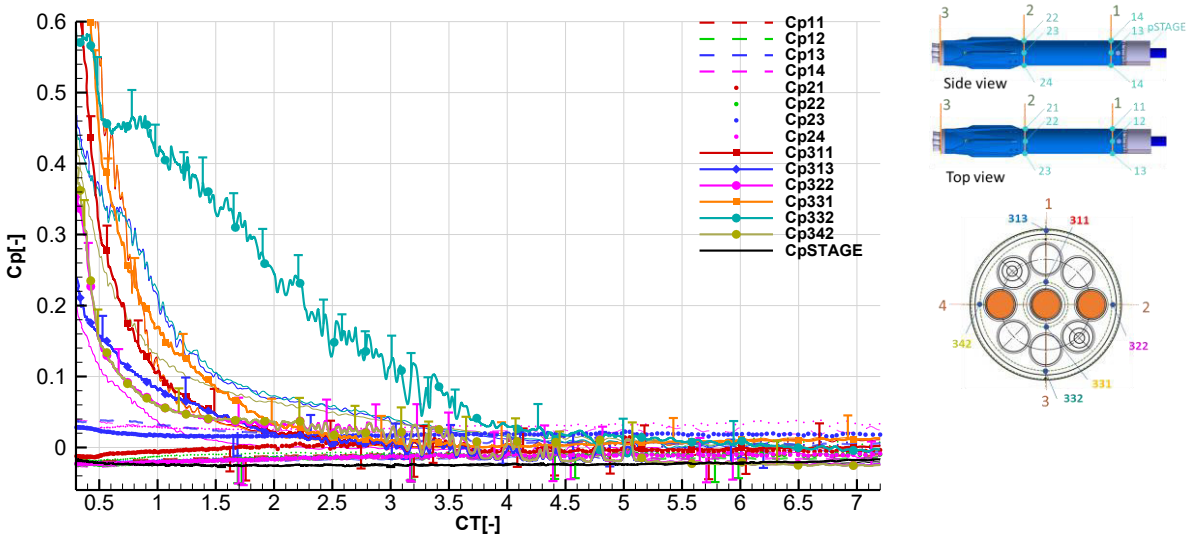

Fig. 98: Angle of attack variation with engines active in the plane perpendicular to the α-plane for the three-engines case, $\alpha = 10°$, $\phi = 0°$ (thin lines) and $\alpha = 10°$, $\phi = 90°$ (thick lines) ($M_\infty = 5.29$, $p_0 = 4\ bar$, $T_0 = 450\ K$)

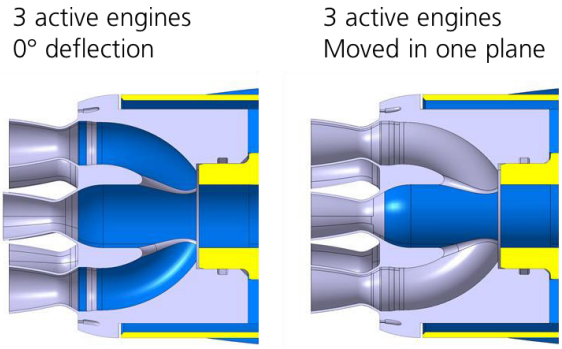

Fig. 99: Center nozzle exit plane moved into the exit plane of the outer engines

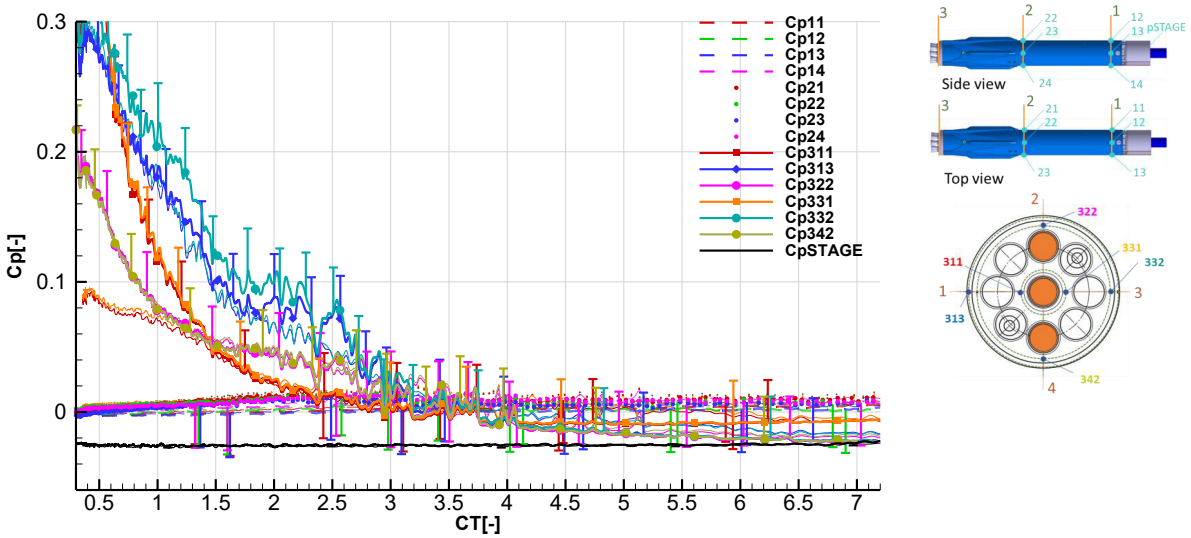

Fig. 100: Variation of the engine exit plane: offset by 150 mm in flight scale (thin lines) and 0 mm (thick lines) ($M_\infty = 5.29$, $p_0 = 4\ bar$, $T_0 = 450\ K$, engine plane: α-plane)

5.2.4. Proper Orthogonal Decomposition and Spectral Analysis

In this section Proper Orthogonal Decomposition (POD) and spectral analyses are presented for a further understanding of the unsteady flow field phenomena.

To this aim a POD over 4000 frames was performed for the hypersonic retro propulsion cases shown in Fig. 84 and Fig. 86. The corresponding values of the pressure measurements are marked with dashed lines in Fig. 91 and Fig. 95. The high speed Schlieren were recorded with a framerate of 20 kHz. Fig. 101 shows the first 12 modes and several higher modes for the cold gas single-engine case. As the mean image was not subtracted from each frame, the zeroth mode shows the steady flow features. The first two modes are axisymmetric, while higher modes do not show any symmetry anymore. The reason for the asymmetry in the modes could be the vortex rings emerging from the Mach disc as described in section 5.2.1, as these strongly alter the flow field, but do not appear in a symmetrical manner. The modes reflect mainly the oscillations in the contact surface and the associated oscillations of the blow shock. In the higher modes (mode 200 and mode 500) also the oscillations in the triple point are reflected. The feedback mechanism for the unsteadiness of the flow field for the blunt mode described in [74] (see section 2.5) can be observed in these modes. The oscillations in the triple point generate pressure waves affecting the bow shock, which feeds back to the EPR. The EPR, in turn, affects the plume shape closing the loop by influencing the oscillations in the triple point. The influence of this effect on the overall flow filed is, however, small in the test case shown in Fig. 101, as the modes in which it appears are high, and cover only a small portion of the overall energy of the flow field.

In Fig. 103 the singular values of the POD are shown. Fig. 104 shows the cumulative energy (sum of singular values up to the current one, divided by the sum of all singular values). It can be seen

that a large number of modes is necessary to capture the energy of the flow. For example, over 2000 modes (of 4000) are needed to capture 80% of the energy.
The first three modes (including the zeroth mode) of the corresponding case with heated air are shown in Fig. 102. Due to differing densities in the plume caused by the heating of the jet, the Schlieren images have a slightly different appearance as explained in section 5.2.2. However, in general, similar modes can be observed. Also the singular values and the cumulative energy of the modes are similar to the cold gas case (see Fig. 103 and Fig. 104).

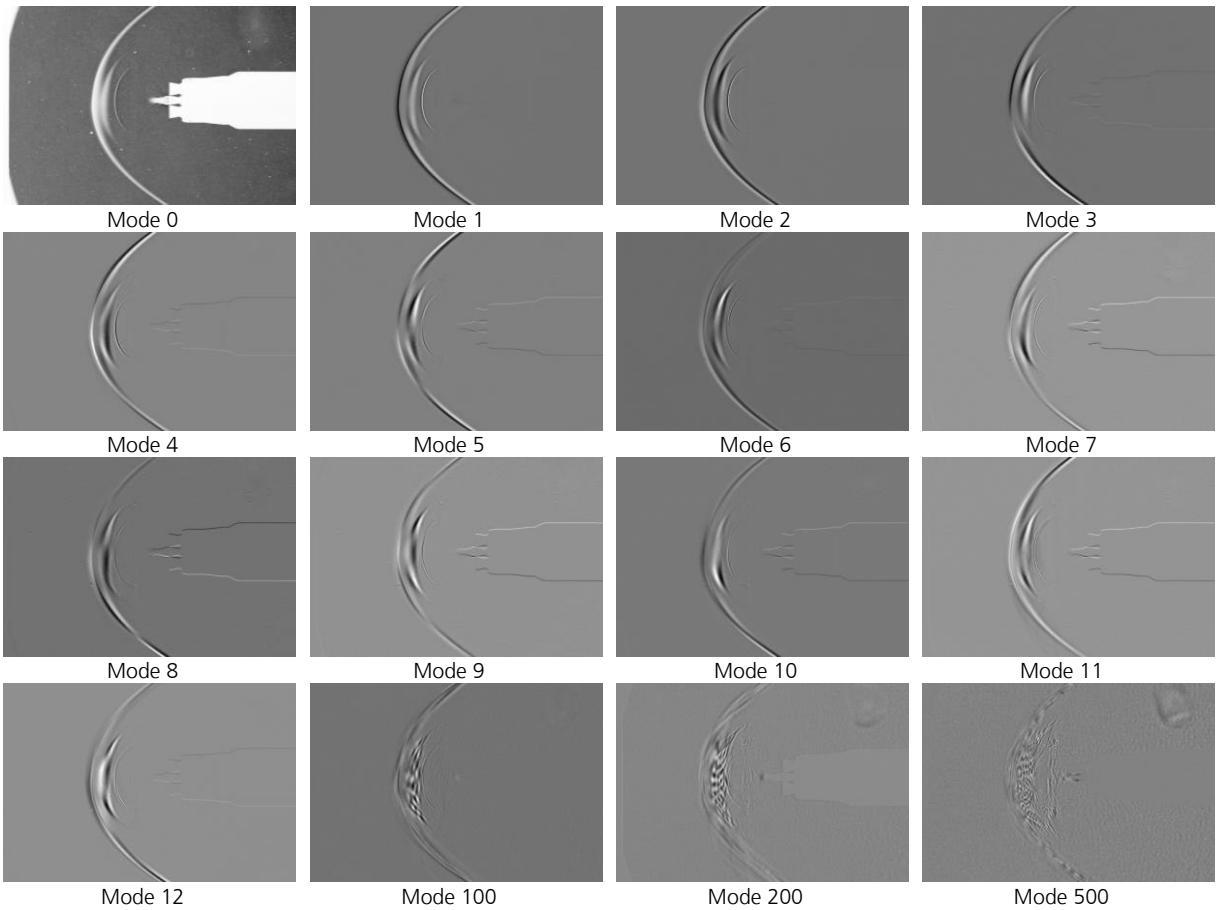

Fig. 101: POD modes of single-engine cold gas case
($M_\infty = 5.29, C_T = 3.69 \pm 0.21, T_{CC} = 303K, p_0 = 4\ bar, T_0 = 450K$)

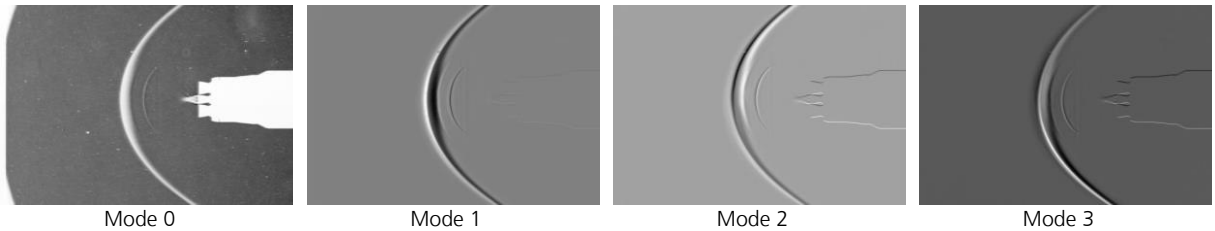

Fig. 102: POD modes of single-engine case with heated air
($M_\infty = 5.29, C_T = 3.85 \pm 0.22, T_{CC} = 589\ K, p_0 = 4\ br, T_0 = 450K$)

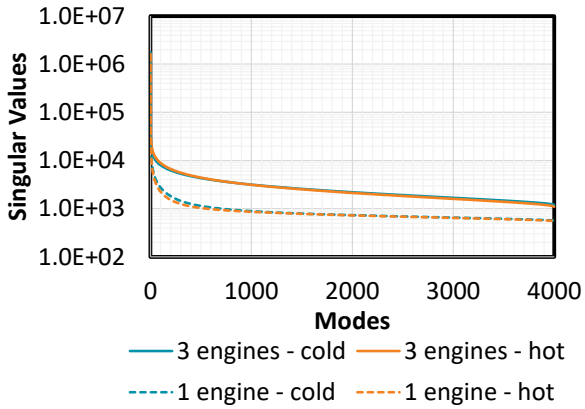

Fig. 103: Singular values of the PODs of the cold and heated air, single-engine and three-engines cases

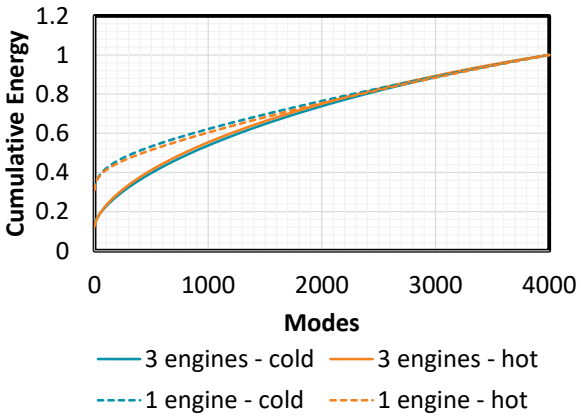

Fig. 104: Cumulative energies of the PODs of the cold and heated air, single-engine and three-engines cases

In Fig. 105 the first 12 modes of the three-engines case are shown for cold and for heated air. The interaction of the jet with the free stream and the resulting unsteady loads on the model lead to an oscillatory movement of the model. These energies are captured in mode 2 and 3 in the cold gas case and in mode 1 in the heated case. As already pointed out in section 5.2.1, the most energetic mode is the switch mode between blunt and long penetration mode for both, the cold gas and the heated air case (neglecting the modes which cover the oscillation of the model). This can be nicely seen in Fig. 106, comparing the first mode of the cold gas case with the variance over 10 images of the long penetration mode and of the blunt mode, which can be used to visualize the unsteady nature of both modes. Fig. 107 shows the time histories of the switching mode for the cold gas and the heated air case, where positive values correspond to the long penetration mode and negative values correspond to the blunt mode. It can be observed that for the cold case, the change between the modes appears more abruptly, while it appears more smoothly for the heated air case. In both cases the blunt mode only appears for short time intervals. This is even more clearly visible for the cold case.

Comparing the cold gas case and the heated air case it can be observed that they slightly differ from each other. For the cold gas case the plume-plume interaction seems to play a larger role, as

the unsteady oblique shocks terminating the plumes are clearly visible in several modes, e.g. mode 4, 9, 10 and 11. For the heated air, the energy seems to be more strongly related to an axial movement of the plume structure, which is, for example, prominent in Mode 7. The difference in the flow fields can be summarized in the average modal solution images of the two cases shown in Fig. 108.

While the heated air flow field is dominated by the switch between the blunt and the long penetration mode, the cold gas case is dominated by the sideways motion of the plume. The differences in the modes could come from an influence of the higher velocity at the nozzle exits due to the higher temperatures, higher viscosities and a temperature effect on the heat capacity ratio. It could also partly come from the varying density gradients in flow field due to the varied temperatures in the jets, which influences the visibility of the flow features in the Schlieren images, as discussed in section 5.2.2.

As shown in Fig. 103 the drop of the singular values over the first modes is lower for the three-engines cases than for the single-engine cases. Hence, the increase of the cumulative energy over the first modes is slower as shown in Fig. 104. This is reasonable, as the unsteadiness of the flow field in the three-engines case is a lot stronger. Therefore, more modes are necessary to capture the energy of the flow field. The singular values and the cumulative energy of the cold and the heated air cases of the three-engines cases are very similar.

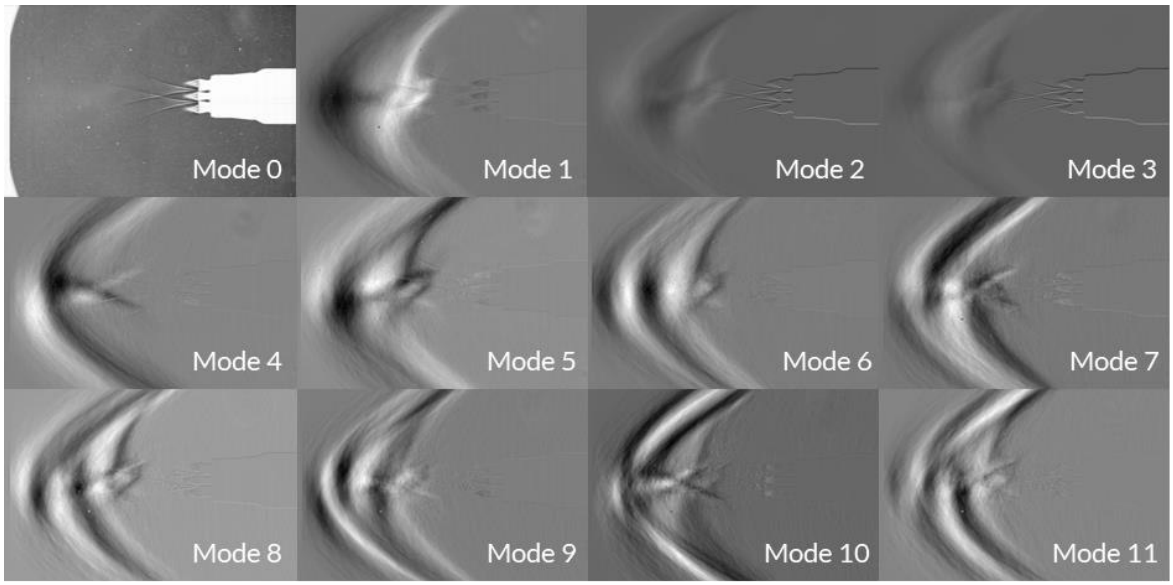

a) Cold gas
$(M_\infty = 5.29, C_T = 2.29 \pm 0.13, T_{CC} = 300\ K, p_0 = 4\ br, T_0 = 450K)$

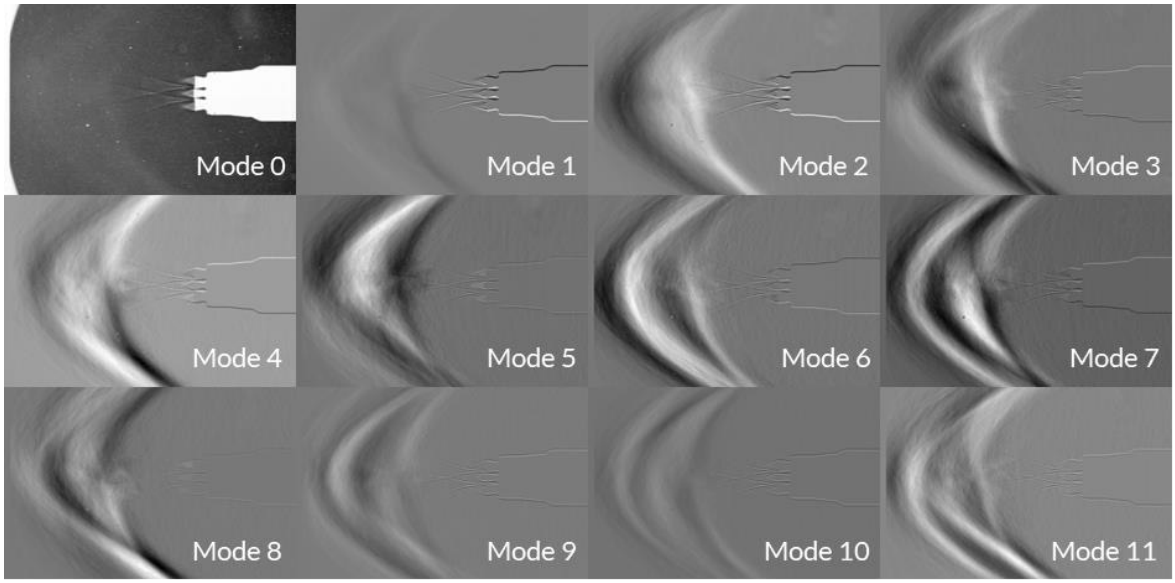

b) heated air

$(M_\infty = 5.29, C_T = 2.43 \pm 0.14, T_{CC} = 632\ K, p_0 = 4\ bar, T_0 = 450K)$

Fig. 105: First 12 POD modes of the three-engines case

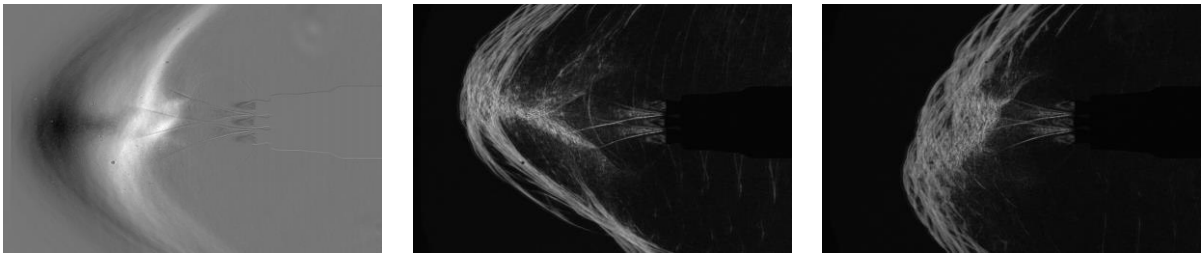

a) First mode of the three-engines cold gas case

b) Variance over 10 images of the long penetration mode

c) Variance over 10 images of the blunt penetration mode

Fig. 106: Comparison of first mode of the three-engines cold gas case with the visualization with the variance over 10 images

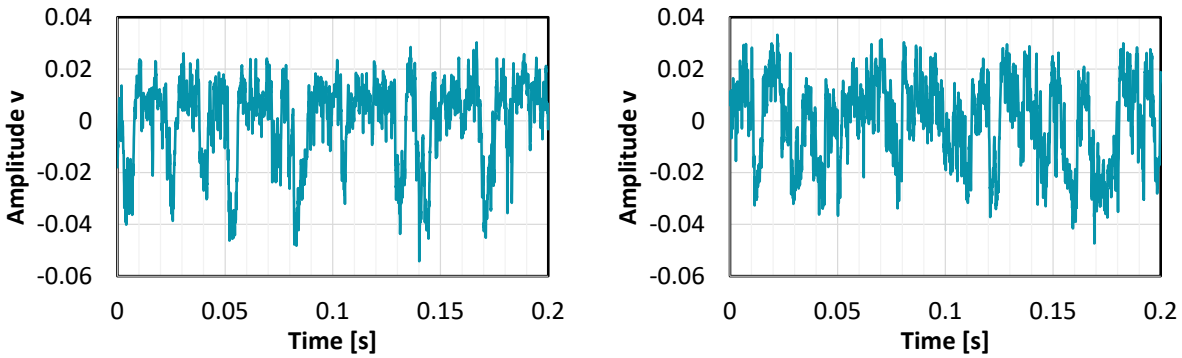

a) Cold gas (Mode 1)

b) Heated air (Mode 2)

Fig. 107: Time histories of the switch mode between blunt and long penetration mode of the three-engines case

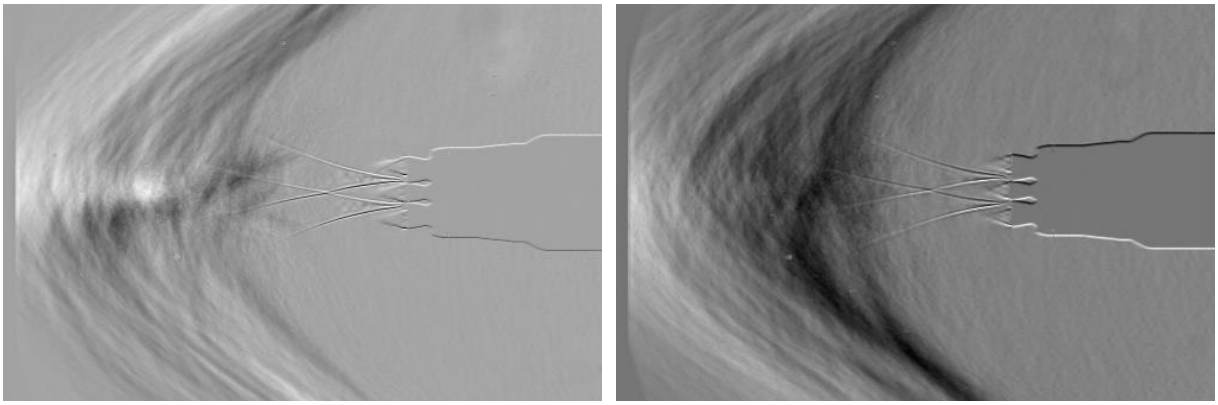

a) Cold gas case b) Heated air case

Fig. 108: Average modal solution images of the three-engines case (Mode 1 to Mode 500)

For a further understanding of the dynamics on the flow field, a PSD of the time series of the POD modes was performed, with a short time Fourier transform that was computed over 4000 time steps. It was performed with a Hann window with a length of 500 with a step size of 8 time steps between single spectra. The spectra were then averaged over the time steps. The frequency was resolved with 2048 bins.

In Fig. 109, the PSD of the first 12 modes are shown for the four hypersonic retro propulsion cases. For the cold gas case, dominant frequencies can be observed at Strouhal numbers of 0.09 and 0.082 for the single-engine and the three-engines case, respectively. For the tests with heated air these frequencies are slightly shifted to higher values of 0.126 and 0.141. In general, the observed frequencies are a lot less prominent than in the subsonic retro propulsion cases (see section 5.3.2).

In Fig. 110, the PSD of the high frequency pressure sensors in the base area and along the cylindrical body of the model is shown for the cold gas case for one and three active engines, where the mean value was subtracted before the PSD was performed. The PSD was performed over 20000 time steps with a Hann window of a width of 500 with a step size of 39 samples between the spectra. The frequency resolution was again 2048 bins. In general, the distribution of the frequencies is similar for both cases. The sensors are clustered by the plane they are in. The sensors 313 and 332, which are on the outer circle of the base and not in the alpha plane, show a slightly different behavior in comparison to the other sensors in plane 3. Dominant frequencies can be observed for the three-engines case. However, they cannot be observed in the single-engine case. There could be three reasons for this behavior: 1) The frequencies could come from a buffeting phenomenon in the base area, as in the subsonic retro propulsion flow field (see section 5.3.2), and in the single-engine case the blunt plume shields the base area better from the incoming free stream, and therefore mitigates those frequencies. 2) The frequencies could come from the unsteady fluctuations of the plume which are only appearing in the three-engines case. 3) As can be seen in Fig. 36 the supply lines of the outer nozzles show a sharp edge where they meet the main supply line. This causes unsteady flow separations and recirculation regions, which were observed in CFD simulations performed on the flow field in the model.

In Fig. 111 a spectrogram of the Strouhal number versus the thrust coefficient is shown for the pressure sensor 311 and 331. It can be observed that the dominant Strouhal numbers of 1.12, 1.16, 1.19, 1.3 and 0.14 which were shown in Fig. 110 appear for a large range of thrust coefficients in the pressure measurements. This is a strong indicator that they don't origin in the outer flow interactions, but from the supply line. In future experiments, unsteady pressure measurements in the supply air should be foreseen in those critical regions, such that these effects can be separated from the frequencies in the outer flow field. The Strouhal number of 0.14 is more likely to come from outer flow field interactions as it is close to the frequency of 0.126 measured in the cold gas single-engine case, where such frequency from the supply line were not observed, as the feed line does not show sharp edges.

The frequencies found in the pressure measurements cannot be observed in the PSD of the POD modes shown in Fig. 109. This is due to the fact that the high speed Schlieren were recorded with 20 kHz while the pressures were recorded with 50 kHz. Therefore, the frequencies of Strouhal numbers of 1.12, 1.16 and 1.16 are out of the measurement range of the Schlieren recordings. For the lower dominant normalized frequencies of 0.056, 0.14 and 0.64, the reason could be that the Schlieren setup was not sensitive enough to capture those fluctuations, even though the Strouhal number of 0.14 was found in the Schlieren videos of the heated air case.

The frequencies observed here are in the range of Strouhal numbers reported in literature for similar configurations. In [71] dominant frequencies were found in the first two POD modes of a single-engine plume, with the lowest normalized frequency close to 0.2 (which can be calculated from the data given in [71]). Chen et al. [73] reported Strouhal numbers of 0.252 and 1.506 for the forces on a similar configuration as in [71].

Fig. 112 shows the normalized root mean square surface pressure fluctuations in the two cold gas test cases. The normalized pressure fluctuations are approximately one order of magnitude smaller than in near-wake flows, which are between 0.01 and 0.06 for Mach numbers between 0.5 and 0.9 [10]. They are higher in the case with three active engines. Presumably this is due to the fact that the shielding of the plume is less effective in this case and the plume itself shows stronger unsteady behavior. Due to the shielding effect of the plume in both cases, the pressure fluctuations on the base area (plane 3) are smaller than downstream of the landing legs (plane 2) or on the cylindrical body (plane 1).

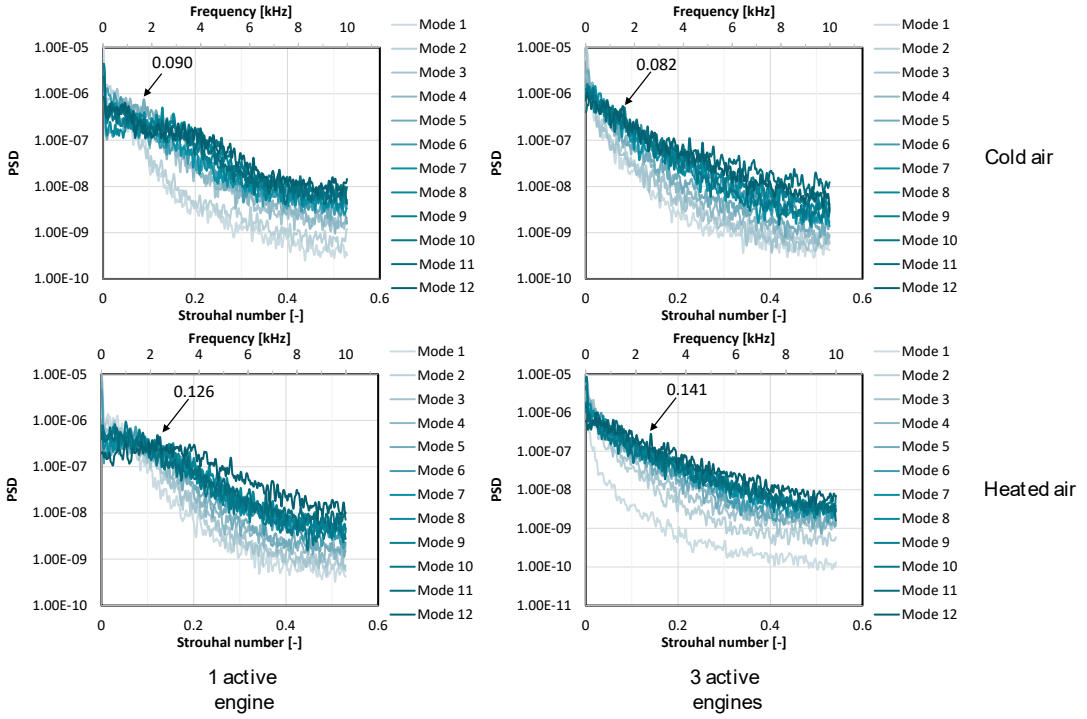

Fig. 109: PSD of the first 12 modes of the Schlieren videos of the hypersonic retro propulsion cases

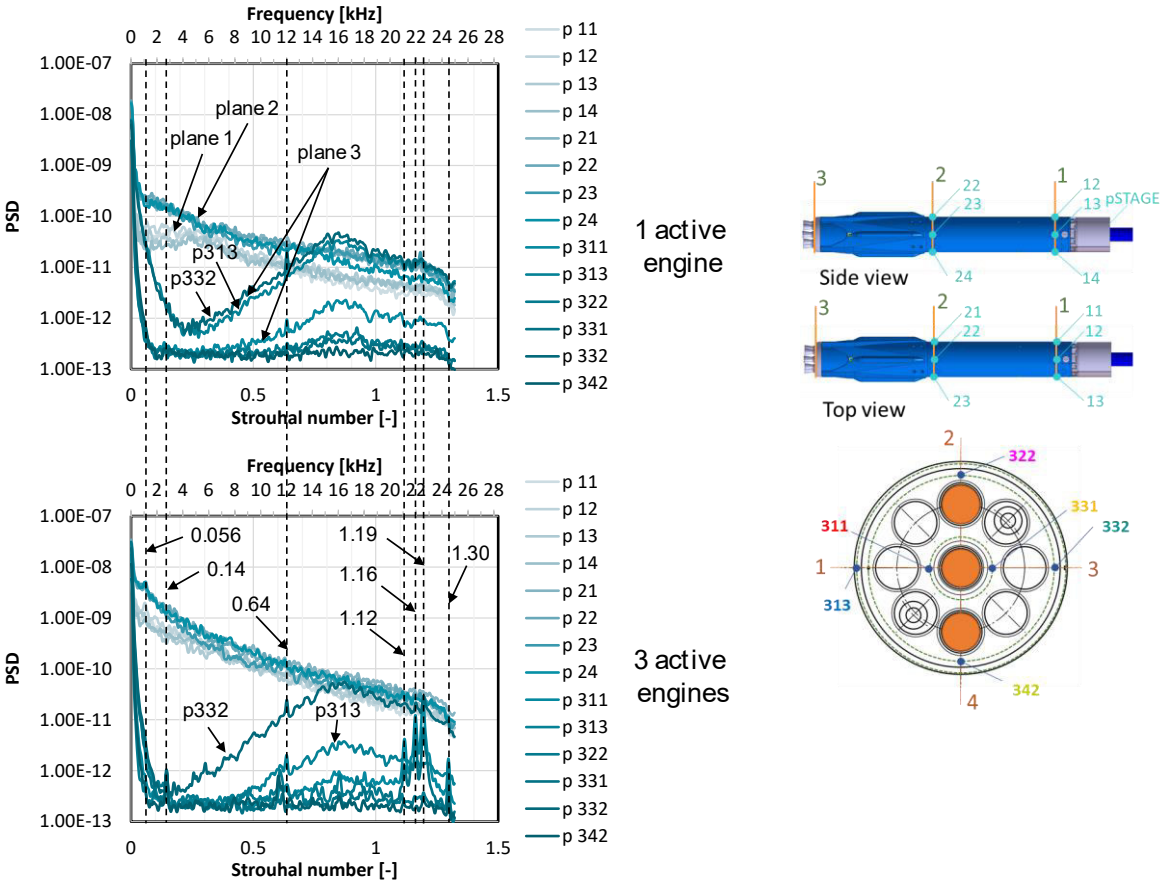

Fig. 110: PSD of the pressure measurements of the hypersonic retro propulsion cases

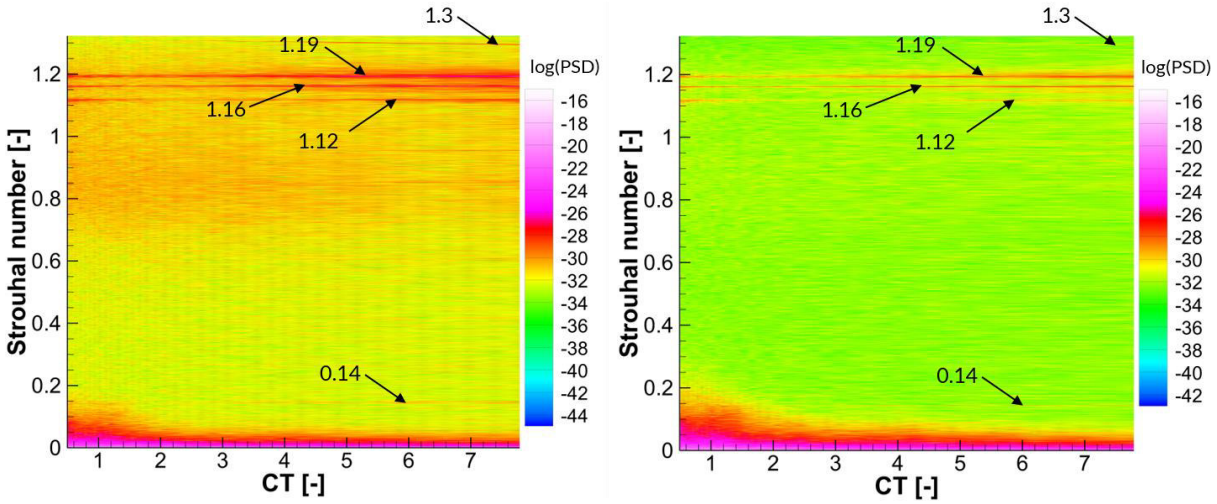

a) Pressure sensor 311 b) Pressure sensor 331

Fig. 111: Spectrograms of pressure measurements on the base area of RETALT1 versus the thrust coefficient, for the cold gas case with 3 active engines

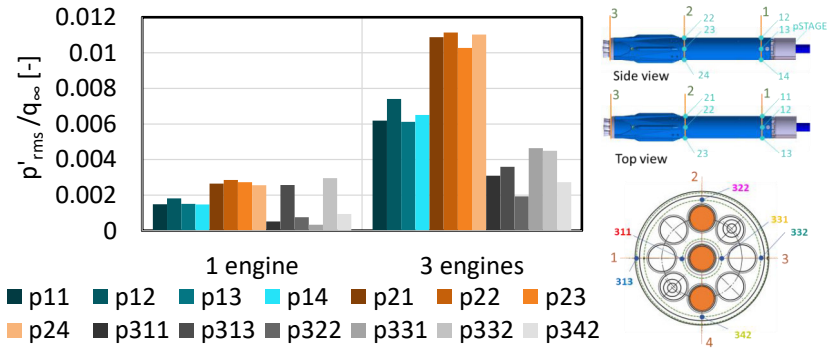

Fig. 112: Normalized rms surface pressure fluctuations in the two cold gas test cases with one and three active engines

5.2.5. Conclusions regarding the Reentry Burn

This section described the experimental results of the hypersonic part of the reentry burn of the RETALT1 launcher configuration. Detailed measurements were presented for the RETALT1 configuration with one and three active engines, for several freestream and jet conditions.

An analysis of the flow features confirmed results from literature that the flow features for the single-engine case scale with the square root of the thrust coefficient. This relation was then also shown for the three-engines case. For the three-engines case a constantly repeating switch from the blunt mode to the long penetration mode and vice versa was observed for all thrust coefficients tested. For the single-engine case, the building up of vortex rings was observed. These vortex rings move upstream from the Mach disc and lead to significant flow disturbances when interacting with the contact surface. They probably result from a disturbance of the Mach disc leading to pressure and velocity gradients between disturbed and undisturbed regions. For the three-engines cases, in general, an unsteady flow behavior was identified.

Condensation in the ambient temperature air plume was visualized and could be shown not to be a local phenomenon in the underexpanded plume of retro propulsion flow fields. It was shown that this could be mitigated by heating the supply air to approximately 600 K. The heating did not influence the static flow features.

The analysis of the pressures along the model surface shows that the Mach number plays a subordinate role, and the Reynolds number seems to have negligible influence on the pressure distribution. The dominating similarity parameter is the thrust coefficient. Between configurations with different numbers of engines, the total thrust coefficient is an adequate scaling parameter. For high thrust coefficients the pressure coefficients generally tend towards very small values. However, the pressure in the wake of the launcher configuration is independent of the thrust coefficient. The pressures far downstream are also less dependent on the thrust coefficient. At an angle of attack, these pressures do not tend to zero, indicating that the normal forces and moment coefficients on the configuration are not negligible even for high thrust coefficients. A variation of the offset of the center engine nozzle exit plane, with respect to the nozzle exit planes of the outer engines showed that the influence is small and is mainly present for small thrust coefficients. The scaling of the surface pressures with the total pressure downstream of the bow shock reaches good results for the base area and in the wake region, while along the cylindrical body of the launcher first stage, the conventional pressure coefficient reaches better similarity.

For the case of a single active engine it was found that the modes of the Proper Orthogonal Decomposition (POD) mainly capture the unsteady fluctuation of the contact surface and the bow shock, probably caused by vortex rings emerging from the Mach disc. In the case of three active engines the flow field is dominated by the switch between the blunt and the long penetration mode.

5.3. Landing Burn – Subsonic Retro Propulsion Landing Maneuver

In this section the subsonic retro propulsion flow field will be analyzed regarding its steady and unsteady flow features.

5.3.1. Discussion of Flow Field Features

Fig. 113 shows a snapshot of a subsonic retro propulsion flow field at Mach 0.8 with an Ambient Pressure Ratio (APR) of 0.389. The flow field shows a strongly unsteady behavior. Various large-scale flow features can be observed, which are the unsteady jet which meets the free stream at the contact surface, pressure waves emerging from the contact surface and large-scale fluctuations downstream of the contact surface. The unsteadiness of the flow field is evident by comparing Fig. 113 with Fig. 114 and Fig. 115, which are images from the same Schlieren video at different points in time. The plume length varies strongly and the jet structure can become asymmetric as shown in Fig. 114.
Fig. 116 shows the mean image of the flow field over 200 images and Fig. 117 shows the standard deviation over these 200 images. It is apparent that unsteady flow features cannot be seen in the mean image (as expected) but the plume structure close to the model nozzle exit is well captured. In the standard deviation image, the flow structures are somewhat clearer than in the mean image.
Fig. 118 shows the mean image over 200 images of the jet without counterflow ($M_\infty = 0$) for approximately the same APR. The multi cell structure of the jet can be well observed, in contrast to the jet with active counterflow.
In Fig. 119 a detail of the flow field near the nozzle exit of the jet without counterflow is shown. The flow features characteristic for such overexpanded jets, are sketched in the image. As the plume is strongly overexpanded it exhibits a Mach reflection at the centerline (see for example [10, 23]) passing through an oblique lip shock and a Mach disc, where the lip shock is reflected at the Mach disc. After the following expansion, the flow is recompressed by a new incident shock, again exhibiting a Mach reflection. Downstream of the second Mach disc also the slip line between the flow passing through the incident shock and its reflection at the Mach disc, and the flow passing through the Mach disc is visible.
In Fig. 120 the flow features as sketched in Fig. 119 are overlaid over the flow field with active counterflow at $M_\infty = 0.8$, with the same APR. Here, instead of the mean image, the standard deviation image was used as it shows the flow structures more clearly. The flow features without counterflow match the exit flow with active counterflow very well. This shows that the APR is the correct scaling parameter for the description of the plume structure at the nozzle exit.
This is an interesting finding, as it stands in contrast to supersonic retro propulsion flows where the APR is not representative for the exhaust plume structure, but rather the ratio of exit pressure and dead air pressure p_d, namely the Exit Pressure Ratio (EPR) (see section 2.5). This is reasonable, as in the case of subsonic retro propulsion the strong bow shock that is present in supersonic retro propulsion flow fields (see section 2.5) is absent. Hence, the alteration of the free stream induced by the jet is weaker and the flow conditions in the recirculation region close to the nozzle exit are

more strongly dictated by the free stream rather than by the jet. Furthermore, with the large plume length, the jet pushes the stagnation point, where the free stream and the jet plume meet, far into the free stream, leaving the nozzle exit area in the wake of the jet, such that the flow field has enough running length to adapt to the free stream parameters. Hence, it is reasonable to assume the static pressure in the free stream, p_∞, to be acting in this region.
In summary, there are two dominant similarity parameters to describe the steady flow field of the subsonic retro propulsion flows: while the Momentum Flux Ratio (MFR) describes the interaction of the jet with the counterflow and the jet plume length [67], the APR describes the flow structure at the nozzle exit.

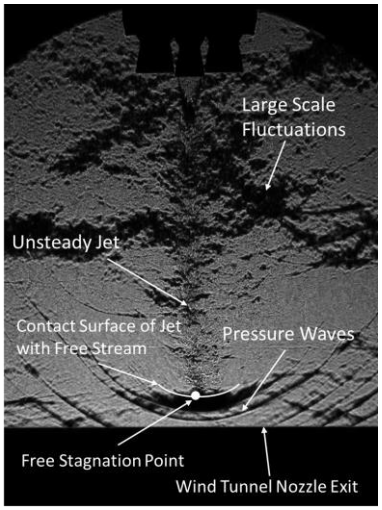

Fig. 113: Snapshot of Schlieren video showing unsteady flow features in subsonic flow field at Mach 0.8 and $APR = 0.389$

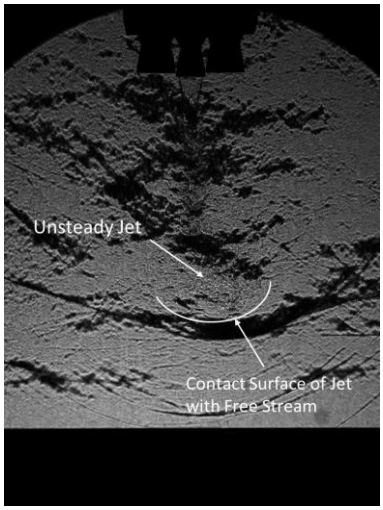

Fig. 114: Asymmetric jet of subsonic retro propulsion flow field at Mach 0.8 and $APR = 0.389$

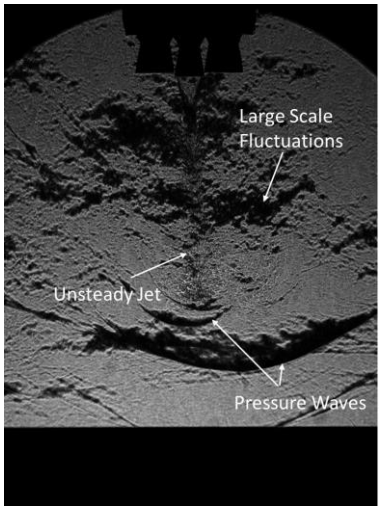

Fig. 115: Snapshot of the same Schlieren recording as in Fig. 114 at a different point in time

Fig. 116: Average over 200 images at Mach 0.8 and $APR = 0.389$

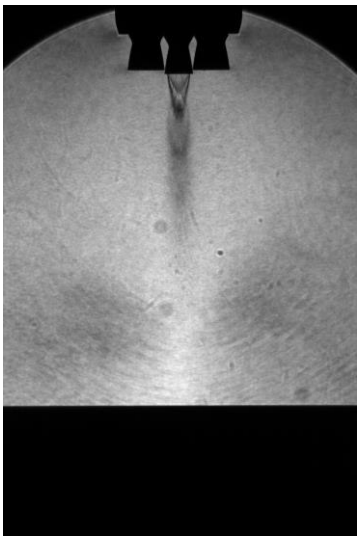

Fig. 117: Standard deviation over 200 images at Mach 0.8 and $APR = 0.389$

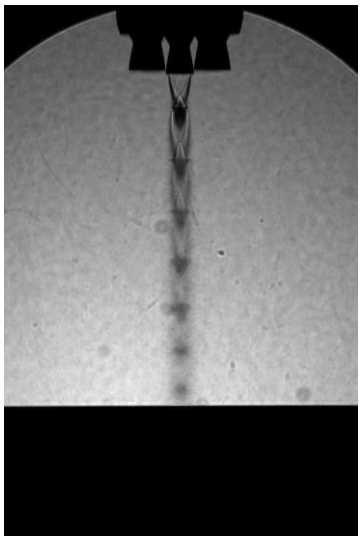

Fig. 118: Mean image over 200 images at Mach 0.0, with $APR = 0.387$

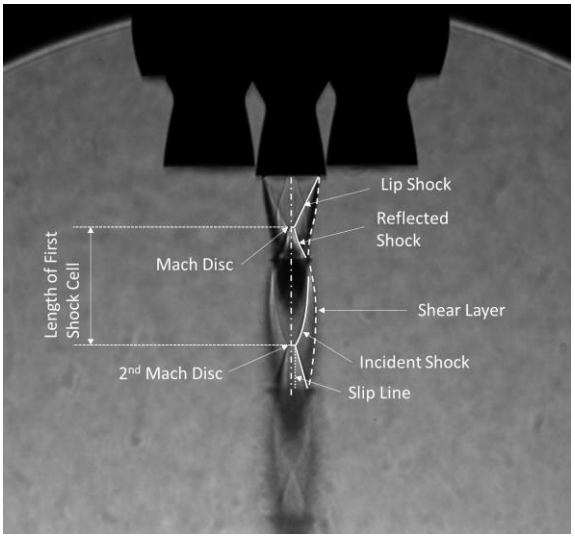

Fig. 119: Detail of mean flow at $M_\infty = 0$ and $APR = 0.387$ (Fig. 118) with sketched flow features

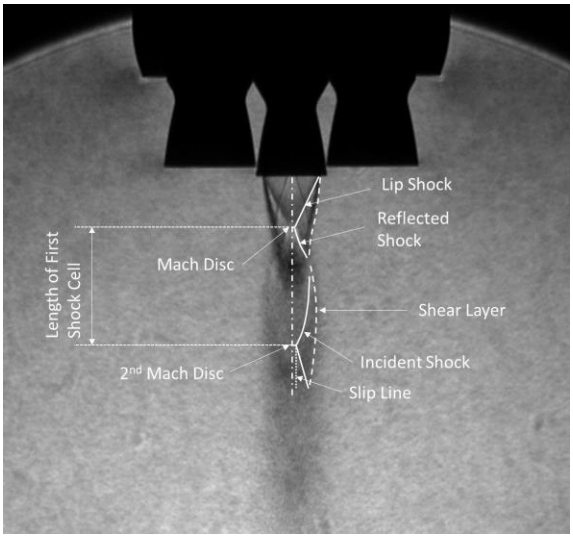

Fig. 120: Detail of standard deviation at $M_\infty = 0.8$ and $APR = 0.389$ overlaid with flow features at $M_\infty = 0$ sketched in Fig. 119

In Fig. 121 the pressure coefficients for different APRs are shown. Due to the increase of the plume length with the MFR (see section 2.6), it increases with increasing APR and with decreasing Mach numbers. That is why in Fig. 121 for higher APRs the lower Mach numbers were not evaluated, as the plume is reaching the wind tunnel nozzle exit. One can observe that the pressure coefficients are clustered by the radial position. The pressures in ring 1 and 2 lie on top of each other. The pressure coefficients in ring 3 are negative as they are positioned around the shoulder of the base area where the flow is expanded. The various APRs show that while a relatively large difference of the jet-off case ($APR = 0$) to the cases with active jet can be observed, the difference between the different jet cases is small. For the active jet, the absolute values of the pressure coefficients decrease and they become quite independent of the Mach number.

The lower pressures in the active jet cases, come from the fact that the jet pushes the stagnation point further upstream in the free stream, as described above, leaving the base area in the wake of the jet. This also explains why the APR and the Mach number have little influence on the pressure values, since the wake area is less dependent on the free stream conditions than the stagnation region.

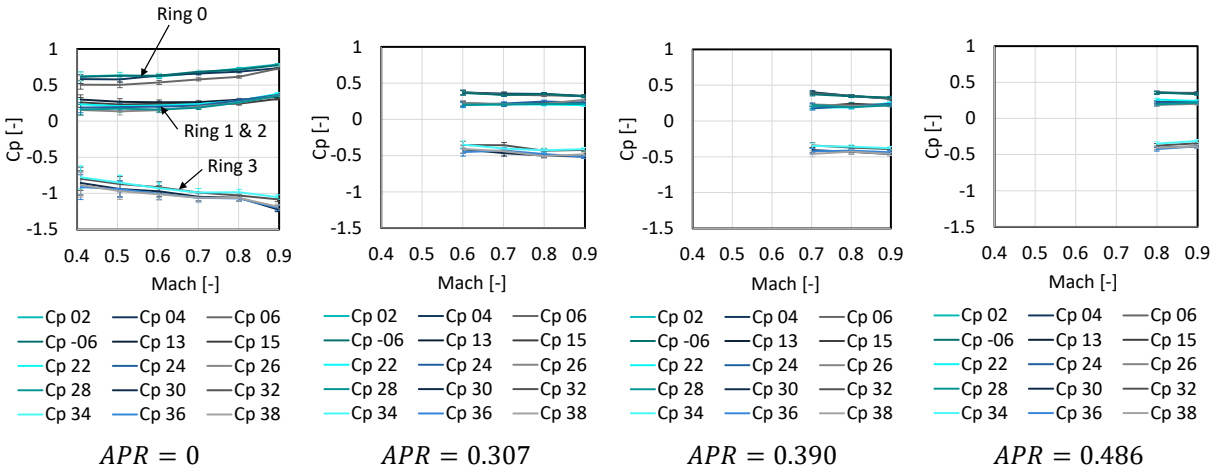

$APR = 0$ $APR = 0.307$ $APR = 0.390$ $APR = 0.486$

Fig. 121: Pressures on the base area for various APRs

5.3.2. Proper Orthogonal Decomposition and Spectral Analysis

To further understand the unsteady behavior of the subsonic retro propulsion flow field, a Proper Orthogonal Decomposition (POD) was performed over 8000 images as described in section 4.4. Fig. 122 shows the first 12 Modes and four higher modes of the same retro propulsion flow field at $M_\infty = 0.8$, $APR = 0.387$, $MFR = 6.52$, and at a Reynolds number of $Re_\infty = 1.68 \times 10^6$. As the mean image was not subtracted from the single Schlieren images before the POD was performed, the zeroth mode shows the steady flow features. The lower modes then show the larger fluctuations, while the larger modes show the smaller structures. For comparison Fig. 123 shows the first eigenmodes of a flow past a cylinder at a Reynolds number of 100. Similarities between these two flow fields can be observed. As for the flow past a cylinder, the first modes of the subsonic retro propulsion flow field are symmetric. For the cylinder flow the first two modes and for the retro prolusion flow field the first 6 modes are symmetric. Furthermore, as for the cylinder, the symmetric modes are followed by antisymmetric modes, which are then followed by symmetric ones again and so forth. However, with higher modes the symmetry is slowly lost.

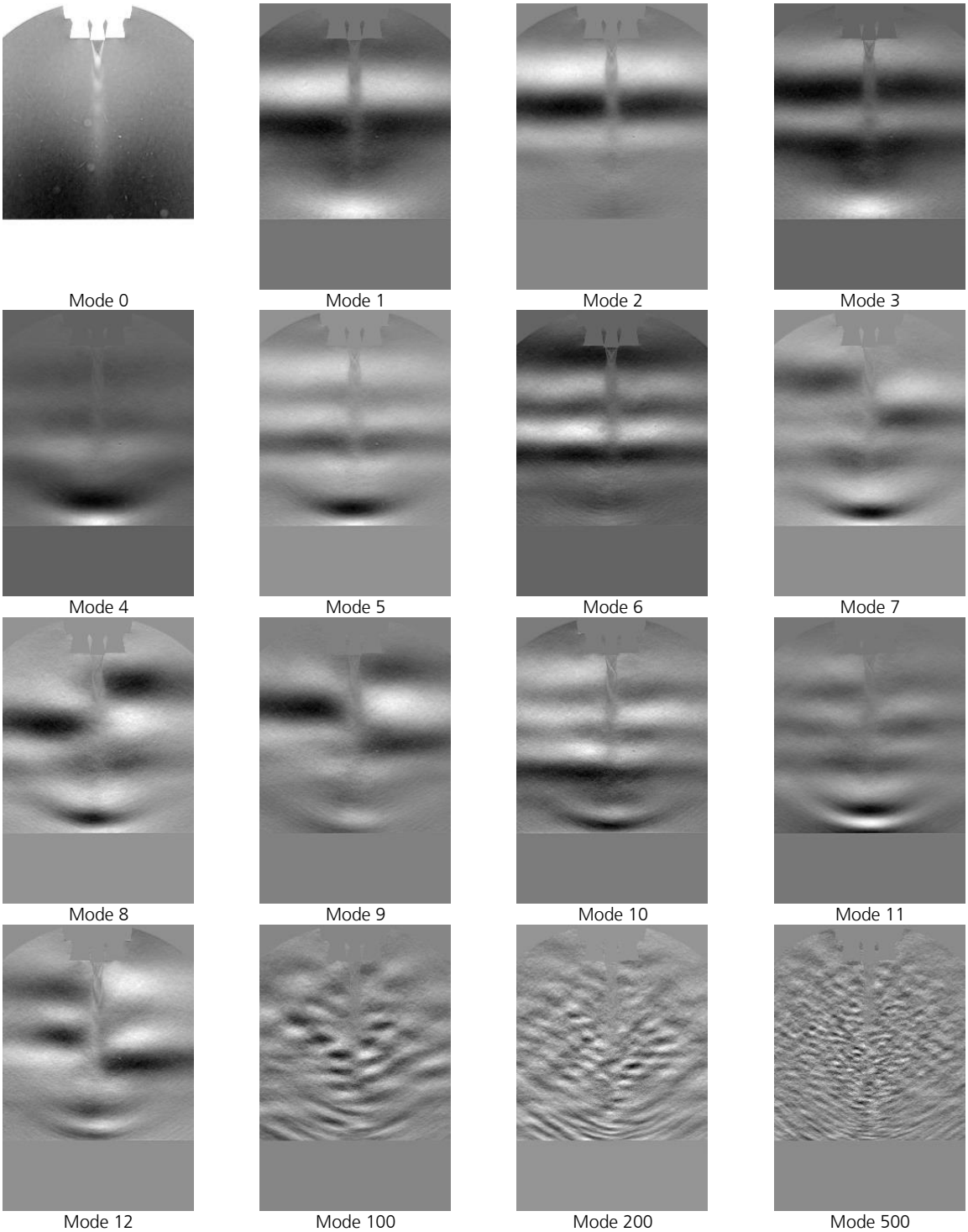

Fig. 122: POD modes of subsonic retro propulsion flow field at $M_\infty = 0.8$, $APR = 0.389$, $MFR = 6.52$ and $Re_\infty = 1.68 \times 10^6$

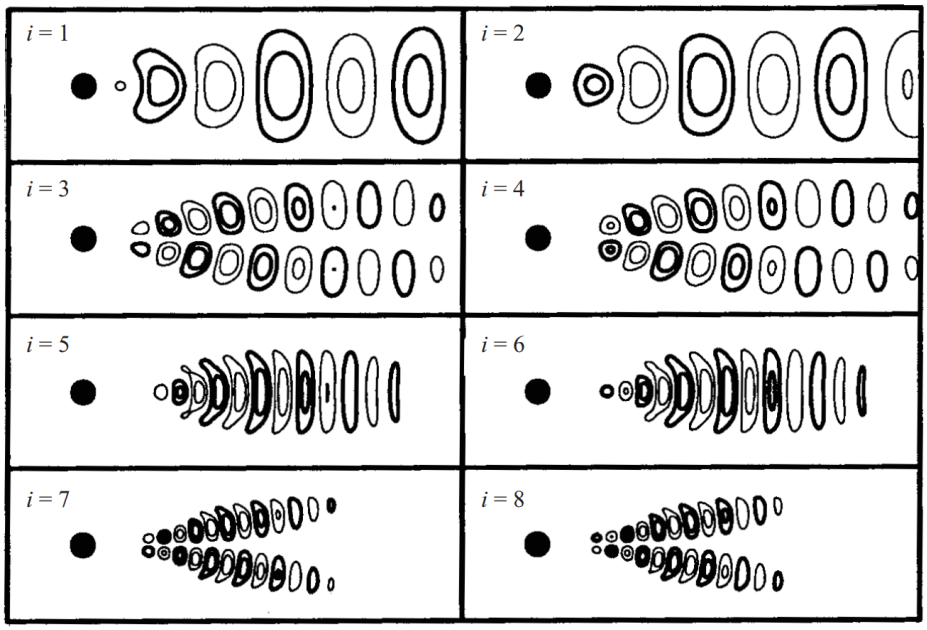

Fig. 123: First eight POD modes of the flow past a cylinder at $Re_\infty = 100$ as shown in [107]

In Fig. 124 and in Fig. 125 the singular values and the cumulative energy of the singular values (sum of singular values up to the current one, divided by the sum of all singular values) are plotted. One can see, especially in the cumulative energy, that a large number of modes is necessary to capture the energy of the flow, e.g. approximately 5000 modes are necessary to capture about 80% of the energy. The reason for this is probably that the pressure waves moving through the flow field need a large number of modes to be captured correctly. However, it was shown in Fig. 122 that the larger modes depict the smaller structures. Hence, if the macroscopic motion shall be represented, less modes are required.

In Fig. 126 the first twelve singular values of the POD modes of the retro propulsion flow field are shown. For comparison, Fig. 127 shows the singular values of the first twelve modes of the flow past a cylinder. For the cylinder flow, the modes can be grouped in pairs of two, as can be seen in Fig. 123 (1, 2; 3, 4; 5, 6), and the energy decays from pair to pair [107]. It seems that the POD modes of the retro propulsion flow field can similarly be clustered into groups of three modes (1,2,3; 4,5,6; 7,8,9 etc.) where the energy decays from group to group. For the higher modes this does not apply anymore.

Due to the similarities of the subsonic retro propulsion modes with the flow past a cylinder, it seems that the subsonic retro propulsion flow field can be interpreted as a combination of two flow phenomena: 1) an unsteady jet, and 2) an unsteady Von Kármán street-like wake downstream of the stagnation area of the jet with the free stream. This interpretation could be a starting point for a further development of a dynamic model of the flow field to enhance its understanding and predictability in the future.

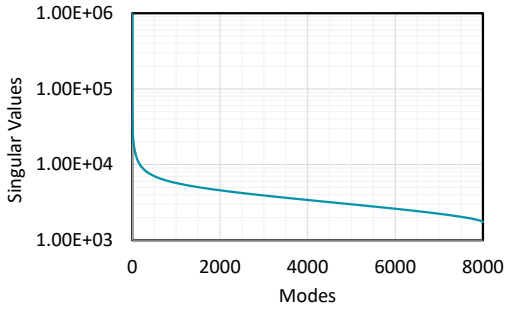

Fig. 124: Singular values of POD modes of retro propulsion flow field ($M_\infty = 0.8$, $APR = 0.389$, $MFR = 6.52$)

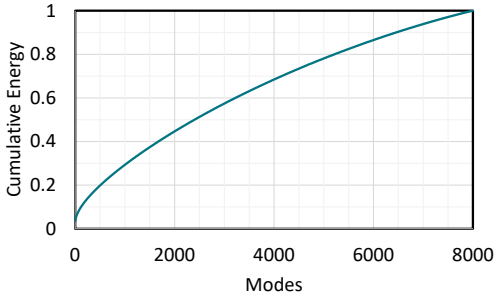

Fig. 125: Cumulative energy of POD modes of retro propulsion flow field ($M_\infty = 0.8$, $APR = 0.389$, $MFR = 6.52$)

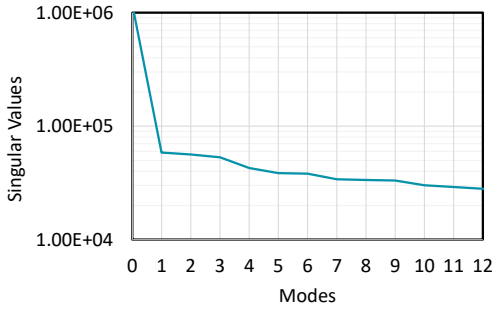

Fig. 126: Singular values of POD modes of retro propulsion flow field ($M_\infty = 0.8$, $APR = 0.389$, $MFR = 6.52$)

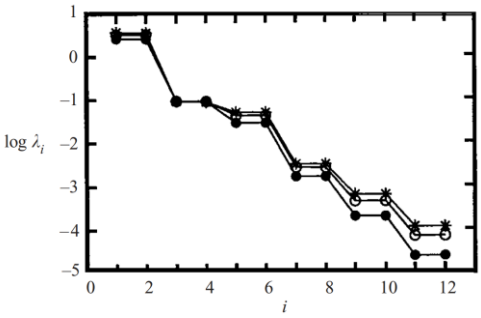

Fig. 127: Singular values of modes of the flow past a cylinder [107]

As can be seen in Fig. 116, the average image does not reveal the flow structure in the retro propulsion flow field as the flow features are disappearing due to the averaging. However, averaging the time series of the Modes, without including the zeroth mode, and reconstructing a mean solution from that, the flow features can be nicely merged in one image. The procedure for the construction of the average modal solution is described in detail in section 4.4.

Fig. 128 shows the averaged modal solution for several APRs and Mach numbers. The square root of the MFR is also reported. The similarity with the MFR can be clearly seen as the flow fields on the diagonals of the image matrix (bottom left to top right) have similar MFRs. It is clearly observable that these flow fields have a similar appearance. In [67] it was shown that the plume length in retro propulsion jets can be estimated with:

$$\frac{x}{D_e} = 3.1\left(\frac{\rho_e u_e^2}{\rho_\infty u_\infty^2}\right)^{\frac{1}{2}}\left(\frac{T_{CC}}{T_e}\right)^{\frac{1}{2}} = 3.1\, MFR^{\frac{1}{2}}\left(\frac{T_{CC}}{T_e}\right)^{\frac{1}{2}} \quad (55)$$

Where ρ_e, T_e and u_e are the density, the temperature and the velocity at the nozzle exit, T_{cc} is the total temperature in the combustion chamber, and ρ_∞ and u_∞ are the density and velocity in the free stream.

The visualizations with the averaged modal solution were used to measure the plume length as indicated in the images in Fig. 128. The stagnation point is assumed to be at the point where the

smaller structures in the plume are still visible. With those measurements the plume length in dependence of eq. (55) can be plotted as shown in Fig. 129. The linear dependency of the plume with the MFR and with the temperature ratio can be confirmed. However, the factor found for the fitting of the data was 2.48 instead of 3.1. Nevertheless, this is a good indication that besides the APR, the MFR and the temperature ratio of the total, and the exit temperature of the nozzle, are important similarity parameters to be considered in the experimental rebuilding of the landing burn. Furthermore, this relation can be helpful for the design of such experiments, as the necessary distance of the model nozzle exit to the wind tunnel nozzle exit can be estimated.

In Fig. 130 the Power Spectral Density (PSD) of the first 12 Modes of the retro propulsion flow field at $M_\infty = 0.8$, $APR = 0.387$ and $MFR = 6.52$ is shown. For the computation of the PSD a short time Fourier transform was computed over 8000 time steps. It was performed with a Hann window with a length of 500, shifting the window by 16 time steps between single spectra. The spectra were then averaged over the time steps. The frequency was resolved with 2048 bins. In the top row of Fig. 130 the PSD is plotted over the frequency, in the bottom row it is plotted over the Strouhal number. The reference length of the Strouhal number was chosen to be the base diameter, which is 70 mm, as this makes the Strouhal numbers comparable to studies on near-wake flows of (ascending) space transportation systems where this definition was used [10].

Especially for the first 4 modes, peaks can be seen at low frequencies of 637 Hz, 1261 Hz and 1812 Hz. For the higher modes, the lowest frequency shifts somewhat to a higher frequency of 733 Hz and also the frequency of about 1800 Hz can be observed again. Furthermore, also for the higher modes (mode 9 and mode 12) the frequency of about 1300 Hz can be observed which was also present in the lower modes (mode 1 and mode 2). For the higher modes a further frequency peak at around 5300 Hz can be observed. Referring to the Strouhal numbers corresponding to the frequencies, the PSD peaks can be observed at 0.180, 0.357 and 0.512 in the lowest modes and at 0.207, 0.376, 0.533,1.506 and 1.513 in the higher modes. Interestingly, the lower Strouhal numbers are close to frequencies expected for near-wake flows. The so-called cross-pumping in near-wake flows commonly occurs at $Sr_D \approx 0.1$, the vortex shedding and cross-flapping motion at $Sr_D \approx 0.2$, and the shear layer swinging at $Sr_D \approx 0.35$ [108, 109]. Hence, the Sr_D at 0.180 and 0.2 observed in the retro propulsion flow field are close to the cross-pumping frequency ($Sr_D = 0.1$) and the vortex shedding and cross-flapping frequency ($Sr_D = 0.2$) and the Sr_D of 0.357 is close to the shear layer swinging ($Sr_D = 0.35$). This should be considered in the design of a vertical landing vehicle, especially as Saile and Gülhan [108] theorized that these mechanisms, if in resonance with the acoustics of the jet (screeching), can generate high unsteady loads on the engine. This was found to be one likely reason for the failure of the maiden flight of the Ariane 5 Evolution Cryotechnique type A (ECA) [10, 108]. Hence, even though the underlying phenomena leading to these frequencies in the retro propulsion flow field differ from the mechanisms in the near-wake flows, the frequencies can be critical. It should be noted that the frequencies presented here are based on cold gas jet experiments. Kirchheck et al. [88] found that the coupling mechanism in near-wake flows and the resulting prominent frequencies differs for cold gas and hot gas experiments.

Hence, a detailed frequency analysis of hot plume retro propulsion experiments should be performed in the future to confirm these findings.

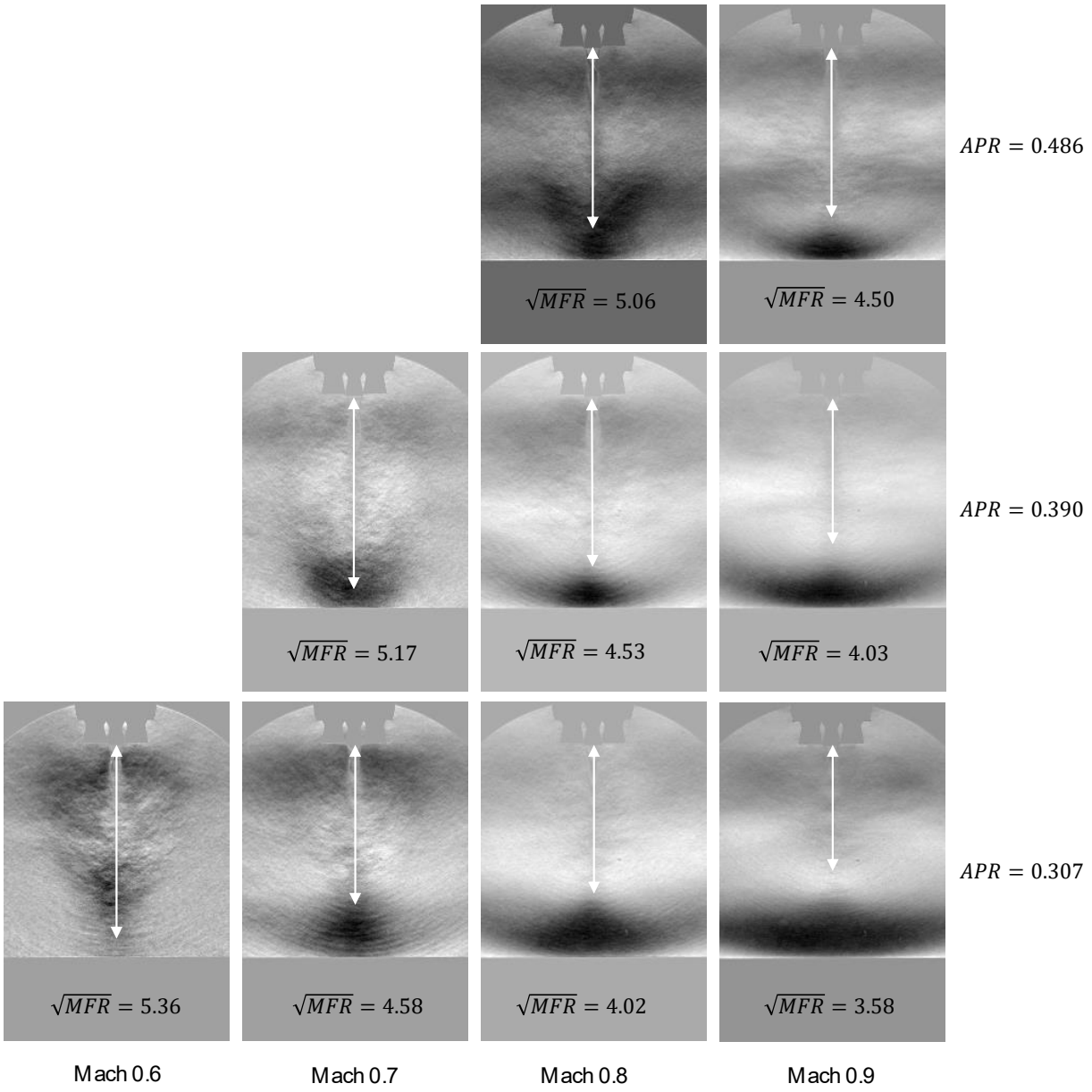

Fig. 128: Average modal solution for various Mach numbers and APRs and MFRs

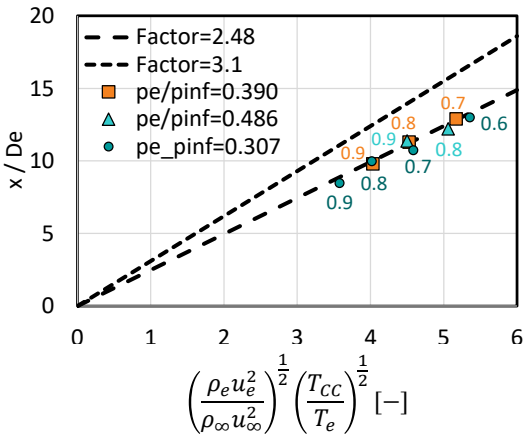

Fig. 129: Plume length versus the square root of the MFR. The numbers on the data points indicate the Mach number

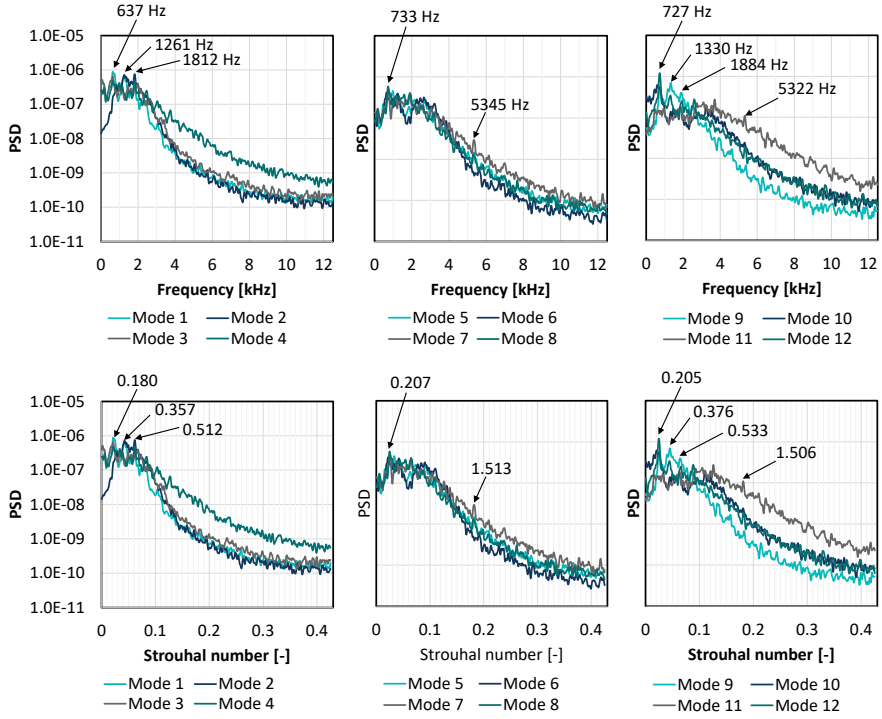

Fig. 130: Power Spectral Density of the first 12 Modes, top row: Frequencies, bottom row: Strouhal number ($M_\infty = 0.8$, $APR = 0.389$, $MFR = 6.52$ and $Re = 1.68 \times 10^6$)

In Fig. 131a the PSD over the frequency is plotted for the first 2000 modes. One can observe that the most dominant frequencies can be found in the lower modes, whereas the higher modes do not show dominant frequencies. Fig. 131b shows the same contour plot but only for the first 200 modes. There is a trend of the dominant frequencies to increase with higher modes. Furthermore, the frequencies associated to Strouhal numbers of 0.512 and to 0.207 are persisting in the frequency content up to higher modes.

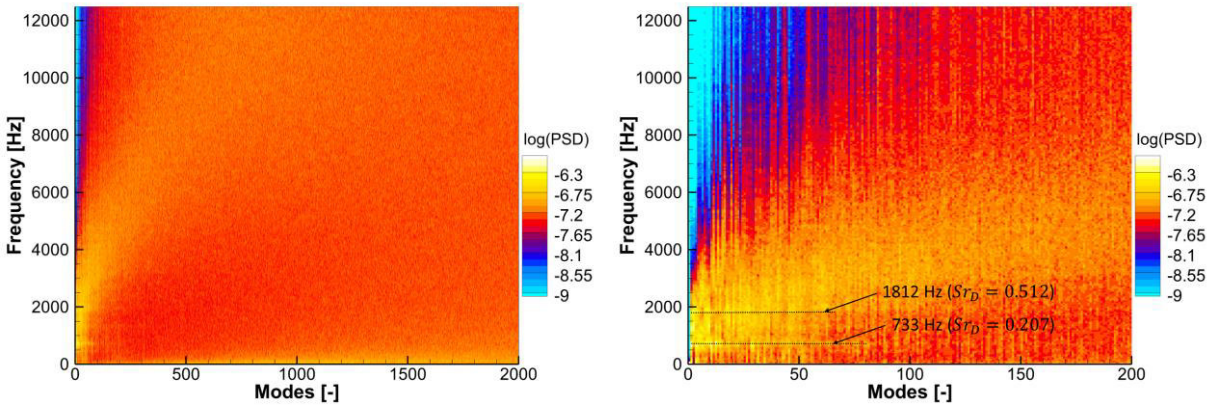

a) First 2000 modes b) First 200 modes

Fig. 131: Contour plot of Power Spectral Density of the first 2000 Modes (left) and the first 200 modes (right) ($M_\infty = 0.8$, $APR = 0.389$, $MFR = 6.52$ and $Re = 1.68 \times 10^6$)

To see if the frequencies found in the modes of the retro propulsion flow field can be directly related to frequencies in the jet, a PSD of the first 12 modes present in the jet, without counterflow, was performed. The result is shown in Fig. 132. It can be seen that there is only one dominant frequency at 7092 Hz. This frequency was not found in the PSD analysis of the retro propulsion jet (see Fig. 130). Hence, the frequencies in the retro propulsion flow field do not seem to come from frequencies in the jet. Fig. 133 shows the PSD of the first 12 modes of a run at Mach 0.8 without active jet, where several peaks can be observed. Also the Strouhal numbers of 0.194, 0.387 and 0.581 are close to the observed 0.207, 0.357 and 0.533 with active retro propulsion. Hence, these frequencies can be associated to an interaction of the vehicle with the free stream. To verify this, a POD was performed for a selected area around the base of the vehicle. The first four spatial modes are shown in Fig. 136 and the PSD of the first 12 modes of this selected area is shown in Fig. 134. The spatial modes reveal that the frequencies observed in the base area can be attributed to unsteady regions near the engines (white circles) which are presumably generated by vortices in these regions. Furthermore, strong unsteady modes can be observed upstream of the engines (black circle) resulting from pressure waves upstream of the base area, which can be seen in the snapshot of the Schlieren video in Fig. 135. Comparing the PSD of the flow field without active engine (no jet) in Fig. 133, with the PSD of the flow field with active jet in Fig. 130, it is apparent that the frequency peaks are much more pronounced in the case without active jet. Hence, if buffeting loads on the engines shall be reduced, it can be advisable to fly through the transonic regime with the engine active. In Fig. 137 the PSD is shown for several Mach number and APR combinations. The dominant frequencies of Sr_D of 0.2, 0.35, 0.5 and 1.5 are highlighted with lines. The bottom row shows the PSD for the condition without counterflow ($APR = 0$). One can see that frequency peaks are observable close to a Strouhal number of 0.2, 1.5 and 3 (harmonic of 1.5) for Mach 0.8. For Mach 0.6 and 0.7, only the Strouhal numbers close to 0.35 and 1.5 can be seen. The strongest frequency peaks for several Strouhal numbers can be observed for Mach 0.8. Interestingly, this is the Mach number at which also the strongest unsteady loads for near-wake flow configurations were observed [108]. For Mach 0.8 with active jet these frequencies are still

visible, however, as mentioned earlier, to a much smaller extent. It seems that the magnitude of the thrust level plays a subordinate role as the frequency content is comparable for all shown APRs. For the higher Mach number of 0.9, the characteristic Strouhal numbers of 0.2, 0.35 and 1.5 cannot be observed and the Strouhal number of 0.5 is not as strongly pronounced as for the lower Mach numbers. However, for this Mach number, in the active jet cases frequencies at Strouhal numbers around 0.15 and 0.25 are visible. In general, in the cases with active jet, the frequency content has a very similar appearance regardless of the Mach number or APR. Hence as for the pressure coefficients (see section 5.3.1) the activation of the jet seems to have a larger influence than the specific jet conditions. For all Mach numbers the presence of the jet seems to dampen the dominant frequencies which appear in the jet-off case.

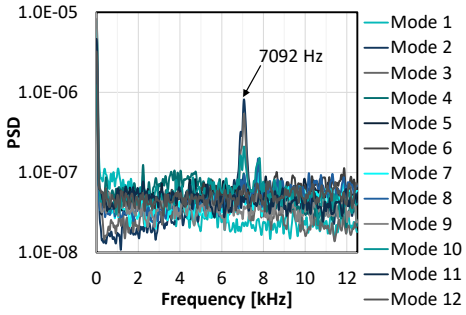

Fig. 132: Power Spectral Density of first 12 modes of jet flow at $APR = 0.387$ without counterflow

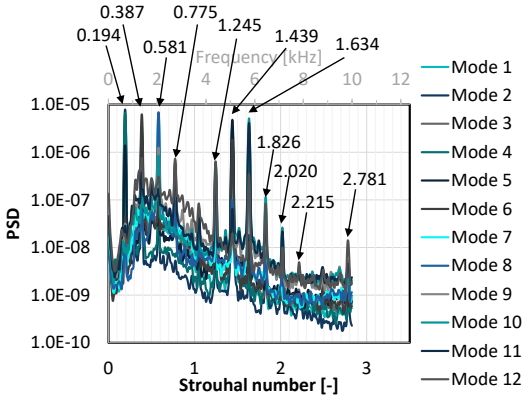

Fig. 133: Power Spectral Density of first 12 modes of the flow field with active wind tunnel at Mach 0.8 without active jet

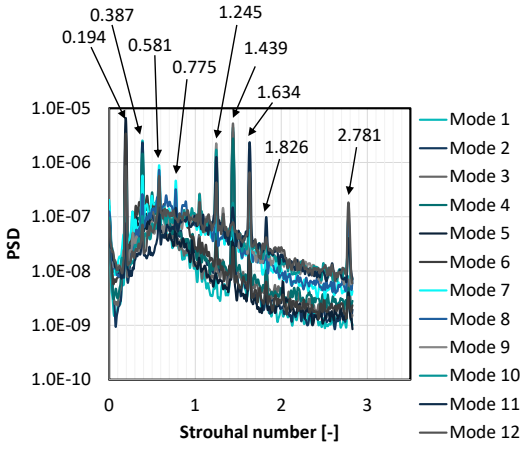

Fig. 134: Power Spectral Density of first 12 modes of the flow field detail with active wind tunnel at Mach 0.8 without active jet

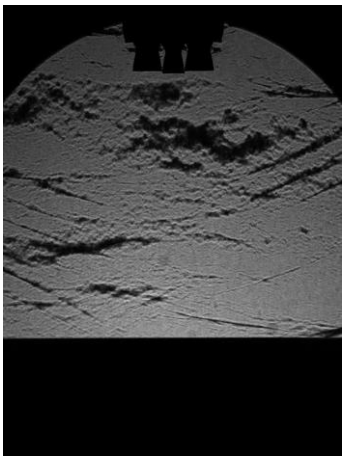

Fig. 135: Schlieren snapshot the flow field with active wind tunnel without active jet at Mach 0.8

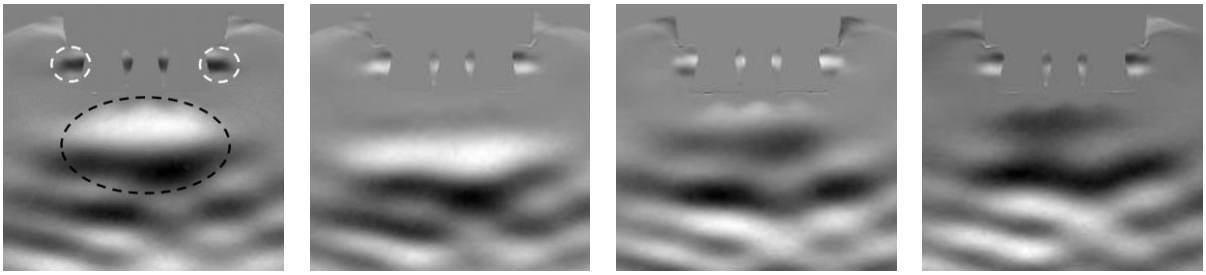

Mode 1 Mode 2 Mode 3 Mode 4

Fig. 136: First four modes of the flow in the base area at Mach 0.8 without active engine

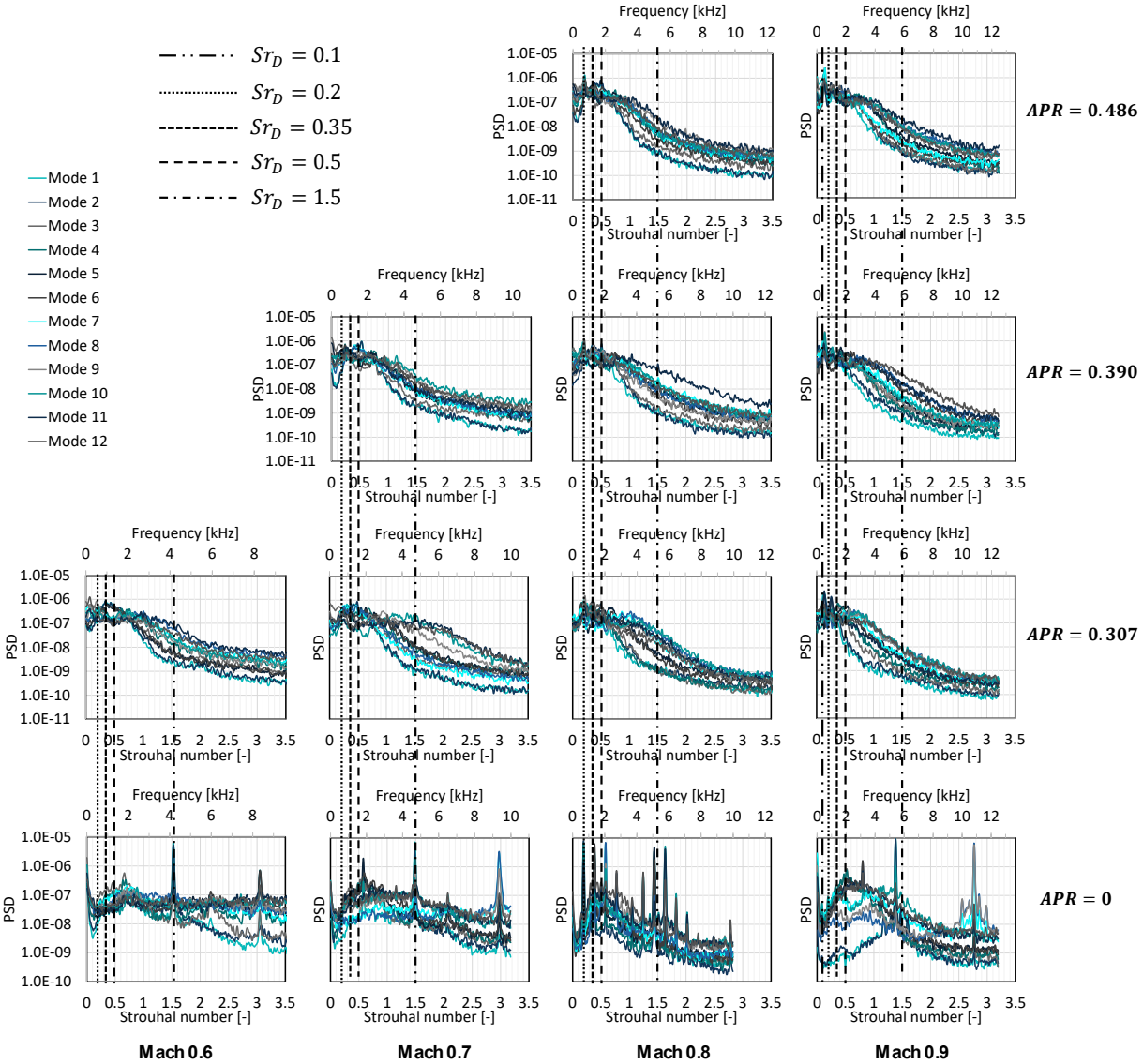

Fig. 137: Power Spectral Density first 12 Modes for several Mach number and APR conditions

Fig. 138 shows the PSD of the high frequency pressure measurements on the base of the wind tunnel model, where the mean value was subtracted before the PSD was performed. The PSD was performed over 20000 time steps with a Hann window of a width of 500 with a step size of 39

time steps between the spectra. The frequencies were again resolved with 2048 bins. The results are shown for the outer two circles of the instrumentation.

For the cases with no jet ($APR = 0$), mainly two normalized frequencies of 0.2 and 1.5 can be observed. However, the Strouhal number of 0.2 can only be observed for Mach 0.8. For all cases with active jet ($APR > 0$), the dominant normalized frequency of 0.2 is found. The reason could be that this frequency comes from the interaction of the jet with the free stream and is therefore absent in the cases with $APR = 0$. For Mach 0.8 the frequency is a combination of the interaction of the free stream with the jet and the strong dominant frequency present in the jet-off case. For Mach 0.9 the additional dominant frequency of 0.1 already found in the Schlieren videos can be observed. Neither the normalized frequency of 1.5, nor the other dominant frequencies which were found in the Schlieren videos (0.35 and 0.5) are observed in the jet-on cases. It seems that the observed frequencies are independent of the thrust level (APR), as for all Mach number and APR combinations the frequency content is very similar. This confirms the statement made above that activating the jet (igniting the engine), regardless of the thrust level, mitigates most frequencies. The peak at 0.2 persists, but it is less prominent.

Fig. 139 shows the root mean square values of the pressure fluctuation normalized with the dynamic pressure ($\frac{p'_{rms}}{q_\infty}$). As for the pressure coefficients (see section 5.3.1), the pressure fluctuations are clustered by the radial position of the sensors. The pressure fluctuations on the base area (ring 2) are higher than the ones around the shoulder (ring 3). For the case without active jet ($APR = 0$), the fluctuations generally decrease with increasing Mach number. For Mach 0.8 a slight peak in this decreasing trend can be observed, due to the strong dominant frequencies for this Mach number. For the cases with active jet, the fluctuations are relatively independent of the Mach number and keep at a level of 0.2 around the shoulder and 0.3 on the base area. Hence, while the activation of the jet mitigates the dominant frequencies, it does not lower the level of pressure fluctuations, but slightly increases it. The level of pressure fluctuations is one order of magnitude higher than in near-wake flows, which were measured to be between 0.06 for Mach 0.5 and 0.01 for Mach 0.9 [10]. This observation emphasizes the importance of the investigation of unsteady pressure loads during the landing burn.

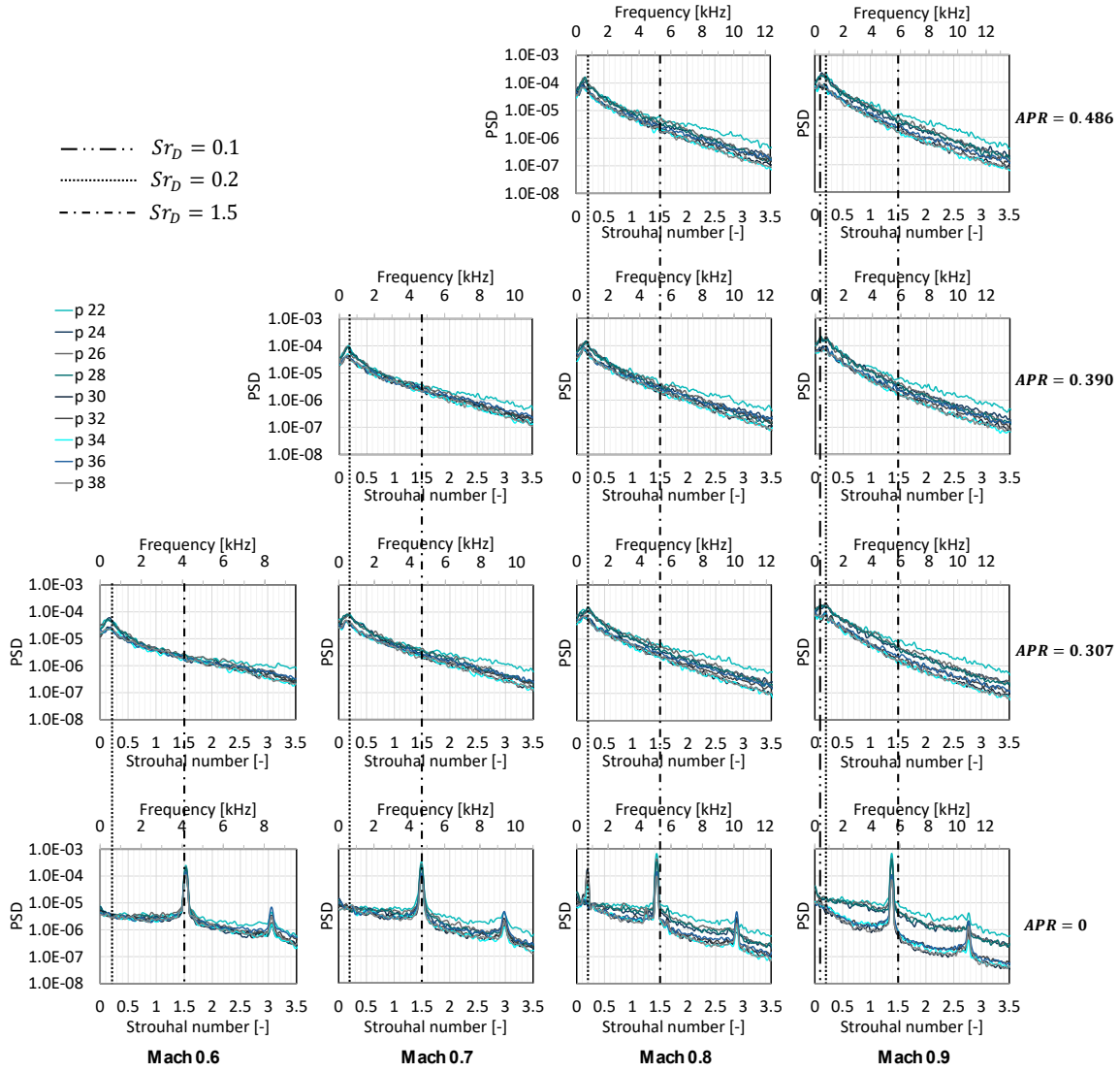

Fig. 138: Power Spectral Density of the high frequency pressure measurements in outer ring of the base for various Mach numbers and APRs

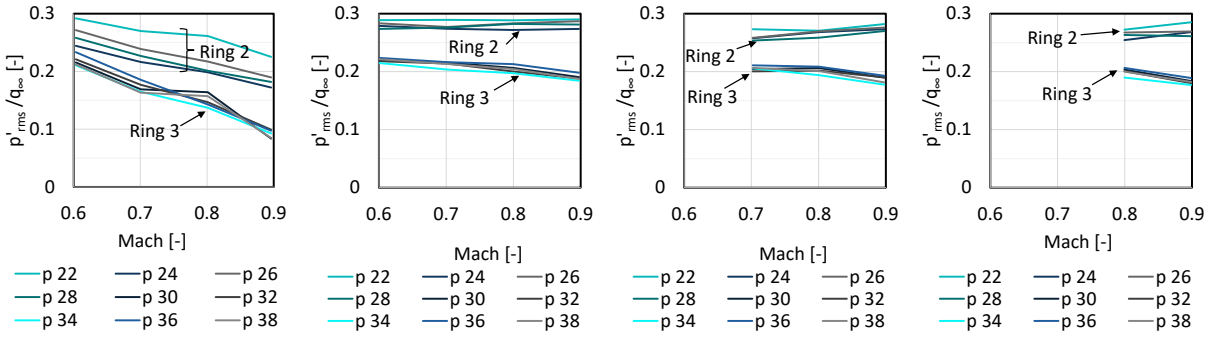

Fig. 139: Normalized rms base pressure fluctuation versus the free stream Mach number for several APR

The results discussed in this subsection can be summarized as follows. In the subsonic and transonic landing phase, strong dominant frequencies can be observed. The Strouhal numbers are around 0.1, 0.2, 0.35, 0.5 and 1.5. In the pressure measurements only 0.1, 0.2 and 1.5 were measured. In particular 0.2 is a critical Strouhal number as this frequency is known to have caused failures in the Ariane 5 ECA maiden flight. Active retro propulsion mitigates most of the strongly prominent frequencies. However, the normalized frequency of 0.2 persists. The pressure fluctuations are one order of magnitude higher than in the near-wake flows, independently of the activation of the jet.

5.3.3. Conclusions regarding the Landing Burn

The analysis of the subsonic retro propulsion flow fields showed that the Ambient Pressure Ratio (APR) is a good scaling parameter for the flow structure close to the engine, while the Momentum Flux Ratio (MFR) is a good scaling parameter for the larger scale flow features. This could be visualized with the aid of the average modal solution. Strouhal numbers of 0.2 and 1.5 could be observed in the subsonic phase of the landing approach, if the jet is not active. They are close to frequencies occurring in near-wake flows which are known to have caused high unsteady loads on the Ariane 5 ECA and are one possible reason for its failure during its maiden flight. The strongest frequency peaks were observed at Mach 0.8 which is the critical Mach number also observed for the near-wake flows. The dominant frequencies are mostly mitigated if the jet is activated. The normalized frequency of 0.2 persists, but is less prominent. Therefore, it could be advisable to start the landing burn at Mach numbers larger than 0.8 to mitigate buffeting loads on the engines in the last phase of the descent and landing. The normalized pressure fluctuations are between 0.2 and 0.3. They are slightly larger if the jet is active and are relatively independent of the thrust level of the jet.

6. Conclusion and Outlook

The work in this thesis investigated the three main flight phases during descent and landing of a vertically landing first stage with the aid of retro propulsion. The detailed conclusions for each phase were given in the respective sections. Here, the overall summary and outlook, and recommendations for the design of retro propulsive descending and landing launcher configurations are given.

In the aerodynamic phase, the main focus was laid on the analytical description of the flow conditions at the Aerodynamic Control Surfaces (ACS) and the trimmability of the configuration. With the methodology presented in section 5.1 the free stream conditions at the ACS can be estimated analytically. This methodology can be applied in the future in the design phase of vertically landing launcher configurations. It can be used for the sizing of the ACS and design decisions, as for example the definition of the maximum deflection angle of the ACS. Furthermore, if ACS shall be tested in wind tunnel facilities independently of the complete launcher configuration, the test conditions can be easily assessed.

For the reentry burn, it was shown that the main scaling parameter for Hypersonic Retro Propulsion (HRP) flow fields is the thrust coefficient. Furthermore, it was found that the total thrust coefficient is an adequate scaling parameter to scale the pressure coefficients between varying numbers of engines. Additionally, it was shown that the pressures at the base and in the wake of the first stage configuration scale well with the total pressure downstream of the normal portion of the bow shock. These investigations on the scaling parameters are useful for the generation of Aerodynamic Databases (AEDBs). Hence, the interpolation in AEDBs of Hypersonic Retro Propulsion maneuvers should be based on the thrust coefficient rather than on the Mach number. The scaling with the total pressure downstream of the normal portion of the bow shock can be used to interpolate or extrapolate pressures at the base and in the wake of the vehicle between Mach numbers. Furthermore, the similarity with the total thrust coefficient can be used in a first approach to apply AEDBs generated for a specific number of engines (3 in the case of RETALT1) to other configurations with differing numbers of engines. This is also helpful for the design of wind tunnel experiments as the blockage of the wind tunnel can be assessed in simplified axisymmetric CFD computations with one central engine and can then be translated to a higher number of active engines.

For the landing burn, the subsonic retro propulsion maneuver, it was found that the Ambient Pressure Ratio (APR) is an adequate scaling parameter for the exhaust plume in the vicinity of the nozzle exit, while the larger flow structures as the plume length is dominated by the Momentum Flux Ratio (MFR). As stated in section 2.6 the thrust coefficient and the MFR can be used interchangeably. Therefore, for the design of vertically landing first stages and for the design of wind tunnel experiments to test them, the expansion conditions at the nozzle exit should be scaled with the APR while the MFR should be considered for the jet in general. The interchangeability of the use of the thrust coefficient and the MFR can be applied for the design of the AEDBs for such configurations, as the MFR can therefore be used as universal scaling parameter for all retro

propulsive phases regardless of whether they appear in the hypersonic, supersonic or subsonic regime.

Regarding the unsteady phenomena during the reentry burn, it was found that, in the case of one active engine, vortex rings emerge from the Mach disc, which strongly alter the flow field, and contribute to asymmetric modes. Also a mechanism was proposed to explain the build-up of the vortex rings. For three active engines, the flow field is dominated by the switching mode between blunt and long penetration mode. Some dominant frequencies were found for the case with three active engines, which were not observed for the single-engine case. The level of pressure fluctuations is approximately two orders of magnitude lower than during the landing burn.

The flow field of subsonic retro propulsion flows was found to be highly unsteady. An averaged modal solution was proposed, and it was shown that it can capture the relevant flow features in these highly unsteady flow fields. In the subsonic retro propulsion flows strongly dominant frequencies were found which are in the same range as the critical frequencies known from near-wake flows. The most dominating frequencies were found at Mach 0.8. The most dominating frequency showed a Strouhal number of 0.2. It was found that the dominant frequencies are damped if the jet is activated. Also the level of pressure fluctuations normalized with the dynamic pressure was found to be high, in the range between 0.2 and 0.3, which is one order of magnitude higher than in near-wake flows.

From this analysis, it seems that for the dynamic loads the landing burn seems to be the sizing case, as the frequencies are more prominent than in the reentry burn. As the critical frequencies vanish in the case of active engines, it could be advisable to start the landing burn in the high subsonic regime and around a flight Mach number of 0.8, to mitigate high unsteady pressure loads. However, even though the dominating frequencies can be partly mitigated by the activation of the jet, the level of pressure fluctuations stays high.

Based on the findings described above, the necessary next steps and future investigations are proposed as follows. In future aerodynamic designs of launchers and experiments, the methodologies developed in this thesis can be applied together with the similarity parameters elaborated to achieve good similarity between experiments and flights. However, still some uncertainties remain regarding the scaling parameters. Vos et al. [49] have, for example shown that the heat capacity ratio is an important scaling parameter for retro propulsion maneuvers to extrapolate from experiment to flight. Therefore, further variations of the scaling parameters should be investigated to further enhance the extrapolation capabilities of wind tunnel experiments to flight. This is especially true for the cases with more than one active engine. The analysis of the unsteady flow features showed that critical frequencies could appear in flight. This should be verified in CFD computations of the flight configurations. It should also be verified if the found Strouhal numbers can be applied in a more general manner to other similar flight configurations. Ultimately, the development of dynamic models could enhance the understanding of the phenomena contributing to the found frequencies and for their predictability. To this aim, further experimental test series should be performed to broaden the available data and generalize the results.

Lastly, as mentioned in section 5.2.4 and 5.3.2, the experiments performed on the retro propulsion maneuvers were performed with ambient temperature air and heated air. However, the flow phenomena could change remarkably for hot cases with combustion products. Therefore, hot plume tests with combustion of hydrogen and oxygen or methane and oxygen should be performed in the future, to validate the data presented here and investigate further effects on the flow fields.

Bibliography

[1] Patureau de Mirand, A., Bahu, J.-M., and Louaas, E., "Ariane Next, a vision for a reusable cost efficient European rocket," *8th European Conference for Aeronautics and Space Sciences*, Madrid, Spain, 2019 https://www.eucass.eu/doi/EUCASS2019-0949.pdf.

[2] Stappert, S., Wilken, J., Bussler, L., Sippel, M., Karl, S., Klevanski, J., Hantz, C., Briese, L. E., and Schnepper, K., "European Next Reusable Ariane (ENTRAIN): A Multidisciplinary Study on a VTVL and a VTHL Booster Stage," *70th International Astronautical Congress*, Washington D.C., USA, 2019, https://elib.dlr.de/132865/.

[3] Dumke, M. and Theil, S., "Auto-Coded Flight Software for the GNC VTVL Demonstrator EAGLE," *8th European Conference for Aeronautics and Space Sciences*, Madrid, Spain, 2019, https://www.eucass.eu/doi/EUCASS2019-0772.pdf.

[4] Rmili, B., Monchaux, D., Bosineau, O., Hassin, J., Querry, S., Besson, S., Poirey, G., Boré, R., Hamada, I., Amrouchi, H., Franc, J., Barreau, M., Mercadié, N., Labois, T., and Grinco, D., "FROG, a Rocket for GNC demonstrations: Firsts flights attempts of the FROG turbojet version and preparation of the future mono-propellant rocket engine," *8th European Conference for Aeronautics and Space Sciences*, Madrid, Spain, 2019, https://www.eucass.eu/doi/EUCASS2019-0197.pdf.

[5] Neculaescu, A.-M., Marin, A., Toader, A., Persinaru, A.-G., Cismilianu, A.-M., Tudose, M., Munteanu, C.-E., Popescu, I., Strauch, H., and Dussy, S., "System Identification and Testing for a VTVL vehicle", 8th European Conference for Aeronautics and Space Sciences," *8th European Conference for Aeronautics and Space Sciences*, 2019, https://www.eucass.eu/doi/EUCASS2019-0925.pdf.

[6] Kirchheck, D., Marwege, A., Klevanski, J., Riehmer, J., Gülhan, A., Karl, S., and Gloth, O., "Validation of Wind Tunnel Test and CFD Technologies for Retro-Propulsion (RETPRO): Overview of a Project within the Future Launcher Preparatory Programme (FLPP)," *International Conference on Flight Vehicles, Aerothermodynamics and Re-entry Missions & Engineering*, 2019, https://elib.dlr.de/137501/1/FAR2019_Kirchheck.pdf.

[7] Dumont, E., Ishimoto, S., Tatiossian, P., Klevanski, J., Reimann, B., Ecker, T., Witte, L., Riehmer, J., Sagliano, M., Giagkozoglou Vincenzino, S., Petkov, I., Rot, Auml, Rmel, W., Schwarz, R., eacute, Seelbinder, D., Markgraf, M., Sommer, J., Pfau, D., and Martens, H., "CALLISTO: A Demonstrator for Reusable Launcher Key Technologies," *Transactions of the japan society for aeronautical and space sciences, aerospace technology japan,* Vol. 19, No. 1, 2021, pp. 106-115, https://doi.org/10.2322/tastj.19.106.

[8] Vila, J. and Hassin, J., "Technology acceleration process for the Themis low cost and reusable prototype," *8th European Conference for Aeronautics and Space Sciences*, Madrid, Spain, 2019, https://www.eucass.eu/doi/EUCASS2019-0097.pdf.

[9] Anderson, J. D., *Fundamentals of Aerodynamics*, 5 ed., McGraw-Hill, 2011.

[10] Saile, D., *Experimental Analysis on Near-Wake Flows of Space Transportation Systems*, Forschungsbericht, Vol. 04, Rheinisch-Westfälische Technische Hochschule Aachen (RWTH), Aachen, 2019, https://elib.dlr.de/130993/.

[11] Anderson, J. D., *Hypersonic and high temperature gas dynamics*, 2 ed., AIAA, 2006.

[12] Daub, D., Willems, S., and Gülhan, A., "Experiments on aerothermoelastic fluid–structure interaction in hypersonic flow," *Journal of Sound and Vibration,* Vol. 531, 2022, p. 116714, https://doi.org/10.1016/j.jsv.2021.116714.

[13] Clemens, N. T. and Narayanaswamy, V., "Low-Frequency Unsteadiness of Shock Wave/Turbulent Boundary Layer Interactions," *Annual Review of Fluid Mechanics,* Vol. 46, No. 1, 2014, pp. 469-492, https://doi.org/10.1146/annurev-fluid-010313-141346.

[14] Gadd, G. E., "Interactions between shock waves and boundary layers," *Grenzschichtforschung / Boundary Layer Research*. Springer, Berlin, Heidelberg, Germany, 1958, pp. 239-255, https://doi.org/10.1007/978-3-642-45885-9_20.

[15] Verma, S. B. and Manisankar, C., "Shockwave/Boundary-Layer Interaction Control on a Compression Ramp Using Steady Micro Jets," *AIAA Journal,* Vol. 50, No. 12, 2012, pp. 2753-2764, https://doi.org/10.2514/1.J051577.

[16] Souverein, L. J., Bakker, P. G., and Dupont, P., "A scaling analysis for turbulent shock-wave/boundary-layer interactions," *Journal of Fluid Mechanics,* Vol. 714, 2013, pp. 505-535, https://doi.org/10.1017/jfm.2012.495.

[17] Sakurai, A., "On the Propagation and Structure of a Blast Wave, II," *Journal of the Physical Society of Japan,* Vol. 9, No. 2, 1954, pp. 256-266, https://doi.org/10.1143/JPSJ.9.256.

[18] Sakurai, A., "On the Propagation and Structure of the Blast Wave, I," *Journal of the Physical Society of Japan,* Vol. 8, No. 5, 1953, pp. 662-669, https://doi.org/10.1143/JPSJ.8.662.

[19] Lukasiewicz, J., "Blast-Hypersonic Flow Analogy Theory and Application," *ARS Journal,* Vol. 32, No. 9, 1962, pp. 1341-1346, https://doi.org/10.2514/8.6281.

[20] Van Hise, V., *Analytic study of induced pressure on long bodies of revolution with varying nose bluntness at hypersonic speeds*, National Aeronautics and Space Administration, 1961, https://ntrs.nasa.gov/citations/19980223577.

[21] Lees, L., "Hypersonic Flow," *Journal of Spacecraft and Rockets,* Vol. 40, No. 5, 2003, pp. 700-735, https://doi.org/10.2514/2.6897. Reprint from IAS-RAeS Proceedings - 1955.

[22] Seltner, P., Willems, S., and Gülhan, A., "Experimental determination of aerodynamic coefficients of simple-shape d bodies free-flying in hypersonic flow," *International Conference on High-Speed Vehicle Science Technology (HiSST 2018)*, Moscow, Russia, 2018, https://elib.dlr.de/124113/.

[23] Frey, M., "Behandlung von Strömungsproblemen in Raketendüsen bei Überexpansion," Dissertation, Universität Stuttgart, Institut für Aerodynamik und Gasdynamik, 2001, https://elib.dlr.de/1519/.

[24] Stark, R. and Wagner, B., "Experimental study of boundary layer separation in truncated ideal contour nozzles," *Shock Waves,* Vol. 19, No. 3, 2009, pp. 185-191, https://doi.org/10.1007/s00193-008-0174-6.

[25] Olivier, H., *Gasdynamik*, Lehr- und Forschungsgebiet Hochtemperatur-Gasdynamik, Stoßwellenlabor, Rheinisch-Westfälische Technische Hochschule Aachen, 2015.

[26] Owston, R., Magi, V., and Abraham, J., "Fuel-Air Mixing Characteristics of DI Hydrogen Jets," *SAE International Journal of Engines,* Vol. 1, No. 1, 2009, pp. 693-712, http://www.jstor.org/stable/26308313.

[27] Crist, S., Glass, D. R., and Sherman, P. M., "Study of the highly underexpanded sonic jet," *AIAA Journal,* Vol. 4, No. 1, 1966, pp. 68-71, https://doi.org/10.2514/3.3386.

[28] Korzun, A. M., Braun, R. D., and Cruz, J. R., "Survey of Supersonic Retropropulsion Technology for Mars Entry, Descent, and Landing," *Journal of Spacecraft and Rockets,* Vol. 46, No. 5, 2009, pp. 929-937, https://doi.org/10.2514/1.41161.

[29] Edquist, K. T., Korzun, A. M., Kleb, W. L., Hawke, V., Rizk, Y. M., Olsen, M. E., and Canabal, F., "Model Design and Pre-Test CFD Analysis for a Supersonic Retropropulsion Wind Tunnel Test," *AIAA Scitech 2020 Forum*, 2020, https://doi.org/10.2514/6.2020-2230.

[30] Korzun, A. M. and Cassel, L. A., "Scaling and Similitude in Single Nozzle Supersonic Retropropulsion Aerodynamics Interference," *AIAA Scitech 2020 Forum*, 2020, https://doi.org/10.2514/6.2020-0039.

[31] Korzun, A. M., Nielsen, E., Walden, A., Jones, W., Carlson, J.-R., Moran, P., Henze, C., and Sandstrom, T., "Computational Investigation of Retropropulsion Operating Environments

with a Massively Parallel Detached Eddy Simulation Approach," *ASCEND 2020*, 2020, https://doi.org/10.2514/6.2020-4228.

[32] Shafner, J. and Korzun, A. M., "Computational Analysis of a Multiple-Nozzle Supersonic Retropropulsion Configuration," *AIAA AVIATION 2021 FORUM*, 2021, https://doi.org/10.2514/6.2021-2556.

[33] Edquist, K. T., "Status of Mars Retropropulsion Testing in the Langley Unitary Plan Wind Tunnel," *AIAA Scitech 2022 Forum*, 2022, https://doi.org/10.2514/6.2022-0911.

[34] Edquist, K. T., Alter, S. J., Glass, C. E., Kleb, W. L., Korzun, A. M., Wood, W. A., Canabal, F., Childs, R., Halstrom, L. D., and Matsuno, K. V., "Computational Modeling of Mars Retropropulsion Concepts in the Langley Unitary Plan Wind Tunnel," *AIAA Scitech 2022 Forum*, 2022, https://doi.org/10.2514/6.2022-0912.

[35] Halstrom, L. D., Pulliam, T. H., Childs, R., and Stremel, P., "OVERFLOW Analysis of Supersonic Retropropulsion Testing on a Blunt Mars Entry Vehicle Concept," *AIAA Scitech 2022 Forum*, 2022, https://doi.org/10.2514/6.2022-0914.

[36] Korzun, A. M. and Edquist, K. T., "Development Status of Powered Descent for High-Mass Mars, Descent, and Landing Systems," *2nd International Conference on Flight Vehicles, Aerothermodynamics and Re-entry Missions and Engineering*, Heilbronn, Germany, 2022.

[37] Korzun, A. M., Nastac, G., Walden, A., Nielsen, E. J., Jones, W. T., and Moran, P., "Application of a Detached Eddy Simulation Approach with Finite-Rate Chemistry to Mars-Relevant Retropropulsion Operating Environments," *AIAA Scitech 2022 Forum*, 2022, https://doi.org/10.2514/6.2022-2298.

[38] Matsuno, K., Childs, R., Pulliam, T. H., Stremel, P., and Garcia, J. A., "OVERFLOW Analysis of Supersonic Retropropulsion Testing on the CobraMRV Mars Entry Vehicle Concept," *AIAA Scitech 2022 Forum*, 2022, https://doi.org/10.2514/6.2022-0913.

[39] Nastac, G., Korzun, A. M., Walden, A., Nielsen, E. J., Jones, W. T., and Moran, P., "Computational Investigation of the Effect of Chemistry on Mars Supersonic Retropropulsion Environments," *AIAA Scitech 2022 Forum*, 2022, https://doi.org/10.2514/6.2022-2299.

[40] Codoni, J. R. and Berry, S. A., "Supersonic Retropropulsion Dynamic Data Analysis from NASA Langley Unitary Plan Wind Tunnel," *Journal of Spacecraft and Rockets,* Vol. 51, No. 3, 2014, pp. 715-723, 10.2514/1.A32619.

[41] Berry, S. A., Rhode, M. N., and Edquist, K., "Supersonic Retropropulsion Validation Experiment in the NASA Langley Unitary Plan Wind Tunnel," *Journal of Spacecraft and Rockets,* Vol. 51, No. 3, 2014, pp. 664-679, https://doi.org/10.2514/1.A32649.

[42] Korzun, A. M. and Braun, R. D., "Conceptual Modeling of Supersonic Retropropulsion Flow Interactions and Relationships to System Performance," *Journal of Spacecraft and Rockets,* Vol. 50, No. 6, 2013, pp. 1121-1133, https://doi.org/10.2514/1.A32464.

[43] Cordell, C. E. and Braun, R. D., "Analytical Modeling of Supersonic Retropropulsion Plume Structures," *Journal of Spacecraft and Rockets,* Vol. 50, No. 4, 2013, pp. 763-770, https://doi.org/10.2514/1.A32391.

[44] Finley, P. J., "The flow of a jet from a body opposing a supersonic free stream," *Journal of Fluid Mechanics,* Vol. 26, No. 2, 1966, pp. 337-368, https://doi.org/10.1017/S0022112066001277.

[45] Jarvinen, P. O. and Adams, R. H., "The aerodynamic characteristics of large angled cones with retrorockets," CR-124720, NASA, 1970, https://ntrs.nasa.gov/citations/19720005324.

[46] Ecker, T., Ertl, M., Klevanski, J., Krummen, S., and Dumont, E., "Aerothermal characterization of the CALLISTO vehicle during descent," *9 th European Conference for*

Aeronautics and Aerospace Sciences (EUCASS), Lille, France, 2022, https://elib.dlr.de/187034/.

[47] Ecker, T., Zilker, F., Dumont, E., Karl, S., and Hannemann, K., "Aerothermal Analysis of Reusable Launcher Systems during Retro-Propulsion Reentry and Landing," *Space Propulsion Conference 2018*, Sevilla, Spain, 2018, https://elib.dlr.de/120072/.

[48] Zilker, F., "Aerothermal Analysis of Re-usable First Stage during Rocket Retro-propulsion," Master Thesis, 2018, https://elib.dlr.de/119265/.

[49] Vos, J., Charbonnier, D., Marwege, A., Hantz, C., and Guelhan, A., "CFD Simulations and Wind Tunnel Experiments for Re-usable Launch Vehicles," *2nd International Conference on Flight Vehicles, Aerothermodynamics and Re-entry Missions and Engineering*, Heibronn, Germany, 2022, https://doi.org/10.5281/zenodo.6759393.

[50] Vos, J., Charbonnier, D., Marwege, A., Guelhan, A., Laureti, M., and Karl, S., "Aerodynamic investigations of a Vertical Landing Launcher configuration by means of Computational Fluid Dynamics and Wind Tunnel Tests," *AIAA Scitech 2022 Forum*, San Diego, CA & Virtual, 2022, https://doi.org/10.2514/6.2022-1308.

[51] Marwege, A., Kirchheck, D., Klevanski, J., and Gülhan, A., "Hypersonic retro propulsion for reusable launch vehicles tested in the H2K wind tunnel," *CEAS Space Journal,* Vol. 14, No. 3, 2022, pp. 473-499, https://doi.org/10.1007/s12567-022-00457-w.

[52] Marwege, A., Hantz, C., Kirchheck, D., Klevanski, J., Vos, J., Laureti, M., Karl, S., and Gülhan, A., "Aerodynamic Phenomena of Retro Propulsion Descent and Landing Configurations," *2nd International Conference on Flight Vehicles, Aerothermodynamics and Re-entry Missions and Engineering*, Heibronn, Germany, 2022, https://doi.org/10.5281/zenodo.6783922.

[53] Marwege, A., Hantz, C., Kirchheck, D., Klevanski, J., Gülhan, A., Charbonnier, D., and Vos, J., "Wind tunnel experiments of interstage segments used for aerodynamic control of retro-propulsion assisted landing vehicles," *CEAS Space Journal,* Vol. 14, No. 3, 2022, pp. 447-471, https://doi.org/10.1007/s12567-022-00425-4.

[54] Laureti, M., Karl, S., Marwege, A., and Guelhan, A., "Aerothermal Databases and CFD Based Load Predictions," *2nd International Conference on Flight Vehicles, Aerothermodynamics and Re-entry Missions and Engineering*, Heibronn, Germany, 2022, https://doi.org/10.5281/zenodo.6759561.

[55] Laureti, M. and Karl, S., "Aerothermal databases and load predictions for Retro Propulsion-Assisted Launch Vehicles (RETALT)," *CEAS Space Journal,* Vol. 14, No. 3, 2022, pp. 501-515, https://doi.org/10.1007/s12567-021-00413-0.

[56] Charbonnier, D., Vos, J., Marwege, A., and Hantz, C., "Computational fluid dynamics investigations of aerodynamic control surfaces of a vertical landing configuration," *CEAS Space Journal,* Vol. 14, No. 3, 2022, pp. 517–532, https://doi.org/10.1007/s12567-022-00431-6.

[57] Bouarfa, M., Bourgoing, A., Carrat, J.-M., Puech, D., Jubera, M., and Brenner, P., "CFD retro-propulsion simulation with FLUSEPA code," *2nd International Conference on Flight Vehicles, Aerothermodynamics and Re-entry Missions and Engineering*, Heilbronn, Germany, 2022.

[58] Scarlatella, G., Tajmar, M., and Bach, C., "Advanced Nozzle Concepts in retro-propulsion applications for Reusable Launch Vehicle recovery: a case study," *72nd International Astronautical Congress (IAC)*, Dubai, UAE, 2021.

[59] Scarlatella, G., Sieder-Katzmann, J., Roßberg, F., Weber, F., Mancera, C. T., Bianchi, D., Tajmar, M., and Bach, C., "Design and Development of a Cold-Flow Test-Bench for Study of Advanced Nozzles in Subsonic Counter-Flows," *Aerotecnica Missili & Spazio,* 2022, https://doi.org/10.1007/s42496-022-00117-6.

[60] Ghosh, D. and Gunasekaran, H., "Large Eddy Simulation (LES) of Aerospike Nozzle assisted Supersonic Retro-Propulsion (SRP)," *AIAA Aviation 2021 Forum*, 2021, https://doi.org/10.2514/6.2021-2489.

[61] Mejia, N. A. and Schmidt, B. E., "Experimental Investigation of Flow Interaction Dynamics in Supersonic Retropropulsion," *Journal of Spacecraft and Rockets,* Vol. 59, No. 5, 2022, pp. 1753-1762, https://doi.org/10.2514/1.A35228.

[62] Huang, W., "A survey of drag and heat reduction in supersonic flows by a counterflowing jet and its combinations," *Journal of Zhejiang University-SCIENCE A,* Vol. 16, No. 7, 2015, pp. 551-561, https://doi.org/10.1631/jzus.A1500021.

[63] Kirchheck, D., Marwege, A., Klevanski, J., and Gülhan, A., "Hypersonic Retrograde Propulsion Experiments–A Basis for Validation of CFD within RETPRO," *9th European Conference for Aeronautics and Space Sciences (EUCASS)*, Lille, France, 2022, https://elib.dlr.de/190741/.

[64] Venkatachari, B. S., Mullane, M., Cheng, G., and Chang, C.-L., "Numerical Study of Counterflowing Jet Effects on Supersonic Slender-Body Configurations," *33rd AIAA Applied Aerodynamics Conference*, 2015, https://doi.org/10.2514/6.2015-3010.

[65] Gutsche, K., Marwege, A., and Gülhan, A., "Similarity and Key Parameters of Retropropulsion Assisted Deceleration in Hypersonic Wind Tunnels," *Journal of Spacecraft and Rockets,* Vol. 58, No. 4, 2021, pp. 984-996, https://doi.org/10.2514/1.A34910.

[66] Desai, S., K, V. P., Kulkarni, V., and Gadgil, H., "Universal scaling parameter for a counter jet drag reduction technique in supersonic flows," *Physics of Fluids,* Vol. 32, No. 3, 2020, p. 036105, 10.1063/1.5140029.

[67] Jarvinen, P. O. and Hill, J. A. F., "Penetration of retrorocket exhausts into subsonic counterflows," *Journal of Spacecraft and Rockets,* Vol. 10, No. 1, 1973, pp. 85-86, https://doi.org/10.2514/3.27737.

[68] Daso, E. O., Pritchett, V. E., Wang, T.-S., Ota, D. K., Blankson, I. M., and Auslender, A. H., "Dynamics of Shock Dispersion and Interactions in Supersonic Freestreams with Counterflowing Jets," *AIAA Journal,* Vol. 47, No. 6, 2009, pp. 1313-1326, https://doi.org/10.2514/1.30084.

[69] Berry, S. A., Rhode, M. N., and Edquist, K. T., "Supersonic Retropropulsion Experimental Results from NASA Ames 9×7 Foot Supersonic Wind Tunnel," *Journal of Spacecraft and Rockets,* Vol. 51, No. 3, 2014, pp. 724-734, https://doi.org/10.2514/1.A32650.

[70] Cordell, C. E., "Computational fluid dynamics and analytical modeling of supersonic retropropulsion flowfield structures across a wide range of potential vehicle configurations," Georgia Institute of Technology, 2013.

[71] Bathel, B. F., Litzner, C. R., Jones, S. B., Berry, S. A., Smith, N. T., and Garbeff II, T. J., "High-Speed Schlieren Analysis of Retropropulsion Jet in Mach 10 Flow," *Journal of Spacecraft and Rockets,* Vol. 57, No. 1, 2020, pp. 33-48, https://doi.org/10.2514/1.A34522.

[72] Montgomery, K. A., Bruce, P. J., and Navarro-Martinez, S., "Dynamics of varying thrust coefficients for supersonic retropropulsion during Mars EDL," *AIAA Scitech 2022 Forum*, 2022, https://doi.org/10.2514/6.2022-0935.

[73] Chen, L.-W., Wang, G.-L., and Lu, X.-Y., "Numerical investigation of a jet from a blunt body opposing a supersonic flow," *Journal of Fluid Mechanics,* Vol. 684, 2011, pp. 85-110, https://doi.org/10.1017/jfm.2011.276.

[74] Schauerhamer, D. G., Zarchi, K. A., Kleb, W. L., Carlson, J.-R., and Edquist, K. T., "Supersonic Retropropulsion Computational Fluid Dynamics Validation with Langley 4×4 Foot Test Data," *Journal of Spacecraft and Rockets,* Vol. 51, No. 3, 2014, pp. 693-714, https://doi.org/10.2514/1.A32693.

[75] Marwege, A., Gülhan, A., Klevanski, J., Riehmer, J., Karl, S., Kirchheck, D., Bonetti, D., Vos, J., Jevons, M., Krammer, A., and Carvalho, J., "Retro Propulsion Assisted Landing Technologies (RETALT): Current Status and Outlook of the EU funded project on Reusable Launch Vehicles," Washington D.C., USA, 2019, https://doi.org/10.5281/zenodo.5770046.

[76] "Website Blue Origin." https://www.blueorigin.com/new-glenn/ (accessed.

[77] Marwege, A., Gülhan, A., Klevanski, J., Hantz, C., Karl, S., Laureti, M., De Zaiacomo, G., Vos, J., Jevons, M., Thies, C., Krammer, A., Lichtenberger, M., Carvalho, J., and Paixão, S., "RETALT: review of technologies and overview of design changes," *CEAS Space Journal,* Vol. 14, No. 3, 2022, pp. 433-445, https://doi.org/10.1007/s12567-022-00458-9.

[78] Klevanski, J., Ecker, T., Riehmer, J., Reimann, B., Dumont, E., and Chavagnace, C., "Aerodynamic Studies in Preparation for CALLISTO - Reusable VTVL Launcher First Stage Demonstrator," *69th International Astronautical Congress (IAC)*, Bremen, Germany, 2018, https://elib.dlr.de/122062/.

[79] De Zaiacomo, G., Blanco Arnao, G., Bunt, R., and Bonetti, D., "Mission engineering for the RETALT VTVL launcher," *CEAS Space Journal,* Vol. 14, No. 3, 2022, pp. 533-549, https://doi.org/10.1007/s12567-021-00415-y.

[80] "Vulcain 2 ESA." https://www.esa.int/Enabling_Support/Space_Transportation/Launch_vehicles/Ariane_5_ECA (accessed 22.05.2023).

[81] "Website Vulcain 2." http://cs.astrium.eads.net:80/sp/launcher-propulsion/rocket-engines/vulcain-2-rocket-engine.html (accessed 05.12.2015).

[82] Stark, R., "Beitrag zum Verständnis der Strömungsablösung in Raketendüsen," Dissertation, RWTH Aachen, 2010. [Online]. Available: https://elib.dlr.de/69234/. [Online]. Available: https://elib.dlr.de/69234/

[83] Arnold, R., Suslov, D., and Haidn, O., "Convective and Film Cooled Nozzle Extension for a High Pressure Rocket Subscale Combustion Chamber," *48th AIAA Aerospace Sciences Meeting Including the New Horizons Forum and Aerospace Exposition*, Orlando, Florida, 2010, https://doi.org/10.2514/6.2010-1150.

[84] Ponomarenko, A., *Rocket Propolsion Analysis*, User Manual, Version 2.2, 2015, http://w.lpre.de/manual/index.htm.

[85] Miketta, M., "Bedienungshinweise für die Trisonische Meßstrecke Köln -TMK-," DLR, Cologne, 2007.

[86] Esch, H., "Die 0.6-m x 0.6-m – Trisonische Meßstrecke (TMK) der DFVLR in Köln-Porz (Stand 1986)," DFVLR, Cologne, Germany, 1986.

[87] Niezgodka, F.-J., "Der Hyperschallwindkanal H2K des DLR in Köln-Porz (Stand 2000)," DLR, Cologne, Germany, 2001.

[88] Kirchheck, D., Saile, D., and Gülhan, A., "Rocket Wake Flow Interaction Testing in the Hot Plume Testing Facility (HPTF) Cologne," *Future Space-Transport-System Components under High Thermal and Mechanical Loads: Results from the DFG Collaborative Research Center TRR40*. Springer International Publishing, Cham, 2021, pp. 145-162, https://doi.org/10.1007/978-3-030-53847-7_9.

[89] Daub, D., *Experimental Investigation of Supersonic Fluid-Structure Interaction for Future Space Transportation Systems*, Forschungsbericht, Rheinisch-Westfälische Technische Hochschule Aachen (RWTH), Aachen, 2023, https://doi.org/10.57676/cbaa-ce26.

[90] Marwege, A., Riehmer, J., Klevanski, J., Gülhan, A., and Dumont, E., "Wind Tunnel investigations in CALLISTO - Reusable VTVL Launcher First Stage Demonstrator," *70th International Astronautical Congress (IAC)*, Washington D.C., United States, 2019, https://elib.dlr.de/132573/.

[91] Riehmer, J., Marwege, A., Klevanski, J., Gülhan, A., and Dumont, E., "Subsonic and Supersonic Ground Experiments for the CALLISTO VTVL Launc her Demonstrator," *International Conference on Flight Vehicles, Aerothermodynamics and Re-entry Missions & Engineering*, Monopoli, Italy, 2019, https://elib.dlr.de/140709/.

[92] *DIN 1319-4: Grundlagen der Meßtechnik*, Teil 4: Auswertung von Messungen Meßunsicherheit, Beuth Verlag, Berlin, 1999.

[93] Gawehn, T., Schleutker, T., and Gülhan, A., "Capsule aerodynamics and shock-wave boundary layer interaction (SBLI) in supersonic and transonic flow," *Experiments in Fluids,* Vol. 63, No. 3, 2022, p. 61, https://doi.org/10.1007/s00348-022-03392-y.

[94] Willems, S., "Strömung-Struktur-Wechselwirkung in Überschallströmungen," Deutsches Zentrum für Luft- und Raumfahrt e.V., 2017, https://elib.dlr.de/116735/.

[95] Gutsche, K., "Experimental and Numerical Study of Launcher Configurations with Retro-Propulsion in the Hypersonic Wind Tunnel Cologne H2K," Masterarbeit, Institute of Aerodynamics and Flow Technology, Supersonic and Hypersonic Technologies, Deutsches Zentrum für Luft- und Raumfahrt e.V. (DLR), 2020. [Online]. Available: https://elib.dlr.de/140499/. [Online]. Available: https://elib.dlr.de/140499/

[96] Böge, A. and Böge, W., *Handbuch Maschinenbau*, 22 ed., Springer Fachmedien Wiesbaden, Wiesbaden, Germany, 2014, https://doi.org/10.1007/978-3-658-06598-0.

[97] Brunton, S. L. and Kutz, J. N., *Data-Driven Science and Engineering: Machine Learning, Dynamical Systems, and Control*, Cambridge University Press, Cambridge, 2019, https://doi.org/10.1017/9781108380690.

[98] Anderson, J., Jr., "A survey of modern research in hypersonic aerodynamics," *17th Fluid Dynamics, Plasma Dynamics, and Lasers Conference*, https://doi.org/10.2514/6.1984-1578.

[99] Jarvinen, P. O., Luce, R. W., and Wachsler, E., "Propulsion Re-Entry Aerodynamics, CR-124720," MITHRAS, a division of Sanders Associates, Inc., MITHRAS Report No. MC68-3001-R1 (BNY), Cambridge, Mass., USA, 1968.

[100] Korst, H. H., "A Theory for Base Pressures in Transonic and Supersonic Flow," *Journal of Applied Mechanics,* Vol. 23, No. 4, 2021, pp. 593-600, https://doi.org/10.1115/1.4011405.

[101] Chapman, D. R., Kuehn, D. M., and Larson, H. K., "Investigation of separated flows in supersonic and subsonic streams with emphasis on the effect of transition," 1958.

[102] Didden, N., "On the formation of vortex rings: Rolling-up and production of circulation," *Zeitschrift für angewandte Mathematik und Physik ZAMP,* Vol. 30, No. 1, 1979, pp. 101-116, https://doi.org/10.1007/BF01597484.

[103] Montgomery, K. "Video of DNS computation posted on LinkedIn." LinkedIn. https://www.linkedin.com/posts/kieran-montgomery-38abb2210_aiaascitech-activity-6890063017288048640-AoAT (accessed 25 February).

[104] Love, E. S., Grigsby, C. E., Lee, L. P., and Woodling, M. J., "Experimental and theoretical studies of axisymmetric fee jets," NASA, no. 4170, 1959, https://ntrs.nasa.gov/citations/19980228067.

[105] Charwat, A. F., "Boundary of underexpanded axisymmetric jets issuing into still air," *AIAA Journal,* Vol. 2, No. 1, 1964, pp. 161-163, https://doi.org/10.2514/3.2256.

[106] Bykerk, T., Fechter, S., Kirchheck, D., and Karl, S., "Condensation Modelling of Expanding Cold Gas Jets during Hypersonic Retro-Propulsion Manoeuvres within the RETPRO Project," *23rd Australasian Fluid Mechanics Conference (23AFMC)*, Sydney, Australia, 2022.

[107] Noack, B. R., Afanasiev, K., Morzynski, M., Tadmor, G., and Thiele, F., "A hierarchy of low-dimensional models for the transient and post-transient cylinder wake," *Journal of Fluid Mechanics,* Vol. 497, 2003, pp. 335-363, https://doi.org/10.1017/S0022112003006694.

[108] Saile, D. and Gülhan, A., "Aeroacoustic Coupling Effect During the Ascent of Space Transportation Systems," *AIAA Journal,* Vol. 59, No. 7, 2021, pp. 2346-2356, https://doi.org/10.2514/1.J059747.

[109] Statnikov, V., Meinke, M., and Schröder, W., "Reduced-order analysis of buffet flow of space launchers," *Journal of Fluid Mechanics,* Vol. 815, 2017, pp. 1-25, https://doi.org/10.1017/jfm.2017.46.

Appendix

A.1. Tables of Test Conditions and Surface Pressures in H2K Experiments

In this section the detailed test condition of the H2K experiments, as well as the pressure measurements and root mean square pressure fluctuations in the dynamic tests are given. The detailed test conditions for the discussion of the flow field features (section 5.2.1), the comparison of cold and heated jets (section 5.2.2) and the discussion of pressure measurements (see 5.2.3) are summarized in Tab. A.1. The conditions for which a detailed analysis of the dynamic flow properties was performed in 5.2.4 are summarized in Tab. A.2. The pressures and the normalized root mean square pressure fluctuations measured for those conditions can be found in Tab. A.3 and Tab. A.4.

Tab. A.1: Summary of test conditions for general flow field discussion results

Description	Measurement	Figures	No. Engines	ϕ [°]	M_∞ [−]	p_0 [bar]	T_0 [K]	Re_∞ [−]	Total C_T [−]	α [°]	T_{CC} [K]
Nominal	Schlieren	Fig. 71, Fig. 72, Fig. 73, Fig. 84	1	-	5.29	4	450	2.36E+05	3.69	0	300
Nominal	Schlieren	Fig. 80, Fig. 86	3	0	5.29	4	450	2.36E+05	2.29	0	300
Nominal	Schlieren	Fig. 81	3	90	5.29	4	450	2.36E+05	2.23, 1.40	0	300
Nominal	Schlieren	Fig. 82	1, 3	0	5.29	4	450	2.36E+05	Sweep	0	300
Condensation	Condensation	Fig. 83a, b	3	0	5.29	4	450	2.36E+05	7, 16	0	300
Condensation	Condensation	Fig. 83c	3	0	5.29	4	450	2.36E+05	6	0	600
Heating	Schlieren	Fig. 84, Fig. 88	1	0	5.29	4	450	2.36E+05	3.85	0	589
Heating	Schlieren	Fig. 86, Fig. 87	3	0	5.29	4	450	2.36E+05	2.43	0	632
Nominal single-engine	Pressures	Fig. 89, Fig. 90, Fig. 91, Fig. 92, Fig. 93, Fig. 94	1	-	5.29	4	450	2.36E+05	Sweep	0	300
Mach variation	Pressures	Fig. 91	1	-	7.04	12.73	610	2.36E+05	Sweep	0	300
Re variation	Pressures	Fig. 92	1	-	5.29	12	450	7.07E+05	Sweep	0	300
α variation	Pressures	Fig. 93	1	-	5.29	4	450	2.36E+05	Sweep	10	300
Nominal three-engines	Pressures	Fig. 94, Fig. 95, Fig. 96, Fig. 97	3	0	5.29	4	450	2.36E+05	Sweep	0	300
Mach variation	Pressures	Fig. 95	3	0	7.04	12.73	610	2.36E+05	Sweep	0	300
Re variation	Pressures	Fig. 96	3	0	5.29	12	450	7.07E+05	Sweep	0	300
α variation	Pressures	Fig. 97, Fig. 98	3	0	5.29	4	450	2.36E+05	Sweep	10	300
ϕ variation	Pressures	Fig. 98	3	90	5.29	4	450	2.36E+05	Sweep	10	300
Exit-plane variation	Pressures	Fig. 100	3	0	5.29	4	450	2.36E+05	Sweep	0	300

Tab. A.2: Test conditions for the discussion of dynamic flow field features

Run	No of Engines	M_∞ [-]	C_T [-]	MFR [-]	T_{CC} [K]	Re [-]	q_∞ [bar]	p_∞ [mbar]	u_∞ [m/s]	ρ_∞ [kg/m³]	p_e [bar]	u_e [m/s]	ρ_e [kg/m³]	$p_{T,2}$ [bar]
90_5	1	5.29	3.69	49.55	303	2.43E+05	0.1076	5.484	871.858	0.0283	1.276	138.225	138.225	0.20041
93_7	3	5.29	2.29	30.76	300	2.40E+05	0.1061	5.408	872.238	0.0279	0.781	136.643	136.643	0.19758
115_2	1	5.29	3.85	51.67	589	2.38E+05	0.1049	5.348	870.959	0.0277	1.297	268.524	268.524	0.19539
117_2	3	5.29	2.43	32.65	632	2.55E+05	0.1044	5.319	850.194	0.0289	0.816	288.302	288.302	0.19449

Tab. A.3: Surface pressures of dynamic test conditions

Run	p 11 [mbar]	p 12 [mbar]	p 13 [mbar]	p 14 [mbar]	p 21 [mbar]	p 22 [mbar]	p 23 [mbar]	p 24 [mbar]	p 311 [mbar]	p 312 [mbar]	p 313 [mbar]	p 322 [mbar]	p 331 [mbar]	p 332 [mbar]	p 333 [mbar]	p 342 [mbar]
90_5	6.510	6.457	6.227	6.738	8.516	8.778	8.189	8.615	6.268	8.389	7.346	6.945	6.298	6.980	8.211	7.962
93_7	6.225	5.973	5.889	6.549	6.757	6.614	6.360	6.683	4.732	6.156	3.731	3.390	4.982	3.697	5.926	3.575

Tab. A.4: Normalized surface pressure fluctuations of dynamic test conditions

Run	p'_{rms}/q_∞ 11 [-]	p'_{rms}/q_∞ 12 [-]	p'_{rms}/q_∞ 13 [-]	p'_{rms}/q_∞ 14 [-]	p'_{rms}/q_∞ 21 [-]	p'_{rms}/q_∞ 22 [-]	p'_{rms}/q_∞ 23 [-]	p'_{rms}/q_∞ 24 [-]	p'_{rms}/q_∞ 311 [-]	p'_{rms}/q_∞ 312 [-]	p'_{rms}/q_∞ 313 [-]	p'_{rms}/q_∞ 322 [-]	p'_{rms}/q_∞ 331 [-]	p'_{rms}/q_∞ 332 [-]	p'_{rms}/q_∞ 333 [-]	p'_{rms}/q_∞ 342 [-]
90_5	0.00148	0.00182	0.00152	0.00148	0.00264	0.00285	0.00273	0.00256	0.00053	0.00257	0.00077	0.00033	0.00296	0.00094	0.00148	0.00182
93_7	0.00618	0.00740	0.00612	0.00650	0.01087	0.01114	0.01027	0.01102	0.00310	0.00360	0.00193	0.00464	0.00449	0.00272	0.00618	0.00740

A.2. Tables of Surface Pressures in VMK Experiments

In this section the surface pressures in the subsonic retro propulsion tests in VMK are summarized in Tab. A.5 and the normalized root mean square surface pressure fluctuations are summarized in Tab. A.6.

Tab. A.5: Surface pressures of subsonic retro propulsion tests in VMK

Run	p 02 [bar]	p 04 [bar]	p -04 [bar]	p 06 [bar]	p -06 [bar]	p 13 [bar]	p 15 [bar]	p 22 [bar]	p 24 [bar]	p 26 [bar]	p 8 [bar]	p 30 [bar]	p 32 [bar]	p 34 [bar]	p 36 [bar]	p 38 [bar]
4_4	1.165	1.169	1.171	1.144	1.168	1.074	1.068	1.062	1.058	1.045	1.048	0.758	0.772	0.769	0.749	0.747
4_5	1.242	1.239	1.244	1.211	1.248	1.101	1.091	1.092	1.084	1.080	1.075	0.647	0.667	0.667	0.642	0.642
4_6	1.343	1.324	1.328	1.291	1.336	1.147	1.122	1.141	1.144	1.128	1.130	0.530	0.544	0.565	0.526	0.529
5_1	1.434	1.435	1.430	1.458	1.208	1.192	1.233	1.223	1.218	1.215	0.319	0.398	0.416	0.331	0.341	1.464
10_3	1.106	1.105	1.107	1.106	1.104	1.067	1.067	1.061	1.062	1.069	1.063	0.905	0.920	0.921	0.895	0.906
10_4	1.130	1.135	1.126	1.130	1.129	1.084	1.084	1.084	1.088	1.084	1.083	0.849	0.887	0.871	0.861	0.858
10_5	1.167	1.170	1.161	1.161	1.169	1.111	1.115	1.104	1.122	1.108	1.108	0.785	0.816	0.818	0.794	0.781
10_6	1.192	1.196	1.194	1.195	1.193	1.139	1.142	1.123	1.144	1.165	1.133	0.718	0.771	0.777	0.717	0.736
28_4	1.155	1.156	1.151	1.151	1.146	1.080	1.085	1.082	1.077	1.097	1.094	0.873	0.896	0.894	0.867	0.855
28_5	1.176	1.176	1.172	1.176	1.174	1.114	1.127	1.103	1.113	1.114	1.103	0.820	0.847	0.853	0.828	0.821
28_6	1.197	1.196	1.208	1.195	1.205	1.147	1.142	1.161	1.154	1.139	1.143	0.752	0.792	0.799	0.767	0.754
8_5	1.170	1.171	1.176	1.174	1.173	1.109	1.114	1.129	1.112	1.096	1.099	0.828	0.841	0.854	0.819	0.828
8_6	1.211	1.213	1.206	1.208	1.203	1.146	1.145	1.149	1.138	1.127	1.135	0.790	0.815	0.833	0.790	0.791

Tab. A.6: Normalized surface pressure fluctuations of subsonic retro propulsion tests in VMK

Run	p'_{rms}/q_∞ 02 [-]	p'_{rms}/q_∞ 04 [-]	p'_{rms}/q_∞ -04 [-]	p'_{rms}/q_∞ 06 [-]	p'_{rms}/q_∞ -06 [-]	p'_{rms}/q_∞ 13 [-]	p'_{rms}/q_∞ 15 [-]	p'_{rms}/q_∞ 22 [-]	p'_{rms}/q_∞ 24 [-]	p'_{rms}/q_∞ 26 [-]	p'_{rms}/q_∞ 8 [-]	p'_{rms}/q_∞ 30 [-]	p'_{rms}/q_∞ 32 [-]	p'_{rms} p'_{rms} /q_∞ 34 [-]	p'_{rms}/q_∞ 36 [-]	p'_{rms}/q_∞ 38 [-]
4_4	0.292	0.244	0.271	0.258	0.216	0.221	0.210	0.233	0.212	0.010	0.292	0.244	0.271	0.258	0.216	0.221
4_5	0.270	0.216	0.239	0.227	0.169	0.177	0.165	0.185	0.163	0.011	0.270	0.216	0.239	0.227	0.169	0.177
4_6	0.261	0.199	0.217	0.201	0.164	0.147	0.137	0.143	0.157	0.019	0.261	0.199	0.217	0.201	0.164	0.147
5_1	0.225	0.172	0.189	0.182	0.084	0.099	0.093	0.097	0.085	0.012	0.225	0.172	0.189	0.182	0.084	0.099
10_3	0.289	0.279	0.283	0.274	0.220	0.218	0.215	0.224	0.221	0.016	0.289	0.279	0.283	0.274	0.220	0.218
10_4	0.289	0.274	0.277	0.276	0.216	0.214	0.203	0.216	0.213	0.016	0.289	0.274	0.277	0.276	0.216	0.214
10_5	0.288	0.272	0.283	0.282	0.206	0.200	0.197	0.213	0.204	0.017	0.288	0.272	0.283	0.282	0.206	0.200
10_6	0.290	0.274	0.287	0.281	0.191	0.188	0.184	0.198	0.187	0.017	0.290	0.274	0.287	0.281	0.191	0.188
28_4	0.273	0.258	0.258	0.254	0.204	0.200	0.206	0.211	0.206	0.016	0.273	0.258	0.258	0.254	0.204	0.200
28_5	0.271	0.268	0.269	0.259	0.206	0.202	0.194	0.209	0.201	0.018	0.271	0.268	0.269	0.259	0.206	0.202
28_6	0.282	0.273	0.276	0.270	0.190	0.190	0.178	0.193	0.181	0.018	0.282	0.273	0.276	0.270	0.190	0.190
8_5	0.272	0.254	0.267	0.263	0.204	0.201	0.190	0.206	0.200	0.018	0.272	0.254	0.267	0.263	0.204	0.201
8_6	0.285	0.268	0.269	0.261	0.184	0.180	0.177	0.189	0.182	0.019	0.285	0.268	0.269	0.261	0.184	0.180